HEXA-X-II

A holistic flagship towards the 6G network platform and system, to inspire digital transformation, for the world to act together in meeting needs in society and ecosystems with novel 6G services

Deliverable D4.3

Early results of 6G Radio Key Enablers

Co-funded by the European Union

6GSNS

Hexa-X-II project has received funding from the Smart Networks and Services Joint Undertaking (SNS JU) under the European Union's Horizon Europe research and innovation programme under Grant Agreement No 101095759.

Date of delivery:	30/04/2024	Version:	1.0
Project reference:	**101095759**	Call:	**HORIZON-JU-SNS-2022**
Start date of project:	01/01/2023	Duration:	30 months

Document properties:

Document Number:	D4.3
Document Title:	Early results of 6G Radio Key Enablers
Editor:	Ahmad Nimr (TUD)
Authors:	Mar Francis De Guzman (AAU), Han Yu (CHA), Hamed Farhadi (EAB), Italo Atzeni (OUL), Roberto Fantini (TIM), Sharief Saleh (CHA), Christian Drewes (APP), Nurul Huda Mahmood (OUL), Mohammad Hossein Moghaddam (QRT), Rafael Puerta (EAB), Gustavo Tejerina (OUL), Charitha Madapatha (CHA), Tommy Svensson (CHA), Efstathios Katranaras (SEQ), Alexander Chiskis (SEQ), Olivier Marco (SEQ), Bikshapathi Gouda (OUL), Omer Haliloglu (EBY), Eduardo Noboro Tominaga (OUL), Henk Wymeersch (CHA), Yu Ge (CHA), Hui Chen (CHA), José Miguel Mateos (CHA), Marie Le Bot (ORA), Bruno Jahan (ORA), Thibaut Rolland (ORA), Emmanuelle Bodji (ORA), Rodolphe Legouable (ORA), Jean-Marc Conrat (ORA), Bruno Melis (TIM), Davide Sorbara (TIM), Elisa Zimaglia (TIM), Meik Dörpinghaus (TUD), Florian Gast (TUD), Simon Lindberg (QRT), Andreas Wolfgang (QRT), Hardy Halbauer (NGE), Ravi Sharan (NGE), Le Hang Nguyen (NGE), Raquel Esteban Puyuelo (EAB), Athanasios Stavridis (EAB), Bo Xu (EAB), Stanislav Zhekov (EAB), Heunchul Lee (EAB), Jaeseong Jeong (EAB), David Sandberg (EAB), Muris Sarajlić (EAB), Luis G. Uzeda Garcia (NFR), Andre Noll Barreto (NFR), Raf Berkvens (IMEC), Dani Korpi (NFI), Jose Flordelis (SON), Rreze Halili (IMEC), Amitha Mayya (BI), Bertram Gunzelmann (APP), Benedikt Schweizer (APP), Philipp Schulz (TUD), Ivo Bizon Franco de Almeida (TUD), Sinuo Ma (TUD), Pekka Kyösti (OUL), Katsuyuki Haneda (AAU), Mikhail Wilhelm (APP), Nil Zaev (APP), Tanesh Kumar (AAU), Petri Mähönen (AAU), Ilkka Harjula (NFI), Oskari Tervo (NFI), Arto Lehti (NFI)
Contractual Date of Delivery:	30/04/2024
Dissemination level:	PU[1]/SEN
Status:	Final
Version:	1.0
File Name:	Hexa-X-II D4.3_v1.0_final

Revision History

Revision	Date	Issued by	Description
0.1	19/09/2023	Hexa-X-II WP4	Document created
0.2	06/03/2024	Hexa-X-II WP4	All contents integrated
0.3	11/03/2024	Hexa-X-II WP4	Compiled version for external review
0.4	30/03/2024	Hexa-X-II WP4	External technical comments addressed
0.5	01/04/2024	Hexa-X-II WP4	Extensive editorial revisions

[1] SEN = Sensitive, only members of the consortium (including the Commission Services). Limited under the conditions of the Grant Agreement

PU = Public

0.6	12/04/2024	Hexa-X-II WP4	Comments during GA review addressed
0.7	24/04/2024	Hexa-X-II WP4	Continuing the GA review
1.0	29/04/2024	Hexa-X-II WP4	Final version

Abstract

This report provides initial results on selected key enablers for 6G radio design, developed within Hexa-X-II work package 4: "Radio Evolution and Innovation". The report begins with an overview of holistic radio design and corresponding enablers. Subsequent technical studies cover a range of topics in channel modelling, radio architecture and deployment for communication and sensing, model and data-driven transmission schemes and signal processing algorithms, spectrum access, and radio trustworthiness. Evaluation results are obtained through simulation frameworks and proof-of-concept platforms. This analysis provides inputs for the second iteration towards the end-to-end 6G system design in the Hexa-X-II project.

Keywords

6G, radio access technology, physical layer (PHY), medium access control (MAC), channel modelling, multiple-input multiple-output (MIMO), distributed MIMO (D-MIMO), massive MIMO (mMIMO), multi-user MIMO (MU-MIMO), integrated access and backhaul (IAB), beamforming, 1-bit analogue-to-digital converter (1-bit ADC), reconfigurable intelligent surfaces (RIS), waveform, artificial intelligence/machine learning (AI/ML), AI-driven air interface design, joint communication and sensing (JCAS), terrestrial network/non-terrestrial network (TN/NTN), spectrum sharing, frequency range 1 (FR1), frequency range 2 (FR2), sub-terahertz (sub-THz), terahertz (THz), spectrum access, proof of concept (PoC), physical layer security (PHY security).

Executive Summary

This report is the second public deliverable (D4.3) of work package 4 (WP4) - “Radio Evolution and Innovation”. It provides an updated perspective on selected radio design enablers introduced in the first public deliverable D4.2 [HEX223-D42] along with preliminary results based on simulation and proof-of-concepts (PoCs) evaluation. The report contributes towards the end-to-end 6G system design in the Hexa-X-II project.

The report begins with an overview of the concept holistic radio design process, aimed at fulfilling emerging communication and sensing requirements, taking into account regulatory aspects and value consideration in sustainability, trustworthiness, and inclusiveness. These considerations pose constrains on material and energy usage and introduce new value-based requirements. The radio design is supported by various technical enablers across different stages. Some enablers address extreme requirements, such as exploring new spectrum, to enable high data rate communication and precise sensing. Various multiple-input multiple-output (MIMO) techniques assisted by reconfigurable intelligent surfaces (RIS), including distributed MIMO (D-MIMO), massive MIMO (mMIMO), and multiuser MIMO (MU-MIMO) have the potential to improve coverage, spectral efficiency, and energy efficiency. Implementing these technologies requires new hardware components and leads to a new propagation behaviour that needs to be understood through modelling tools. Other enablers focus on efficient resource utilization, such as joint communication and sensing (JCAS) for sharing network infrastructure and devices, radio resources, and signals to obtain sensing and localization information. Flexible spectrum access and sharing mechanisms enable efficient utilization of scarce spectrum resources. Moreover, a set of enablers aim to enhance key value indicators (KVIs), including mechanisms to improve security, extend connectivity, and reduce energy consumption. Furthermore, advanced computational AI/ML tools are exploited in the design and operation to provide efficient solutions. Additionally, simulation and prototyping platforms are crucial for validating radio design prior to commercial deployment. The report then delves into the evaluation of various enablers, highlighting preliminary evaluation outcomes.

The report explores channel models for the sub-THz and THz bands, and modelling aspects for RIS and JCAS. It presents extensions of existing standard channel models, including adjustments for sub-THz parameters, near-field effects, and the reflection coefficient of various materials at the sub-THz band. Additionally, it examines the impacts of THz frequency path loss on coverage, as well as signal modelling in RIS environments and JCAS-related channel features essential for sensing.

The report outlines various architecture and transmission schemes. For D-MIMO, it introduces a clustering method to optimize the worst-case spectral efficiency by maintaining relatively similar performance for all users on average. It presents a distributed beamforming method incorporating over-the-air (OTA) signalling that improves average sum-rate performance in both unicasting and multicasting scenarios compared to local and centralized methods. It highlights a coherent joint transmission (CJT) strategy using analogue fronthaul (FH) links combined with centralized processing. For MU-MIMO, the performance of rotary uniform linear array (ULAs) is investigated, showing improvement over static ULAs. A flexible effective antenna (EA) is proposed to reduce complexity by reducing channel matrix dimension. For mMIMO, the report discusses leveraging a sub-6 GHz macro network to support sub-THz signals with ML-assisted channel state information (CSI). One-bit analogue-to-digital converters (ADCs) are considered in multi-cell setup for low-complexity implementation, showing significant sum-rate improvements over traditional methods such as exhaustive single-UE data detection with zero forcing (ZF)/minimum mean squared error (MMSE) receivers. It compares performance of one-bit digital-to-analogue convertors (DACs) against full-resolution DACs noting similar performance with lower complexity and power consumption. Other topics focus on the analysis of sub-THz mMIMO in various deployment and coded caching. The report emphasizes RIS technology for enhancing D-MIMO and integrated access and backhaul (IAB) transmissions, analysing SINR and energy efficiency, coverage enhancements, and the challenges of channel estimation under mobility. Additionally, an innovative RIS reflecting modulation is proposed for low-rate data transmission in RIS-assisted systems.

The report delves into the development of extended and novel waveform and modulation schemes, specifically tailored for (sub-)THz communications, which are important assets to meet 6G requirements on spectral and energy efficiency. These include an analysis of standardized waveforms and their numerology in sub-THz

taking hardware models into account, and the design of 1-bit quantized zero crossing modulation (ZXM) and polar hardware-friendly constellations. Additionally, it introduces waveform and modulation enhancement approaches, such as adaptive multicarrier modulation scheme resistant to Doppler shifts and out-of-band emissions. It presents a new matrix design for low-density parity check (LDPC) codes, and an optimized delayed bit interleaved coded modulation (DBICM).

The report explores the convergence of wireless technology evolution and AI/ML tools, aiming to meet the increasing demands posed by 6G networks. It presents a systematic exploration of AI-driven solutions across four pivotal aspects of radio interface design: modulation and coding, CSI acquisition and compression, MIMO transmissions, and compensation for hardware impairments. The application of AI to waveform modulation and coding not only optimizes established techniques but also introduces novel signal design approaches, promising significant enhancements in spectral efficiency and reliability. The report further details advancements in AI-based CSI acquisition, highlighting the role of intelligent compression and prediction techniques in minimizing overhead while maximizing spectral utilization. Additionally, AI-enhanced MIMO transmissions presents innovative solutions for specific challenges, such as imperfect or limited CSI, power consumption optimization, and pilot assignment. Furthermore, it highlights the potential of AI to mitigate hardware impairments, with a particular focus on power amplifier non-linearities.

The report provides assessment of JCAS deployment and resource optimization. It examines the deployment of emerging 6G technologies, such as non-terrestrial networks (NTN) and RIS, for localization purposes, showing that positioning accuracy depends on the satellite position relative to RIS orientation, and is bounded by the weak RIS path. Sensing fusion is studied using random finite set theory for the integration of monostatic and bistatic deployment, and relies on non-coherent fusion methods within a central processing unit in bistatic deployment. The impact of cyclic prefix (CP) duration on sensing distance in OFDM-based bistatic sensing systems is investigated, showing the dependency of sensing distance on angles of arrival, and that increasing the CP duration increases the maximum sensing distance. Other study explores enhancing communication and positioning performance through the optimization of beamformers at base station (BS), user equipment (UE), and RIS, while utilizing tracking estimates of the UE position and orientation. It illustrates that various beamforming strategies are needed to tackle different uncertainty levels about the UE's position and orientation. Lastly, it introduces a protocol to facilitate bistatic sensing between UEs while exploiting network assistance.

Flexible spectrum access solutions are detailed in the report, covering technical enablers for spectrum sharing and low-latency spectrum access. To facilitate a smooth transition from 5G to 6G, the report presents derivations of the requirements for multi-radio access technology (RAT) spectrum sharing. It particularly focuses on spectrum sharing between terrestrial networks and satellite services in the S and Ku bands, refining model assumptions to extend sharing opportunities, and proposing optimization for handover within NTN. Methods to access higher frequency ranges up to sub-THz with a low access latency are derived, alongside probabilistic random-access methods to augment scheduled access when interference created to others is acceptable. Additionally, the report introduces a method to predict interference based on a transformer model.

Trustworthiness is one of the three core values targeted by Hexa-X-II. Different aspects of a trustworthy 6G radio design are explored in this report. These include, solutions for exploiting the physical properties of wireless channel and device hardware to ensure security against eavesdropping attack; investigating methods to assess the impact of jamming against and localize a jammer; and analysing the security and privacy analysis of a general cellular JCAS system, including the UE related aspects.

The report highlights various PoCs and simulation tools for the evaluation of 6G technologies. Key areas include the development of a link-level simulation tool for evaluation of various schemes like D-MIMO and beamforming. It introduces an AI-native air interface PoC, demonstrating the practical applications of ML in enhancing CSI feedback and facilitating pilotless OFDM transmissions. It provides an overview of flexible modulation and transceiver design. JCAS is explored in a PoC, demonstrating the potential of using the same hardware for both communication and sensing. Furthermore, the report investigates crucial aspects of power consumption in JCAS systems, providing insights into power efficiency strategies. An EMF assessment framework is developed for evaluating electromagnetic field (EMF) exposure from advanced MIMO systems. Initial results for MIMO deployments demonstrate that EMF exposure levels are far below the international and EU recommended EMF limits. Lastly, comprehensive channel measurement data and modelling tools are presented, offering valuable resources for further research and development in 6G technology.

Table of Contents

List of Tables

List of Figures

Acronyms and abbreviations

Term	Description
6DoF	6 Degrees of Freedom
A2C	Advantage Actor Critic
AAS	Active Antenna System
AE	Antenna Element
AI	Artificial Intelligence
ANN	Artificial Neural Network
AP	Access Point
API	Application Programming Interface
ARoF	Analogue Radio over Fibre
ASA	Azimuth Angle Spread of Arrival
ASD	Azimuth Angle Spread of Departure
AuE	Auto Encoder
AWG	Arbitrary Waveform Generator
BCE	Binary Cross Entropy
BER	Bit Error Rate
BG	Base Graph
BLER	Block Error Rate
BR	Best Response
BR-GS	Best Response – Group Specific
BS	Base Station
CCO	Constrained Cardinality Optimization
CDF	Cumulative Distribution Function
CDL	Clustered Delay Line
CHO	Conditional Handover
CM	Coded Modulation

CNN	Convolutional Neural Network
CoMP	Coordinated Multi-Point
CPE	Common Phase Error
CP-OFDM	Cyclic Prefix Orthogonal Frequency Division Multiplexing
CPU	Central Processing Unit
CQI	Channel Quality Indicator
CRB	Cramér-Rao Bound
CRC	Cyclic Redundancy Check
CS	Common Signalling
CSF	Channel State Feedback
CSI	Channel State Information
CSI-RS	Channel State Information Reference Signal
CSMA	Carrier-Sense Multiple Access
D2D	Device-to-Device
DAC	Digital-to-Analogue Converter
DAPS	Dual-Active Protocol Stack
DBICM	Delayed Bit Interleaved Coded Modulation
DFE	Digital Frontend
DFT	Discrete Fourier Transform
DL	Downlink
DLR	Deutsches Zentrum für Luft- und Raumfahrt (German Aerospace Centre)
D-MIMO	Distributed MIMO
DMRS	Demodulation Reference Signal
DNN	Deep Neural Network
DPD	Digital Pre-Distortion
DQN	Deep Q-Network
DRU	Distributed Radio Unit
DS	Delay Spread

DSP	Digital Signal Processor
DSS	Dynamic Spectrum Sharing
DU	Distributed Unit
E2E	End-to-End
EM	Electromagnetic
eMBB	Enhanced Mobile BroadBand
EMD	Empirical Mode Decomposition
EMF	Electromagnetic Field
ES	Earth Station
eType2	Enhanced Type2
EVM	Error Vector Magnitude
FCNN	Fully Connected Neural Network
FDD	Frequency Division Duplexing
FMCW	Frequency Modulated Continuous Wave
FoV	Field of View
FR	Frequency Range
FSS	Fixed Satellite Service
GB	Gradient based
GG	Greedy Genie
GNN	Graph Neural Network
GoB	Grid of Beams
HAPS	High Altitude Platform Station
HARQ	Hybrid Automatic Repeat Request
HO	Handover
HW	Hardware
I/N	Interference to Noise ratio
ICIC	Inter-Cell Interference Cancellation
ICNIRP	International Commission on Non-Ionizing Radiation Protection

ICRB	Intrinsic Cramér-Rao Bound
ID	Identifier
IE	Information Element
IF	Intermediate Frequency
IMF	Intrinsic Mode Function
IMT	International Mobile Telecommunications
InF	Indoor Factory
InH	Indoor Hotspot
IoT	Internet of Things
JCAS	Joint Communication and Sensing
JQRM	Jointly Mapped Quadrature Reflection Modulation
JRM	Jointly Mapped Reflection Modulation
JRPM	Jointly Mapped Reflection Pattern Modulation
JT-CoMP	Joint Transmission Coordinated Multi-Point
KPI	Key Performance Indicator
KVI	Key Value Indicator
LBT	Listen Before Talk
LCG	Learn to Code on Graph
LDPC	Low Density Parity Check
LEO	Low-Earth Orbit
LLR	Log-likelihood ratio
LNA	Low-Noise Amplifier
LoS	Line-of-Sight
LS	Least-Squares
LSP	Large-Scale Parameters
LTE	Long Term Evolution
MB-ML	Model-Based Machine Learning
MCS	Modulation and Coding Scheme

MDS	Maximum Distance Separable code
MF	Matched Filter
MIMO	Multiple-Input Multiple-Output
MISO	Multiple-Input Single-Output
ML	Machine Learning
mMIMO	Massive Multiple-Input Multiple-Output
MMSE	Minimum Mean Squared Error
mMTC	Massive Machine-Type Communications
mmWave	Millimetre-wave
MPC	Multipath Components
MRC	Maximum Ratio Combining
MRSS	Multi-RAT Spectrum Sharing
MRT	Maximum Ratio Transmission
MSE	Mean Squared Error
MU-MIMO	Multi-User MIMO
MUT	Material Under Test
NAM	Neural Antenna Muting
NC-JT	Non-Coherent Joint Transmission
NLoS	Non-Line-of-Sight
NN	Neural Network
NR	New Radio
NTN	Non-Terrestrial Network
NW	Network
OCB	Occupied Channel Bandwidth
OFDM	Orthogonal Frequency-Division Multiplexing
OMP	Orthogonal Matching Pursuit
OTA	Over-the-Air
PA	Power Amplifier

PAM	Pulse Amplitude Modulation
PAPR	Peak-to-Average Power Ratio
PCI	Physical Cell Indicator
PDCCH	Physical DL Control Channel
PHY	Physical Layer
PMI	Precoding Matrix Indicator
PN	Phase Noise
PoC	Proof-of-Concept
PPS	Pulse-Per-Second
PRB	Physical Resource Blocks
PSO	Particle Swarm Optimization
QAM	Quadrature Amplitude Modulation
QoS	Quality of Service
RAT	Radio Access Technology
RCS	Radar Cross Section
RF	Radio Frequency
RIS	Reconfigurable Intelligent Surface
RL	Reinforcement Learning
RLC	Radio Link Control
RM	Reflection Modulation
RMSE	Root-Mean-Square Error
RNN	Recurrent Neural Network
RPC	Remote Procedure Calls
RPM	Reflection Pattern Modulation
RR	Round Robin
RRH	Remote Radio Head
RSRP	Reference Signal Received Power
RU	Radio Unit

RX	Receive
SA	Standalone
SAR	Specific Absorption Rate
SB	Sub-Band
SC-FDE	Single Carrier Frequency Domain Equalization
SCS	Subcarrier Spacing
SDR	Software Defined Radio
SE	Spectral Efficiency
SER	Symbol Error Rate
SF	Shadow Fading
SFN	Single Frequency Network
SIB	System Information Block
SINDR	Signal to Interference, Noise and Distortion Ratio
SINR	Signal to Interference and Noise Ratio
SISO	Single-input and Single-output
SL	Supervised Learning
SLNR	Signal to Leakage and Noise Ratio
SNR	Signal-to-Noise Ratio
SRM	Separately Mapped Reflection Modulation
SSB	Synchronization Signal Block
SSL	Semi-Supervised Learning
SSL	Semi-supervised Learning
STFBC	Space-Time-Frequency Block Code
STU	Single Transmission Unit
SU-MIMO	Single-User MIMO
SVD	Singular Value Decomposition
TA	Timing Advance
TDD	Time-Division Duplex

TN	Terrestrial Network
TRX	Transceiver
TX	Transmit
TXRU	Transmit Radio Unit
UAV	Unmanned Aerial Vehicle
UC	Use Case
UE	User Equipment
UL	Uplink
ULA	Uniform Linear Array
URLLC	Ultra-Reliable Low-Latency Communications
VNA	Vector Network Analyzer
WP4	Work Package 4
XR	Extended Reality
ZF	Zero Forcing
ZSA	Zenith Angle Spread of Arrival
ZSD	Zenith Angle Spread of Departure
ZXM	Zero-Crossing Modulation

1 Introduction

Hexa-X-II is the 6G Flagship project under the European Union Horizon Europe research and innovation program, Smart Network and Services Joint Undertaking (SNS JU), for building a system blueprint of sustainable, inclusive, and trustworthy 6G platform. This document is the third deliverable (D4.3) of work package 4 (WP4) - "Radio Evolution and Innovation". The work in WP4 focuses on the development of radio access solutions that meet the requirements of 6G services for communication and sensing. The research and innovation within WP4 focus on the following key aspects:

- Sustainable, trustworthy and inclusive holistic radio design
- Towards THz communications
- Joint communications and sensing
- Intelligent radio air interface design
- Flexible spectrum access solutions

The second deliverable of WP4 (D4.2) [HEX223-D42] analyses 6G use cases and defines 6G radios scenarios and, along with corresponding key performance indicators (KPIs) and key value indicators (KVIs) requirements for communications and sensing. It also presents and describes key 6G radio design enablers which guide the work in WP4.

1.1 Objective of the document

This report presents the initial analysis results of selected radio enablers described in (D4.2) [HEX223-D42]. These enablers cover various aspects of holistic radio design at both the physical layer (PHY) and medium access layer (MAC), including new spectrum and access solutions, efficient transmission schemes, architecture and deployment approaches for both communication and sensing. It also discusses radio link modelling and simulation tools, advanced signal processing and algorithms based on artificial intelligence (AI) and machine learning (ML), as well as proof-of-concept (PoC) and prototyping platforms. In addition, solutions are considered for enhancing KVI-related to sustainability, inclusiveness, and trustworthiness. These include optimization methods for improving energy efficiency, integration of terrestrial network (TN) and non-terrestrial network (NTN), physical layer security, and techniques to overcome jamming. The report contributes to the Hexa-X-II WP4 objectives as outlined in the following:

WPO 4.1: Develop an inclusive, trustworthy, and flexible radio design tailored to meet given 6G KPIs and KVI requirements through analysis and integration of HW architectures, transmission schemes and security solutions.

Sustainable, trustworthy and inclusive holistic radio design is discussed in D4.2, which defines radio scenarios and determines KPIs and KVIs requirements for communications and sensing services based on initial analysis of use cases. Moreover, D4.2 presents the impact of these use cases and scenarios on various components of the radio design. Additionally, D4.2 describes enablers for flexible, inclusive, sustainable and trustworthy 6G radio design.

In D4.3, Chapter2 introduces a holistic radio design framework and categorizes various enablers into groups to facilitate the integration of the radio enablers in the end-to-end (E2E) 6G system. The radio scenarios and use cases are revised and updated based on D2.1 [HEX223-D12]. Chapter 9 provides initial results of radio enablers focusing on trustworthiness, including secret key generation based on PHY security, analysing the impact of jamming on communication, and evaluating of sensing security. Moreover, Section 8.3 focuses on inclusive radio interface via TN/NTN enhancement, particularly presenting initial results on handover. In addition, Section 10.6 presents a simulation tool for electromagnetic field (EMF) assessment, and provides examples of various deployment scenarios.

WPO 4.2: Provide a suitable channel model and develop novel broadband air-interface techniques to enable energy-efficient operations in the (sub-)THz bands, including new energy-efficient waveforms/modulations and advanced massive MIMO techniques.

While D4.2 provides descriptions of the corresponding enablers for transmissions in the sub-THz range, D4.3 introduces their initial numerical results. Section 3.1 presents a channel modelling framework, Section 3.2

introduces a methodology for modelling near-filed components, Section 3.3 provides initial analysis of THz coverage, and Section 3.4 presents results on wave interaction with material covering various frequency ranges (5-40 GHz, 110-170 GHz, 170-260 GHz).

Initial results on sub-THz waveforms are presented in Section 5.1, for 5G new radio (5G NR) compatible waveforms, and for zero-crossing modulation (ZXM). A link modelling simulation framework is introduced in Section 10.1 for the evaluation of various channels, including sub-THz. Section 4.2.2 presents initial results on 1-bit analogue-to-digital (ADC) in a fully digital massive multiple-input multiple-output (mMIMO), which is particularly considered as a solution for sub-THz radio. Additionally, Section 4.1.4 provides results on improving beam search in sub-THz distributed MIMO (D-MIMO) scenario assisted by sub-6 GHz macro network.

WPO 4.3: Provide solutions that enable flexible, cross-functional joint communication and sensing over a unified radio infrastructure, including new architectures, signals, methods, and protocols.

Joint communication and sensing (JCAS) enablers are described in D4.2 considering deployment, waveforms and resource allocation, as well as security and privacy aspects. D4.3 provides initial evaluation results of several topics, while others are still under investigation. In particular, Section 7.1 focuses on deployments, including NTN and reconfigurable intelligent surfaces (RIS)-aided localization, integration of mmWave monostatic and bistatic sensing, and multistatic sensing. Section 7.2 is dedicated to JCAS resource optimization considering MIMO and OFDM. Section 6.1.2 introduces results on AI-based JCAS waveform and proceeding performance under hardware impairments. Additionally, security and privacy aspect of JCAS are presented in the context of worthiness in Section 9.4 and Section 9.5. An initial PoC on bistatic JCAS is presented in Section 10.4. Additionally, Section 3.6 delves into JCAS channel modelling feature requirements.

WPO 4.4: Design intelligent radio air interface to improve one or a combination of KPIs including spectral efficiency, energy efficiency, coverage, or lower cost at FR1 and FR2 spectrum.

D4.2 presents various air interface methods for improving communication in frequency rang 1 (FR1) and FR2. These include AI-driven air interface design, D-MIMO transmissions, and RIS-assisted transmission schemes. Initial evaluation results are introduced in D4.3. In Section 4.1, various D-MIMO architectures and beamforming designs are evaluated in terms of throughput, spectral efficiency, and coverage. Section 4.2 focuses on massive and multiuser MIMO architectures for enhancing energy efficiency. Results on assisted RIS transmission are presented in Section 4.3 for channel estimation, control procedures, and employing RIS reflecting patterns to convey information. Moreover, RIS signal modelling is discussed in Section 3.5, with results on enhancing the link budget. Chapter 6 focuses on AI/ML-based solutions for learning waveforms, channel state information (CSI) acquisition and feedback, MIMO optimization, and for hardware impairment compensation. Initial results on AI-native air interface PoC are presented in Section 10.3.

WPO 4.5: Develop spectrum sharing and medium access mechanisms for enabling an efficient transition to 6G (coexistence) and low-latency service access.

D4.2 describes solutions for flexible spectrum access solutions, including enablers for spectrum sharing and for low-latency spectrum access. D4.3 introduces improvements to the assumptions and models in spectrum sharing. Studies are proposed for the case of co-channel coexistence of international mobile telecommunications (IMT) and fixed satellite service (FSS) ground stations in Section 8.1.1. Section 8.1.2 provides a study on TN-NTN spectrum sharing in the S-band (2 GHz) using stochastic geometry. Section 8.1.3 discusses multi-radio access technology (RAT) spectrum sharing (MRSS) with 5G. Section 9.2.1 presents initial results on spectrum access methods for sub-THz, which can also be applied to FR 2. Section 8.2.2 presents a probabilistic approach for risk-informed random access for local communication, considering criteria such as inducing extra interference to other users.

1.2 Structure of the document

Chapter 2 presents an overview of the holistic radio design concept and introduces group of enablers, around which the remaining chapters are structured. Each main section in these chapters consists of subsections focusing on interrelated topics. Subsections present studies and initial results following an extended abstract structure; They begin by presenting the main problem, then introduce the methodology and system model, and

finally summarize the numerical results and their discussions. Further details are presented in the appendices under similar tiles.

Chapter 3 is dedicated to channel modelling in various scenarios, including sub-THz, coverage analysis for THz, link modelling for RIS, and channel modelling concepts for JCAS. Chapter 4 introduces MIMO transmission solutions, with a particular focus on architectures and deployment scenarios for D-MIMO, mMIMO, and RIS-assisted transmission. Chapter 5 presents waveforms and modulations for 6G radio transmissions in sub-THz and other frequency ranges. Chapter 6 discusses radio air interface design leveraging AI/ML methods, covering techniques for waveform and constellation learning, CSI prediction and feedback, solutions for tackling MIMO challenges, and AI for hardware impairment compensation. Chapter 7 covers radio enablers for joint communications and sensing, focusing on deployment and recourse optimization. Chapter 8 focuses on MAC aspects for flexible spectrum sharing and coexistence, random access methods, and enhancement of TN/NTN integration. Chapter 9 summarizes topics and studies related to trustworthiness in communication and sensing. Chapter 10 is dedicated to validation, including PoC and simulation tools. The report is concluded in Chapter 11.

2 Sustainable, trustworthy and inclusive holistic radio design

This chapter presents a brief overview of holistic radio design aspects, which are detailed in D4.2 [Chapter 2, HEX223-D42]. First, Section 2.1 provides an overview of the generic design process, highlighting various considerations. Section 2.2 describes the use cases analysis procedure and provides an update on the radio scenarios in relation to HEXA-X-II use cases. A radio design framework is presented in Section 2.3, with an overview of various modules and groups of enablers. Section 2.4 focuses on architecture and deployment options in the context of functional split placement.

2.1 Holistic radio design process overview and technical enablers

Holistic radio design integrates comprehensive considerations, from technical specifications to societal impacts, ensuring that the systems developed are not only technologically advanced but also sustainable, trustworthy, and inclusive.

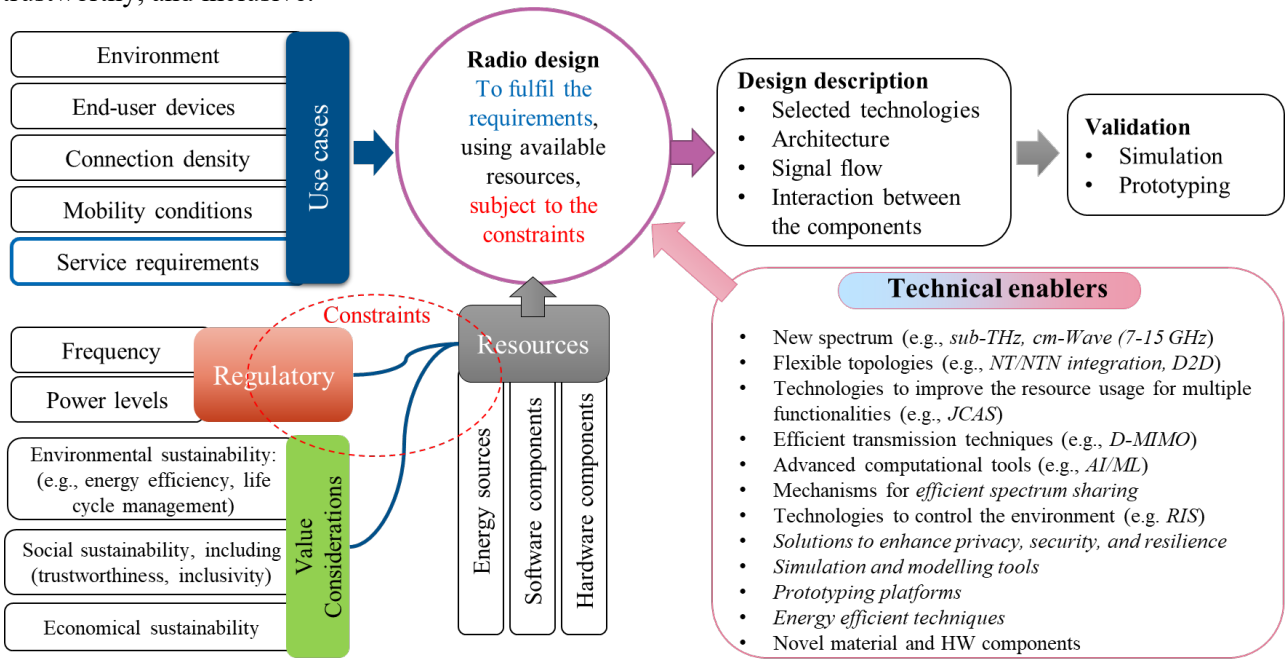

Figure 2-1: Radio design process, emphasising value consideration and technical enablers of HEXA-X-II.

As shown in Figure 2-1, the radio design process is a dynamic framework that evolves with each generation of technology. At its core, it takes specific use cases and their associated requirements as inputs, with the goal of satisfying these requirements through innovative solutions under given constrains, such as regulatory aspects for frequency and spectrum usage, as well as power level. Moreover, 6G radio design in HEXA-X-II emphasizes key values considerations for environmental, social, and economic sustainability [HEX223-D31]. These constraints impose restrictions on the usage of resources for energy, material, software/hardware components. Therefore, innovative technologies and solutions are needed to balance performance with value-based requirements. These include

- New spectrum for meeting the increased demand on data rate. This requires exploring the corresponding channel model, radio frequency (RF) transceiver, hardware (HW) components, and advanced waveform and transmission techniques. In HEXA-X-II, WP4 studies (sub)-THz communication (above 100 GHz) and cm-Wave (7-15 GHz).
- Flexible topologies enable adaptable network configurations to efficiently meet varying use cases demands and environment, as discussed in [HEX223-D32]. WP4 investigates the impact of various topologies on the radio design, particularly the integration of terrestrial network (TNs) and non-terrestrial networks (NTNs), as well as device-to-device (D2D) communication.
- Technologies to improve the resource usage for multiple functionalities, such as joint communications and sensing (JCAS), which aims to leverage network infrastructure and devices for providing sensing

and localization information. Such information in turns can be used to improve overall communication. WP4 explores various approaches for JCAS deployment and resource sharing across different frequency ranges in Chapter 7.

- Efficient transmission techniques to improve spectral efficiency, energy efficiency, and coverage. WP4 considers various multiple-input multiple-output (MIMO) techniques in Chapter 4, at different frequency ranges, including distribute MIMO (D-MIMO), massive MIMO (mMIMO), and multiuser MIMO (MU-MIMO). WP4 also investigates advanced and enhanced waveforms and modulations schemes in Chapter 5.
- Advanced computational tools, such as artificial intelligence (AI) / machine learning (ML) models. WP4 considers AI/ML for signal processing, resource allocation, and HW impairment compensation in Chapter 6.
- Mechanisms for efficient spectrum sharing to improve spectrum utilization and reduce interference among different radio access technologies (RATs). For instance, WP4 explores sharing solutions for non-terrestrial networks (NTN) spectrum, such as fixed satellite, with terrestrial networks (TN), as well as multi-RAT spectrum sharing (MRSS) in Chapter8.
- Technologies to control the propagation environment, such as deploying reconfigurable intelligent services (RIS), which is considered in WP4 for mitigating blockage and improving coverage, as introduced in Section 4.3.
- Solutions to enhance, privacy, security, and resilience, such as exploiting channel characteristics in physical layer (PHY) security, and sensing and localization to identify and localize jamming. Theses aspects are investigated in Chapter 9.
- Energy efficient techniques, including optimization of deployment, HW, and transmission schemes, in addition to solution for reducing signalling overhead. WP4 emphasises energy efficiency in the design and operation of radio systems.
- Novel material and HW components with minimal environmental impact in terms of reduced energy consumption, and improved durability and recyclability. HW related enablers are presented in [HEX224-D53].

The outputs of the design process are the technologies chosen, system architecture, and detailed mapping of signal flows and component interactions. Validation is executed through simulations and prototyping, ensuring that the system design meets its intended goals. The validation process is enabled by

- Simulation and modelling tools to provide mathematical models for channels and HW components for design and evaluation. WP4 focuses on channel and link modelling for link-level simulations, which are presented in Chapter 3.
- Prototyping platforms for experimental validation prior to commercialization. WP4 utilizes such platforms in various proof-of-concept (PoCs), as introduced in Chapter 10.

2.2 Use cases analysis and radio scenarios

A successful radio design begins with a precise definition of its use cases. These use cases represent diverse needs and scenarios in which the radio system operates, from urban high-density connectivity to remote access in rural areas. Over generations, use cases have evolved, with increased demands for bandwidth, low latency, high reliability, and massive connectivity. Defining specific radio scenarios and their requirements sets the foundation for a radio system design.

In a typical process, as illustrated in Figure 2-2, a wide range of application use cases are analysed and categorized into families with similar service requirements. The service requirements are mapped to corresponding radio requirements, and a set of scenarios are derived based on extreme radio requirements. The grouping based on extreme requirements provides the most challenging and demanding conditions for radio design. This approach ensures that a radio system designed and optimized for an extreme scenario can meet diverse economic and social needs. A comprehensive analysis based on HEXA-X-II 6G use cases is presented in [Section 2.3, HEX223-D42], leading to four scenarios, each focusing on extreme requirements in one parameter while allowing flexibility in other parameters as flexible.

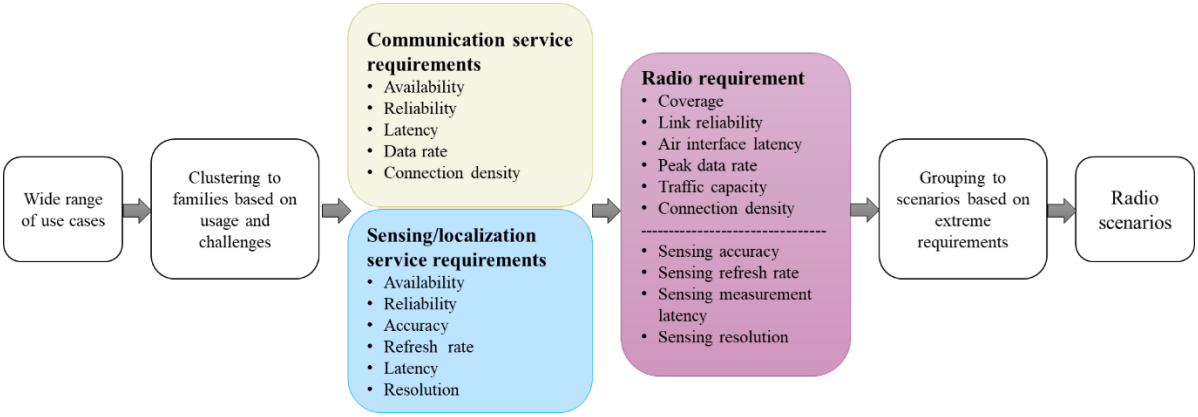

Figure 2-2: Framework for use cases analysis and radio scenario definition.

These scenarios are denoted as (1) Extreme coverage, (2) Extreme data rate, (3) Extreme connection density, (4) Extreme low latency and high reliability. Table 2-1 provides a summary of these scenarios, including radio requirements and various sub-scenario parameters, with a mapping to the HEXA-X-II use case families presented in [HEX223-D12], and the ITU usage scenarios [ITU-M.2160].

Table 2-1: Summary of basic radio scenarios with corresponding radio requirements.

	Extreme coverage	**Extreme data rate**	**Extreme connection density**	**Extreme low latency and high reliability**
ITU usage scenario	Ubiquitous connectivity	AI and communication, Immersive communication	Immersive communication, Massive communication	Hyper reliable and low-latency communication, Integrated sensing and communication
HEXA-X-II use case family	Fully connected world, Physical awareness	Immersive experience	Digital twins Trusted environment	Collaborative robots
Representative HEXA-X-II use case	Ubiquitous network, Network-assisted mobility	Seamless immersive reality	Realtime digital twins Human-centric services	Cooperative mobile robots
Radio devices	Enhanced 5G (mMTC, eMBB) devices, Energy neutral devices	Access points for backhaul, Gateway for sensors	Reliable high data rate with bounded latency devices	High reliability & low latency devices
Environment	Mobile indoor, Public indoor, Outdoor (urban, suburban, rural),	Controlled and semi-controlled indoor and outdoor	Urban indoor/outdoor with high density of users High-rise	Indoor, Embedded network
Mobility	Static, up to 300 km/h	Static, up to 10 km/h, controlled mobility (velocity information available)	Static, up to 100 km/h	Static, up to 20 km/h, controlled mobility (velocity information available)
Deployment options	Long/short range, Fixed/temporary, Mobile infrastructure, TN/NTN integration	Small cell, Fixed access, D2D, Sensor network with a gateway	High density of cells, Macro cell, Micro cell, Cell-free	Small cell, On premises, Infrastructure, Sensor network
Frequency	Sub-GHz, sub-6 GHz, 7-15 GHz, satellite frequency ranges	mmWave, sub-THz, mixed and unlicensed for local connections	Sub-6 GHz, 7-15 GHz, mmWave	Private frequency, sub-GHz, sub-6, GHz, 7-15 GHz, mmWave, sub-THz for sensing

Peak data rate (PHY)	< 1 Gbit/s	(10-100 Gbit/s)	< 10 Gbit/s	< 10 Mbit/s
Link reliability	Variable	Variable	Variable	(99.999%-99.999 99%)
Air interface latency	Variable	Variable	Variable	(0.1-10) ms
Connection density	Variable	$<10^6$ device/km^2	(10^6-10^8) device/km^2	Variable
Coverage	Availability (99.99%-99.999 999%)	Local	Variable	Local coverage
Sensing capabilities	Variable	Variable	Variable	Positioning accuracy (0.1-1) cm

2.3 Overview of holistic radio design framework

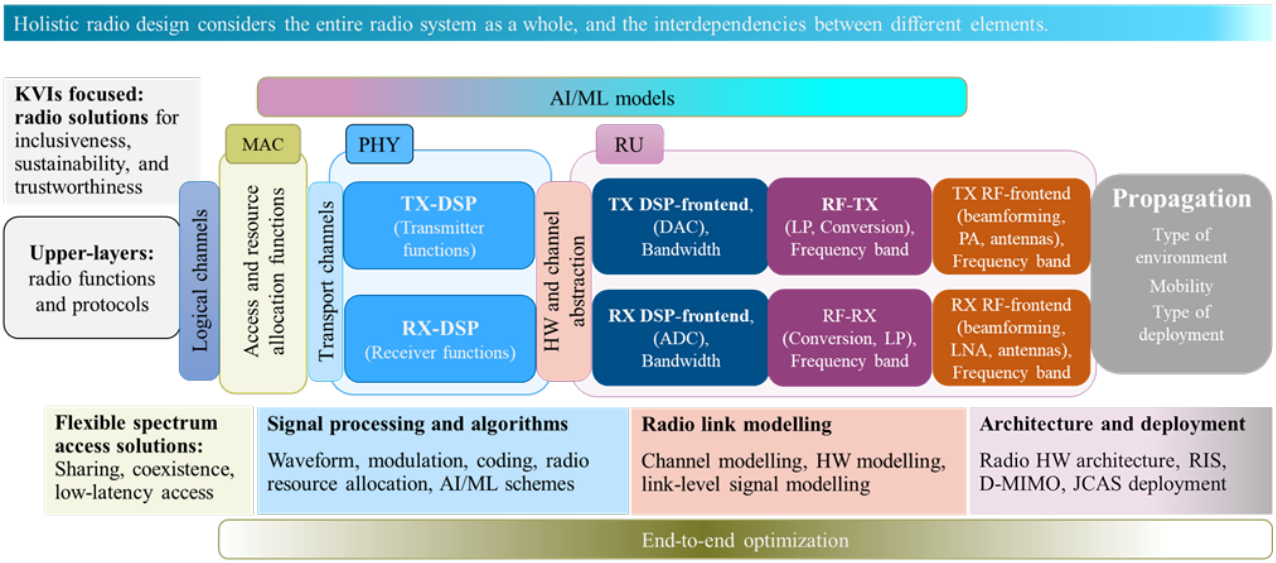

Figure 2-3: Holistic radio design framework.

The holistic radio design approach treats the entire radio system as a whole and considers the interdependencies between different elements. The radio hardware and software are jointly designed to optimize the performance and efficiency of the system. The radio design framework shown in in Figure 2-3 illustrates the different modules within the radio system and their interfaces, as well as the group of enablers related to each module.

Propagation environment: It considers physical environment effects on the signal, including obstacles, reflectors, atmospheric effects, etc. It is influenced by the environment, deployment type, and mobility.

RU: The radio unit (RU) consists of RF frontend, frequency conversion, digital/analogue (D/A) conversion. It interacts with the propagation environment through the antennas and with the physical layer (PHY) via digital samples. From the PHY perspective, RU functionality can be abstracted by means of hardware and channel modelling. Various RF transceiver architectures can be implemented in RUs, determined by the number of RF chains and antennas, as well as the resolution of the digital-to-analogue converters (DACs) and analogue-to-digital (ADCs), as illustrated in Figure 2-4. For example, fully digital MIMO architecture, Figure 2-4 (a), employs one chain per antenna, whereas hybrid beamforming, Figure 2-4 (b), uses analogue beamforming, with more antennas than RF chains. Low-resolution DAC/ADC can be used in fully digital architecture, such as 1-bit ADC/DAC massive MIMO, as discussed in Section 4.2.2. Additionally, there are various types of analogue beamforming architectures using fully or partially connected phased arrays, or switched beam antenna lenses [HEX224-D53].

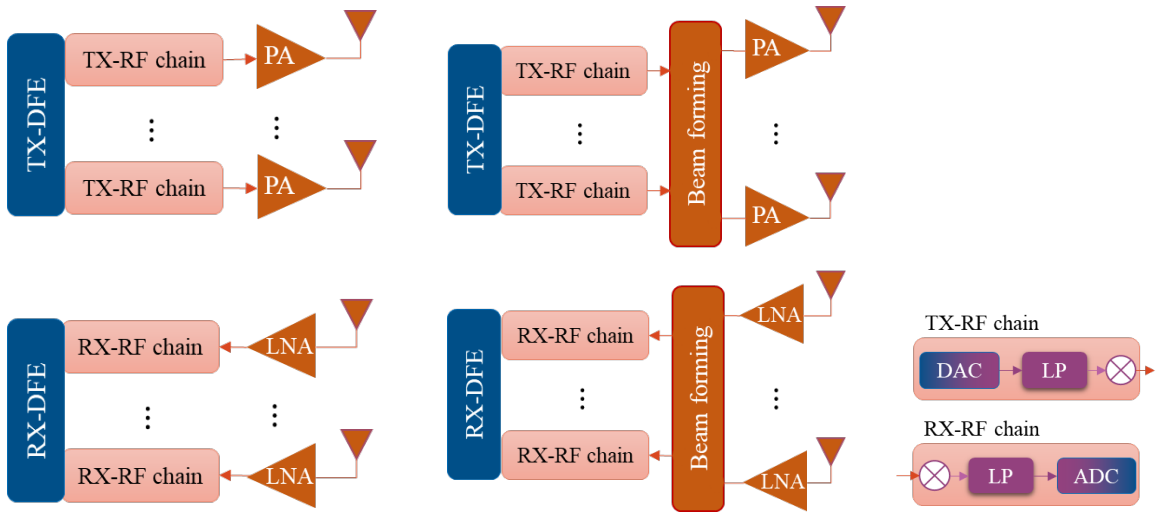

(a) Digital MIMO architecture **(b) Hybrid beamforming architecture** **(c) RF chains**

Figure 2-4: Radio unit architecture options.

Radio link modelling: This is an essential aspect in radio design, providing simulation models for the channel and HW components. Various abstracted channels can be obtained at different levels, as follows:

- Wireless channel: this abstracts the effects of the propagation channel and account for the impact of RF frontend. The characteristics of this channel depends on the frequency range, bandwidth, beamforming, RUs distribution, and deployment scenario. Channel modelling aims to capture the key characteristics and behaviours of wireless channels with respect to the radio signal [TR 38.901]. Details on channel modelling are presented in Chapter 3. Modelling at this level also includes aspects like obtaining models for antenna coupling, power amplifier (PA), and low-noise amplifier (LNA). HW modelling focused on sub-THz is presented in [Chapter 2, HEX224-D53].
- Baseband channel: This extends the wireless channel by considering the effects of frequency converters, including phase noise (PN) and low-pass (LP) filtering.
- Digital baseband channel: This incorporates, in addition to the baseband channel, the effects of DAC and ADC resolution, and digital frontend (DFE) processing, such as filtering and pre-distortion.

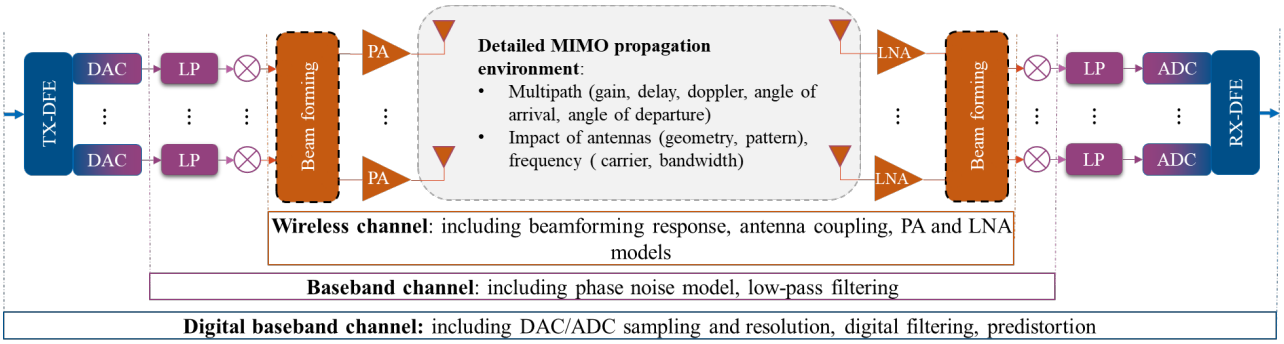

Figure 2-5: Link modelling and equivalent channels.

PHY: It encompasses a broad range of functions related to transmission, detections, channel state information (CSI) feedback, and sensing, as illustrated in Figure 2-6. It provides transport channels to the medium access control (MAC) layer and interacts with the discrete baseband channel. The PHY functions can be implemented using conventional model-based solutions, or employing AI/ML data-driven models, which can address individual functions or a combination of them. Various AI/ML solutions are presented in Chapter 6, whereas Chapter 5 focuses on conventional PHY methods.

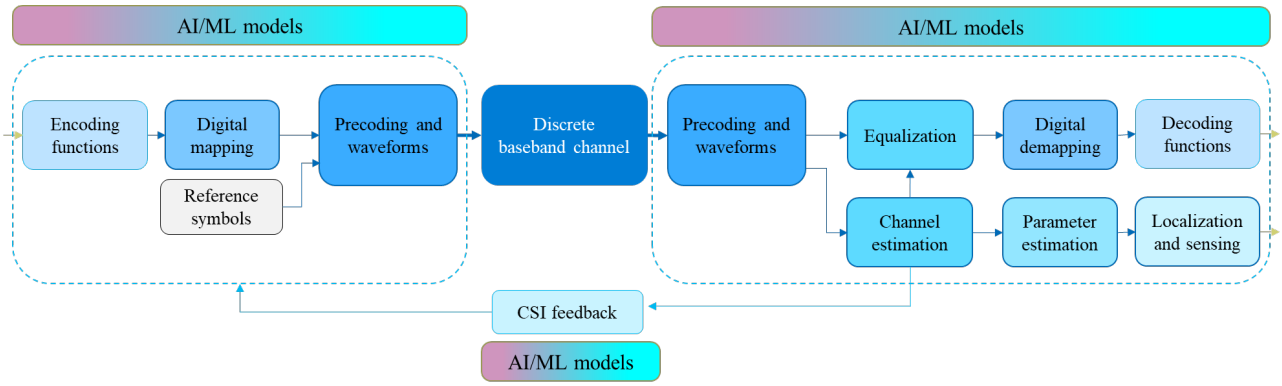

Figure 2-6: PHY functions.

MAC: It is responsible for spectrum access and physical resource allocation. It includes functions for flexible spectrum sharing, coexistence, and low-latency random access. It provides logical channels to the upper layers. Various MAC aspects are presented in Chapter 8.

Upper layers: These layers consist of various radio function and protocols, such as radio link control (RLC), packet data convergence protocol (PDCP), and radio resource control (RRC), which operate on top of MAC/PHY [HEX223-D22].

Values focused solutions: These include operational techniques that work alongside the radio infrastructure and PHY/MAC, such as PHY security and anti-jamming mechanisms to improve trustworthiness, as discussed in Chapter 9. Other solutions include proactive resource allocation, presented in Section 8.4, and minimizing signaling overhead that contribute to energy efficiency and improve the user experience, as discussed in Section 8.3.

2.4 Flexible radio architecture and deployment

In radio design, multiple degrees of flexibility in terms of implementation and deployment of various functions can be achieved. Flexibility at PHY/MAC is typically implemented through variable waveform numerologies, adaptive modulation and coding, and dynamic radio resource allocation. This allows the system to adjust to changing conditions and requirements. In the RU, flexibility can be achieved following a software-defined radio (SDR) approach that enables the configuring of carrier frequencies, bandwidth, power level, the number of active chains, as well as controlling the radiation patterns in the case of analogue beamforming frontend.

Different layers within the system may generate configuration commands for various modules, providing the ability to tailor the radio system to specific requirements and operating conditions.

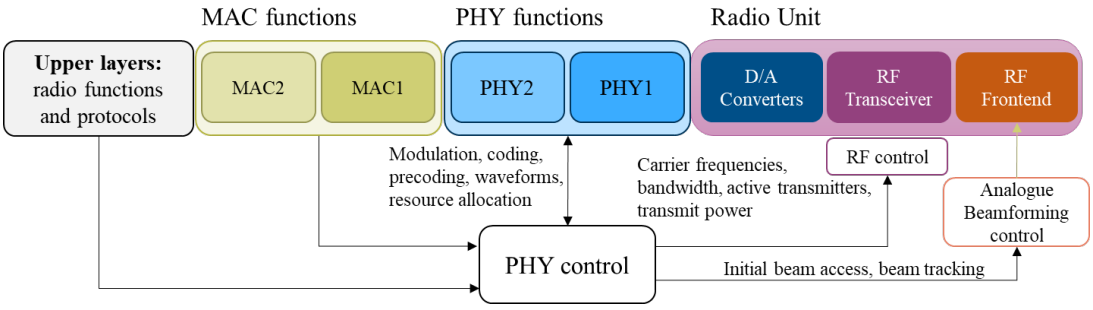

Figure 2-7: Radio logical functional split and configuration parameters.

Figure 2-7 illustrates a logical functional split of MAC, PHY, and RU functions, along with their corresponding configuration parameters. In typical devices, these functions are often collocated to achieve higher integration and reduce material costs. However, in the radio access network (RAN) infrastructure, implementing various functional splits can offer additional flexibility, enabling a more modular approach. These splits can be beneficial in a range of scenarios, allowing for optimized resource usage and scalability. However, they also

affect infrastructure requirements, such as fronthaul capacity and signal processing design. Figure 2.5 provides examples of the functional splits discussed in this deliverable:

- Centralized RAN: In this configuration, the MAC, PHY, and RU functions are collected and controlled at higher layer. This setup can support dual connectivity at PDCP level.
- Distributed MAC: Here, the MAC functions are split into centralized and distributed entities Partially centralized MAC functions enable carrier aggregation across different frequency ranges, offering flexibility in managing resources.
- Centralized MAC: In this setup, controls multiple PHY instances are centrally controlled by MAC. This allows, for example, carrier aggregation in the same frequency range.
- Distributed PHY: This deployment corresponds to D-MIMO with distributed processing. It reduces fronthaul capacity requirements by offloading part of the PHY processing close to RUs, such as partial channel estimation and precoding, as discussed in Section 4.1.3.
- Centralized PHY: This is a conventional D-MIMO setup with centralized processing, where all samples from RUs are collected and centrally processed, as in Section 4.1.1. Other related D-MIMO split options is using analogue fronthaul, as in Section 4.1.5, where the D/A converters are placed closer to PHY.

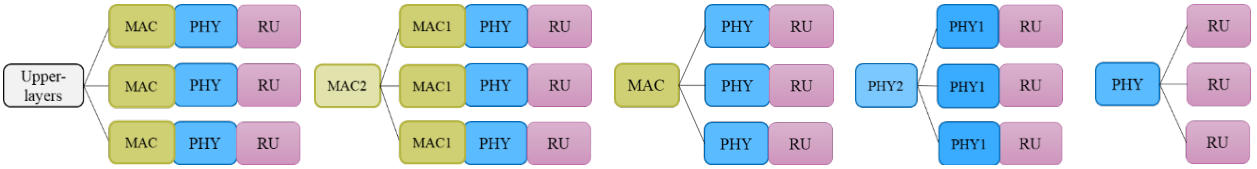

(a) Centralized RAN **(b) Distributed MAC** **(c) Centralized MAC** **(d) Distributed PHY** **(e) centralized PHY**

Figure 2-8: RAN deployment options.

Further deployment scenarios correspond to the placement of transmitters and receiver as in JCAS deployment, such as bistatic, monostatic, and multistatic sensing, as discussed in Section 7.1.

3 Channel modelling

In sixth-generation cellular communications, there is a growing interest in utilizing the sub-THz band and implementing new technologies such as the reconfigurable intelligent surfaces (RIS) and joint communication and sensing (JCAS). Due to the relatively unexplored nature of the sub-THz band, developing new and updating existing channel models, and analysing the coverage of a sub-THz cellular system must be considered. Additionally, channel models must be developed to account for the unique characteristics of these emerging technologies and ensure their effective design and evaluation across different use cases.

The standard channel model, 3GPP TR 38.901 [38.901], presently supports frequencies only up to 100 GHz and does not accommodate near field conditions. These two issues are partially addressed in Section 3.1.1 and 3.1.2, by reporting channel parameter values at the sub-THz band and proposing a simple modification on the per antenna pair propagation lengths. Higher bandwidths can be utilized at higher frequencies but at the cost of higher propagation losses. In Section 3.1.3, the coverage reduction due to the increased path loss at a higher frequency, assuming fixed gain isotropic antenna at both link ends, is investigated. Meanwhile, the reflection loss of different materials at the sub-THz band, which is particularly relevant for deterministic channel modelling, must be considered. Section 3.1.4 addresses the deviation of the reflection coefficient from the ITU-R P2040 model [ITU P.2040-3] for rough or coated surface materials. A potential solution to various propagation issues is the use of RIS, which can steer the incoming signal to the RIS towards the receiver, resulting in improved signal reception. The modelling of the received signal power in an environment with RIS is discussed in Section 3.2. Finally, as the current channel models are originally designed solely for communication, modifications to these models must be considered to support the evaluation of JCAS. Section 3.3 presents the JCAS use cases, channel model features relevant to sensing, and their relation to current channel models.

3.1 3GPP-like channel model

Problem statement: The standardized stochastic channel model 3GPP TR 38.901 is a widely used model capable of reproducing plausible channel responses for various scenarios [38.901]. It can generate statistically consistent wideband propagation channels, including the polarimetric path gain, azimuth and zenith angles of arrival and departure, and path delay. This means that the probability density functions of the channel parameters of the generated channels of such stochastic channel model are approximately identical to those of the measured channels for a given scenario. To use this model, input channel parameter values derived from the measurements are required. The input channel parameter values, extracted from sub-THz measurements in indoor entrance hall and outdoor residential, are presented in this chapter. The measurements cover frequencies from 140 to 144 GHz in line-of-sight (LoS) and non-LoS (NLoS) conditions. In addition, these measured channels are compared with the generated channels using the 3GPP parameter values specified in [38.901] and parameter values extracted from the measurements.

Methodology: The double-directional multipath data were first obtained from the channel measurement campaigns described in detail in [DH23]. The channel parameter values such as the large-scale (LSP), small-scale, and cross-correlation parameters are then extracted from these data as listed in Tables Table A.1-1, Table A.1-2, and Table A.1-3 in Section A.1.1. The delay spread, angular spread, and path loss are calculated using [DH24, Equations (5), (6), and (2)]. The measured path loss estimates are fitted using the least-squares method to the floating-intercept path loss model to estimate the distance-dependent coefficient α and the best-fit path loss offset β. To derive the cluster parameters, the measured multipath components (MPCs) are clustered along the azimuth and zenith angles of arrival and departure, and path delay using the agglomerative hierarchical clustering method [NHP16]. The MPCs up to 40 dB below the strongest MPC were considered in obtaining these channel parameter values. The channel parameter values for indoor-office and UrbanMicro-street canyon specified in the 3GPP [38.901] are also included in the same tables for comparison with the entrance hall and outdoor residential parameter values. Although the 3GPP model supports frequency only up to 100 GHz, the parameter values in these scenarios are obtained by substituting $f_c = 142$ GHz in frequency-dependent model parameters. The channel responses, represented as discrete multipath parameters containing azimuth and zenith angles of departure and arrival, delay and amplitude, are generated using the modelling framework shown in Figure 3-1.

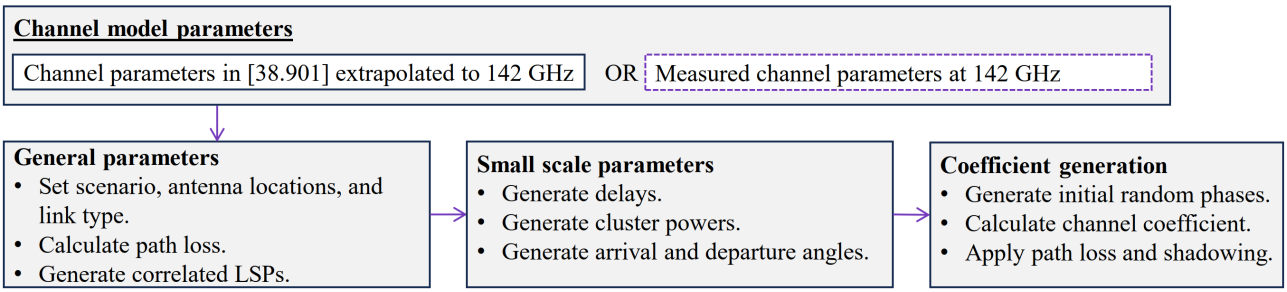

Figure 3-1: Channel Modelling Framework.

Two sets of channel responses, (S1) using the extrapolated parameter values specified in [38.901] and (S2) uses the parameter values derived in this section, are generated using the channel modelling framework shown in Figure 3-1. The channel response is represented as discrete multipath parameters containing azimuth and zenith angles of departure and arrival, delay and amplitude. For each set, 300 channel responses are generated, with each assuming a link with the Tx placed at the origin $(0,0,1.8)$ of the Cartesian coordinate system. The Rx is placed along the x-axis $(d, 0,1.8)$ where d is randomly drawn from the same distribution of the link distances in measurements. Both antennas are placed at the same height, $z = 1.8$ as in the measurements. The y-coordinate is fixed at $y = 0$ and should not affect the comparison as the MPCs' departure and arrival angles are normalized with respect to the reference direction given by the Tx/Rx directions seen from the Rx/Tx locations. Only Section 7.5 of [38.901]and the additional modelling component, large bandwidth and large antenna array modelling, in Section 7.6.2 of [38.901], are implemented here.

Results: To measure the consistency of the generated channels with the measured channels, the absolute percent error of the parameter values between the measured and generated channels is calculated as $\text{PE} = |(\mu_{\text{LSP,m}} - \mu_{\text{LSP,g}})/\mu_{\text{LSP,g}}| \cdot 100\%$. The variables $\mu_{\text{LSP,m}}$ and $\mu_{\text{LSP,g}}$ are the mean values of an LSP of the measured and generated channels. The LSP includes delay spread (DS), azimuth angle spread of departure (ASD) and arrival (ASA), zenith angle spread of departure (ZSD) and arrival (ZSA), shadow fading (SF), Rician K factor (K), and the path loss parameters α and β. The percent error estimates, along with the reference values, are listed in Table 3-1. It can be observed that the PEs of S2 across the environments and link conditions are generally lower than the PEs of S1. This discrepancy can be attributed to the differences in environments considered in this chapter as to those considered in the 3GPP. Therefore, the parameter values found in the entrance hall and residential environments reported in Section A.1.1 can be utilized to create realistic channels that are helpful for evaluating links and systems at the sub-THz band.

Table 3-1: Percent error between the LSP mean of the measured and generated channels.

Parameter			LoS									NLoS							
			DS (ns)	ASD (°)	ASA (°)	ZSD (°)	ZSA (°)	SF (dB)	K (dB)	α (dB)	β	DS (ns)	ASD (°)	ASA (°)	ZSD (°)	ZSA (°)	SF (dB)	α (dB)	β
Indoor	Ref.	$\mu_{\text{LSP,m}}$	14.5	12.3	24.5	2.3	5.2	0.9	6.2	73.6	2.1	24.0	20.9	34.7	3.4	6.8	7.3	74.4	2.8
	PE (%)	S1	37	53	43	1484	36	71	8	2	21	45	40	9	76	64	9	5	26
		S2	9	5	12	7	3	0	5	0	0	12	15	8	32	34	0	0	1
Outdoor	Ref.	$\mu_{\text{LSP,m}}$	18.2	7.8	9.8	1.1	2.0	1.1	7.8	79.2	1.7	21.4	5.8	20.9	1.4	3.0	8.2	52.5	3.9
	PE (%)	S1	28	25	55	591	56	73	10	3	15	57	69	51	90	72	5	27	19
		S2	32	75	54	43	35	0	8	0	1	82	54	75	37	19	0	7	6

3.2 Channel model component for near-field condition

Problem statement: The goal of this work is to provide a simple modification to the legacy channel modelling approach in 3GPP TR 38.901 [38.901]. The modification makes the model more physical and solves many issues related to prior prerequisites of confined array sizes, relatively small bandwidths, and link distances

satisfying the far field condition. This work has been contributed to ETSI in document [(23)000238]. The model component is best suited for higher mmWave channel modelling but may be useful for lower frequencies as well.

In physical reality, antenna elements of Tx and Rx arrays have slightly different propagation lengths on LoS path. These per antenna pair propagation lengths depend on geometries and orientations of the arrays. Similarly, there are different propagation lengths on NLoS paths, which depend on the previously mentioned aspects and on the interaction type and position of the interacting object. These slightly different path lengths cause frequency-dependent phase offsets between signals on antenna elements. Moreover, the Doppler phenomenon is essentially caused by temporal variation of the electrical path length, and it is therefore dependent on the radio frequency.

Assumptions for the near-field model component can be summarized as follows:

- The model component is intended for extending geometry-based stochastic channel (GSCM) models, such as those in [38.901].
- Antenna arrays with spatially separated elements with known array geometries are used.
- Modelled environments can be either indoor or outdoor and in LoS or NLoS condition.
- All wave material interactions between link-ends are specular reflections. This assumption is least arguable at upper mmWave radio frequencies.

The model component provides enhancements both for the near-field and wideband cases. It is applicable both for the base station (BS) and user equipment (UE) type transceivers as well as RISs.

Methodology: The idea of the proposed solution is to provide a simple means to determine the propagation distance between each Tx and Rx antenna element. In mobile channels, the time-variant propagation delays are determined. These per antenna propagation delays can be used to substitute the departure/arrival related phase terms of antenna arrays and the phase terms related to the Doppler shift, as they are used in legacy models. For the LoS path it is straightforward to calculate distances between Tx and Rx arrays since array locations and element locations within arrays are known. In the case of NLoS paths this is not trivial, since the model provides only angles and delay, but not locations or types of interacting objects. If the location, orientation and other characteristics of, e.g., a reflecting surface or a diffracting edge were known, one could determine per antenna path lengths, but the model does not provide this information.

Simple operations to approximate virtual array positions for each propagation path can be done to overcome this problem. It is done by rotating the Tx antenna array in the global cartesian coordinate system such that the arrival and departure angles are pointing towards each other and the distance between array centres corresponds to the original path length in metres. Per antenna distances can be calculated similarly as in the LoS path case, based on the original Rx antenna coordinates and the new virtual Tx antenna coordinates. This operation is performed separately for each path. The underlying assumption is that the interaction is reflection, which is the most common and highest gain interaction type at sub-THz frequencies. Specular reflection can be well assumed in the absence of interaction type information in the 3GPP model [38.901] and similar stochastic models.

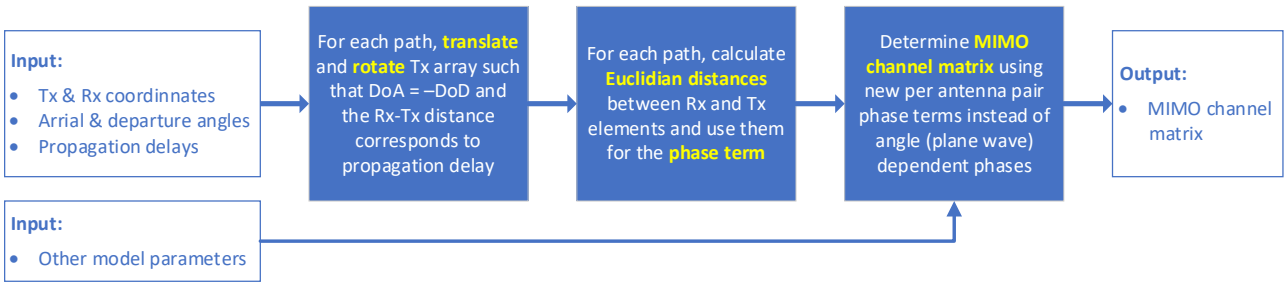

Figure 3-2: A block diagram of the near-field component for 3GPP type geometry based stochastic channel models.

The block diagram of Figure 3-2 illustrates the steps of the model component. Input are channel model parameters of 3GPP and similar geometry-based models. First Tx antenna array is rotated and translated in the global coordinate system separately for each (sub-)path such that arrival and departure angles point at each

other and the distance between Rx array and virtual Tx array centre corresponds to the propagation delay. Then Euclidean distances are calculated between each Rx and virtual Tx element pair, again separately for each path. Finally, this per path per antenna pair distance information is used to determine phase terms that characterize multiple-input multiple-output (MIMO) array geometries. Resulting phase fronts will be curved, in the near-field condition. Finally, these phase terms are used to calculate MIMO channel matrices together with all other propagation parameters of the 3GPP model [38.901] such as, e.g., polarimetric path gain matrices.

3.3 Coverage analysis at THz frequencies

Problem statement: THz frequencies (300 GHz – 3 THz) are located between millimetre-wave (mmWave) band (30–300 GHz) and far infrared (3–20 THz) bands and provide increased bandwidths (in the order of tens up to hundreds of GHz) compared to the ones achievable with mmWave, leading to meet the demands for increased data rates up to Tbps. The countereffect is represented by a conspicuous reduction of radio coverage compared to the one achievable with mmWave, due to the experienced high propagation loss.

The propagation loss challenges posed by THz frequencies are analysed in case of LoS in terms of spreading loss and molecular absorption loss. The target is to provide an estimation, based on theoretical analysis, in terms of radio coverage impacts compared to the one achievable at 100 – 300 GHz.

Methodology: Figure 3-3 reports the sequence of blocks leading to the coverage reduction evaluation at THz frequencies compared to the achieved coverage at mmWave.

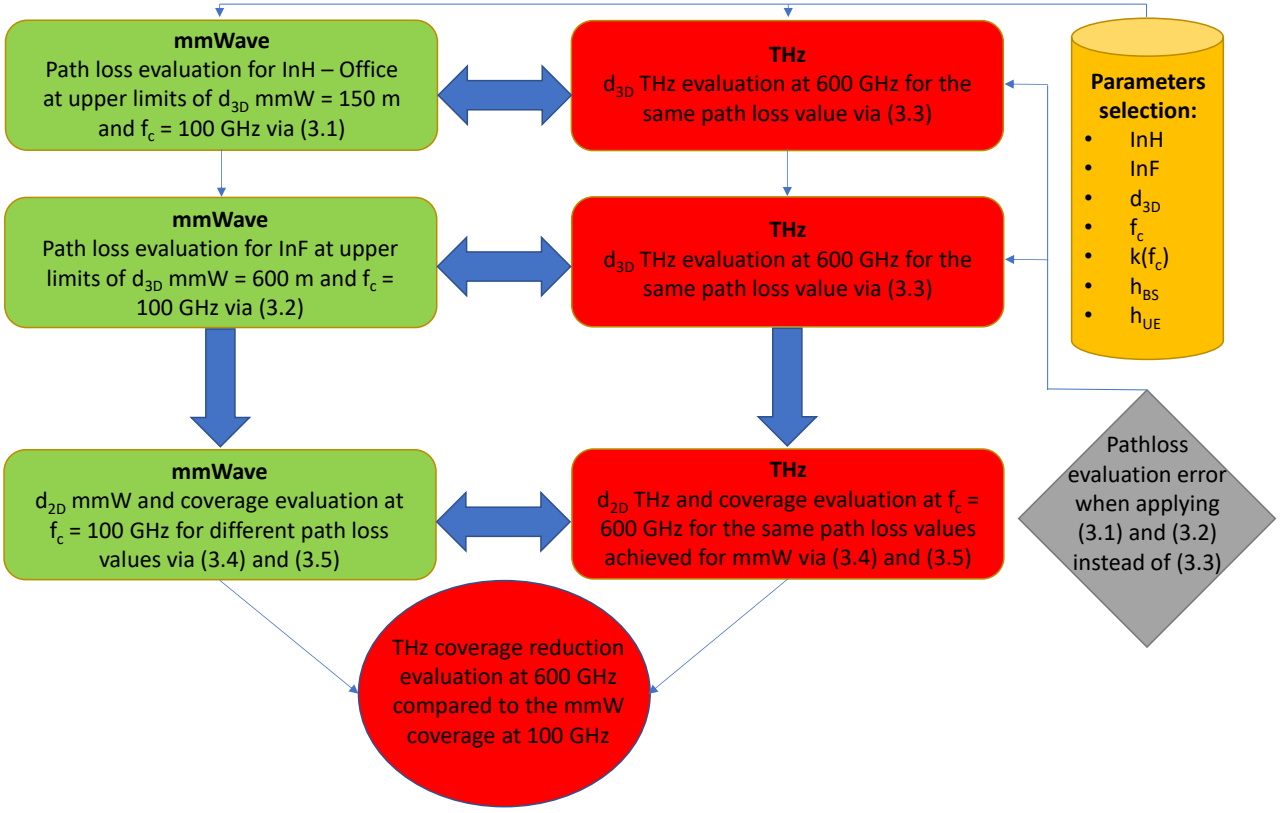

Figure 3-3: Block diagram of the overall coverage analysis at THz frequencies.

The evaluation is provided by path loss theoretical analysis for both mmWave and THz frequencies, leading to the achievable distances and coverage for both the channel models.

Evaluation metrics definition:

- **Path loss [dB]: mmWave Indoor Hotspot (InH) – Office – LoS (d_{3D} [m], f_c [GHz])**

$$PL_{mmW\ InH-LoS} = 32.4 + 17.3\log_{10}(d_{3D}) + 20\log_{10}(f_c), \quad 1\text{ m} \le d_{3D} \le 150\text{ m}, 0{,}5\text{ GHz} \le f_c \le 100\text{ GHz} \tag{3-1}$$

- **Path loss [dB]: mmWave Indoor Factory (InF) – LoS (d_{3D} [m], f_c [GHz])**

$$PL_{mmW\ InF-LoS} = 31.84 + 21.5\log_{10}(d_{3D}) + 19\log_{10}(f_c), \quad 1\text{ m} \le d_{3D} \le 600\text{ m}, 0{,}5\text{ GHz} \le f_c \le 100\text{ GHz} \tag{3-2}$$

- **Path loss [dB]: THz – LoS (d_{3D} [m], f_c [Hz])**

$$PL_{THz-LoS} = k(f_c)d_{3D}10\log_{10}(e) + 20\log_{10}(4\pi f_c d_{3D}/c),\ 300\text{ GHz} \le f_c \le 3\text{ THz} \tag{3-3}$$

The first term in **(3-3)** represents the molecular absorption loss, whilst the second one denotes the spreading loss.

The cell radius d_{2D} for any considered d_{3D} for both mmWave and THz frequencies is evaluated via **(3-4)**.

- **Cell radius [m]**

$$d_{2D} = \sqrt{(d_{3D})^2 - (h_{BS} - h_{UE})^2} \tag{3-4}$$

The coverage reduction for any considered path loss for mmWave and THz frequencies is evaluated via **(3-5)**.

- **Coverage reduction [%]**

$$Coverage\ reduction\ [\%] = (1 - \frac{\pi(d_{2D\ THz})^2}{\pi(d_{2D\ mmW})^2})100 \tag{3-5}$$

Results: The results in terms of impact on the system are reported in Table 3-2 highlighting the resulting THz coverage reduction at 600 GHz compared to the mmWave coverage at 100 GHz (derived from the achieved d_{3D} at 600 GHz and at 100 GHz, respectively) for the same values of path loss. As expected, it is shown a conspicuous reduction of THz radio coverage compared to the one achievable with mmWave, due to the experienced high propagation loss. THz frequencies are therefore suitable for providing focused coverage spots, in a range up to roughly 100 m, depending on the acceptable path loss requirements of the overall system.

Table 3-2: THz coverage reduction evaluation compared to mmWave coverage.

	Benchmark	**Achievement**	**Impact on the system**
	mmWave @ 100 GHz	**THz @ 600 GHz**	**THz @ 600 GHz vs mmWave @ 100 GHz**
Path loss [dB]	**d_{3D} mmWave [m]**	**d_{3D} THz [m]**	**Coverage reduction [%]**
110	150	10	99.57%
130	600	45	99.44%
147.6	N/A	100	N/A

System model, mathematical model, assumptions, and results evaluation for coverage analysis at THz frequencies are reported in Section A.1.2.

3.4 Impact of rough and coated surfaces on reflection coefficients

Problem statement: Ray tracing are popular deterministic propagation channel models to evaluate the performance of wireless radio interfaces or to predict the coverage area. They use a geographical database or digital map to compute all possible rays i.e., direct, reflected, transmitted, diffracted, scattered paths, between two or more points such as transmitter, receiver, RIS, relay, etc. The ray amplitude and geometrical features

are given by physical laws according to the interaction type between the electromagnetic (EM) wave and the environment. This section focuses on reflected paths. The reflection coefficient indicates the reflection gain experienced by a path when reflected by a surface. The reflection coefficients are theoretically given by the Fresnel equations for a planar infinite surface. They depend on the material relative permittivity, the incidence angle and the EM wave polarization. For instance, the reflection coefficient *r* at the air-material interface and at a normal incidence is equal to $\frac{1-\sqrt{\varepsilon_r}}{1+\sqrt{\varepsilon_r}}$, ε_r being the material relative permittivity. Many deterministic simulations use the relative permittivity proposed by the ITU-R model [ITU P.2040-3] where the permittivity is considered as a constant regardless of the frequency. It implies that the reflection loss does not depend on the frequency. The ITU-R P2040 model is mainly defined up to 100 GHz but recent work performed in the Hexa-X project [HEX23-D23] shows that the model could be extended up to 300 GHz with homogeneous and flat surface materials such as glass or plexiglass. Nevertheless, some differences were observed for materials with rough or coated surfaces at frequency above 50 GHz. The goal of this section is to address the reflection coefficient deviation from the ITU-R P2040 model for rough or coated surface materials.

Methodology: The measurement equipment is based on a vector network analyser (VNA) and frequency extenders. The measurement is divided into three sub-bands defined by the frequency limits of the VNA, extenders, or antennas (5-40 GHz, 110-170 GHz, 170-260 GHz). The antenna is a dual-ridge ultra-wideband antenna for frequencies below 40 GHz and a standard horn pyramidal antennas for frequencies above 50 GHz. Figure 3-4 illustrates the mechanical part that allows a free space measurement for reflection coefficients. The material under test was placed at normal incidence in front of the Tx/Rx antenna. Common building materials such as raw and coated plasterboard, raw and melamine faced chipboard, mortar with different roughness, patterned glass and carpet tile were measured.

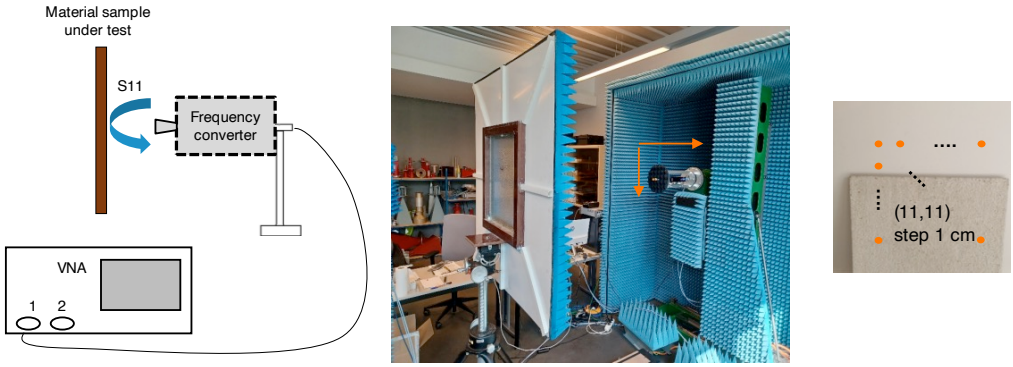

Figure 3-4: Measurement system for material reflection loss estimation

The Tx/Rx measurement antenna can move on a vertical plane and therefore can scan the material by performing an $m \times n$ measurement matrix. An 11×11 measurement matrix with points separated by 1 cm was performed. The role of the measurement matrix is to check the impact of the reflection point location on the reflection coefficient. $H^{\mathrm{MUT}}(f,m,n)$ represents the intrinsic reflection frequency response of the material under test (MUT). Details on the measurement procedure and data processing can be found in [HEX23-D23]. $ppH_{mean}^{MUT}(f)$ is defined as the average power profiles of $H^{\mathrm{MUT}}(f,m,n)$ and is equal to $\frac{1}{mn}\sum_{m,n}\left|H^{\mathrm{MUT}}(f,m,n)\right|^2$.

Results: At time of writing, the data analysis was still ongoing, therefore this section reports very initial results on the impact of rough surfaces. Refined analysis on rough surfaces or results related to coated surfaces will be included in a future deliverable.

Figure 3-5 displays $ppH_{mean}^{MUT}(f)$ for different rough or non-flat materials and compares them with the theoretical power reflection coefficient $|r|^2$. When the surface is rough, then scattering occurs and the wave power reflected in the specular direction is diminished as a portion of the incident wave is reradiated in various scattered directions. Mortars A, B, C, D are characterized by a low, medium, high and very high roughness, respectively. They illustrate the surface roughness impact on the reflection coefficient due to the scattering. When the frequency increases and/or when the surface roughness increases, $ppH_{mean}^{MUT}(f)$ decreases. For

frequencies below 40 GHz, $ppH_{mean}^{MUT}(f)$ is close to $|r|^2$ for mortars A, B, C indicating that scattering is negligible. But at frequencies above 100 GHz, $ppH_{mean}^{MUT}(f)$ is reduced compared to $|r|^2$ by more than 10 dB for mortars C and D. Sub-THz wireless systems should target more indoor environment including airport or train station halls where raw or painted concrete walls would have a surface roughness like that of mortars A and B. The average reflection gain reduction should be limited to 5 dB. The reflection gains given in this section are average values on the measurement matrix, but it strongly depends on the reflection point location. For instance, the mortar A reflection gain standard deviation calculated on the $m \times n$ measurement point matrix is always lower than 1 dB but reaches 5 dB for mortars C and D above 100 GHz. Scattering may erase the reflected path at some points as the reflection gain is around -30 dB for frequencies above 100 GHz. Conclusions drawn to rough surfaces such as mortar surfaces can be extended to any non-flat surface such as patterned glass or carpet as illustrated by Figure 3-6.

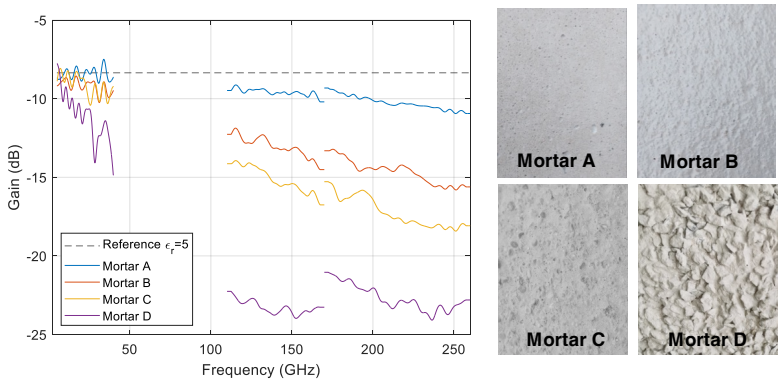

Figure 3-5: $ppH_{mean}^{MUT}(f)$ for different mortars.

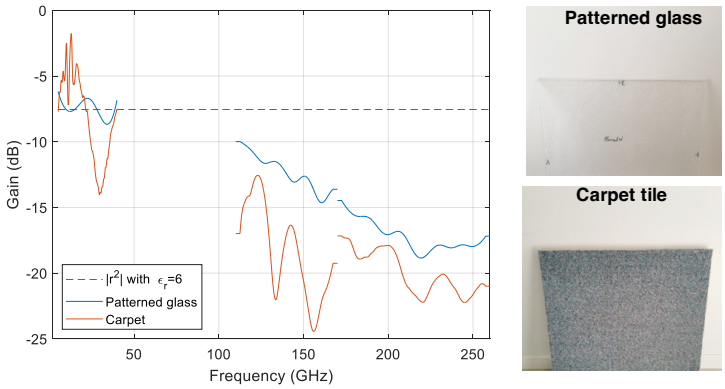

Figure 3-6: $ppH_{mean}^{MUT}(f)$ for a carpet tile and a patterned glass.

3.5 Signal level analysis for RIS in a simplified scenario

Problem statement: The derivation of a signal model for passive RIS highlights the "double fading" effect, for which the equivalent path loss of the transmitter-RIS-receiver link is the product, instead of the summation, of the path losses of the transmitter-RIS link and RIS-receiver link [OBL+19]. The path loss of the reflected link is then usually much larger than that of the direct link and the expected gains from the introduction of RIS may reduce when the direct link is not completely blocked. To overcome this physical limit, the concept of active RIS that can also amplify the reflected signal has been recently proposed [ZDC+23]. A signal model for calculation of the signal-to-noise ratio (SNR) at the user receiver is derived, considering both passive and active RIS. The effect of RIS on the signal received by the user is then determined in a simplified propagation scenario, as the one depicted in Figure 3-7. The effect of the direct link, with different levels of blockage, is also analysed to highlight the potential gains from the introduction of RIS in the system.

A signal model for an RIS assisted wireless system requires two key elements: a suitable far-field path loss model and a signal model/equation for SNR calculation at the receiver. The approach for path loss modelling used in this analysis is based on [Ell21], where the scattering by the RIS is computed as the discrete sum of

fields scattered from each RIS element. The key performance indicator (KPI) used to evaluate the effect of the RIS in the system is the SNR at the receiver, which is directly related to the radio coverage improvement that the RIS can provide.

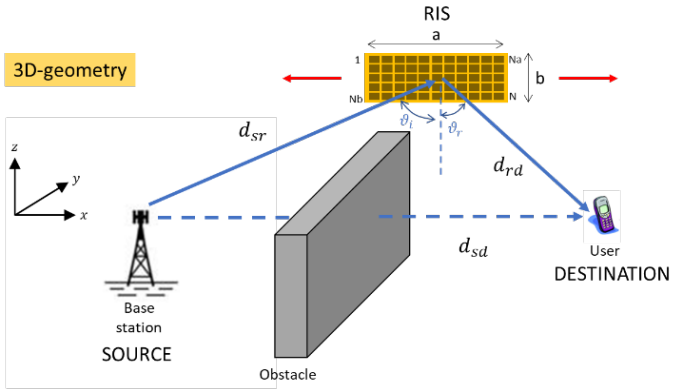

Figure 3-7: System model for the analysis of the effect of the RIS.

Methodology: A Single-Input Single-Output (SISO) configuration is considered and the RIS is in the far field region of the transmitter as well as the receiver is in far field with respect to the RIS. Ideal operation of the RIS is assumed, with perfect channel state information knowledge so that the RIS reflection coefficients can be set to achieve perfect coherent combination at the user receiver. The signal received by the user in case of a passive RIS can be expressed as:

$$y_{\text{pas}} = \sqrt{P_{\text{t}}}\left(\sqrt{\beta_{\text{RIS}}^{(s)}}\mathbf{h}_{\text{rd}}\,\boldsymbol{\Theta}\,\mathbf{h}_{\text{sr}} + \sqrt{\beta_{\text{sd}}}e^{j\phi_{sd}}\right)x + n \tag{3-6}$$

where P_{t} is the BS transmit power, $x \sim CN(0,1)$ denote the symbol transmitted from the BS, $\mathbf{h_{sr}} \in \mathbb{C}^{\boldsymbol{N,1}}$ and $\mathbf{h}_{\text{rd}} \in \mathbb{C}^{\boldsymbol{1,N}}$ are the normalized line of sight BS-RIS and RIS-user channel respectively, $\boldsymbol{\Theta} = \text{diag}\{p_1 e^{j\phi_1}, \ldots, p_N e^{j\phi_N}\} \epsilon\, \mathbb{C}^{N,N}$ is the reflection matrix of the RIS, with $\phi_n \in [0, 2\pi]$ representing the adjustable phase shift and $p_n \epsilon [0,1]$ is the adjustable amplitude factor of the n-th RIS element, $\beta_{\text{RIS}}^{(s)}$ is the coupling loss (i.e., propagation loss + antenna gains) between transmitter and receiver over the indirect path through the n-th RIS element, β_{sd} is the coupling loss on the direct path between transmitter and receiver, ϕ_{sd} is the phase shift accrued on the direct path, N is the number of RIS elements and finally $n \sim CN(0, \sigma^2)$ represents the thermal noise at the receiver. In case of an active RIS the received signal can instead be expressed as follows:

$$y_{\text{act}} = \underbrace{\sqrt{P_{\text{t}}}\left(\sqrt{\beta_{\text{RIS}}^{(s)}}\mathbf{h}_{\text{rd}}\,\boldsymbol{\Theta}\,\mathbf{h}_{\text{sr}} + \sqrt{\beta_{\text{sd}}}e^{j\phi_{\text{sd}}}\right)x}_{\text{useful signal}} + \underbrace{\sqrt{\beta_{\text{rd}}}e^{j\phi_{\text{rd}}}\mathbf{h}_{\text{rd}}\,\boldsymbol{\Theta}\,\boldsymbol{n_r}}_{\text{noise introduced by the RIS}} + \underbrace{n}_{\substack{\text{thermal}\\ \text{noise at RX}}} \tag{3-7}$$

where $\boldsymbol{n_r} = \left[n_{r,1}, n_{r,2}, \ldots, n_{r,N}\right]^T \sim CN(0, \sigma_r^2 \boldsymbol{I_N})$ denotes the thermal noise introduced by active RIS components and β_{rd} is the coupling loss over the link between RIS and user. From the equations above it is then possible to derive the SNR expression at the user receiver in case of a passive and active RIS. The signal level analysis looks to the net impact in terms of received power. The direct path with blocking attenuation and the reflected path through the RIS are combined in terms of power at the receiver (i.e., no phase coherence between direct and reflected path is assumed).

The source (BS transmitter) is located in cartesian coordinates (expressed in metres) at the position $(s_x, s_y, s_z) = (0,0,0)$ m, the user receiver is placed at position $(u_x, u_y, u_z) = (300,0,0)$ m. The RIS is moved horizontally in different positions with step Δ_x of 10 m and the position of its centre can be expressed as $(r_x, r_y, r_z) = (\text{m} \cdot \Delta_x, 50, 0)$ with $m = 0,1,\ldots,30$. The case of a square RIS with N=256 reflecting elements and a carrier frequency of 26 GHz with bandwidth of 100 MHz is considered. In case of passive RIS the reflecting elements are modelled with an amplitude reflection factor $p_n = 1\ \forall n$, while for active RIS the

reflecting elements are modelled with an amplitude reflection factor $p_n = 10\ \forall n$ that corresponds to a power gain of each element equal to $G_{\text{RIS}} = 20$ dB and Noise Figure $NF_{\text{RIS}} = 10$ dB.

Results: The Figure 3-8 shows the gain in terms of SNR at the receiver between the RIS assisted wireless system and a baseline system without RIS. In the latter case only the direct propagation path between transmitter and receiver provides the connectivity, while the reflected path through the RIS is turned off by setting the amplitude gain of the RIS elements to zero (i.e., $p_n = 0\ \forall n$). The abscissa represents the x-axis position of the RIS in metres and the ordinate is the SNR increment at the user receiver in dB obtained by introducing the RIS. The five curves in each figure are obtained for a different value of the additional propagation loss caused by blockage on the direct path between the transmitter and user receiver. The considered values of additional attenuation caused by blockage are $L_{\text{blk}} = \{0, 10, 20, 30, 40\}$ dB, where $L_{\text{blk}} = 0$ dB corresponds to the absence of obstacles (i.e., free space propagation).

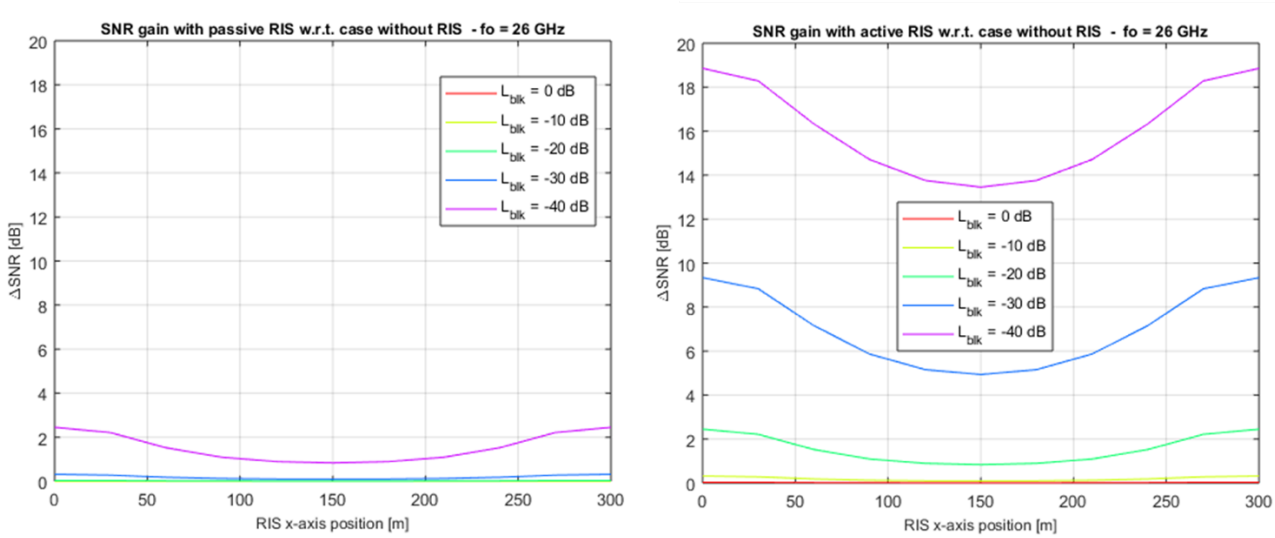

Figure 3-8: SNR gain with respect to a system without RIS at 26 GHz frequency (left: passive RIS 16×16, right: active RIS 16×16).

It can be observed that the gain achievable by the passive RIS is almost negligible when there is a strong direct path and the additional attenuation caused by blockage is lower or equal than 20 dB. On the contrary an active RIS shows a significant SNR gain even in case of a strong direct path, and only in the case of absence of obstacles ($L_{\text{blk}} = 0 - 10$ dB) also the active RIS provides a negligible SNR gain. It can be also noticed that the SNR at the receiver tends increase as the RIS is placed near to the transmitter or the receiver, while the minimum SNR is reached for the RIS placed in the middle position between the transmitter and the receiver.

3.6 JCAS channel models

The purpose of the section is to delve deeper in the models needed to support sensing and JCAS use cases. Sensing use cases are first reviewed, based on which a set of relevant sensing aspects or features are determined that the JCAS channel models should support. A selection of currently available models is then provided and related to these features.

3.6.1 JCAS use cases

While many use cases for sensing and JCAS have been discussed, the current document limits this discussion to those from [HEX223-D12] and from [22.837]. In [HEX223-D12], five use cases involve sensing, namely:

1. Seamless Immersive Reality: “Some service scenarios may include JCAS or may apply sensor fusion of network and sensor data of connected devices”.
2. Cooperating Mobile Robots: “Robots and cobots depend on capturing the environmental context. Network-integrated sensing may complement or replace dedicated onboard sensors. Efficient transport of data/information from connected external sensors is likely needed.”

3. Network-Assisted Mobility: “Object detection probability, Object location accuracy/resolution, Object velocity accuracy/resolution, Object size accuracy/resolution.”
4. Realtime Digital Twin: “Network-sensing: accuracy, resolution, and range to enrich the digital twin model.”
5. Human-Centric Services (precision healthcare, public safety): “[Sensing] Relevant for most of the scenarios.”

On the other hand, [22.837] lists 32 use cases, including detection of intruders or people in indoor and outdoor settings, tracking of various types of automated vehicles (ground and aerial), support for automated driving functions, gesture and pose classification, as well as integration with non-3GPP sensors, such as radar and lidar. Overall, the use cases span a wide variety of sensing modalities, including monostatic, bistatic, and multi-static sensing, for detection and tracking as well as for classification.

3.6.2 JCAS channel model features

From the use cases, it becomes apparent that several features must be supported by channel models to evaluate JCAS performance. Below is a non-exhaustive list of such features. Not all features must be supported simultaneously since they are not all relevant for each use case.

1. *Objects in a coordinate system:* objects (e.g., buildings, cars, people, unmanned aerial vehicles (UAVs)) should be provided in a globally consistent coordinate system with associated 3D position, 3D orientation, and 3D velocity vectors. Objects refers both to objects of interest (e.g., to be detected and tracked) and to objects that are part of the background and that generate clutter.
2. *Different object types:* the objects should include large flat objects (e.g., walls, floors, which have wave interaction points that depend on locations of transmitter and receiver) and small objects (e.g., pillars, tables), which have interaction points that are independent on the location of transmitter and receiver. The notions of large and small should be considered relative to the signal wavelength. The object classes should include objects of interest to the use cases, such as people (hands), animals, cars, UAVs, as they lead to different channel responses and can affect the polarization of the signals.
3. *Radar cross section (RCS) of objects:* Both RCS for monostatic and bistatic sensing, and RCS for deterministic and stochastic object modelling should be supported. For large bandwidths, frequency dependence of the RCS may become important.
4. *Extended objects:* For large models with several resolved interaction points, each interaction point should be described with an RCS or reflection coefficient, accounting for aspect angles.
5. *Mobility and Doppler:* Movement of objects should be supported (e.g., direction and speed), as well as movement of transmitters and receivers, as well as their corresponding Doppler shifts.
6. *Micro-Doppler:* In addition to Doppler shifts induced by objects, mechanical vibration or rotation of parts of these objects leads to micro-Dopplers (sidebands around the main Doppler shift). Such micro-Dopplers of objects should be supported.
7. *Space/time consistency:* the set of channels from a transmitter to one or more objects (in the global coordinate system) to several spatially separated receivers should be possible to generate. Similarly, the set of channels from several transmitters to one or more objects (in the global coordinate system) to a receiver should be possible the generate. These channels much be spatially consistent and correctly account for the field of view of each transmitter and receiver. Similarly, correlations across time of the transmitters, receivers, or objects move must be supported.
8. *Near-field effects:* Wave-front curvature, between transmitter and objects, between objects and receiver, and between transmitter and receiver should be supported. This curvature becomes significant when the distance between object and transmitter or receiver is less than the Fraunhofer distance $2D^2/\lambda$ [Mol11], for maximum array size D and wavelength λ. Moreover, channel non-stationarity across larger arrays (i.e., variations of amplitude and phase due to differences in distance and blockages) is an additional near-field effect. Note that far-field effects are implicitly included.

9. *Ability to generate data sets for classification use cases:* Such use cases require labelled training data for classification (e.g., gesture recognition, pose classification), when these are not provided as inputs.
10. *Relation between communication and sensing channel:* the communication and sensing channel between a transmitter and a receiver are in principle identical, including channel reciprocity.

Some use cases may need to include additional features (e.g., different types of reconfigurable intelligent surfaces) to be included, but these are not considered in this document.

3.6.3 Relation between existing channel models and JCAS channel model features

Current channel models describe the channel between a transmitter and a receiver, i.e., the environment, where this environment may contain objects. They can be grouped into 4 categories (Section 4 of [HEX223-D12]):

- **Statistical geometrical models:** Communicating devices are defined on a coordinate system. Clusters or objects contributing to clusters are statistically defined either through multipaths characteristics such as angle-of-arrivals, angle-of-departure, or time-of-arrival (3GPP, ITU-R and METIS models) or through their locations on the same coordinate system as the communicating device (COST 2100). *Examples:* ITU-R M.2135 [M.2135], 3GPP 36.873 [36.873], METIS [MET15-D14], 3GPP 38.901 [38.901], QuaDRiGa [QDR], ITU-R M.2412 [M.2412-0].
- **Site-specific model:** Communicating devices are defined on a map. The map can vary from simple and featureless ones with only flat walls and grounds to complex ones including walls with detailed I structure and cluttering and time-varying objects. Material properties and radar cross sections of objects are necessary in deriving polarimetric multipath gains. The site-specific model is a deterministic channel model and does not include any stochastic modelling component, unlike a hybrid model. *Examples:* ITU-R P.2040 [ITU P.2040-3] and commercial ray tracing.
- **Hybrid models:** Communicating devices are defined on a simple map consisting of, e.g., parallel, and perpendicular streets forming a rectangular grid for an outdoor microcellular scenario. By applying the raytracing/launching, reflected, scattered, and diffracted paths are identified. Scattering objects are placed in a random manner on the map, creating transmitter-object-receiver paths. *Examples*: [KLM+17], "3GPP TR 38.901 map-based option" [38.901], and IEEE 802.11ay [802.11ay], targeting specific environments.
- **Stored channel models:** Stored channel model consists of processed measured channel responses, e.g., in the form of discrete multipaths. The multipaths include reflected, transmitted, diffracted, and scattered paths due to the environment. The measured channels are specific at the measurement site, antenna locations, carrier frequencies. Representing the multipaths as discrete entity makes it possible to consider varying antennas and bandwidth. *Examples:* Hexa-X models [DHK23].

As these models are widely used and well-understood, it is possible to assess whether they provide support for the JCAS channel model features described in Section 3.6.2. This analysis is provided in the table below. It is important to note that this analysis is not exact and, in some cases, features may be subject to multiple interpretations and may thus be supported with minor changes to these existing models.

3.6.4 Outlook

In this section, JCAS channel model features were proposed, which are required to enable evaluation of the JCAS use cases. Not all features must be supported simultaneously, but rather a subset, depending on the use case. Existing channel modelling approaches are evaluated in terms of to what extent they can support these features. Overall, the widely used statistical geometric models can only support a small subset of these features, but modifications are possible to support around half of the features. Site-specific models and hybrid models can already support around half of the features and can in principle be extended to support nearly all features. Finally, stored channel models can support all features, provided the corresponding data is present. Hence, dedicated data set would need to be collected for each use case and scenario.

This analysis indicates that for performance evaluation purposes, hybrid models or site-specific models may be preferred over the classical statistical geometric models.

Table 3-3: Relation between the desired JCAS features and the existing channel models. ((A) = is the concerned feature currently present? (B) = is it possible to include the concerned feature with little effort or without significant changes to the methodology? If (A) is answered Yes, then (B) is shown "N/A".).

JCAS feature	Statistical geometric models (e.g., 3GPP TR 38.901)	Site-specific models (e.g., REMCOM Wireless InSite)	Hybrid models (e.g., 3GPP TR 38.901 map-based option)	Stored channel (e.g., [DHK23])
Objects in a coordinate system	(A) No, except for some model e.g., COST2100. (B) Yes, e.g., in case of 3GPP 38.901, this is provided by the hybrid model.	(A) Yes (B) N/A	(A) Yes (B) N/A	(A) No (B) Yes, if assisted by ray tracing e.g., [DH23]
Different object types	(A) No (B) No. It is quite difficult to consider specular reflections in the model.	(A) No, though surfaces with different material are supported (B) Yes	(A) Yes (B) N/A	(A) Yes, if measurements include the feature (B) N/A
RCS	(A) No (B) Yes, the gain of a propagation path can be determined with a specific RCS of the cluster or sub-path.	(A) Yes, as diffuse scattering (B) N/A	(A) Yes, as diffuse scattering (B) N/A	(A) Yes, implicit in the path gain estimates (B) N/A
Extended objects	(A) No (B) No. It is quite difficult to associate different clusters to objects.	(A) Not explicitly (B) Yes	(A) No (B) No	(A) Yes, if such objects are covered in the measurements. (B) N/A
Doppler due to the mobility of communicating devices	(A) Yes (B) N/A	(A) Yes (B) N/A	(A) Yes (B) N/A	(A) Yes, if the measurement covers a dynamic scenario. (B) N/A
Doppler and Micro-Doppler due to motions of wave scattering objects	(A) No (B) Yes	(A) No (B) Yes, a specific micro-Doppler is determined for each propagation path	(A) No (B) Yes, a specific micro-Doppler model is required for each propagation path	(A) Yes, if the measurement covers it. (B) N/A
Space/time consistency	(A) No, except for COST2100 and QUADRIGA models (B) Yes, like QUADRIGA	(A) Yes (B) N/A	(A) Yes (B) N/A	(A) Yes (B) N/A
Near-field	(A) No (B) Yes, with the knowledge of objects' coordinate system and the plane wave model replaced by the spherical wave model.	(A) No (B) Yes	(A) Yes (B) N/A	(A) Yes, if the measurement covers such cases. (B) N/A
Data sets for classification use cases	(A) No (B) No	(A) No (B) To some extent	(A) No (B) No	(A) Yes, if such data are measured (B) N/A
Communication and sensing channel compatibility, and reciprocity	(A) No, because spatial consistency is not ensured for widely separated devices. (B) Yes, like QUADRIGA.	(A) Yes (B) N/A	(A) Yes (B) N/A	(A) Yes, the channel sounder is usually a simple device but it is assumed that channels are reciprocal after proper sounder calibration. (B) N/A

4 MIMO transmissions

Over the last few decades, multiple-input multiple-output (MIMO) technology has been recognized as a crucial component in the evolution of wireless communication, spanning from 3G to 5G. It continues to get significant interest from both industries and academics for 6G. Within the framework of 6G, MIMO is expected to have a significant role, offering the potential to enhance the capacity and efficiency of wireless communication systems even further to satisfy future communication demands. This chapter focuses on exploring the techniques of MIMO within the context of 6G. Specifically, it explores three major technologies: distributed MIMO (D-MIMO), massive MIMO, and reconfigurable intelligent surface (RIS). The chapter presents a collection of crucial techniques related to MIMO and provides initial evaluation results.

The first section analyses D-MIMO schemes and architectures, focusing on both coherent and non-coherent transmission. This section also explores decentralized transmission and analogue fronthaul, as well as investigates the rotary antenna and one-bit analogue-to-digital converter (ADC) system. Additionally, it discusses the sub-THz D-MIMO assisted by a sub-6GHz macro network. The second section covers the massive MIMO schemes and architectures. This part includes the analysis of enhanced data detection using a 1-bit ADC. It then explores the design of a beamformer for sub-THz frequencies, as well as the investigation of hybrid analogue-digital architectures for MIMO. Additionally, it discusses the multi-user MIMO and location-dependent coded caching. The final section analyses the RIS-assisted transmission. This section focuses on the discussion of D-MIMO-assisted with RIS and RIS-assisted integrated access and backhaul (IAB). In addition, this section investigates the channel estimation of RIS, RIS reflecting modulation (RIS-RM), and non-radiative RIS transmission.

Overall, this chapter provides an adequate discussion of three primary MIMO technologies, including D-MIMO, massive MIMO, and RIS, within the context of 6G.

4.1 D-MIMO schemes and architectures

Distributed MIMO (D-MIMO), an extension of classical MIMO technology, involves using multiple antennas for transmitting and receiving data in wireless communication. However, unlike the classical MIMO where antennas are grouped at a single location, in D-MIMO they are scattered across a wider area. This distribution of antennas helps in covering a larger area more effectively, enhancing the capacity of the network, and improving the reliability. It leads to increased data rates and reliability, as different data streams can be sent and received simultaneously through various antennas each experiencing different propagation paths. This technology reduces interference since the antennas are not closely packed and is more closely located to the users, hence, the transmit power can be lowered. One of the main benefits of D-MIMO is its scalability and flexibility. Networks can be expanded by adding more antennas as needed, and the deployment can adapt to various environments and requirements. However, this advancement comes with challenges. D-MIMO requires more complex signal processing and coordination among antennas. In particular, practical challenges such as acquiring accurate CSI and synchronization for beamforming are challenging. This section covers different methods to address these challenges including methods for distributed CSI acquisition, coherent transmission using analogue fronthaul, and non-coherent transmission for the cases with lacking precise CSI.

4.1.1 Coherent joint transmission – D-MIMO link-level performance evaluation

Problem statement: D-MIMO will be studied as a solution to propagation channel blockage in mmWave / sub-THz bands.

Methodology: Massive MIMO is a physical-layer wireless technology that has allowed 5G to reach such good performances in term of throughput. One limitation in such deployment is the quality of service of cell-edge users due to inter-cell interference. One way to tackle this interference is to use joint transmission coordinated multi-point (JT-CoMP) which enables coherent transmission from a cluster of access points (APs).

Because greater throughput is needed in today's applications, higher bandwidth is required. To find such resource, higher carrier frequency is used. This leads to a new problem: communication reliability. Indeed, at high frequencies the signal attenuation is increased, the available output power of semiconductors is lowered, and most importantly phenomenon of blockage is worsened [CTT+16].

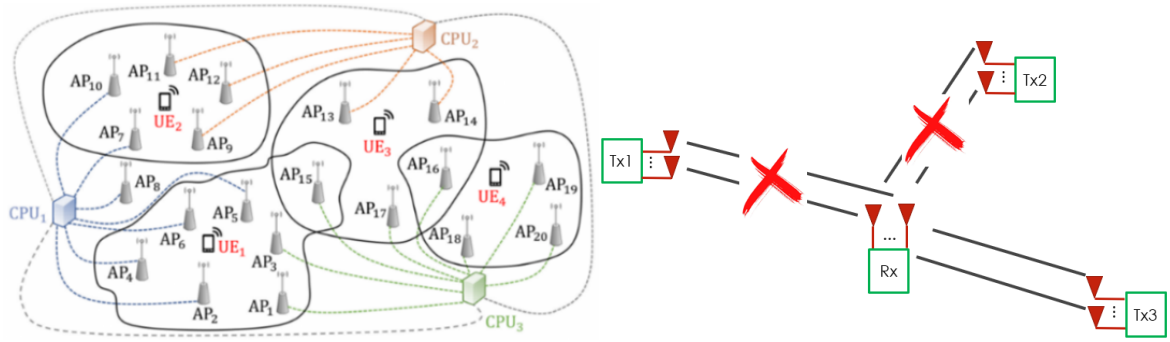

Figure 4-1: Example of D-MIMO (Left) and illustration of blockage (Right).

D-MIMO (Figure 4-1, left) is a technique using both aspects of JT-CoMP and massive MIMO. In fact, with D-MIMO the user equipment (UE) receives signals from multiple APs (like JT-CoMP). Moreover, with high-density deployment, the number of APs is large (like massive MIMO), however, the antennas in D-MIMO are distributed. The densification will reduce the likelihood of blockage in the context of mmWave (Figure 4-1, right). D-MIMO will be implemented in 3GPP scenarios (see [38.901]) like the Urban Micro for example.

The objective is to study innovative, scalable multi-antenna techniques adapted to the different 6G frequency bands. To do so, a 6G PHY-layer communication chain will be fully implemented using Python to obtain bit error rate (BER) versus SNR at the output as discussed in Section 11.1. The chain will implement coding, modulation, combined D-MIMO and OFDM technique with precoding to focus energy on UE direction. The main challenge will be the channel modelling in the THz frequencies through the choice of modelling blockage (time, blocker size, probability law). This will have a significant impact on the final performances when comparing D-MIMO with MIMO.

In a future deliverable, the chain will be validated using a known channel statistical model like Rayleigh fading one to be able to derive BER equation and check whether it matches with simulation. Also, a more advanced channel is going to be added to bring it closer to reality in the sub-THz spectrum (Chapter 3). Of course, power normalization will be done for fairness.

To obtain performance evaluation, several assumptions are made: RF imperfections, power amplifiers nonlinearities, hardware impairments and phase noise (PN) are omitted. The evaluations will be done with frequency range 2 (FR2) frequencies and beyond.

4.1.2 Non-coherent Space-time Coded Transmission

Problem statement: The mmWave frequency band faces challenges in reliable communication due to high path loss and shadowing. Besides, channel estimation can be tricky in several scenarios, e.g., high mobility, lack of uplink/downlink reciprocity, hardware calibration conditions and pilot contamination. Non-Coherent Joint Transmission (NC-JT) schemes defined in 3GPP [36.741], can be used to address these issues, however, it is not clear how to use them with distributed and massive number of antennas. The aim is to explore robust transmission modes in challenging conditions by using orthogonal space time frequency block codes (STFBC) in D-MIMO precoding to enhance diversity at the UE side and maintain certain data rates even without precise channel state information (CSI).

Methodology: A downlink (DL) D-MIMO network is considered, comprising M radio units (RUs) equipped with L antennas each, all connected to a distributed unit (DU) with baseband capability through fronthaul links, and K UEs equipped with N antennas each. An RU-UE clustering is carried out to establish disjoint clusters of RUs jointly serving UEs, within each of which a suitable STFBC is going to be applied. It is assumed that the DL pilot signals are transmitted and channels are perfectly estimated at the UE side, but not known at RUs. An example D-MIMO network is depicted in Figure 4-2

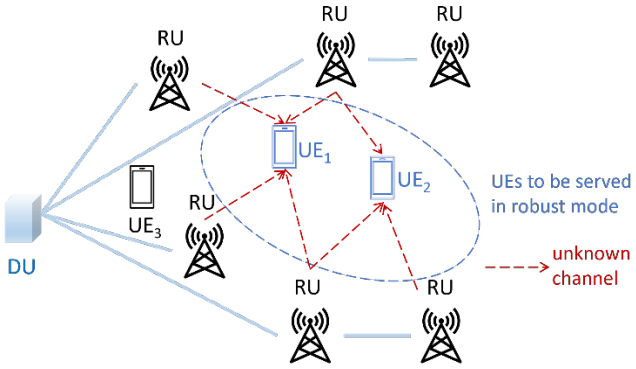

Figure 4-2: An example D-MIMO network where some UEs are in robust transmission mode.

Alamouti-like Orthogonal Codes in D-MIMO: Alamouti-like orthogonal codes are used to realize the robust transmission mode, which use time, frequency and space diversity at the UE side. The code is set on transmitting only $0, s, -s, s^*, -s^*$ where s is the information carrying complex symbol. A code matrix $C_{Q,P,T}$ is defined, where Q, P, T denote the number of transmit antennas, number of complex symbols transmitted within one code period, and code period, respectively, with dimensions $T \times M$ where the (i, j)-th entry includes the transmitted signal from j-th antenna at the i-th time/frequency instant. A code is considered orthogonal if, for all complex symbols, the columns of the code matrix are mutually orthogonal. Alamouti introduced a code with the following code matrix, $C_{2,2,2} = \begin{bmatrix} s_1 & s_2 \\ -s_2^* & s_1^* \end{bmatrix}$ [A98]. Orthogonal codes providing the highest rates for a given M are derived in [SXL+4].

A single cluster including all RUs with a larger STFBC is not practical since the code rate decreases as the code period increases. For lower fronthaul traffic and sufficiently short code period, three smallest perfectly orthogonal codes ($C_{2,2,2}, C_{3,3,4}, C_{4,6,8}$) have been considered. To apply Alamouti-like orthogonal codes in D-MIMO, separate RU-UE clusters are determined where each cluster can use a different orthogonal code and within each cluster by sharing symbols among UEs. It is important to note that the conventional STFBC framework is designed for a single UE transmitting multiple symbols, which can be applied by sharing symbols among multiple UEs and each UE can locally decode its intended symbol. Herein, sharing symbols between multiple UEs decreases the diversity gain and SE. Nevertheless, in case of high inter-user interference, particularly among closely located UEs, adopting a multi-user clustering approach may bring additional benefits.

Achievable User SEs: Based on the selected STFBC and the time/frequency index, RUs transmit one of the symbols s, $-s$, s^*, $-s^*$, 0. For a given cluster of RUs and UEs, the received signal at the k-th UE can be written as

$$\mathbf{r}_{k,n} = \sum_{i \in S_k} \mathbf{h}_{k,n,i} s_i + \sum_{i \in \frac{C_k}{S_k}} \mathbf{h}_{k,n,i} s_i + \sum_{i \notin C_k} \mathbf{h}_{k,n,i} s_i + \mathbf{z}_{k,n}, \quad \textbf{(4-1)}$$

where s_i is the transmit symbol, $\mathbf{r}_{k,n}$ is the received signal vector at the n-th antenna of the k-th UE. S_k and C_k represent the set of indices for symbols intended for k-th UE and symbols transmitted within the cluster of k-th UE, respectively. The augmented channel vector $\mathbf{h}_{k,n,i}$ is defined as the channel for the n-th antenna of k-th UE for the symbol s_i. and this vector includes the channels of serving RUs according to the cluster of k-th UE and the order of symbol s_i in that cluster. $\mathbf{z}_{k,n}$ follows a complex normal distribution $CN(0, \sigma_k^2 \mathbf{I})$ as the noise vector at the n-th antenna of k-th UE. Given that a perfectly orthogonal code is provided, the augmented channel vectors become orthogonal, i.e., $\mathbf{h}_{k,n,i}^H \mathbf{h}_{k,n,j} = 0$ for all $i \neq j$ and $i, j \in C_k$. Due to the orthogonality of the code and the disjoint clusters, the k-th UE can eliminate symbols in the difference between two sets, C_k / S_k, while interference from outside the cluster C_k remains. Hence SINR for the symbol s_i for any $i \in S_k$

is found as $\text{SINR}_{k,i} = \frac{\sum_{n=1}^{N} \mathbf{h}_{k,n,i}^{H} \mathbf{h}_{k,n,i} P_t}{\sum_{j \notin C_k} \text{E}\left[\sum_{n=1}^{N} \mathbf{h}_{k,n,j}^{H} \mathbf{h}_{k,n,j}\right] P_t + \sigma_k^2}$ where P_t is the transmit power. Since instantaneous CSI is not known at the RU, achievable outage user SEs can be found with various approaches:

Ergodic SE can be found as $SE_{ergodic,k,i} = \frac{1}{T_0} \sum_{i \in S_k} \text{E}[\log_2(1 + \text{SINR}_{k,i})]$. All codes are extended to T_0 time samples considering multiple code periods. To evaluate ergodic SE, probability density function of $\sum_{n=1}^{N} \mathbf{h}_{k,n,i}^{H} \mathbf{h}_{k,n,i}$ need to be calculated. The solution and proofs can be found in [KHR+23].

Outage SE assuming a constant transmission rate and successful decoding in case instantaneous SINR surpassing a threshold $\text{SINR}_{min,k,i}$. Monte-Carlo method is used for numerical evaluation and outage SE can be found as $SE_{outage,k,i} = \left(1 - \Pr\left(\text{SINR}_{k,i} < \text{SINR}_{min,k,i}\right)\right) \sum_{i \in S_k} \log_2\left(1 + \text{SINR}_{min,k,i}\right)$

Cluster Formation: The primary objective is to identify RU-UE clusters to optimize the overall performance. A heuristic clustering method is proposed based on closed-form ergodic SEs, where clusters are grouped in a three-step algorithm that utilizes large-scale fading and correlation parameters and is executed at the DU. The steps can be summarized as (i) one-to-one association of RU antenna and UE to form *K* disjoint clusters, (ii) iteratively merging clusters based on minimum ergodic SE in clusters, (iii) adding remaining antennas. More details can be found in [KHR+23].

Results: Numerical simulations are performed in an indoor factory of area 120 × 60 meters, where operating frequency is 28 GHz with 200 MHz bandwidth. Path loss and shadowing is set as in [38.901], and small-scale channel model is Rayleigh distributed. Maximum transmission power (P_t) is 0.2W and UE noise figure is 9 dB. Outage probability is set as 0.01. Alamouti-like STFBC in D-MIMO is compared with small cells and NC-JT case 2b (single frequency network (SFN)) transmission [36.741] . Figure 4-3 shows the per-UE cumulative distribution functions (CDFs) for outage and ergodic SEs, where it is observed that STFBC together with optimized clustering outperforms baseline methods, i.e., small-cell and SFN in terms of outage SEs, and provides 5th percentile ergodic SEs compared to small-cell and SFN. Another observation is that a significant enhancement of the 5th percentile user ergodic SEs can be achieved with STFBCs, while the mean values are similar both for STFBC and small-cell, and this shows that the clustering can optimize the worst-case SEs by maintaining a similar performance for all users on average.

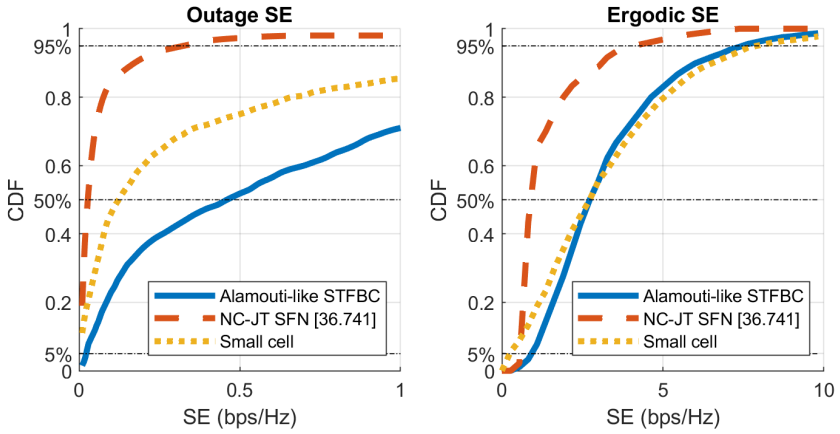

Figure 4-3: CDFs of per-user outage and ergodic SEs for Alamouti-like STFBC, SFN and small cell approach $M = 16, K = 4, N = L = 1$.

4.1.3 Distributed OTA cooperative beamforming design

Problem statement: D-MIMO emerges as a promising technology capable of enhancing spectral efficiency beyond the confines of traditional cellular networks. Diverging from the conventional approach, D-MIMO integrates all APs within a specific area under the same operator, serving all the UEs. This configuration diminishes intercell interference, making it especially well-suited for small-cell applications. Despite the predominant focus in the literature on non-cooperative beamforming strategies (example, based on maximum ratio transmission, local minimum mean squared error), where each AP locally designs its beamformer without

exchanging CSI through fronthaul links, recent studies highlight the potential for cooperative beamforming strategies (example, based on global minimum mean squared error) to yield even greater performance gains. However, the cooperative beamforming design requires the CSI exchange via fronthaul links, which may not be feasible due to the fronthaul bandwidth limitations and not scalable. This work provides a cooperative beamforming design without exchanging the CSI via fronthaul links, using the bi-directional training.

Methodology: Considering the downlink communication, the cooperative beamformers is designed using bi-directional training, where the UEs update their combiners using downlink pilots (DL), and APs update their precoders using uplink pilots (UL-1 and UL-2) using iterative bi-directional training.

The considered D-MIMO system consists of B APs, and K UEs with 4-antennas randomly distributed in a 500m\ X\ 500 m geographic area. the APs are connected to a central processing unit (CPU) via fronthaul connections. The channel between k^{th} UE and b^{th} APs is $\boldsymbol{H}_{b,k}$, which includes both large-scale fading coefficient and small-scale fading coefficient. The sum-mean squared error (MSE) minimization is considered to optimize the precoders at the AP and combiners at the UE, where the MSE of UE 'k' is given as

$$MSE_k = \sum_{\bar{k}} |\sum_b \boldsymbol{v}_k^H \boldsymbol{H}_{b,k}^H \boldsymbol{w}_{b,\bar{k}}|^2 - 2Re\left[\sum_b \boldsymbol{v}_k^H \boldsymbol{H}_{b,k}^H \boldsymbol{w}_{b,k}\right] + \sigma^2 |\boldsymbol{v}_k|^2 + 1\,, \qquad \textbf{(4-2)}$$

where $\boldsymbol{v}_k$ is the combiner at UE k, $\boldsymbol{w}_{b,k}$ is the UE k precoder at BS b. σ^2 is the AWGN power at UE k.

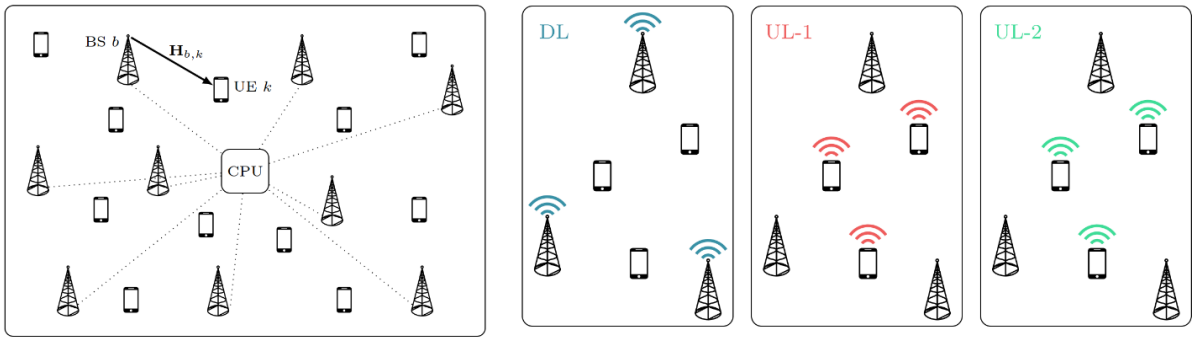

Figure 4-4: D-MIMO systems (left). Single Bi-directional iteration consists of a DL and two UL pilot signal (The BSs in the figure can be treated as APs).

The MSE is not convex jointly with respect to both the combiner and precoder. Therefore, alternating optimization is used to minimize the MSE, where combiner is minimized for a fixed set of precoders and vice-versa in an iterative manner using bi-directional training [AGT21].

Considering the TDD system, each UE computes the combiner using the DL pilot signals from all the base stations (BSs) (see Figure 5-4). Each AP computes the precoder based on two UL signals (see Figure 5-4). UL-1 comprises local UE channel information (where each UE transmit precoder pilots), while UL-2 contains the cross-channel information among the APs (where each UE transmit the received DL pilot signal as UL). Thus, the combiners and precoders are iteratively updated until the convergence or a predefined criteria is met using the bi-directional training iterations. The complexity of the proposed method is much less than the CPU based design. For more details about the implementation and complexity, please check [AGT21].

Results: The evaluation considers 25 BS placed on square grid of 500m×500m area. 16 multiantenna UEs are randomly placed. The channel between UEs and APs follows Rayleigh fading, and the carrier frequency is 2.5 GHz. The proposed distributed beamforming method with OTA signalling, i.e., distributed-OTA, distributed GB, distributed best response (BR), distributed best response-group specific (BR-GS) outperform the local (Local minimum mean squared error (MMSE), MF) and centralized methods in both unicasting and multicasting. The number of OTA resources required for unicasting depends on the number of UEs, while the number of OTA resources required for multicasting depends on the number of multicasting groups. Note that the imperfect channel includes AWGN at APs and UEs.

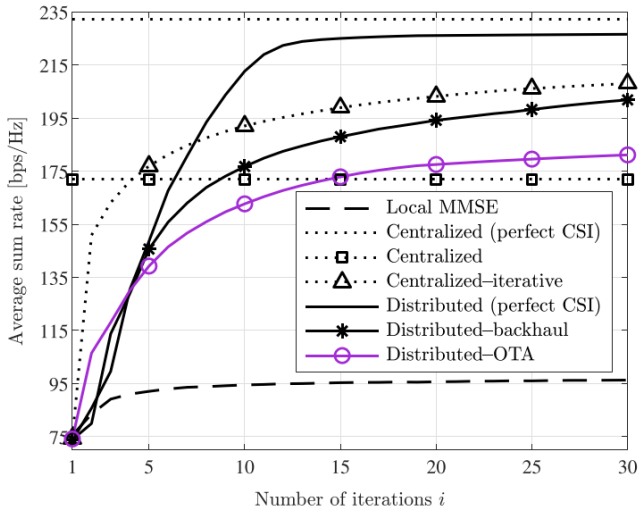

Figure 4-5: Unicasting scenario: the proposed distributed OTA scheme approaches to the distributed-backhaul, and outperform the centralized and local beamforming methods [ATG21].

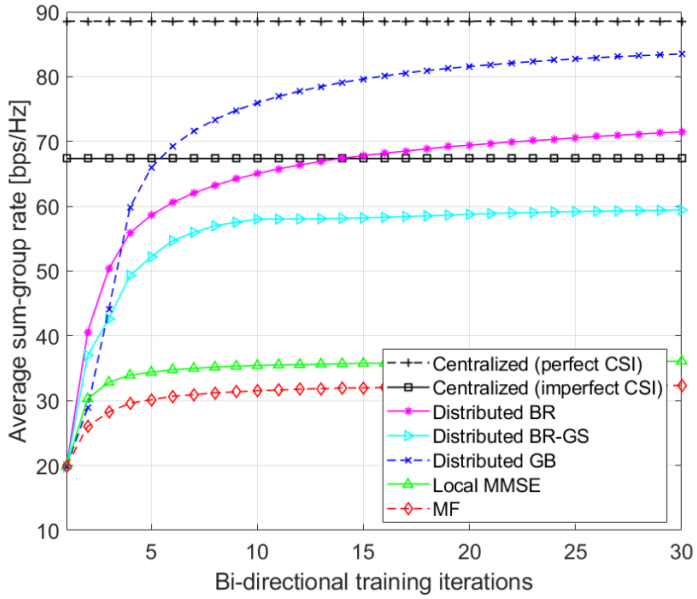

Figure 4-6: Multicasting scenario: the proposed distributed GB with reduced training resources outperform the other methods.

4.1.4 D-MIMO with rotary ULAs

Problem statement: Traditional wireless communication systems adopt static antennas, that is, antennas or antenna arrays without any movement capabilities. Nevertheless, the idea of antenna elements with movement capabilities has recently gained traction among the research community [ZMZ23]. Movable antennas can exploit wireless channel variation in the continuous spatial domain. This additional degree of freedom can enhance the quality of wireless links, and consequently the communication performance.

The movable antennas for multi-user MIMO (MU-MIMO) that have recently been studied in the literature consist of antennas that can move in a confined 2D or 3D region [ZMZ23]. Such systems require many components such as mechanical controllers, drivers, and cables. Consequently, they are complex, bulky, expensive to be deployed and maintained, and can potentially have mechanical robustness issues. In this contribution, a movable antenna system that presents lower complexity, deployment and maintenance costs is proposed. More specifically, the performance of MU-MIMO systems where the APs are equipped with rotary

uniform linear array (ULA) is studied. A rotary ULA consists of a ULA coupled to a servo motor, which controls its rotation. Industrial servo motors can perform high speed rotations (on the order of hundreds of microseconds to few milliseconds) with very high precision (angular resolution on the order of 0.1°). Thus, rotary ULAs are suitable to enhance the connectivity in low mobility scenarios where the same subset of devices are transmitting/receiving data during a sufficiently long period of time. Considering an indoor industrial scenario, the numerical results show that the adoption of APs equipped with rotary ULAs can significantly enhance the mean per-user achievable SE when compared to deployments with static APs.

Methodology: An indoor square coverage area with dimensions $l \times l\ m^2$ is considered. The coverage area is served by Q APs, each equipped with a ULA with $S=M/Q$ half-wavelength spaced antenna elements, where M is the total number of antenna elements of the system. the APs are deployed at the ceiling of the coverage area, at height h_{AP}.

Several single antenna devices are randomly and uniformly distributed on the coverage area. From this large number of potentially active devices, a random subset of K devices is active and seeks to transmit data in the uplink in each time slot. All devices are positioned at the same height h_{MTD}.

Fully centralized processing is considered, where all the APs simultaneously serve all the devices, and they are connected to a common CPU through fronthaul connections. The CPU is responsible for performing all the signal processing tasks of the system, including the optimization of the orientation of the rotary ULAs and the computation of the centralized zero forcing (ZF) receive combining vectors.

In this contribution, it is assumed that there are no hardware impairments, and there is perfect synchronization among the APs. Moreover, CSI is available at the APs.

Assuming that CPU has estimates of the positions of all the devices subscribed to the network, for each subset of K active devices, there is an optimal orientation for the APs that enhances the quality of the wireless links between the APs and the devices. The optimal position of the Q APs is jointly computed by the CPU using particle swarm optimization (PSO). The procedure for the location-based optimization of the positions of the APs is illustrated in Figure 4-7.

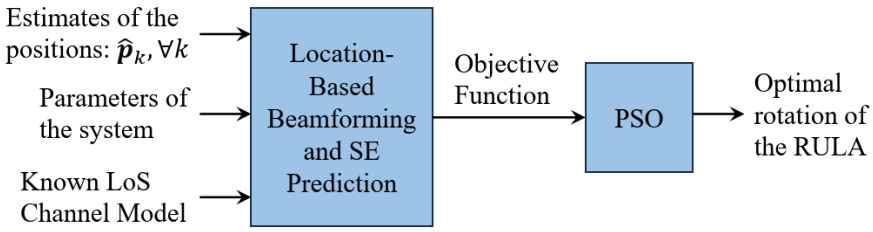

Figure 4-7: Block diagram of the location-based optimization of the rotation of the rotary ULAs.

Results: Monte Carlo simulation results are generated using MATLAB. The numerical results are averaged over multiple network and channel realizations. For each network realization, a new set of positions of active devices is generated, which corresponds to a new set of LoS channel vectors. Then, for each network realization, several channel realizations are generated. Each channel realization corresponds to a set of NLoS components for the active devices. The reader can refer to the Appendix A.2.1 for the detailed assumptions and simulation parameters. The numerical results are shown in Figure 4-8. The results for the case of APs equipped with static ULAs are compared to the results for the case of APs equipped with the proposed rotary ULAs. The curves show that the performance improvement of the rotary ULAs compared to the static ones grows with the Rician factor. When the Rician factor is low, the wireless channels are dominated by non-line-of-sight (NLoS) components. In this case, the rotation of the ULAs does not bring performance gains. On the other hand, when the Rician factor grows, the power of the LoS components increases. In this new situation, where the channels are dominated by LoS, the rotation of the ULAs brings significant enhancement to the spectral efficiency. Moreover, the curves also show that the intermediate setups with Q=2 and Q=4 achieve the best performance, which shows that there is a "sweet spot" between the number of APs and number of antenna elements per AP that yields the best performance.

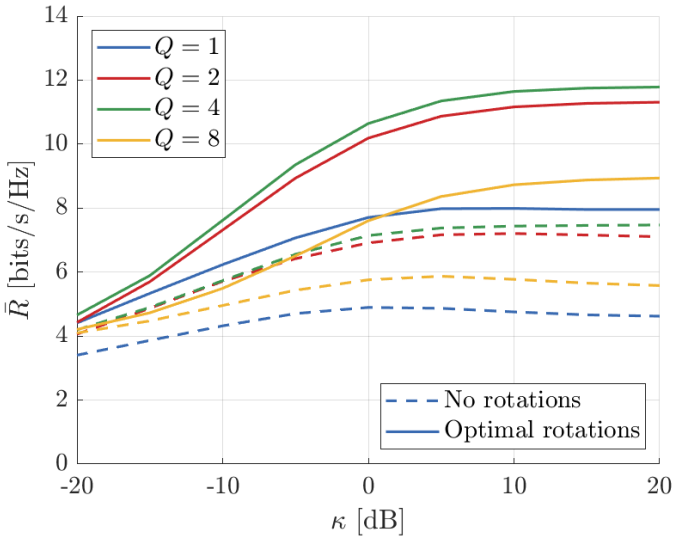

Figure 4-8: Mean per-user achievable SE $\bar{R}$ versus the Rician factor K, for different number of APs Q.

4.1.5 Distributed-MIMO with analogue fronthaul

Problem statement: D-MIMO networks show better performance compared to traditional co-located systems. However, D-MIMO introduces new challenges related to higher demands on bandwidth, synchronization, and power consumption [IBN+19]. Therefore, innovative solutions are essential to harness the potential of D-MIMO in a cost-effective manner. To fully leverage the diversity and power gains of D-MIMO networks, coherent joint transmission (CJT) involving two or more transmit/receive points (TRxPs) must be supported. However, meeting the stringent synchronization requirements with sub-nanosecond precision becomes crucial for CJT. One practical approach to achieving CJT is by employing analogue fronthaul (FH) links in combination with centralized processing since channel estimation includes the phase and amplitude change of both the wired path (i.e., fronthaul link) and wireless path of each transmitter, providing all the necessary information for CJT precoding.

Methodology: A simple multiple-input single-output (MISO) setup is assumed involving an N-TRxP D-MIMO network and a single UE. Both the UE and all TRxPs within the network are assumed to have a single antenna. Expressing the baseband received signal at the UE in the downlink direction mathematically yields:

$$y = \mathbf{h}\mathbf{w}s + n \tag{4-3}$$

where $\mathbf{h} = [h_1, h_2, \ldots, h_N]$ represents the $1 \times N$ channel vector assumed to exhibit flat-fading behaviour, s denotes the transmitted data symbol, $\mathbf{w}$ stands for the N×1 precoding weights vector, and n characterizes the additive white Gaussian noise (AWGN) scalar distributed as $\mathcal{CN}(0, N_0)$ where N_0 denotes the noise power spectral density. To maximize the signal-to-noise ratio (SNR), the precoder $\mathbf{w}$ must be computed in a manner that aligns the signals from different TRxPs coherently (i.e., phase aligned). For instance, employing maximum ratio transmission (MRT) precoding enables achieving the highest SNR gain. Consequently, the SNR received over the AWGN channel can be expressed as indicated in reference [TV05]:

$$\mathrm{SNR} = \frac{\mathrm{P}\|\mathbf{h}\|^2}{\mathrm{N_0}} = \sum_{\mathrm{i}=1}^{\mathrm{N}} \frac{\mathrm{p_i}|\mathrm{h_i}|^2}{\mathrm{N_0}} \tag{4-4}$$

where p_i represents the average transmit power assigned to each TRxP.

Experimental results: The experimental setup with two TRxPs is detailed in Appendix A.2.2. D-MIMO CJT is assessed using a 10 MHz OFDM signal carrying high-order 256-QAM symbols across all subcarriers. For

fair CJT evaluation, the error vector magnitude (EVM) performance for both TRxPs is adjusted to be nearly identical during separate transmissions. To assess D-MIMO flexibility with analogue FH links, TRxP 1 has an 800m fibre FH link, while TRxP 2 uses a 1.2m coaxial cable, resulting in a ~3.897 µs delay difference (considering fibre's light propagation speed at ~68.46% of vacuum speed). This exceeds the cyclic prefix (CP) duration for OFDM signals of 2.34 µs (at 30 kHz subcarrier spacing [38.104]), needing more than signal precoding alone for CJT, i.e., delay difference measurement and time alignment. Figure 4-9 shows the received symbol constellations from individual wireless transmissions of TRxP 1 and TRxP 2, with EVM root mean square (RMS) values of around 9.14% and 9.27%, showing similarity. The measured delay difference of 3.906 µs closely aligns with the theoretical 3.897 µs, accounting for additional delays from optical and electrical devices.

For CJT, separate channel estimation is performed for TRxP 1 and TRxP 2. These estimates are used to compute the precoder for the TRxP 2 signal. The precoded signal is aligned in time in accordance with the measured delay difference between FH links. Figure 4-10 shows the received symbol constellations, with and without precoding and time alignment, i.e., non-CJT and CJT, when both TRxPs are transmitting simultaneously. Without CJT processing, an EVM of 99.74% is measured due to the lack of coherency and inter-symbol interference (ISI). Conversely, by applying precoding and time alignment, an EVM of 5.01% is achieved, maximizing network diversity and power gains by aligning the transmitted signals in time and phase.

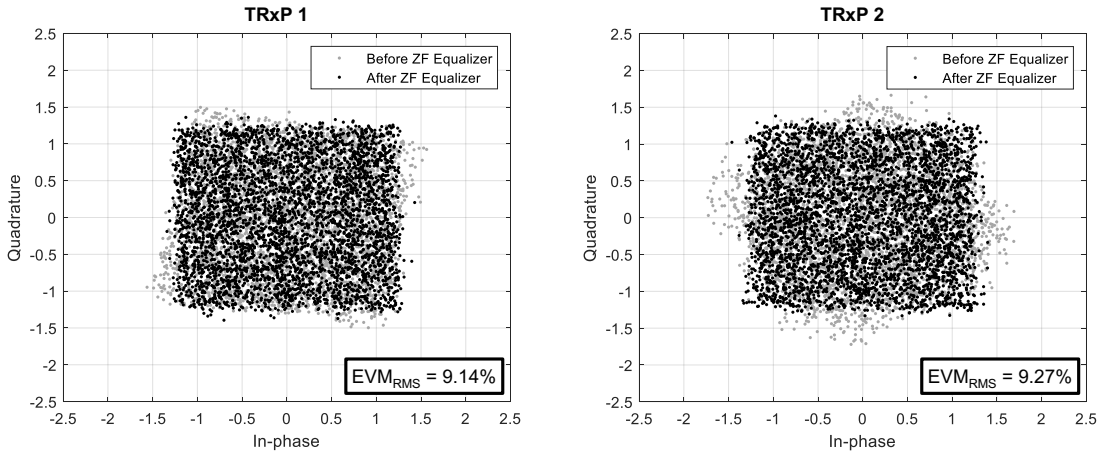

Figure 4-9: TRxP 1 and TRxP 2 received symbols constellations and EVM before and after ZF equalization.

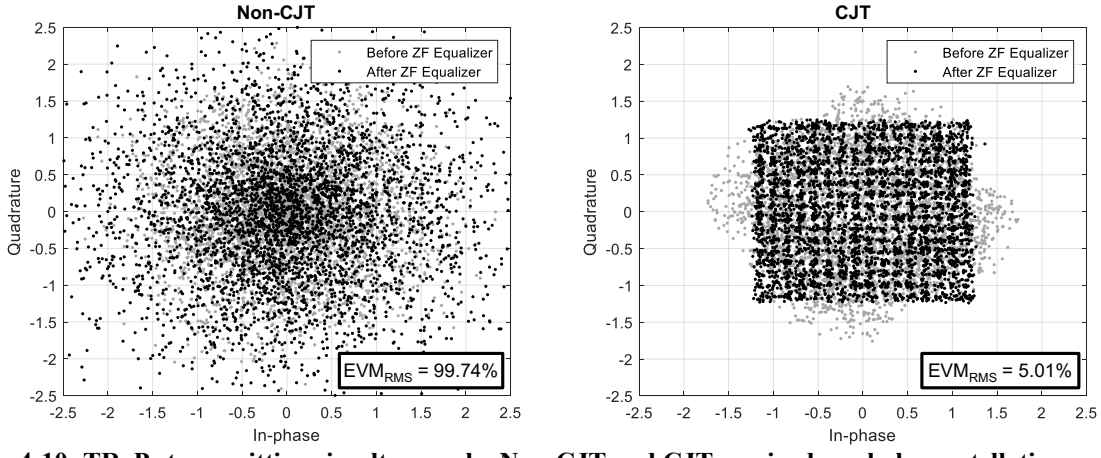

Figure 4-10: TRxPs transmitting simultaneously. Non-CJT and CJT received symbols constellations and EVM before and after ZF equalization.

As the transmission channel conditions of the TRxPs closely resemble flat fading the next relationship between the EVM and SNR [BHH+18] is valid for assessing the combined diversity and power gains in the network:

$$\mathrm{SNR} \approx \frac{1}{\mathrm{EVM}_{\mathrm{RMS}}^2} \quad \textbf{(4-5)}$$

Thus, the CJT gain approximates ~5.35 dB when compared to TRxP 2 transmissions alone and approximately ~5.22 dB in comparison to TRxP 1 transmissions. It is important to note that for a two TRxPs D-MIMO network, the theoretical CJT gain is expected to be 6.02 dB. The observed lower experimental CJT gain is attributed, firstly, although the EVM performance of both TRxPs was adjusted to be equal, differences in wireless distances between antennas led to unequal transmit power between TRxPs. Additionally, the antennas of both TRxPs are not identical, and the wireless transmissions do not occur in a perfectly flat-fading channel.

4.1.6 One-bit ADC for multi-cell setup

Problem statement: The next generation of wireless systems, beyond 5G, may operate at extremely high frequencies up to 1 THz with large bandwidths, which requires larger antenna arrays and increasingly sharp beamforming to maintain a consistent signal-to-noise ratio. However, the analogue-to-digital converters (ADCs) /digital-to-analogue converters (DACs) used in current systems consume a lot of power. One solution is to use low-resolution ADCs / DACs with 1 to 4 quantization bits to enable the use of massive MIMO arrays, which require hundreds or thousands of antennas. 1-bit ADCs/DACs are particularly appealing due to their minimal power consumption and simplicity. Additionally, the fully digital architectures can overcome limitations associated with hybrid analogue-digital beamforming at sub-THz frequencies. However, the SINR with 1-bit ADC is non-monotonic. Therefore, tuning the UE power to optimal SINR across D-MIMO scenario is challenging.

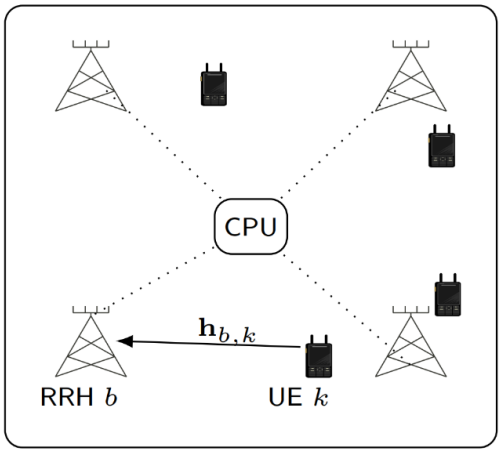

Figure 4-11: Distributed massive MIMO system. Here RRHs send the data to the CPU.

Methodology: To maintain the monotonic behaviour of the SINR in 1-bit ADC remote radio head (RRHs), the noise level is tuned at the RRHs. Thus, the signal to interference, noise and distortion ratio (SINDR) is monotonic with increasing UE power, and the UE powers are adjusted using gradient, block coordinate descent, and fixed-point iterative algorithms for multiple UE cases.

The distributed massive MIMO system consists of B RRHs and K single antenna UEs. The RRHs are separated by 100 m and UEs are clustered and move in-between the RRHs. The RRHs are connected to a CPU via fronthaul connections. The channel between kth UE and bth RRH is $\boldsymbol{h}_{b,k}$, which includes both large-scale fading coefficient and small-scale fading coefficient. This study focuses on the uplink scenario.

The min-power and max-min SINDR designs are considered to optimize the UE power levels and the BS noise levels. The following equation represents the max-min-SINDR problem used for optimization.

$$\max_{\boldsymbol{p_k},\boldsymbol{\sigma_b}} \min \mathbf{SINDR_k}$$

$$\boldsymbol{p_k} \leq \boldsymbol{p_{UE}} \quad \textbf{(4-6)}$$

$$\sigma_b \geq \sigma_{min}$$

where SINDR_k is the signal to interference noise and distortion ratio of UE k considering 1-bit ADC RRHs [GAT23]. p_k is the UE k power and p_{UE} is the maximum UE transmit power. σ_b is the noise level at the RRH and σ_{min} is the minimum noise level at the RRH corresponding to the AWGN. For a fixed noise level at the RRHs, the power of UEs can be optimized using a gradient, fixed-point iteration, or BCD methods. For the noise level optimization (which is more than the thermal noise), linear search is applied over the possible noise values.

Results: The evaluation considers 2 RRH placed with 100 m distance between them. The carrier frequency is 28 GHz, Rayleigh fading channel is used. the UEs are moved from one RRH to other RRH, and UEs transmit powers and RRH noise levels are optimized for each distance from the reference RRH. The power control with dithering tuning improved the SINDR of the UEs. The impact of dithering (i.e., RRH artificial noise level) is more pronounced when the UEs are closer to an RRH [GAT23].

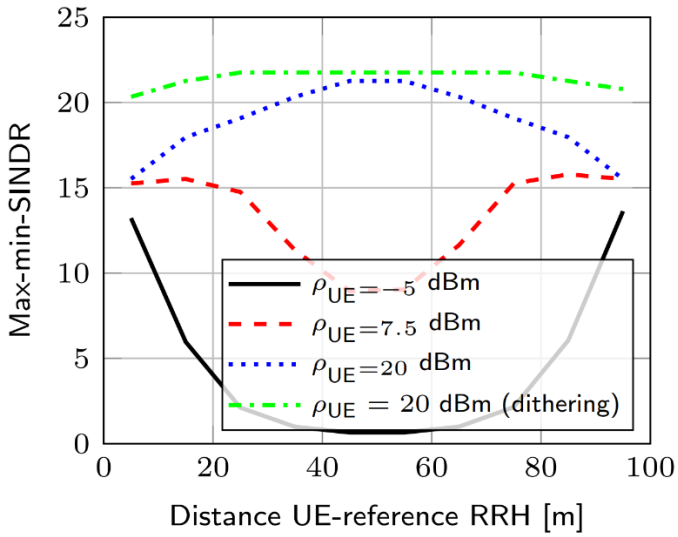

Figure 4-12: Two-RRH case: max-min-SINDR vs distance to UE-reference RRH.

4.1.7 sub-THz D-MIMO assisted by a sub-6 GHz macro network

Problem statement: Link quality at sub-THz frequencies is sensitive to blockage – LoS links will be relied on for providing satisfying link budget and outage probability. A D-MIMO network in form of sub-THz radio access nodes connected to a CPU ensures high probability of LoS at sub-THz frequencies. When a device moves or rotates, the serving beam needs to be updated. This entails a beam search procedure where the network sends reference signals in candidate beams and the device measures and reports the best beams. For radio access nodes with only one transceiver chain, beam sounding (sending reference signals in candidate beams) will be performed one beam at a time. In a system with many APs and many beams per AP (can be on the order of 1000 or 10000 beams in the entire D-MIMO system), the beam search procedure over all the beams in the system will take a prohibitively long time, incurring latency and/or system capacity reduction.

Methodology: As the first step of the solution to the problem above, the list of candidate beams for the beam search has to be reduced to a small subset of beams. A fundamental problem to solve is then *how to determine the list of candidate beams.* The proposed solution to the above problem is using the uplink channel characteristics from the target user device to a macro coverage node operating at a frequency substantially lower than sub-THz (concretely, below 6 GHz) to infer the candidate list for a beam search in the downlink of the sub-THz D-MIMO network towards the target UE. The proposed concept, broken down in 3 distinct steps, is illustrated in Figure 4-13.

Beam candidate list can be obtained by means of a neural network (NN) classifier trained to output approximations of posterior probabilities $p(\text{subTHz beam } k \text{ has best link quality} \mid \text{sub} - 6 \text{ GHz channel})$. One such classifier architecture is a feedforward NN with *cross-entropy loss function* and *softmax output activation function***.** Training and test phases are outlined in Figure 4-14.

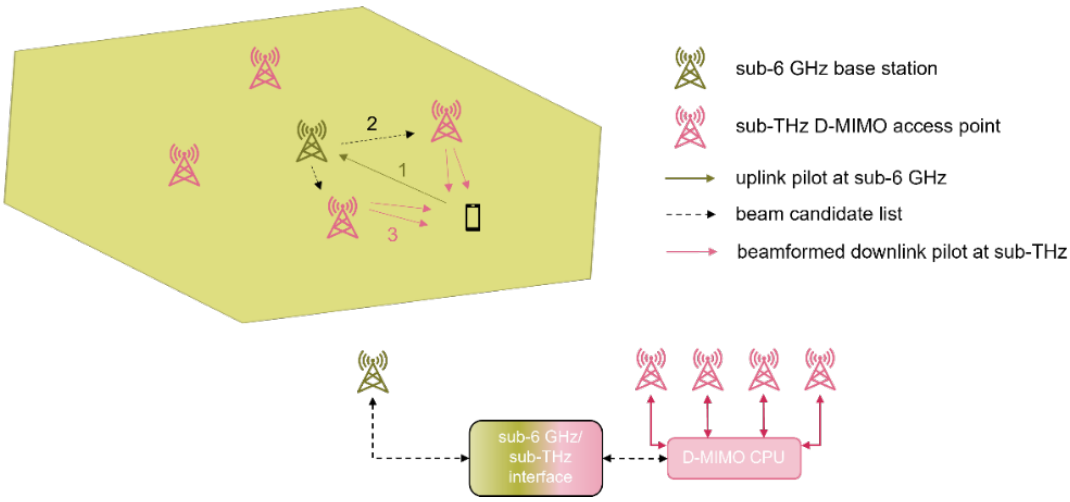

Figure 4-13: sub-6 GHz assisted beam search in sub-THz D-MIMO.

In a practical deployment, the training would be performed over a number of different device positions and different devices in the coverage area, such that the coverage area is properly sampled. In the test/exploitation phase, the probabilities $p_k = p(\text{sub} - \text{THz beam } k \text{ is best} \mid \text{sub} - 6 \text{ GHz channel})$ at the output of the classifier are used to compile the beam candidate lists. In this contribution, two strategies for compiling beam candidate lists are used:

- sort p_k in descending order, pick K beams with highest p_k for the list (***K* most likely beams**)
- sort p_k in descending order, sum sorted p_k until the cumulative sum > threshold, pick beams that enter the cumulative sum (**variable length list**).

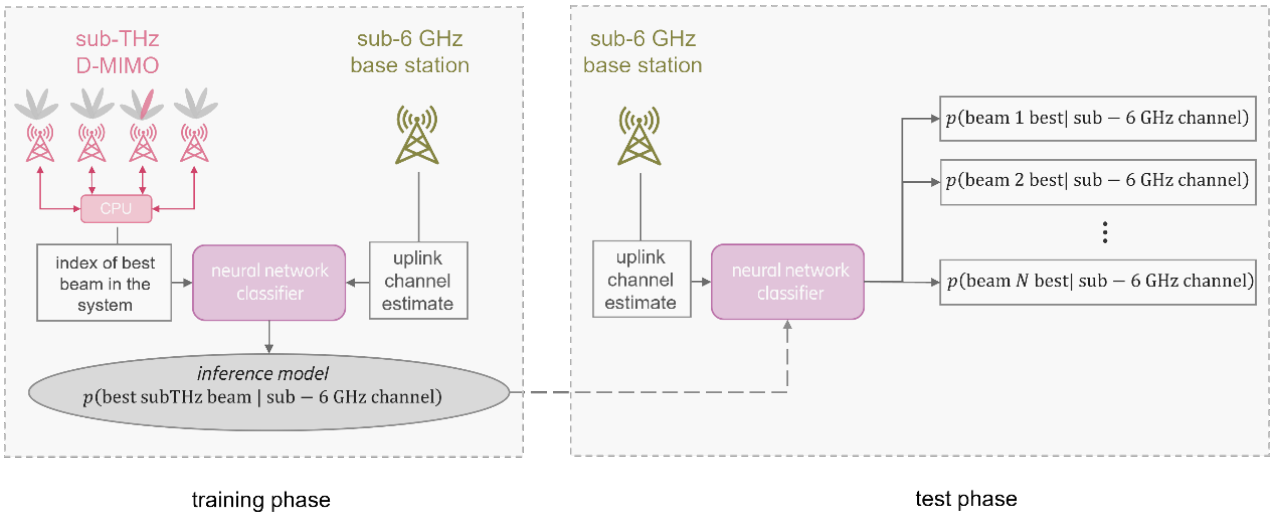

Figure 4-14: Training and test phases.

Results: The neural network classifier consists of N_{AP} single-layer classifiers with 150 nodes in the hidden layer, for inferring best beam per AP, and one single-layer classifier with 50 nodes in the hidden layer for inferring the best AP. The outputs are combined as $p(\text{best beam per AP}) \cdot p(\text{best AP})$ to produce p_k. Best beam is here taken as beam with highest receive power at the device. The feature (input) of the neural network is vectorized *2D instantaneous angular power spectrum of the multiantenna channel in DFT angular domain* with 64 dimensions.

Data is collected from an emulated 3D deployment shown in Figure 4-15, where a ray-tracing, spatially consistent channel model is used to generate channels. User positions are distributed over a 4×4 meter grid, for a total of 8504 positions over the shown coverage area. Data from 5000 positions, sampled uniformly over the coverage area, are used for training, 1000 for model validation and 2504 for testing. There is a total of 128*20 = 2560 beams in the system.

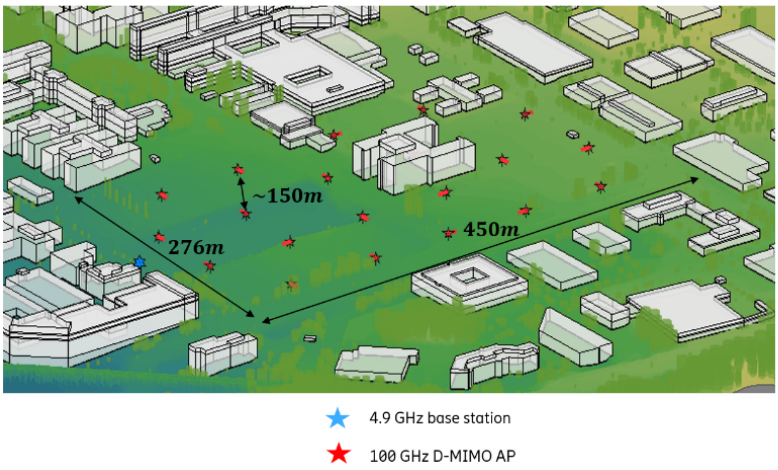

No. D-MIMO APs	20
Beams per AP	128 (16 azimuth, 8 elevation)
Carrier freq. BS	4.9 GHz
Carrier freq. D-MIMO	100 GHz
Tx power per antenna, device (4.9 GHz)	20 dBm
Tx power per antenna, APs (100 GHz)	15 dBm

Figure 4-15: Deployment configuration with relevant system parameters.

Statistical distribution of received power in the downlink, labelled as reference signal received power (RSRP) for the proposed scheme and setup are shown in Figure 4-16, alongside two benchmarks: 1) choosing the best beam from a randomly chosen set of K beams, 2) choosing the best beam from the set of K beams most commonly chosen as best over the training set. For the two benchmarks, no sub-6 GHz information and no machine learning (ML) training is necessary; the goal is to see if the proposed ML-based approach with sub-6 GHz assistance beats the benchmarks. Indeed, when a list of 50 beams is compiled based on the suggestion by ML based on sub-6 GHz data, the performance comes a few fractions of dB within the exhaustive search (black dashed line). The number of scanned beams in the 50-beam list example is only 50/ (128*20) = 1.9% of the total number of beams in the system, indicating an enormous resource overhead reduction when applying the proposed scheme.

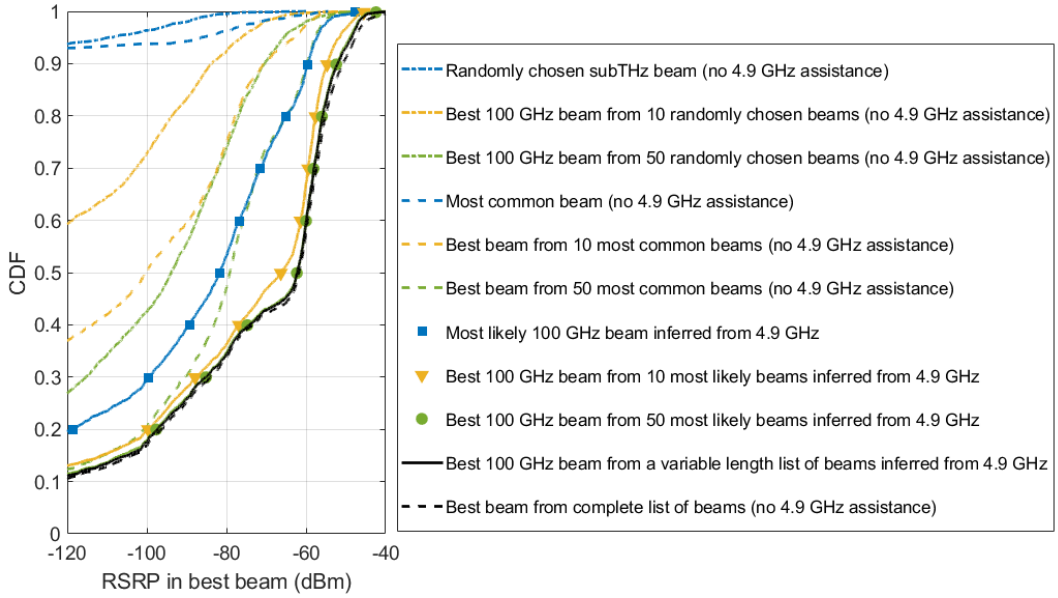

Figure 4-16: Distribution of received power at the device (RSRP) for the proposed scheme and two benchmarks.

4.2 Massive MIMO schemes and architectures

Massive multi-input multi-output (massive MIMO) is a crucial technology in the 5G and future wireless communication systems. It has already been implemented in several network scenarios and will continue to be used extensively. By augmenting the quantity of antenna elements, the massive MIMO system has the potential to greatly enhance spectral efficiency, reliability, coverage, and energy efficiency. By increasing the number of antennas and using high-frequency bands e.g., mmWave and sub-THz, the communication performance improves. However, massive MIMO encounters numerous challenges. This subchapter addresses several

critical problems, including massive MIMO transmission with one-bit converters and data detection, sub-THz beamformer design, coded caching, and the multi-user transmission systems.

4.2.1 Enhanced data detection for massive MIMO with 1-bit ADCs

Problem statement: New insightful results are presented on the uplink multi-user data detection for massive MIMO systems with 1-bit ADCs [RAT23b]. Specifically, the previous works [AT22] and [RAT23a], which characterized the expected values of the soft-estimated symbols (i.e., after the linear combining and prior to the data detection) for multiple UEs and with maximum ratio combining (MRC) receiver at the BS, are extended. Considering K UEs and a transmit constellation of L data symbols, the exhaustive single-UE data detection method proposed in [RAT23a] maps each soft-estimated symbol of the target UE to one of the LK expected values of the soft-estimated symbols based on the minimum distance criterion. This method has two main drawbacks: on the one hand, it performs an exhaustive search over the set of expected values of the soft-estimated symbols corresponding to the target UE resulting from all the possible data symbol vectors, whose size grows exponentially with the number of UEs; on the other hand, it does not take advantage of the interdependence among the soft-estimated symbols of the interfering UEs as it treats each UE individually. Moreover, the analysis in [AT22] and [RAT23a] is limited to the case of MRC, whereas more sophisticated linear receivers such as the ZF and MMSE receivers generally lead to better performance.

The expected values of the soft-estimated symbols when ZF and MMSE are adopted at the BS are evaluated numerically. Interestingly, these expected values can be obtained by simple scaling of their MRC counterparts, for which a closed-form expression was derived in [RAT23a]. Then, new data detection strategies are proposed based on the minimum distance criterion with respect to the expected values of the soft-estimated symbols. A joint data detection strategy is proposed, which considers parallel data detection over all the UEs and exploits the interdependence among their soft-estimated symbols. Furthermore, a low-complexity variant of the joint detection is presented, which is obtained by reducing the size of the search space. Numerical results show that ZF and MMSE provide substantial gains in terms of symbol error rate (SER) compared with MRC thanks to the reduced dispersion of the soft-estimated symbols around their expected values. In addition, the proposed joint detection and its low-complexity variant greatly outperform the exhaustive single-UE data detection method described in [RAT23a] since the latter does not account for the interdependence among the soft-estimated symbols of the interfering UEs.

Methodology: Consider a single-cell massive MIMO system where a BS, equipped with M antennas, serves K UEs in the uplink. Each BS antenna is connected to two 1-bit ADCs, one for the in-phase and one for the quadrature component of the received signal. The system model is illustrated in Figure 4-17.

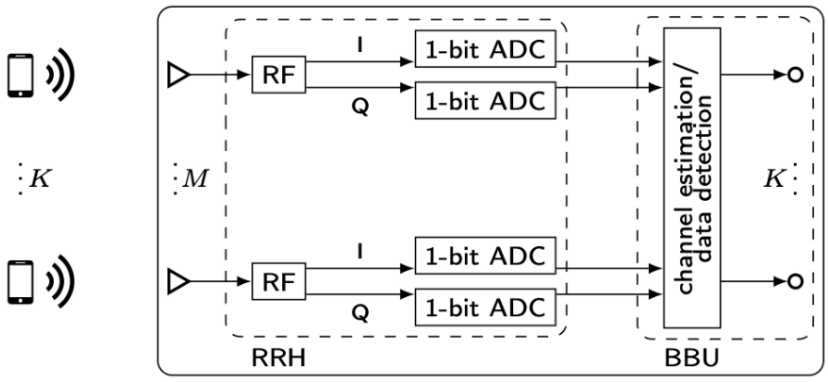

Figure 4-17: Fully digital massive MIMO system with 1-bit ADCs.

The received signal before the 1-bit ADCs is given by $\boldsymbol{y} = \sqrt{\rho}\boldsymbol{H}\boldsymbol{x} + \boldsymbol{z} \in C^{M\times 1}$, where ρ is the signal-to-noise ratio (SNR), $\boldsymbol{H} \in C^{M\times K}$ is the channel matrix, $\boldsymbol{x} \in C^{K\times 1}$ is the data symbol vector, and $\boldsymbol{z} \in C^{M\times 1}$ is the additive white Gaussian noise (AWGN) vector. A general correlated Rayleigh fading model is assumed for the channel. Then, the received signal after the 1-bit ADCs is given by $\boldsymbol{r} = Q(\boldsymbol{y}) \in C^{M\times 1}$, where $Q(.)$ is the 1-bit quantisation function. Finally, the BS obtains a soft estimate of $\boldsymbol{x}$ via linear combining as $\hat{\boldsymbol{x}} = \boldsymbol{V}^{\mathbf{H}}\boldsymbol{r} \in C^{K\times 1}$,

where $\boldsymbol{V} \in C^{M \times K}$ is the combining matrix. Imperfect CSI, obtained via the Bussgang linear MMSE estimator with pilot length τ, is assumed for the design of the combining matrix. The expected values of the soft-estimated symbols with MRC can be derived in closed form as a function of the signal-to-noise ratio (SNR), the pilot matrix used during the channel estimation, the Bussgang gain matrix resulting from the Bussgang decomposition, the covariance matrix of the quantised received signal during the channel estimation, and the cross-covariance matrix between the quantised signals received during the uplink data transmission and channel estimation.

Results: 16-QAM data symbols are considered. The channel covariance matrices are generated based on the one-ring channel model with no pathloss. The expected values of the soft-estimated symbols with ZF and MMSE are difficult to derive analytically and can be obtained using Monte Carlo simulations. Interestingly, the expected values with ZF/MMSE can be obtained by simple scaling of their MRC counterparts. This is illustrated in Figure 4-18 (a). In general, there is a significant gain for all the data detection strategies obtained with the ZF and MMSE compared with their MRC counterparts. The SER gain for the ZF/MMSE receivers is not due to their expected values but the reduced dispersion of the soft-estimated symbols around them. The proposed joint data detection (JD) and its low-complexity variant (N-JD) provide a significant boost in comparison with the exhaustive single-UE data detection (Exh. SUD) with the ZF/MMSE receivers. This means that taking advantage of the interdependence among the soft-estimated symbols of the interfering UEs gives a notable gain over the data detection strategies that treat each UE individually. This is illustrated in Figure 4-18 (b). Therein, it can be observed that the SER curves feature an optimal SNR operating point: at low SNR, the AWGN is dominant; at high SNR, the soft-estimated symbols corresponding to the data symbols with the same phase are hardly distinguishable. In between these regimes, the right level of AWGN produces a proper scrambling of the 1-bit quantised signals at the M antennas [AT22] and [RAT23b].

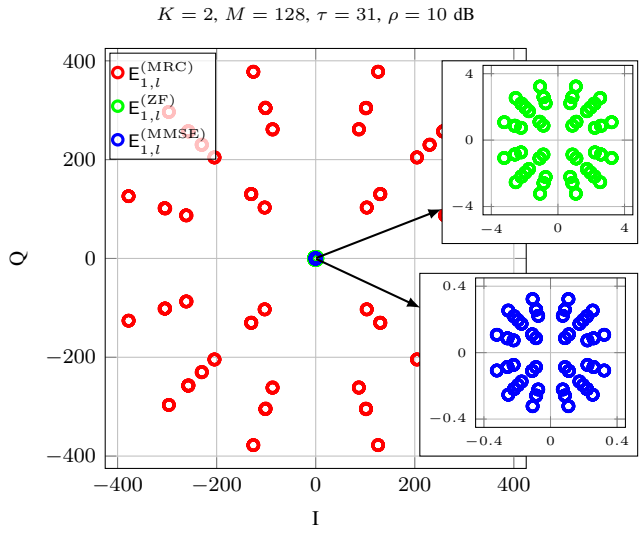

(a) Expected values of the soft-estimated symbols of UE 1 when UE 2 transmits all the possible data symbols and MRC, ZF, or MMSE is adopted at the BS

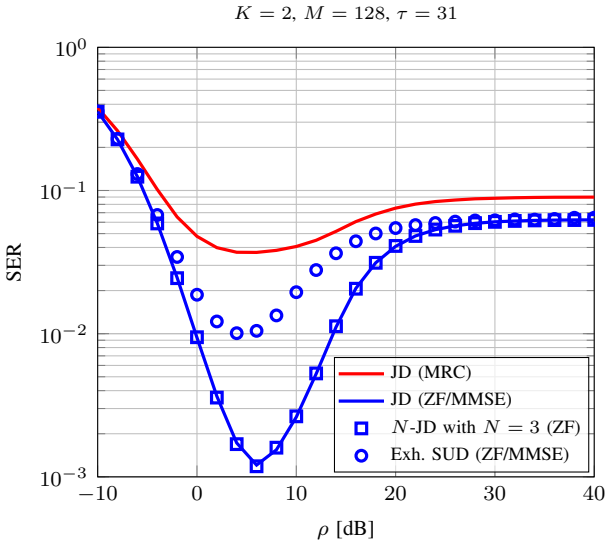

(b) SER versus SNR obtained with different data detection strategies and different receivers

Figure 4-18: Evaluation of enhanced data detection for massive MIMO with 1-bit ADCs.

4.2.2 Massive MIMO with 1-bit DACs and ADCs

Problem statement: Enabling communications in the (sub-)THz band will call for massive MIMO arrays at either the transmit- or receive-side, or at both. To scale down the complexity and power consumption when operating across massive frequency and antenna dimensions, a sacrifice in the resolution of the DACs/ADCs will be inevitable. Simple 1-bit DACs/ADCs can also alleviate the overall complexity and power consumption of the RF chains. For instance, 1-bit DACs at the transmitter allow the use of low-cost power amplifiers that are not constrained to operate with backoff [LMS+21], whereas 1-bit ADCs at the receiver relax the

requirements on the automatic gain control [NSN21]. Massive MIMO systems with low-resolution data converters have been generally studied assuming coarse quantisation at the base station (either in the DACs [ATD21] or in the ADCs [ATD21], [AT22], [RAT23a], [RAT23b]) and full-resolution user equipment (UE). The extreme scenario where both the transmit- and receive-side are equipped with fully digital massive MIMO arrays and 1-bit DACs/ADCs is analysed here, which is referred to in the following as *doubly 1-bit quantized massive MIMO* [ATN+23]. Indeed, combining 1-bit DACs and ADCs leads to a fully digital system with minimum RF complexity, cost, and power consumption. Note that the system model considered in this section can be considered as an extension of the model in Figure 4-17 by including 1-bit DACs.

Considering a point-to-point system, the Bussgang decomposition is utilised to unfold the relation between the transmitted data symbols (at the input of the transmitter's 1-bit DACs) and the soft-estimated symbols acquired via linear combining of the quantized received signal (at the output of the receiver's 1-bit ADCs). Assuming perfect CSI, a tractable approximation of the mean squared error (MSE) between the transmitted data symbols and their soft estimates is derived along with the combining strategy that minimizes it. This approximation is accurate in the regime of a large number of transmit antennas. Numerical results show that, despite its simplicity, a doubly 1-bit quantized massive MIMO system with very large antenna arrays can deliver an impressive performance in terms of MSE and SER, which is not far from that of a massive MIMO system with full-resolution DACs and 1-bit ADCs.

Methodology: Consider a point-to-point doubly 1-bit quantised massive MIMO system where a transmitter, equipped with N antennas and 1-bit DACs, transmits K data streams to a receiver with M antennas and 1-bit ADCs. Such a point-to-point system may represent, e.g., a wireless backhaul scenario. The system model is illustrated in Figure 4-19.

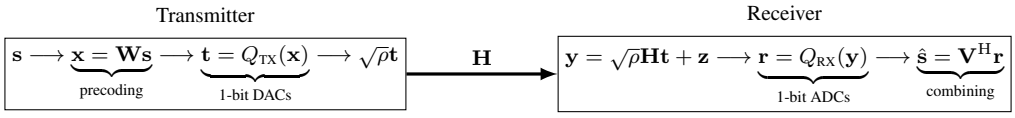

Figure 4-19: Doubly 1-bit quantised massive MIMO system.

The transmitter aims at conveying the data symbol vector $\boldsymbol{s} \in \mathbf{C}^{K\times 1}$ to the receiver. In this setting, $\boldsymbol{s}$ is first precoded as $\boldsymbol{x} = \boldsymbol{W}\boldsymbol{s} \in \boldsymbol{C}^{N\times 1}$, where $\boldsymbol{W}$ is the precoding matrix, and then quantised at the 1-bit DACs as $\boldsymbol{t} = \boldsymbol{Q_{tx}}(\boldsymbol{x}) \in C^{N\times 1}$, where $\boldsymbol{Q_{tx}}(.)$ is the 1-bit quantisation function at the DACs. Then, the signal arriving at the receiver is $\boldsymbol{y} = \sqrt{\rho}\boldsymbol{H}\boldsymbol{t} + \boldsymbol{z} \in C^{M\times 1}$, where ρ is the signal-to-noise ratio (SNR), $\boldsymbol{H} \in C^{M\times K}$ is the channel matrix, and $\boldsymbol{z} \in C^{M\times 1}$ is the additive white Gaussian noise (AWGN) vector. At the 1-bit ADCs, $\boldsymbol{y}$ is quantized as $\boldsymbol{r} = \boldsymbol{Q_{rx}}(\boldsymbol{y}) \in C^{M\times 1}$, which is the signal observed at the receiver and is the result of a double quantisation step. Finally, the receiver obtains a soft estimate of $\boldsymbol{s}$ via linear combining as $\hat{\boldsymbol{s}} = \boldsymbol{V}^{\mathbf{H}}\boldsymbol{r} \in C^{K\times 1}$, where $\boldsymbol{V} \in C^{M\times K}$ is the combining matrix. Perfect CSI is assumed for the design of both the precoding and the combining matrix. The MSE between $\boldsymbol{s}$ and its soft estimate $\hat{\boldsymbol{s}}$ can be written as $\epsilon = \frac{1}{K}E_{\boldsymbol{s},\boldsymbol{z}}[||\hat{\boldsymbol{s}} - \boldsymbol{s}||^2]$. To obtain a tractable expression of the MSE, Gaussian data symbols are considered. This allows one to apply the Bussgang decomposition to express the doubly 1-bit quantized signal observed at the receiver as a linear function of the original transmitted signal. In general, the Bussgang decomposition allows one to write the output of a nonlinear system as a scaled version of the input plus an uncorrelated distortion.

Results: Truly massive antenna arrays at both the transmitter and receiver (e.g., $N, M \geq 1000$) are necessary to achieve impressive values of the MSE. This is illustrated in Figure 4-20, where $\tilde{\epsilon}$ denotes the approximate MSE (which is derived analytically as described above). Assuming 16-PSK data symbols, remarkably small SER values can be obtained with truly massive antenna arrays at both the transmitter and receiver, although an acceptable SER can be achieved also for moderate array sizes [ATN+23]. In general, the performance of the considered doubly 1-bit quantised massive MIMO system is not far from that of a massive MIMO system with full-resolution DACs and 1-bit ADCs. In particular, replacing the 1-bit DACs with full-resolution ones provides a modest MSE or SER gain at the cost of much higher RF complexity and power consumption at the transmitter. It can be observed that, for fixed numbers of antennas, there is an optimal number of data streams: on the one hand, judiciously increasing the number of data streams generates a useful scrambling of the 1-bit

quantised signals at the M receive antennas; on the other hand, the inter-stream interference becomes dominant for large values of K [ATN+23].

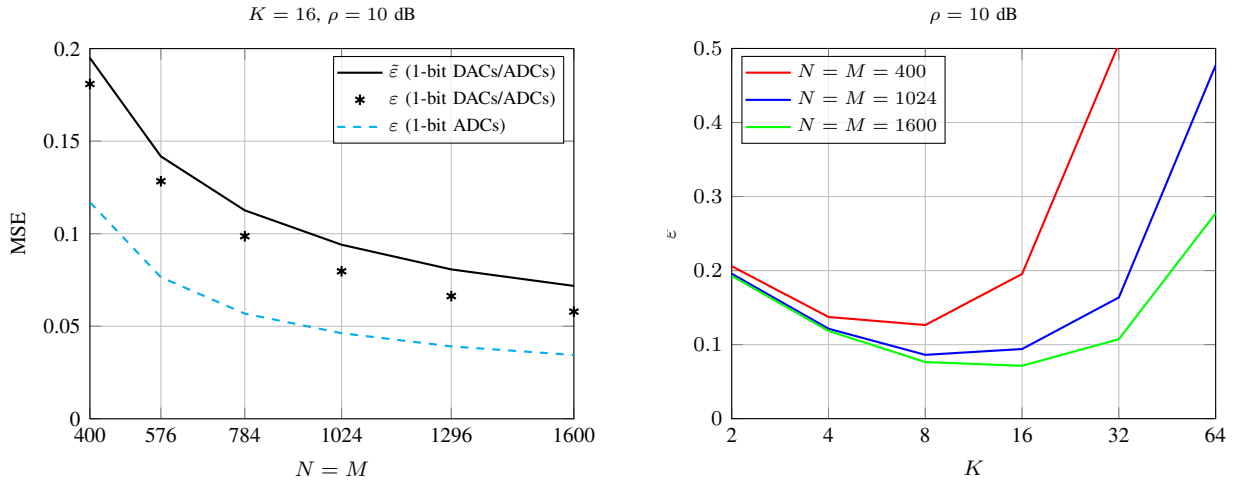

(a) MSE for 1-bit DACs/ADCs and full-resolution DACs/1-bit ADCs versus the number of transmit/receive antennas

(b) approximate MSE for 1-bit DACs/ADCs versus the number of data streams

Figure 4-20: Evaluation results of doubly 1-bit quantised massive MIMO.

4.2.3 Energy efficient beamforming architecture and deployment for sub-THz

Problem statement: Scope of this study is the spectral and energy efficiency trade-off of different beamforming architectures and BS placements, with focus on indoor scenarios and hybrid beamforming at the BS. With system level simulations the coverage and throughput of different deployment arrangements with different numbers of BS and randomly distributed UEs is evaluated. To assess the related energy efficiency, the power consumption is derived with a refined power consumption model based on that introduced in [HW21]. The expected outcome is to be in the position to derive most efficient deployment in terms of meeting coverage/throughput requirements with best energy efficiency.

Methodology: An indoor scenario with a size of 30m × 60m is considered Figure 4-21. It represents a generalized assessment scenario reflecting shopping malls or large conference or office areas. The intention is to match the scenarios for which channel measurements are available [HEX21-D22]. Base stations are located equally spaced at the walls of the longer side at a height of 4 meters and transmitting towards the room. In the initial scenario 8 BS are applied which transmit with a grid of beams (GoB) of 4 × 4 beams. For a fixed number of randomly distributed UEs (4, 8 and 16) the average UE throughput for different transmit power of the BS, the number of BS and the number of UEs is analysed. A first coarse power consumption assessment is given.

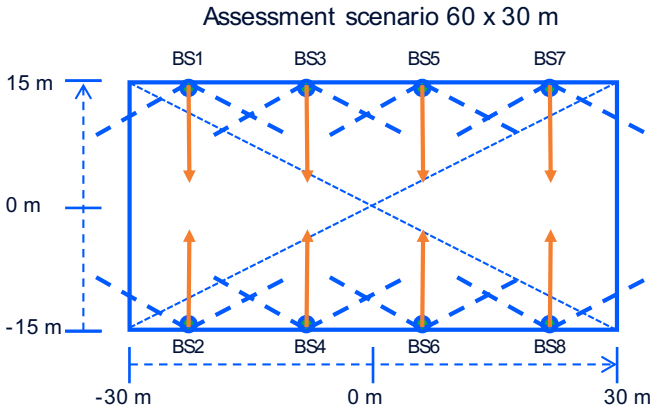

Figure 4-21: Indoor scenario with multiple BS used for assessment

Assumptions: For this analysis basic SINR evaluations are simulated, based on transmit power of the BS, antenna characteristics (Uniform rectangular array, with selection of ideal beam from a GoB) and a 3GPP channel model adapted to 140 GHz based on Hexa-X measurements from Aalto University [HEX21-D22] following the methodology described in the section on channel modelling of this deliverable. The assumed carrier frequency is 144 GHz, the signal bandwidth is approximately 4 GHz.

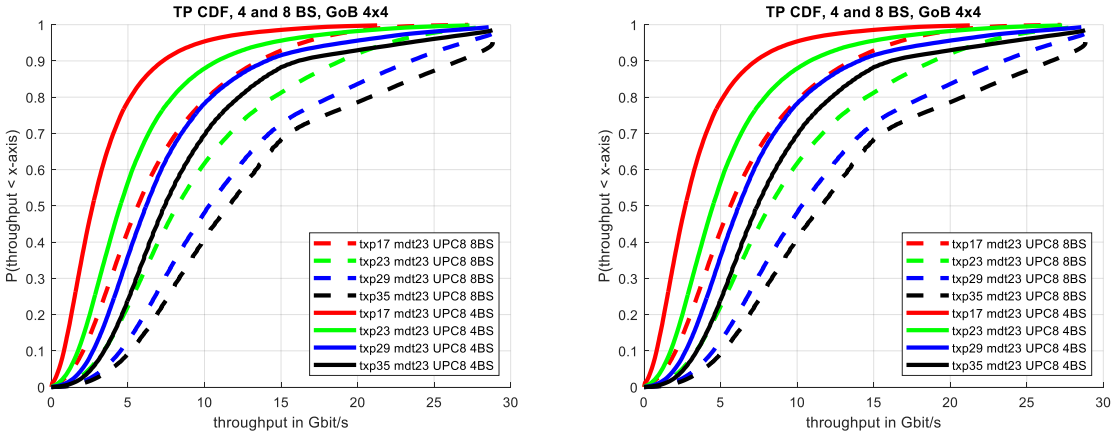

8 simultaneous UEs **16 simultaneous UEs**

Figure 4-22: Throughput CDFs for 8 and 16 UEs within simulation area, varying BS transmit power (TXP).

Results: Initial simulations show the UE throughput CDFs for 8 and 16 UEs within the covered area, with the transmit power (txp17 = 17dBm … txp35 = 35 dBm) and the number of base stations (4 or 8 BS) as parameter. The mechanical downtilt of the antenna is 23 degrees (indicated as mdt23 in the figures).

Figure 4-22 indicates that the deployment with 8 BS and a transmit power of 17 dBm per BS (red dashed line) shows similar coverage and throughput of the deployment with 4 BS and a transmit power of 29 dBm (solid blue line). This effect is even larger for an increasing number of UEs. On the right part of Figure 4-22 the 4 BS with 35 dBm transmit power (black solid line) serve the 16 UEs with similar throughput performance of 8 BS, but they need only 17 dBm transmit power. The difference in transmit power per BS between deployments with 4 BS and 8 BS is 12 dB per BS for 8 UEs and 18 dB per BS for 16 UEs. Taking into account twice the number of BS, there is still a benefit of 9 dB and 15 dB for the 8-BS-deployment.

A very coarse assessment of the related power consumption can be done based on the power amplifiers (PAs) only, since they are the components contributing most to the power consumption of the radio frontend. Assuming a (still optimistic) PA efficiency of 0.1 (10%), the additional power consumption of 4 BS compared to 8 BS for the 8UE case is roughly 27 W:

$17\ dBm\ \triangleq 50\ mW, 8 \cdot 50\ mW / 0.1 = \mathbf{4\ W},\ \ 29\ dBm \triangleq 794\ mW, 4\ \cdot 794\ mW / 0.1 = \mathbf{31.7\ W}$

For the 16UE case a similar consideration leads to a difference of about 122 W:

$17\ dBm\ \triangleq 50\ mW, 8 \cdot 50\ mW\ / 0.1 = \mathbf{4\ W},\ \ 35\ dBm \triangleq 3.16\ W, 4\ \cdot 3.16\ W / 0.1 = \mathbf{126\ W}$

However, further impacts need to be considered for a more accurate analysis, like the trade-off between number of BS, the impact of hybrid arrays with analogue GoB per subpanel, and the related signal processing. Therefore, the existing power consumption model needs to be enhanced to cover all these effects. Further simulations are also needed to analyse impacts of various sub-THz specific design aspects and consider them in power consumption evaluation. This is still subject to ongoing work.

4.2.4 MU-MIMO optimization in diverse device scenarios

Problem statement: MU-MIMO is a key tool for increasing the capacity of cell or user groups, using multiple antennas at both the transmitter and receiver, and allowing multiple users to access simultaneously the same channel. Since its conception [T99], theoretical exploration of practical systems [SPS+04], [PS08], and of efficient decoding of multi-user transmissions [YH15], the important question in modern large MU-MIMO systems has moved onto efficient learning and delivery of the channel at both BS and UE.

This work focuses on DL MU-MIMO for time-division duplex (TDD) scenario, where challenges include the accurate channel knowledge at BS due to weak UE transmit power and impracticality of frequent updates, the communication with different users in a way that reduces or eliminates interference among them, as well as the complexity (both hardware and computational) originating from multiple antennas and implementation of MU-MIMO schemes. These specific challenges will be significantly augmented in expected 6G deployments of ~10 devices per m^2, where a BS will have to concurrently deal with several UEs of diverse architecture (antenna number, hybrid analogue-digital array architecture, BW capability, etc.) and a vast amount of user antennas in total. The full optimization of all DL MU-MIMO scheme parameters (e.g., precoding, channel estimation, feedback, etc.) will be prohibitively difficult.

Methodology: The aim of this work is to investigate intelligent optimization methods and trade-offs to deliver required performance but also reduce the computational cost (and related energy consumption) on the BS and UE sides. To this end, the approach of dimensionality reduction via "effective antennas" (EAs) has been followed (initially introduced in [SSH04] but for number of EAs equal to information layers per UE). The term EA, for receiver (RX) or transmitter (TX) antenna array, is defined as a set of linear combinations over RX or TX array with the purpose of transforming the actual channel into more tangible effective channel related to virtual EAs (instead of physical antennas). These "clean" from interference channels can be then the aim for the MU-MIMO DL precoder. AI/ML tools can be used together with the flexible EA approach to address computationally intensive steps within the communication procedure and optimise trade-offs between system performance and complexity/energy cost on the BS and UE sides. The general methodology is represented in Figure 4-23.

It is envisioned that development of flexible EAs approach will allow to solve *fundamental* MU-MIMO problems, allowing for practical implementations, including:

- incorporate very large and diverse arrays into MU-MIMO (diverse in number of antennas, array architectures, ability to possess different number of RX and TX antennas).
- speed up the UE-BS communication for channel knowledge and update (since only EAs channels are needed to be delivered to the BS).
- incorporate the outer cell interference rejection inside dimensionality reductions and alleviate users in the cell boundary or in dense small cell deployments from interference limitations.
- address the TDD channel ageing problem originating from differently experienced and known channel at RX and TX.

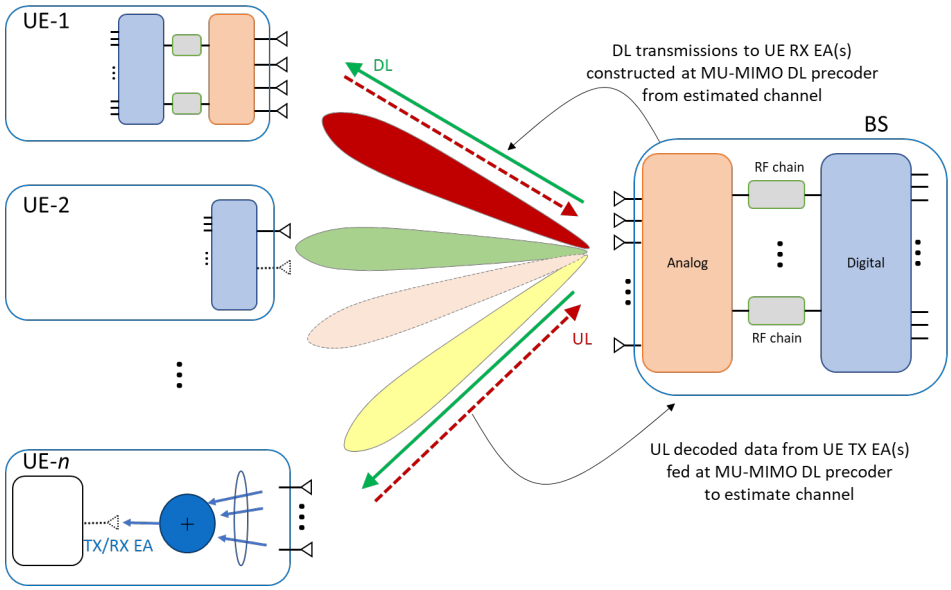

Figure 4-23: MU-MIMO optimization in diverse device scenarios using dimensionality reduction via flexible effective antennas (EA) approach.

Results: Main progress in this work so far includes the development of the flexible EA concept as a generalised dimensionality reduction at arrays for DL MU-MIMO communication in TDD. Preliminary numerical

simulations of the interference rejection scenario have been also run to confirm the importance and potential of optimizations using the proposed approach. Detailed description of the system model, the mathematical formulations and the initial results is provided in Appendix A.2.3. The performance comparison among different single-user MIMO (SU-MIMO) systems, with and without dimensionality reduction, shows significant gain potential from an optimized EA approach. AI/ML tools can help to harness fully this potential when system dimensions and computational complexity increase. In next steps of this work, it is planned to focus on specific AI- AI-assisted optimisation scenarios (e.g., case of TX eAs=RX EAs which would allow to address the channel ageing problem in TDD systems) and investigate the respective performance trade-offs under various practical assumptions.

4.2.5 Hybrid analogue-digital architectures – Link-level signal modelling

Problem statement: In 5G systems, the general MIMO precoding architecture is a hybrid scheme including a baseband digital part and an analogue part, as illustrated by Figure 4-24. Digital precoding offers flexibility but requires a dedicated transceiver chain per antenna element. Nevertheless, at high frequencies such as in mmWave and sub-THz contexts, the closely spaced antenna elements, resulting from the shorter wavelengths, pose challenges in allocating physical space for individual RF chains. The implementation of RF chains, which includes components like power amplifiers, becomes impractical and costly. As a result, hybrid precoding has emerged as a preferred solution in mmWave contexts. Hybrid precoding combines baseband digital processing with analogue components, enabling a more efficient utilization of hardware resources while still achieving the desired performance. This approach not only addresses the physical space limitations but also helps mitigate the high costs associated with RF chains [AMG+14].

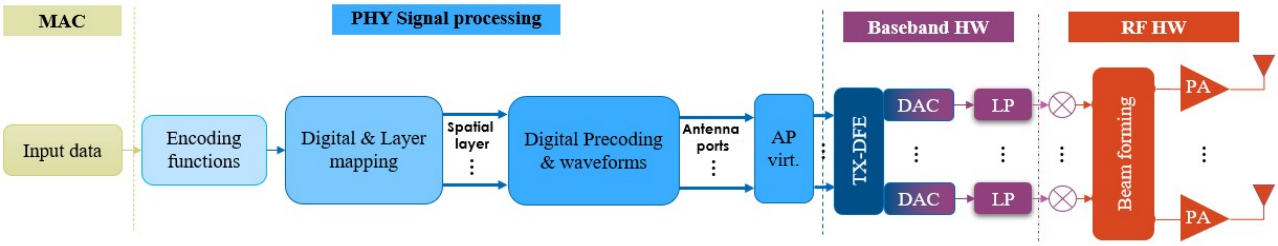

Figure 4-24: General hybrid MIMO precoding.

Methodology: This section presents possible hybrid beamforming solutions for mmWave / sub-THz communications. Their performance will be evaluated in a future deliverable, through comprehensive simulations. The streams of complex symbols at the spatial layers are first multiplied with a baseband frequency selective digital precoder, before OFDM modulation. The antenna ports are logical antenna from the receiver point of view, linked with reference signals (e.g., CSI- reference signal (RS)). A two-stage virtualization then applies. The first stage maps the antenna ports to the transceivers units (TXRU), each one including a digital to analogue converter. The second virtualization maps the TXRUs to the antenna elements (AE) via an analogue precoder applied to the time-domain signal, the waves are then transmitted in a preferred direction (beam) thanks to phase shifters. The analogue precoder can be configured with fully or partially connected antenna array structures.

The hybrid MIMO precoding architecture proposed in this study is shown by Figure 4-25. The antenna panel is either single polarized or cross-polarized, and one spatial layer is assumed per polarization. In case of cross-polarization, half of the AE corresponds to a first polarization slant angle, the other half corresponds to a second polarization slant angle, orthogonal to the first one. As for the antenna port-to-TXRU virtualization, a one-to-one mapping is assumed in this study [36.897] [NKA19].

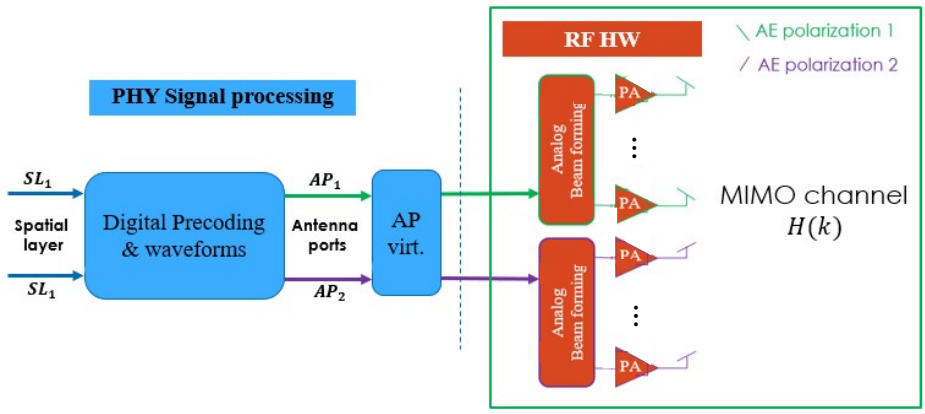

Figure 4-25: Proposed hybrid MIMO precoding.

The analogue beamforming $\boldsymbol{W}_A$ is first optimized for the MIMO channel frequency responses $\boldsymbol{H}(k)$, across the whole bandwidth. Then, the digital precoding is optimized at each subcarrier frequency k, based on the effective channel matrix defined by $\boldsymbol{H}_{eff}(k) = \boldsymbol{H}(k)\boldsymbol{W}_A$.

In a future deliverable, the performance will be evaluated using the link-level simulation tool depicted in Section 10.1, specifically in terms of BER vs. SNR.

4.2.6 Multi-antenna location-dependent coded caching

Problem statement: New data-intensive services like wireless extended reality (XR) applications driven by 5G and beyond demand stringent quality of service (QoS), requiring both low latency (<10 milliseconds) and high throughput (6.37 - 95.55 Gbps). Meeting these demands necessitates more advanced solutions beyond simply increasing bandwidth. Coded caching (CC), introduced by Maddah-Ali and Niesen in 2014 [MN14], has garnered attention for its superior global caching gain compared to traditional schemes, achieved through intelligent utilization of aggregate cache memory across the network. This scalability appeals particularly to multi-user collaborative scenarios like XR applications, with CC also leveraging spatial multiplexing gains from multi-antenna transmissions. However, there is a research gap in applying multi-antenna CC techniques to XR setups, especially in exploiting their location-dependent content access characteristics.

Methodology: In a wireless XR setting with multi-antenna transmitters and single-antenna users, user mobility and location-dependent content requests result in a significant multimedia traffic volume, requiring guaranteed QoS across the environment. To address this, a location-dependent memory allocation strategy is implemented based on predicted data rates to reduce the delivery time at each location, reflecting wireless connectivity quality. This differs from conventional CC methods, where equal memory portions are assigned to all files, necessitating a new packet generation approach to accommodate varying cache ratios. Additionally, a multicast beamforming scheme with multi-rate modulation is proposed to simultaneously leverage global caching and multiplexing gains, thereby enhancing QoS compared to existing methods.

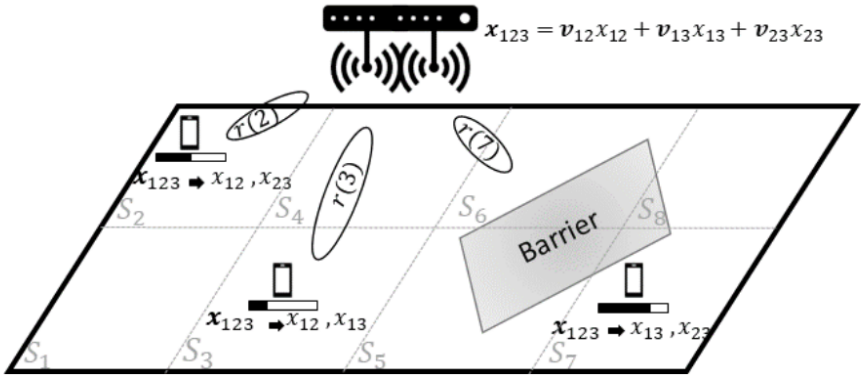

Figure 4-26: An XR application environment with 3 users and 8 single transmission units (STUs). The black bar below each user shows the amount of cached data based on the connectivity conditions.

Methodology: In a wireless XR setting with multi-antenna transmitters and single-antenna users, user mobility and location-dependent content requests result in a significant multimedia traffic volume, requiring guaranteed QoS across the environment. To address this, a location-dependent memory allocation strategy is implemented based on predicted data rates to reduce the delivery time at each location, reflecting wireless connectivity quality. This differs from conventional CC methods, where equal memory portions are assigned to all files, necessitating a new packet generation approach to accommodate varying cache ratios. Additionally, a multicast beamforming scheme with multi-rate modulation is proposed to simultaneously leverage global caching and multiplexing gains, thereby enhancing QoS compared to existing methods.

An XR application in a bounded $N \times N$ m² room, where a different 3D image is needed to rebuild the the field of view (FoV) in every tile of size 1x1 m², resulting in $S = N^2$ STUs.

A transmitter with L antennas and spatial multiplexing gain of $\alpha \leq L$, located in the middle of the room on the ceiling.

The small-scale fading of the channel is assumed to follow Rayleigh distribution.

The path loss for a user at state $s \in [S]$ is modelled as:

$$PL(s) = 32.4[dB] + 20\log_{10}(f) + 10\eta\log_{10}(d_s) + \zeta, \quad \textbf{(4-7)}$$

where d_s shows the distance between the center of the state s and the transmitter, $\eta = 3$ denotes the path-loss exponent, f represents frequency, and $\zeta \sim \mathbb{N}(0, \sigma)$ models the impact of randomly-placed objects obstructing the propagation path between the transmitter and the receivers.

In this regard, after allocating the memory based on the state, the delivery time of the user can be computed as $T_T = \frac{F}{r(s)}$, with the state-specific rate $r(s)$ for a user at state s is

$$r(s) = \frac{\Omega}{F} C_p \mathbb{E}\left[\log\left(1 + \frac{P_T \left|\boldsymbol{h}_{k_s}\right|^2}{N_0}\right)\right] \quad \textbf{(4-8)}$$

where C_p is a pre-log scaling factor containing any practical overhead, P_T is the transmission power, Ω is the communication bandwidth, and $\boldsymbol{h}_{k_s}$ is the channel vector between the server and a user k located in state s, and F is the file size.

The transmit power is normalized such that the received SNR at the room borders is equal to $0[dB]$ (ignoring the 'shadowing' effect ζ). Optimal beamformers are assumed to achieve the rate in (5-8).

Results: Considering the Rayleigh fading channel with pathloss in (5-7), considering the memory allocated parameter $\boldsymbol{\phi}$ different methods are proposed to evaluate the content delivery time. The methods are described as:

- **Proposed, $\boldsymbol{\phi} \gg \frac{\boldsymbol{\alpha}}{\boldsymbol{K}}$, w/unicasting**, with non-uniform content placement prioritizing the local caching gain (i.e., trying to limit the delivery time as much as possible), and delivery by unicasting (i.e., using the spatial multiplexing gain only and ignoring coded caching techniques),
- **Proposed, $\boldsymbol{\phi} \gg \frac{\boldsymbol{\alpha}}{\boldsymbol{K}}$,** with non-uniform content placement prioritizing the local caching gain, and delivery by the new, proposed multicast techniques,
- **Proposed, $\boldsymbol{\phi} = \frac{\boldsymbol{\alpha}}{\boldsymbol{K}}$,** , with non-uniform content placement prioritizing the global caching gain (i.e., trying to maximize the data rate), and delivery by the new, proposed multicast techniques,
- **MS**, with uniform cache placement and classic coded caching content delivery.

For small σ values (i.e., less variation in large-scale fading among states), the traditional MS scheme outperforms other methods. This is because, in the proposed schemes, the global caching gain is sacrificed for a higher local caching gain. However, as σ becomes larger (i.e., there are more attenuated states), the MS scheme performs worse than the proposed schemes. This is because, with larger σ, it is more likely for users to experience poor connectivity, increasing the effectiveness of the local caching gain in decreasing the total delivery time.

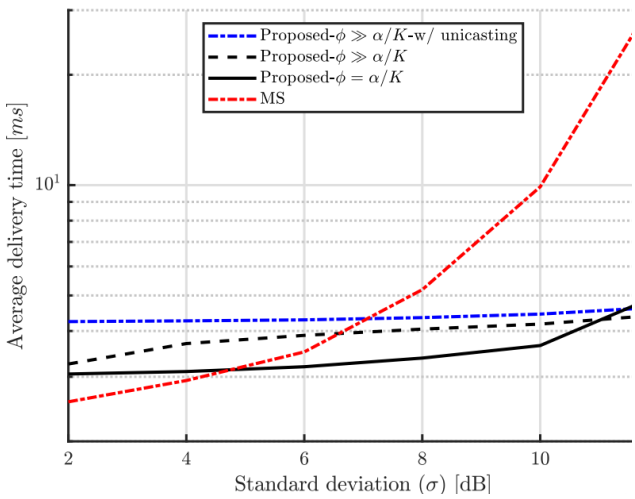

Figure 4-27: Average delivery time versus σ, where $K = 6, \frac{M}{S} = 0.33$, and $\alpha = 2$.

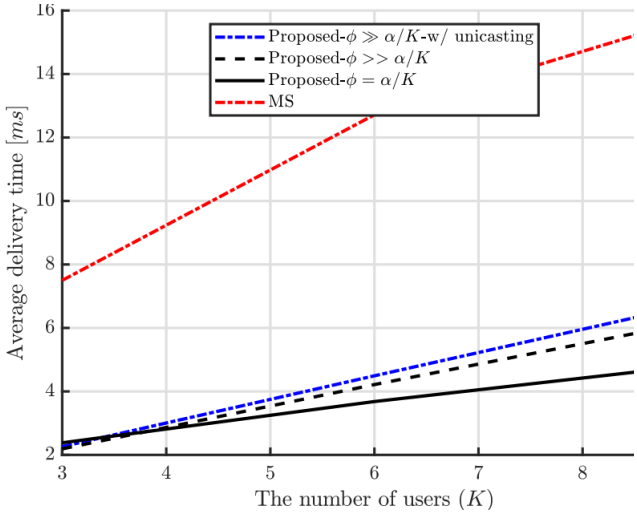

Figure 4-28: Average delivery time versus the user count K, where $\sigma = 10, \frac{M}{S} = 0.33$, and $\alpha = 2$.

Considering the effect of the network size K, since a larger K also means more data to be delivered, the delivery time generally grows with the number of users. However, since the global caching gains also scale with K, the number of users served in parallel (i.e., the DoF) also increases for larger K, resulting in an overall performance improvement for all the CC-based schemes.

4.3 RIS-assisted transmission

Reconfigurable intelligent surface (RIS) is an emerging technology in the field of telecommunications, offering a novel way to enhance the performance of wireless networks. These surfaces consist of electronically controllable elements that can manipulate electromagnetic waves, allowing for improved signal propagation in wireless communication systems. At its core, a RIS is a thin layer of material with many small programmable elements. These elements can alter the phase, amplitude, and polarization of incoming radio frequency (RF) signals. By doing so, a RIS can effectively control the propagation environment, which is a major shift from traditional approaches where the environment is typically considered given and uncontrollable. The primary advantage of RIS is its ability to direct or reflect signals to areas that are otherwise hard to reach with direct transmissions, such as blocked indoor regions or non-line of sight regions. This can significantly enhance signal coverage and reduce dead zones in a network. Moreover, RIS can be used to focus energy more efficiently towards intended users, improving the overall energy efficiency of the network. It is expected that the RIS to be a candidate for a cost-effective and energy-efficient solution to meet the increasing demand for high-speed and reliable wireless communication. This would require extended end-to-end validations to be verified. There are challenges regarding the integration of these surfaces into existing and future wireless networks which includes developing effective algorithms for dynamic RIS configuration, understanding the interaction of RIS with various signal propagation environments, and integrating RIS with other advanced technologies like MIMO and beamforming. This section covers methods addressing some of these challenges including integration of RIS for D-MIMO and IAB transmissions, channel estimation methods for RIS transmissions, and RIS control procedures.

4.3.1 D-MIMO assisted with RIS

Problem statement: In evolving 5G and future 6G networks, scalability of D-MIMO systems to large networks in a practically feasible way is challenging. Exploitation of cost-effective and energy-efficient dynamic clustering techniques, and densification enablers is crucial for such systems to sustain. RIS is well regarded as a low cost, rapidly deployable, energy-efficient candidate offering extra diversity in the spatial domain. This work explores RIS-aided multi-AP systems attaining certain prescribed KPIs, while considering the energy consumption in the system.

Methodology: To understand how RISs can help improve current communications systems, this study compares the performance of i) a system consisting of $N_{\mathrm{AP}} = 18$ APs, each equipped with $M_{\mathrm{AP}} = 16$ antennas, communicating with $N_{\mathrm{UE}} = 18$ single-antenna UEs, ii) the same system assisted by $N_{\mathrm{RIS}} = 18$ RISs, each comprising $M_{\mathrm{RIS}} = 64$ reflective elements, iii) the system with RISs but with single-antenna APs, and iv) the same system as in iii) but with $M_{\mathrm{RIS}} = 256$. For easy of simulation, it is assumed assume that the RISs are always located with LoS to both the AP and the UE they assist. In the initial setup, each UE is served by a different AP. When RISs are present, a UE is associated with the nearest RIS to obtain an additional signal path. The discrete-time signal received by UE k, with $k = 1, \dots, N_{\mathrm{UE}}$, can be written as

$$y_k = \sqrt{P_{\mathrm{T}}}\left(\boldsymbol{f}_{k,m} + \boldsymbol{g}_{k,n}\boldsymbol{\Phi}_n\boldsymbol{H}_{n,m}\right)\boldsymbol{q}_m x_k + \sum_{\substack{k'=1 \\ k'\neq k}}^{N_{\mathrm{UE}}} \sqrt{P_{\mathrm{T}}}\left(\boldsymbol{f}_{k,m'} + \boldsymbol{g}_{k,n'}\boldsymbol{\Phi}_{n'}\boldsymbol{H}_{n',m'}\right)\boldsymbol{q}_{m'} x_{k'} + n_k, \tag{4-9}$$

where $\boldsymbol{f}_{k,m} \in \mathbb{C}^{M_{\mathrm{AP}}\times 1}$ is the channel vector between AP m and UE k, $\boldsymbol{H}_{n,m} \in \mathbb{C}^{M_{\mathrm{RIS}}\times M_{\mathrm{AP}}}$ denotes the channel matrix between AP m and RIS n, $\boldsymbol{\Phi}_n = \mathrm{diag}(\phi_1, \dots, \phi_{M_{\mathrm{RIS}}})$ is a diagonal matrix containing phases of the RIS reflective elements, where $\phi_i = \exp(j\theta_i)$ and $\theta_i \in [0, 2\pi)$, for $i = 1, \dots, M_{\mathrm{RIS}}$, $\boldsymbol{g}_{k,n} \in \mathbb{C}^{M_{\mathrm{RIS}}\times 1}$ is the channel vector between RIS n and UE k, and $n_k \sim \mathcal{CN}(0, \sigma^2)$ is a random variable representing the additive noise at the receiver of UE k. AP m transmits the complex-valued symbol x_k to UE k, with associated RIS n, so that $E[|x_k|^2] = P_{\mathrm{T}}$. Similarly, neighbouring APs transmit $x_{k'}$ to UE k', with associated RIS n', where it is assumed assume that $E\left[x_k x_{k'}^*\right] = 0$, for $k \neq k'$. Finally, $\boldsymbol{q}_m \in \mathbb{C}^{M_{\mathrm{AP}}\times 1}$ denotes the beamforming vector applied by AP m, which is assumed to have unit norm, i.e., $||\boldsymbol{q}_m|| = 1$, for $m = 1, \dots, N_{\mathrm{AP}}$. The pathloss and large-scale fading of the links are generated following the indoor office channel model from 3GPP [38.901]. To jointly design the transmit beamformer $\boldsymbol{q}_m$ and the RIS phase matrix $\boldsymbol{\Phi}_n$ associated with UE k, the optimization method proposed in [ZRS+21] is used, with the consideration to align the phases of the RIS-reflected and the direct signal paths. With that, the SINR experienced by UE k can be written as

$$\gamma_k = \frac{P_{\mathrm{T}}\left\|\boldsymbol{f}_{k,m} + \boldsymbol{g}_{k,n}\boldsymbol{\Phi}_n\boldsymbol{H}_{n,m}\right\|^2}{\sum_{k'=1,k'\neq k}^{N_{\mathrm{UE}}} P_{\mathrm{T}}\left\|\boldsymbol{f}_{k,m'} + \boldsymbol{g}_{k,n'}\boldsymbol{\Phi}_{n'}\boldsymbol{H}_{n',m'}\right\|^2 + \sigma^2}, \tag{4-10}$$

where $\sigma^2 = kT_0BF_{\mathrm{UE}}$, with $k \approx 1.38 \times 10^{-23}$ J/K is the Boltzmann constant, $T_0 = 290$ K, B is the system bandwidth in Hz, and F_{UE} is the noise factor of UE k's receiver. The SE of the system, in bits/s/Hz, is given by

$$R = \sum_{k=1}^{N_{\mathrm{AP}}} \log_2(1 + \gamma_k). \tag{4-11}$$

To evaluate the energy efficiency of the investigated RIS-assisted setup, the total dissipated power needs to be computed. Based on the model proposed in [HZA+19], the total dissipated power can be calculated as

$$P = N_{\mathrm{AP}} \cdot \left(P_{\mathrm{T}}\,\xi + P_{\mathrm{dis,AP}} + P_{\mathrm{dis,UE}} + M_{\mathrm{RIS}}P_{\mathrm{dis,RIS}}\right), \tag{4-12}$$

$P = N_{\mathrm{AP}} \cdot \left(P_{\mathrm{T}}\,\xi + P_{\mathrm{dis,AP}} + P_{\mathrm{dis,UE}} + M_{\mathrm{RIS}}P_{\mathrm{dis,RIS}}\right)$,where $1/\xi$ is the efficiency of the APs transmit power amplifier, $P_{\mathrm{dis,AP}}$ is the static power dissipated by one AP, $P_{\mathrm{dis,UE}}$ is the static power dissipated by one UE, and $P_{\mathrm{dis,RIS}}$, the static power dissipated by one RIS reflective element. The energy efficiency of the system, in bits/J, can then be obtained by the expression

$$\eta_{\mathrm{EE}} = \frac{B \cdot R}{P} = \frac{B \cdot \sum_{k=1}^{N_{\mathrm{AP}}} \log_2(1 + \gamma_k).}{N_{\mathrm{AP}} \cdot \left(P_{\mathrm{T}}\,\xi + P_{\mathrm{dis,AP}} + P_{\mathrm{dis,UE}} + M_{\mathrm{RIS}}P_{\mathrm{dis,RIS}}\right)}. \tag{4-13}$$

Results: Figure 4-29 (a) shows the CDFs of the SINR experienced by the UEs in setups i) through iv). For the case of $M_{\mathrm{AP}} = 16$-antenna APs, it can be observed that RISs can improve the median SINR from 18 dB to 21 dB. More importantly, the 10-percentile SINR is improved by about 6 dB. One can also ask whether RISs can

help reduce the size of the AP antenna arrays while attaining some prescribed performance—thereby trading expensive antenna arrays for low-cost RIS devices. Setups iii) and iv) attempt to address this question. At least up to $M_{RIS} = 256$ elements, out initial simulations provide a negative answer. Future work may investigate whether deploying multiple RISs per cell and optimizing the deployment locations of the RISs, as well as using cell clusters, can help close the observed performance gap.

Figure 4-29 (b) summarizes the initial evaluation of the feasible energy efficiency (EE) gains provided by RISs, for the case of single-antenna APs, i.e., $M_{\mathrm{AP}} = 1$ and RIS sizes from $M_{\mathrm{RIS}} = 20$ to $M_{\mathrm{RIS}} = 200$ elements. To obtain the curves, the simulation parameters are $B = 100$ MHz, $\xi = 1.2$, $P_{\mathrm{T}} = 25$ dBm, $P_{\mathrm{dis,AP}} = 39$ dBm and $P_{\mathrm{dis,UE}} = 10$ dBm [HZA+19]. For the power dissipated by each RIS element, $P_{\mathrm{dis,RIS}}$, the values .01 dBm, 5 dBm and 10 dBm were selected. These values agree well with the power consumption of RIS prototypes reported in [WTL+22]. In particular, implementations of RIS unit cells based on PIN diode dissipate in the order of 10 dBm [WTL+22], while CMOS-based implementations only dissipate power when the state of the unit cells changes, e.g., during the transient period. The figure shows that even with P_{b} power dissipation values as high as 10 dBm per reflecting element, deploying RISs holds the potential for improving the system's energy efficiency.

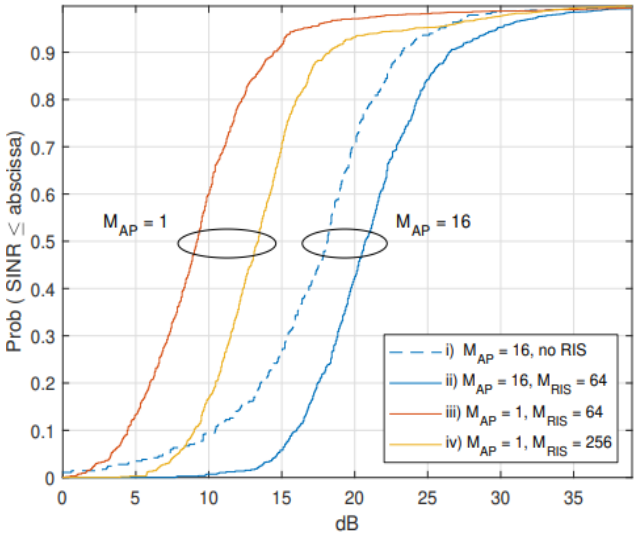

(a) SINR experienced by UEs in deployments i) through iv)

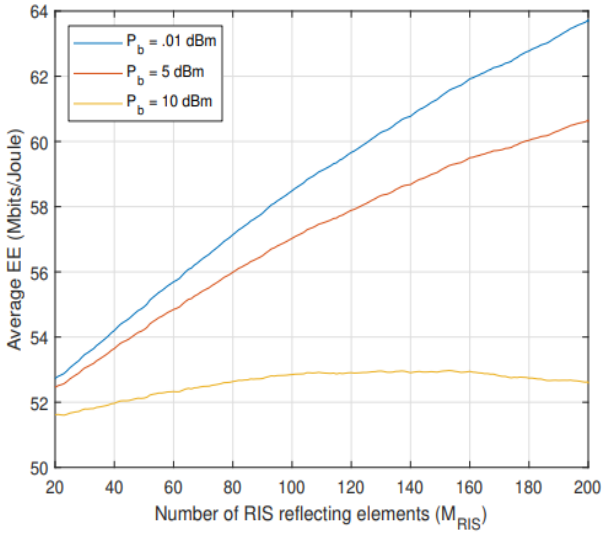

b) Average energy efficiency (EE) as a function of the number of RIS elements (M_{RIS}) for single-antenna APs ($M_{AP} = 1$), $B = 100$ MHz, $P_{\mathrm{T}} = 25$ dBm, $\xi = 1.2$, $P_{\mathrm{dis,AP}} = 39$ dBm, $P_{\mathrm{dis,UE}} = 10$ dBm.

Figure 4-29: Performance evaluation of D-MIMO assisted with RIS.

4.3.2 RIS assisted integrated access and backhaul

Problem statement: The sub-urban IAB networks have been impacted by the tree foliage on signal propagation. The attenuation and scattering of wireless signals caused by leaves and branches can lead to a considerable performance degradation in these networks [ITU-P.833-4]. Consequently, it is of utmost importance for network designers and operators to adopt innovative strategies, cope with such issues, especially in maintaining reliable and sufficient data rates in the backhaul links. RISs due to their unique capabilities, can be helpful in bypassing the tree foliage affected direct backhaul links. This work explores RIS-aided IAB system attaining certain prescribed KPIs, including service coverage probability.

Methodology: The work is to optimize the network and address the tree foliage issue in IAB networks, for the sub-urban areas, focusing on the backhaul links. In particular, a mmWave channel model is adapted, with 5G channel model (5GCM) urban macro (Uma) close in model for pathloss modelling [RXM+17]. Codebook-based beamforming is used due to its less complexity and better efficiency as it replaces the normal beamforming strategy with a comparatively simpler amplitude and phase-changing method.

Results: Service coverage probability defined as the fraction of the UEs which have instantaneous UE data rates, R_U higher than or equal to a threshold, R_{th} can described as below is considered as the performance metric,

$$Service\ Coverage_{prob} = \Pr(R_U \geq R_{th})\,. \tag{4-14}$$

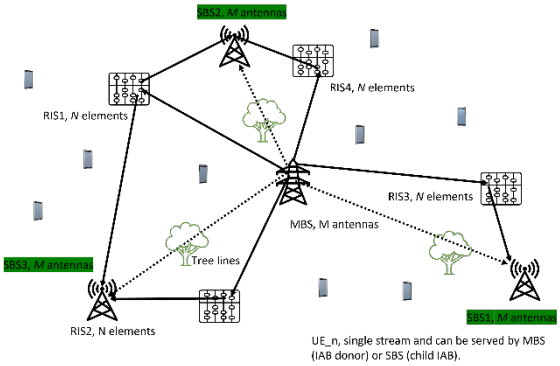

Figure 4-30: Illustration of RIS-assisted IAB scenario in the presence of tree foliage.

Figure 4-31 depicts the service coverage probability as a function of tree depth r for sub-urban use case considering in-leaf percentages, i.e., the percentages of leaf cover in the trees of 25% and 75% resembling the seasonal variations. Ae see in Figure 4-31 for small r values, the traditional IAB network is depicting similar performance to a RIS-aided network. However, as the r becomes larger, the RIS-aided network outperforms the IAB only backhauled network. This is because, with larger r it is more likely for the backhaul links to be affected by tree foliage than the double path-loss of RIS-aided backhaul link.

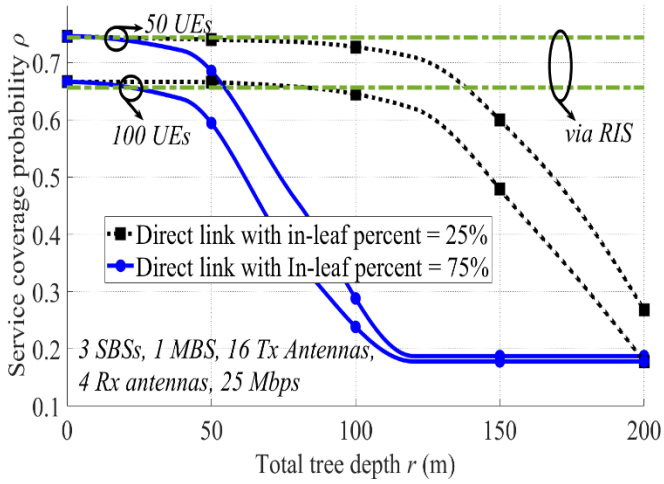

Figure 4-31: Service coverage probability as a function of tree-line depth for sub-urban use case.

4.3.3 Channel estimation for RIS

Problem statement: Frequent connectivity issues are inherent to millimetre wave (mmWave) vehicular communication systems due to severe path loss under blockages. A RIS can be used to improve link quality under blockage by establishing a reflected link. However, finding the optimum phase shifts at RIS requires the availability of accurate channel state information. Considering a passive RIS, the uplink channel estimation schemes rely on the feedback received at the base station by transmitting a pilot sequence to estimate the channel. Further, a large number of reflecting elements are required at RIS to facilitate a satisfactory performance, which requires a large pilot overhead. Furthermore, the mobility of vehicles demands frequent channel estimation, thus creating an intolerable pilot overhead. This work focusses on uplink channel estimation under mobility in an RIS aided millimetre wave communication system. The objective of the study is to improve channel estimation accuracy while utilizing fewer pilot resources.

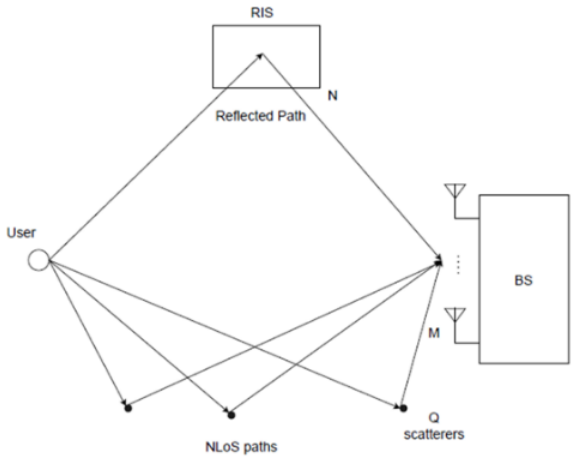

Figure 4-32: An illustration of the RIS aided channel, where UE-BS link is no NLoS and reflected link through RIS consists of NLoS components.

Methodology: As illustrated in Figure 4-32, the uplink channel consists of a NLoS direct channel and a reflected channel through RIS which has LoS components. The cascaded channel through RIS can be thought of as a controllable scatterer where the gain can be tuned by changing the phase shifts. Considering a mmWave scattering channel model, the compound channel at each symbol is represented as function of the RIS channel, multipath gains, Doppler shifts of the multipaths, transmitter and receiver antenna azimuth and elevation departure and arrival angles of each path (angle of departures – AoDs and angle of arrivals – AoAs), and the velocity of the user vehicle. The study considers a pilot sequence corresponding to phase shifts at RIS obtained from a codebook. The received pilot symbols are used to estimate the channel parameters. However, the resulting optimization problem is non-convex due to the coupling of optimization variables. Still, an approximate solution can be found using alternative optimization. However, the accuracy of the solution is compromised due to power leakage caused by non-ideal angular grid. Therefore, a machine learning based approach is proposed to predict the AoAs. The Figure 4-33 below shows the architecture of the proposed neural network.

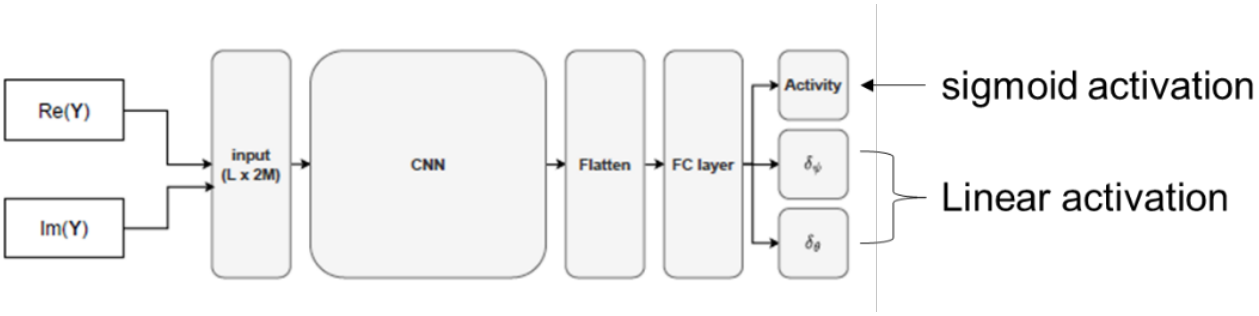

Figure 4-33: The proposed neural network architecture for RIS channel estimation.

Results: Channel estimation accuracy is used as the evaluation metric for performance comparison. The results compare the normalized mean square error (NMSE) of the direct and RIS channels when using different channel estimation algorithms. The DeepMIMO dataset is used to generate channel parameters (i.e., AoAs, AoDs and complex path gains) for a system with career frequency 28 GHz.

Figure 4-34 shows the NMSE performance of the proposed machine learning-based channel estimation algorithm (denoted as Algorithm 5 in the figure) in comparison to optimisation-based algorithm (denoted as Algorithm 4 in the figure) and the baseline with known AoAs, for stationary and mobile user scenarios. It can be observed that the machine learning solution outperform optimisation -based algorithm in both stationary and mobile user cases.

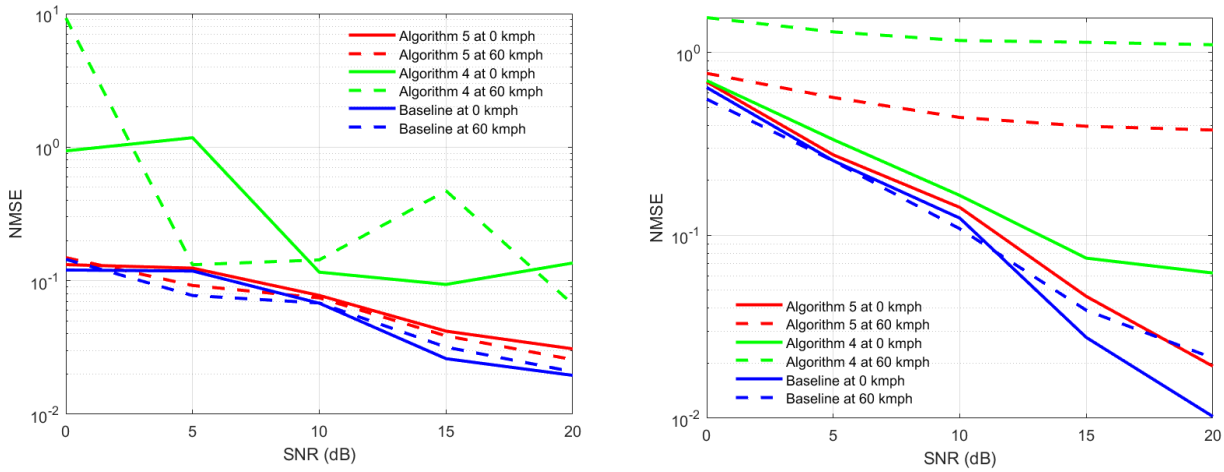

(a) Direct channel **(a) Reflected channel**

Figure 4-34: Comparison of the NMSE for the proposed for RIS channel estimation. algorithms under stationary and mobile channels (Algorithm 4: Optimization based, Algorithm 5: ML-based, Baseline: known AoAs).

4.3.4 Control procedures for non-radiative RIS

Problem statement: The focus is on design control procedures for RIS with wireless control. There is a distinction between infrastructure RIS and personal RIS, where the latter is assumed to be located close to UEs, operate in mmWave or sub-THz spectrum and be transparent or non-transparent to the network. Given the considered target use cases of personal RIS and high frequency indoor propagation, the wireless control of RIS can be split between the UE, a local RIS controller and a remote controller of RIS whose placement is flexible. An investigation is carried out for the options of functionality split to identify the best one from the perspective of signalling overhead, latency and implementation complexity.

Methodology: It is assumed that RIS configuration is selected and provided to RIS by a RIS controller. Typically, it is not required for RIS controller to be co-located with RIS, therefore it can be called remote controller**.** The location of remote controller is not specified. The entity that is located at RIS and is responsible for a part of RIS control functionality can be called local controller. The study considers two options of control functionality split between remote and local RIS controllers.

In both option it is assumed that RIS is stationary and purely passive, operates in mmWave or sub-THz frequency band, local RIS controller has connectivity with the served UE and a remote RIS controller.

The first option is based on the exchange of control model. The control model means a mathematical formula (e.g., an AI/ML model or an algorithm) that takes as an input local information: (relative) position and orientation beam information (if available, e.g., SSB) of the served UE, and the state information of RIS such as switched on/off RIS elements, RIS orientation and position, etc.) and outputs the RIS reflecting coefficients. In this case, remote controller periodically computes a control model and provides it to the local controller.

Local controller supports the following functionality:

- Receives control model and UE local information.
- Combine UE local information with RIS local information.
- Applies control model to the local information to obtain reflecting coefficients.
- Applies the reflecting coefficients.

The period of the local information update is typically shorter than the control model update, which reduces the communication overhead of RIS control.

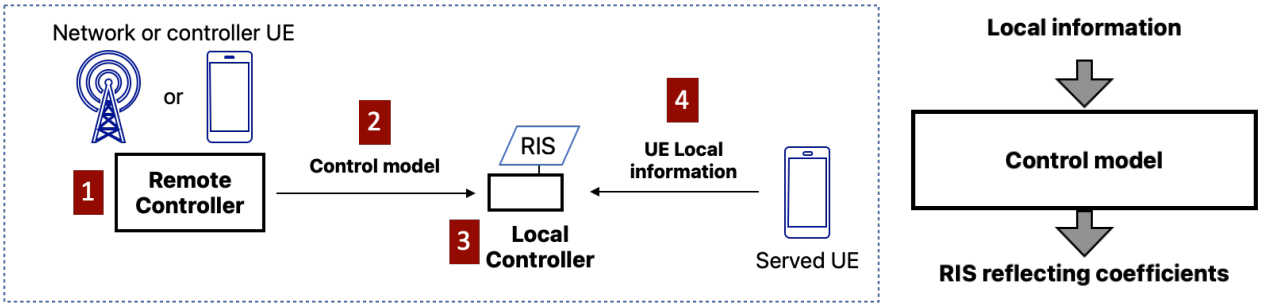

Figure 4-35: Block diagram for control split option #1.

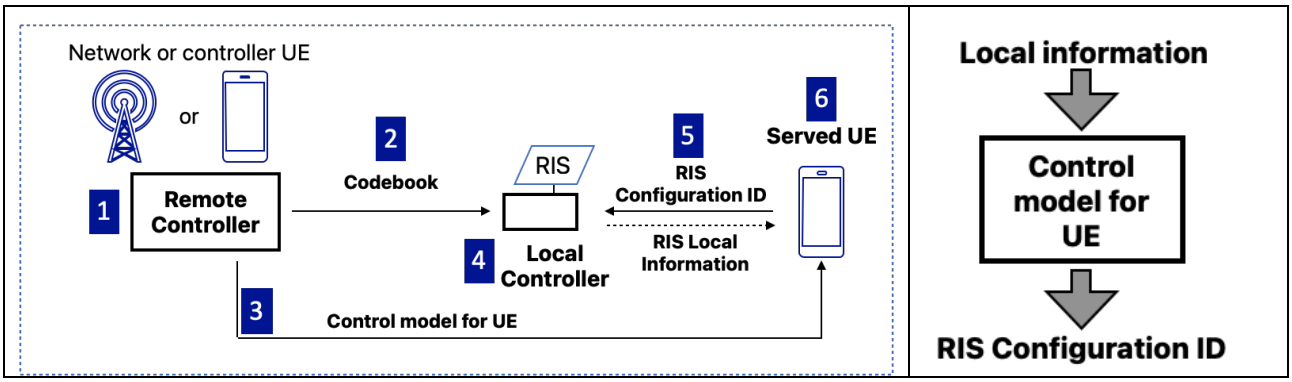

Figure 4-36: Block diagram for control split option #2.

The second option is based on the exchange of a pair of a codebook and a control model for UE. By codebook an enumerated set of RIS configurations is considered, where each configuration corresponds to a set of reflecting coefficients. Control model for UE is a mathematical formula (e.g., an AI/ML model or an algorithm) that takes local information as an input and outputs RIS configuration identifier (ID) of the accompanying codebook. This split option assumes that remote controller periodically computes a pair of control model for UE and a codebook. The codebook is then provided to the local controller, while the control model for UE is provided to UEs served by the RIS.

The expected local controller functionality in this case:

- Receives *codebook* and *RIS configuration ID.*
- Selects the ID element from the *codebook* and applies the corresponding reflecting coefficients for the RIS.
- (Optionally) periodically transmits RIS local information to UE.

Local information is defined the same way as in the split option #1 (described above). Served UE is assumed to be capable of receiving a control model for UE, (optionally) RIS local information, and periodically use (RIS and UE) local information as an input for the model to obtain RIS configuration ID. In practice, the served UE can receive and store multiple control models from different RIS. In this case, UE selects an appropriate model after establishing connection with a particular local controller RIS. As in the option #1, the period of RIS configuration ID update is typically smaller than the control model update, which reduces the overhead of RIS control.

Results: Qualitative analysis shows that the considered control split has the following advantages compared with baseline option without control split:

1. **Reduced communication overhead**. In the baseline option, the served UE should provide CSI to RIS remote controller, while the remote controller should communicate the decision to the RIS. In the considered split options, the remote controller typically makes updates in a much slower rate than RIS configuration is updated. The UE communicates the dynamic RIS control information only locally.

2. **Assistance for coverage extension**. In the baseline option, it is challenging to use RIS for coverage extension. The remote controller does not have CSI information of out-of-coverage UE; thus, a complicated beam search procedure is required. In the split option #1 UE and RIS local controller communicate locally to enable the UE to provide the information to local RIS controller and configure RIS for coverage extension.
3. **Privacy preserving.** Many RIS control algorithms are based on positioning information. In this case, without a split, UE position should be shared with remote controller which might violate privacy preserving requirements. In the considered split options, UE position information is shared only locally with RIS, or not shared at all. It is possible to keep position information at UE and share with RIS only the best configuration.

4.3.5 Learn RIS reflecting modulation

Problem statement: RIS-based communications with reflection modulation (RM) have garnered attention in literature as the RIS does not require additional RF chains to modulate information. RM schemes can be classified into two methods based on bit-mapping, where the transmitter and the RIS reflecting pattern either separately or jointly deliver information, namely, separately mapped RM (SRM) and jointly mapped RM (JRM). In SRM, the RIS delivers its own information from its reflection patterns, in addition to reflecting the signals coming from the transmitter. In JRM, the RIS and AP jointly deliver information available at the AP. In contrast to the conventional RIS where the RIS controller only adjusts the phase shifts depending on the channel information, here the RIS controller is actively involved in the transmission. In JRM, since a part of information is transmitted via the reflection patterns, the controller needs to have control links to and from both the AP and the RIS module to convey corresponding reflection patterns, CSI etc.

There are numerous SRM schemes explored in literature. Two such schemes are reflection pattern modulation (RPM) and quadrature reflection modulation (QRM), proposed by [LZA+21] and [LCW+22] respectively. In RPM, a subset of RIS elements is turned off to generate reflection patterns, while in QRM, a subset of RIS elements is given a 90-degree phase shift. SRM provides a solution to a specific use case, such as delivering some local sensor data available at the RIS. In contrast, the studies on the more general application of JRM are scarce.

The aim of this work is to provide a more scalable, less restricted solution that reduces BER for the more general application JRM, such that the RIS reflection patterns and transmit signals are jointly incorporated for the constellation design. In cases where the AP and user equipment (UE) direct link is NLoS, JRM can effectively deliver information to the user with the aid of the RIS and the joint constellation design. The RIS reflection pattern generation methods studied in SRM can be effectively used, thus two solutions are proposed and compared: jointly mapped reflection pattern modulation (JRPM) and jointly mapped quadrature RM (JQRM). A jointly active and passive beamforming design is also considered.

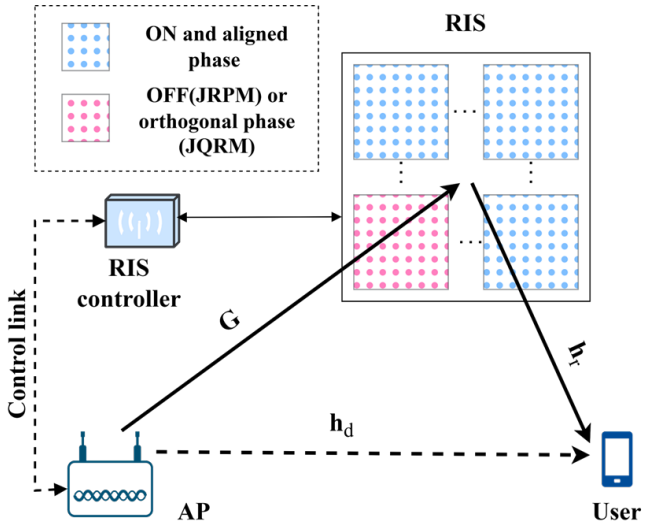

Figure 4-37: The system model for RIS RM.

Methodology: A single-user downlink system as shown in Figure 4-37 is studied under the full CSI assumption. The joint constellation is designed such that each constellation point comprises of a tuple of a transmit signal and a RIS reflection pattern. Thus, the required transmit constellation size can be reduced, increasing the adjacent symbol separation. At the receiver, the tuple can be jointly detected with maximum likelihood detection.

The neighbouring RIS elements are grouped to have the same reflection coefficient to improve scalability and lower complexity in the design of the constellation and beamforming. The RIS phase shifts are designed to align the phase of the effective channel, thus in JQRM, for a given reflection pattern, a group of elements are tuned to be orthogonal to the effective channel. In JRPM, a group of elements are turned off. An alternating optimization algorithm is used for the jointly active and passive beamforming design.

Results: In Figure 4-38 , the BER performance of the proposed JQRM and JRPM schemes are compared with their respective theoretical upper bounds and equivalent SRM schemes, i.e., QRM and RPM, for single-input single-output (SISO) and multiple-input single-output (MISO) systems respectively. Simulations are conducted over 100 independent fading blocks, each with a block length of 10000 bits. The AP-UE direct channel is assumed to undergo Rayleigh fading while the AP-RIS and RIS-UE links are assumed to be Rician fading channels. The RIS elements are split into 4 groups to generate 4 reflection patterns, thus a joint constellation with 8-bit symbols only requires 64-QAM transmit signal set, while the separately mapped counterparts deliver 6 bits from the AP and 2 bits from the RIS. Given full CSI, maximum likelihood detection is performed at the receiver by jointly searching for all the possible tuples in the JRM constellation points.

Both JQRM and JRPM shows superior BER performance compared to their separately mapped counterparts due to higher energy per bit achieved by the joint constellation design. The simulated BER of both JRPM and JQRM performs below their respective theoretical upper bounds. Overall, the QRM-based methods outperform the RPM-based methods due to the full aperture gain achieved by having all the RIS elements turned on.

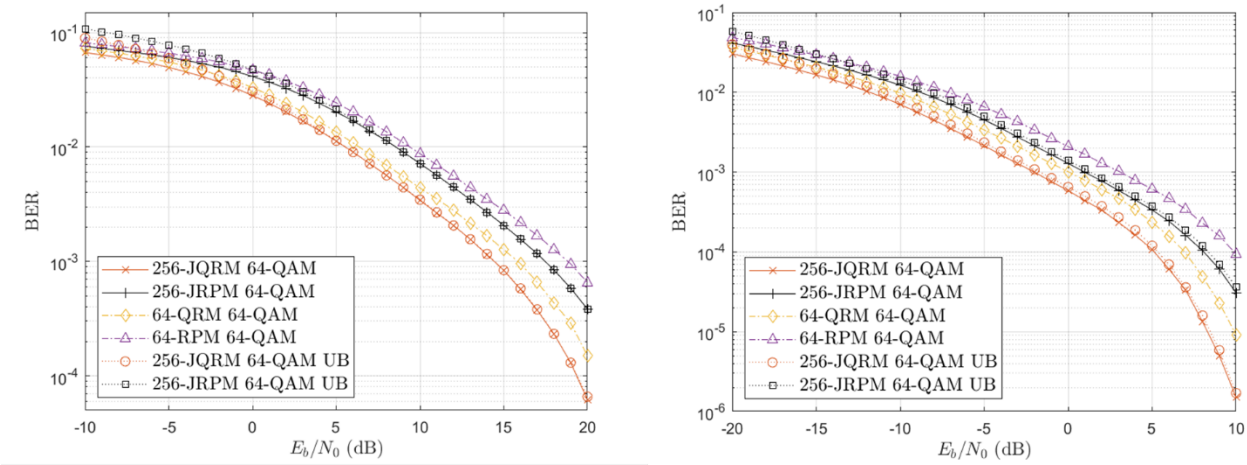

(a) SISO system **(b) MISO system**

Figure 4-38: BER performance of learn RIS reflecting modulation.

5 Waveforms and modulations

In modern wireless systems, waveform and modulation schemes are essential for efficient and reliable transmission. With these techniques, communication systems can increase spectral efficiency while balancing energy constraints. As technology evolves, new applications arise demanding unprecedented data rates leveraged mostly by expanding the transmission's frequency to sub-THz levels. This novel approach will substantially increase the system's bandwidth whilst affecting power consumption, phase noise, and other performance factors. In this context, designing innovative waveforms and modulation schemes is fundamental for harnessing the potential of future communications systems, regardless of the frequency band.

Hence, this chapter investigates waveform and modulation candidates for sub-THz communications and new enhancements to known techniques. The first section introduces the candidates by analysing 5G NR numerology and standardized waveforms, i.e., cyclic prefix orthogonal frequency division multiplexing (CP-OFDM), and by exploring 1-bit quantized zero crossing modulation (ZXM) and polar and hardware-friendly constellations. In the second section, enhancements to waveforms and modulation schemes are proposed, including an adaptative multicarrier modulation resistant to Doppler shift and out-of-band emissions, a new matrix design for low-density parity check (LDPC) codes, and an optimized delayed bit interleaved coded modulation (DBICM).

5.1 Sub-THz waveform and constellation candidates

This section analyzes waveform and constellations candidates for sub-THz communications. Here, the contributions address some of the main challenges inherent to these frequencies, namely energy efficiency, high mobility speed, and phase noise. The first work investigates the waveform candidates for sub-THz systems by analyzing their numerology and robustness towards phase noise and reduced energy consumption. The second contribution employs ZXM schemes to 1-bit ADC and explores their energy efficiency through an optimization problem. Next, new polar constellations are proposed to resist phase noise and high Doppler shifts. The last contribution analyzes the feasibility of SC-FDE waveforms over real-world sub-THz transceivers.

5.1.1 Evolution of New Radio numerology and waveforms towards sub-THz frequencies

Problem statement: Current 5G new radio (5G NR) specifications do not cover operation in the sub-THz frequencies. This section addresses the changes needed in the 5G NR numerology, such as the subcarrier spacing (SCS) and cyclic prefix (CP) length to support communications in the sub-THz frequencies. This works also addresses the performance differences between the waveforms already standardized for the 5G NR, namely CP-OFDM and discrete Fourier transform spread orthogonal frequency division multiplexing (DFT-s-OFDM), in the presence of known hardware limitations specific for the sub-THz frequencies. The following discussion focuses on three sub-THz specific aspects and their impact on the numerology and waveform selection, namely support for the large bandwidth required for Tbps communications, increased need for robustness towards phase noise (PN), and compensation of reduced power amplifier (PA) peak output power in the form of reduced peak-to-average power ratio (PAPR) of the waveform. More comprehensive study on the RF nonidealities in the sub-THz frequencies is given in Hexa-X-II D5.3 [HEX224-D53].

Methodology: 5G NR has been designed for scaled numerology, where the bandwidth and the frame structure scale according to SCS following the Rel-15 scaling principle [38.211]. This enables easy and flexible frequency- and time-domain alignment of different numerologies. Current 3GPP numerology has been designed from under 7.125 GHz frequency range (FR1) up to 71 GHz (FR2-1 and FR2-2). For FR2-2, only mandatory SCS of 120 kHz has been specified, and 480 kHz and 960 kHz are optionally supported [38.101 Table 5.3.5-1]. Here, it is assumed that the supported SCSs in sub-THz communications follow the scaling principle of 15 kHz, with the multiplier being in the powers of two, corresponding to 120 / 240 / 480 / 960 / 1920 / 3840 kHz.

Considering the available bandwidth in the lower sub-THz frequencies, the potential frequency bands in this region include especially W-band (75 to 110 GHz) but also D-band (110 to 170 GHz) [XR21]. The largest

available bandwidth is at the D-band, spanning total of 12.9 GHz and 151.1 – 164 GHz frequencies. With 264 physical resource blocks (PRB) and 4096 IFFT size, the SCS of 3840 kHz is capable of providing the occupied channel bandwidth (OCB) of 12.17 GHz that just fits the largest available band of 12.9 GHz at the D-band (see Appendix A.3.1).

However, the wider the SCS is, the shorter the symbols become in the time domain. This may not be a problem from the inter-symbol interference point-of-view, because narrow beams result in very small delay spreads, but an insufficient CP may become a problem for the beam-based transmission, if the beam switching delay is assumed to be comparable to CP length. In addition, this may also pose a challenge from RF component group delay response perspective. Furthermore, increasing the SCS may have larger impact on the system design as, e.g., the scheduling periods become too short and control channel coverage can be degraded [TLP+20].

Results: Since CP-OFDM and DFT-s-OFDM use multiple orthogonal subcarriers to transmit data, they are affected quite similarly by the PN distortion. A major impairment in the sub-THz frequencies compared to FR1 and FR2 is the PN, which, when using a frequency multiplier, increases 6 dB for every doubling of the carrier frequency [DPS18]. For example, going from 28 GHz to 90 GHz causes a ten-fold increase of PN. Thus, the maximum currently supported SCS of 120 kHz for data transmissions may be not enough to facilitate the PN. Current 5G NR handles the PN distortion by exploiting phase tracking reference signals (PTRS), which are inserted into OFDM or DFT-s-OFDM symbols to be able to track the PN variations. PN causes common phase error (CPE) which affects all subcarriers similarly [SLI+19]. However, the significantly higher PN in the considered frequency range will cause also inter-carrier interference (ICI), which comes from the convolution of the PN frequency response with the data bearing subcarriers. The OFDM uses distributed frequency-domain PTRSs, which enable the receiver to compensate only the common phase error part of the PN. This leads to degraded performance with 5G NR Rel-15 numerology when considering communications in sub-THz frequencies. The degrading effect of ICI can be mitigated by increasing the SCS or by applying somewhat more complex ICI compensation which can be done either with distributed or block-based PTRS [TPS+20]. The currently supported waveforms CP-OFDM and DFT-s-OFDM perform differently under different PTRS designs and related PN mitigation techniques and one of the main design challenges is the choice of the waveform and numerology, together with effective PN compensation methods. However, the simulations demonstrate that SCS of 960 kHz and 1920 kHz can facilitate the PN for both CP-OFDM and DFT-s-OFDM in the sub-THz frequencies (see Appendix A.3.2).

Besides PN, another major drawback requiring consideration in sub-THz frequencies is the decreased PA efficiency in higher carrier frequencies. For example, in [38.803 Section 6.1.9.1], it is shown that the output power of PAs for a given integrated circuit technology roughly degrades by 20 dB per decade. This imposes a significant need to support waveforms and modulations that allow to achieve very low PAPR in order to achieve better power efficiency in base station (BS) and user equipment (UE) side, and to achieve the targeted maximum transmitted power levels which in turn translates directly into coverage. It is well known that CP-OFDM signal has larger PAPR than DFT-s-OFDM [DPS18], especially at lower modulation orders, which emphasizes the importance of supporting DFT-s-OFDM in downlink and uplink for sub-THz communications. Depending on the modulation order, CP-OFDM requires approximately from 3 dB to 5 dB more output power back-off, indicating that DFT-s-OFDM is able to provide significantly better coverage [TPS+20] (see Appendix A.3.3).

Finally, the above discussion demonstrates that in addition to CP-OFDM, it would be very beneficial to support discrete Fourier transform spread frequency division multiple access (DFT-s-OFDMA also for downlink (DL) sub-THz communications. DFT-s-OFDM provides consistently better link performance under phase noise with only minor changes in the Rel-15 PTRS design. The DFT-s-OFDM waveform can also enable better coverage, because it provides larger power amplifier output power than CP-OFDM, especially with low-order modulations. For the overall numerology, it is also shown that SCSs from 960 kHz to 1920 kHz can provide a good baseline for sub-THz communications, allowing Tbps communications by supporting large bandwidths, and providing necessary enhancement in the PN mitigation for both CP-OFDM and DFT-s-OFDM waveforms. Although 3840 kHz SCS provides widest contiguous bandwidth still available in W- and D-bands, insufficiently short CP may become a problem, and thus a more conservative value of 1920 kHz should be taken as the starting point for the first efforts to design a system numerology for sub-THz communications. Increasing CP length dynamically might solve this problem, but it comes with a cost of increased overhead, complexity, and processing times.

5.1.2 Energy-efficiency of 1-bit quantized zero crossing modulation

Problem statement: The usage of high bandwidths at sub-THz carriers necessitates high sampling frequencies. For sampling frequencies above 300 MHz, the power consumption of the analogue-to-digital converter (ADC) increases quadratically with the signal bandwidth [Mur23], leading to a potentially problematic increase in power consumption. However, as the ADC power consumption is exponentially dependent on the ADC resolution, decreasing the ADC resolution can potentially mitigate the increase in power consumption due to higher sampling frequencies. Reducing the ADC resolution to a minimum of 1 bit, essentially shifts the information-carrying signal domain from the amplitude to the time domain.

Addressing the ADC power consumption challenge with 1-bit quantizers involves rethinking modulation design. Hence, zero-crossing modulation (ZXM) [FDB+19] is considered, which utilizes a combination of runlength-limited (RLL) sequences and faster-than-Nyquist signalling [LDG18], matching the shift from amplitude resolution to time resolution at the ADC.

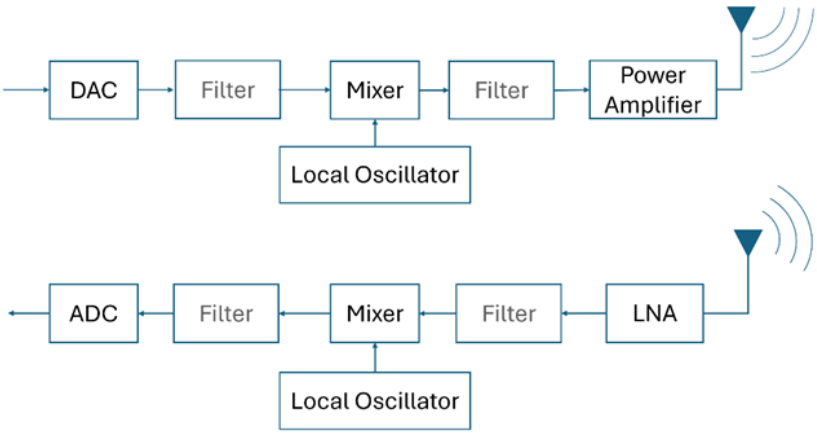

Figure 5-1: Considered front-end components.

In this regard, the scope is to estimate the advantage in energy efficiency of the ZXM approach in comparison to conventional M quadrature amplitude modulation (M-QAM) with high ADC amplitude resolution for sub-THz frequencies. For both modulation schemes, the achievable spectral efficiency is considered together with hardware power models for the corresponding analogue radio front ends. To evaluate ZXM and QAM transceiver power consumption, a closer examination of analogue front-end components is necessary. Front-end components exhibit dependencies on various parameters, e.g., the system bandwidth, the required transmit power, etc., influencing the overall power consumption. Expressions for receiver and transmitter power consumption, considering the mentioned dependencies, are based on previous analysis [GDS+24]. The components considered can be seen in Figure 5-1, while the filters are assumed to be passive, thus, consuming no power. The required frontend components for ZXM and QAM are identical, although ZXM requires temporally oversampled 1-bit ADCs, while M-QAM requires $\frac{1}{2}\log_2 M$ bit ADCs, as hard demapping is assumed. For QAM, M describes the constellation size, and for ZXM M_{tx} describes the faster-than-Nyquist signalling factor.

Methodology: To estimate the energy consumption of the frontend components, a power consumption model similar to the one described in [GDS+24] is used except for the assumption, that the power consumption of the DACs scales linearly with the FTN factor M_{tx} used in ZXM. As the ADC needs to at least match the rate of the DAC, it is required require that the ADC samples at the same rate as the DAC and, thus, assume that the ADC power consumption scales linearly with M_{tx} as well.

The dependencies of the power consumption of the frontend components, discussed in more detail in [GDS+24], can be summarized as follows. As the data rate is assumed to be a given quantity and different modulation schemes exhibit different achievable spectral efficiencies, the required receiver SNR is, thus, in direct relation with the required rate, the achievable spectral efficiency, and the available bandwidth. For the DAC, a binary-weighted current-steering DAC is assumed, whose power consumption depends on the bandwidth and its resolution in bits. As there are no general equations regarding the power consumption of local oscillators and mixers, literature-based measurements are used. As such, the power consumption of

mixers and LOs is fixed, identical for both modulation schemes, and not influenced by the optimization. The consumption of the power amplifier is modelled based on the power-added efficiency (PAE) and is dependent on the transmit power and the carrier frequency. For the LNA, the gain is assumed sufficiently high and that non-linear distortions are negligible, allowing us to use a bandwidth-dependent power model, depending on the bandwidth, gain and noise figure. For the ADC, the model is based on the Walden Figure-of-merit and a survey containing several ADCs [Mur23]. The ADC power consumption is, thus, dependent on bandwidth and the ADC resolution.

Using the models for the power consumption of the transmitter P_{Tx} and receiver P_{Rx} [GDS+24], a minimization of the energy per bit E_{bit} is performed over the transmit power P_T and the bandwidth B given a required data rate R. For ZXM the achievable spectral efficiencies S depending on the received signal-to-noise ratio (SNR) were evaluated using Monte-Carlo simulations, while the spectral efficiency for hard demapping QAM is evaluated analytically. As such this analysis incorporates quantization noise effects. To account for frequency-dependent path loss, the standard path loss model, also employed in [GDS+24], is used, which is based on the Friis transmission formula. From a mathematical perspective, the following optimization is performed

$$\begin{aligned} \min E_{bit} &= \frac{P_{Tx} + P_{Rx}}{R} \\ s.t. \quad R &= B\,S \\ 0 &\le P_T < P_{\max} \\ 0 &\le B < B_{\max}. \end{aligned} \tag{6-1}$$

Results: The minimum energy per bit, i.e., the result of the optimization above, can be seen in Figure 5-2 for $f_c = 120$ GHz, $\mathrm{B}_{\max} = 12$ GHz, $P_{\max} = 10$ W for the transmit antenna, a distance of $d = 20$ m, antenna gain of receive and transmit antenna of 6 dB and a path loss exponent of $\beta = 2$. It is important to note that the evaluation does not incorporate the effect of the modulation scheme on the PAPR and the resulting backoff. Thus, it is likely that the energy efficiency of ZXM is underestimated, particularly as highly spectral-efficient QAM modulations have a high PAPR, degrading the PA efficiency. As can be seen, ZXM is significantly more energy efficient up to a rate of about 30 Gbps. Interestingly, a faster-than-Nyquist signalling factor of $M_{\mathrm{tx}} = 2$ seems to be most efficient in the considered setting for most rates.

Exploring alternative waveforms for the sub-THz band, ZXM demonstrates higher energy efficiency than conventional QAM, considering analogue frontend power consumption. While ZXM sacrifices peak data rate, its energy efficiency makes it suitable for scenarios prioritizing energy efficiency over data rate.

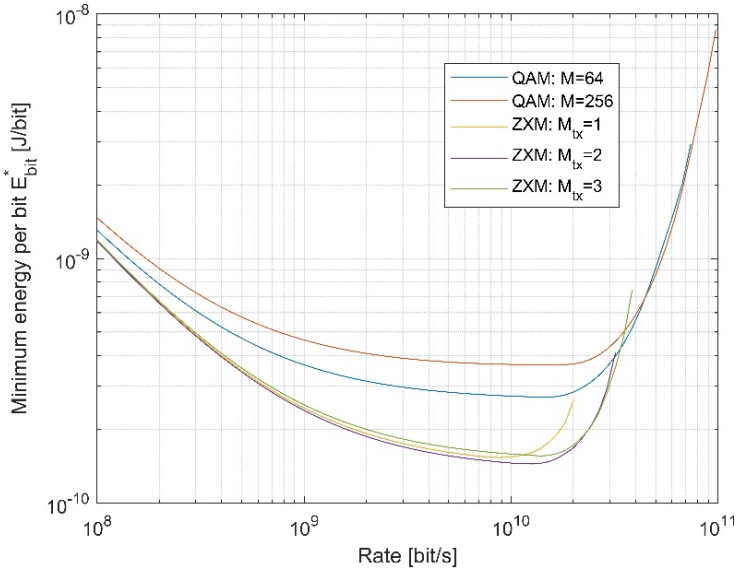

Figure 5-2: Energy per bit of ZXM and QAM.

5.1.3 Polar constellations

Problem statement: The polar constellations are an alternative to the classical QAM Mapping. It is especially well-adapted for FR2 bands and THz bands where the oscillators integrated on the devices are not very accurate leading consequently to a greater lack of synchronization. This phenomenon will entail phase noise.

Furthermore, the proposal is agnostic to any frequency band and could be also used in frequency bands below 6 GHz and, in this case, mainly interesting for high mobility speed that entails Doppler shift. Both phenomena, high frequency and/or high mobility speed, will induce rotation of the constellation (bits to symbols mapping) in reception. The goal is to create new types of constellations robust to phase noise and Doppler shift.

Methodology: Polar constellations are combined, in the system design, to a multicarrier waveform like CP-OFDM. Those new types of constellations induce to implement an advanced (but simple) demodulator (Figure 5-3) designed to correct CPE of the received polar constellations symbols.

Initially, the bit error rate (BER) (or block error rate (BLER)) is evaluated through an additive white Gaussian noise (AWGN) channel with Doppler Shift effect; in a second time the evaluation of this new constellation will be evaluated with some 3GPP channels with Doppler Shift model. The Block diagram is described in the Figure 5-3 with detailed description of the relevant blocks.

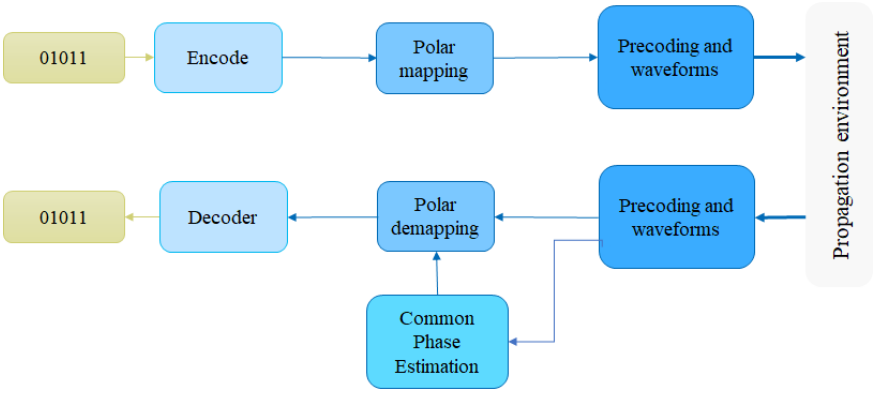

Figure 5-3: The Polar Constellation impact the Modulation and the Detector modules.

To build the spiral constellation, the following equation is used,

$$\boldsymbol{c(i) = a_i e^{j\varphi_i}}, \quad \textbf{(6-2)}$$

with a_i and φ_i being the amplitude and the phase of the i-th point respectively. For the spiral constellation all amplitudes a_i are different, $a_i = a_0 + i\Delta a$, with for example $a_0 = 1$ and $\Delta_a = 1$ the phase $\varphi_i$is optimized to have the better performances against AWGN channel. For a second solution presented in this part x-PC (x points of Polar Constellation), this is the same equations but limited to a quadrant. At the receiver side, the common phase error (CPE) can be estimated with the following formula,

$$\Delta_{\varphi} = \frac{1}{N}\sum_{i=1}^{N} \Delta_{\varphi(i)}, \quad \textbf{(6-3)}$$

wherein N is the number of OFDM carriers used to estimate the phase variations. The advanced detector for polar constellations estimation applies the following steps:

1. First, estimation of the amplitude of the received point.
2. Then, estimate the common phase error by comparing the data projected on the I and Q axes with the data transmitted (closest amplitude).
3. Calculate the phase difference between received and sent points is given by:

$$\Delta_{\varphi(i)} = \varphi_{(i)} - \varphi_{r(i)} + b_i, \quad \textbf{(6-4)}$$

4. By adding the different estimates to each OFDM carrier, it is possible to improve the estimate of CPE, expressed above, and reduce the influence of white noise.

5. Finally, the Doppler shift of each OFDM symbol can be estimated and correct it.

Interest to be noticed is that this system does not need any pilot symbols, only a preamble symbol at the beginning of transmission for channel estimation.

Results: The simulations are carried out with the assumptions of perfect CSI and synchronization. To evaluate the performances of the constellations, the metric is BER (or BLER) versus AWGN channel and Doppler Shift.

Two types of polar constellations are proposed for evaluation, the first one is the spiral (blue points in Figure 5-4 (a)) which is high robust against Doppler and the second one (16-PC): red points in Figure 5-4 (b)) that is similar close to an 16QAM (blue points in Figure 5-4 (b)) and that gives better performance than classical 16QAM over AWGN and Doppler shift channel.

Figure 5-4 (a) illustrates the effect and the correction of Doppler shift for the spiral constellation showing the interest of the CPE estimate and correction.

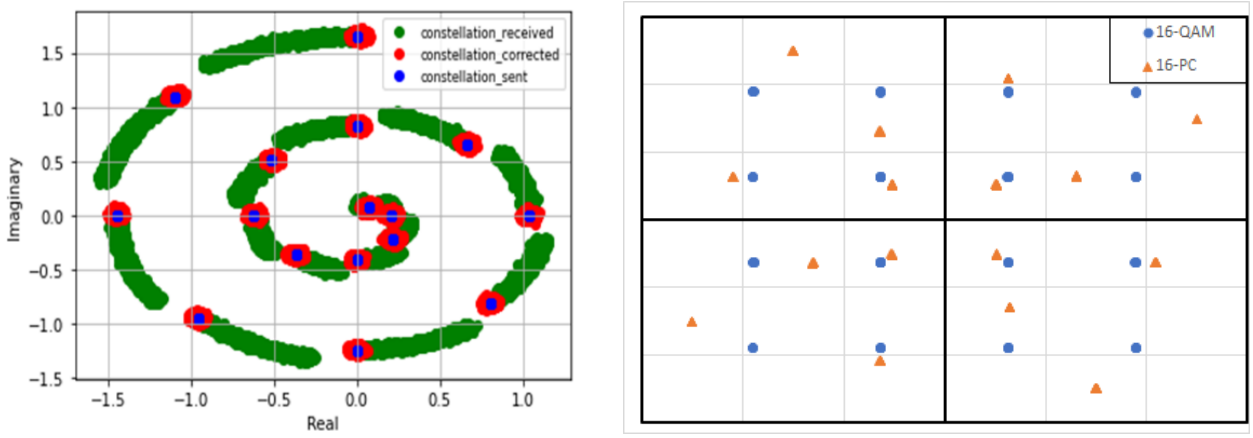

(a) Polar constellation at the transmitter/receiver sides

(b) 16QAM and 16-PC representations at the transmitter sides

Figure 5-4: Polar Constellation types.

Figure 5-5 shows the performance of the different constellations according to Doppler frequency effect versus the E_b/N_0 value needed to obtain one BER equals to $5x10^{-5}$. At Doppler frequency below 60 Hz, classical 16QAM gives the best performance. It can be noticed that the advanced detector gives significant gain especially for the spiral constellation where around 200 Hz Doppler gain is obtained leading the 16-Spiral with advanced detector to support around 280 Hz against 100 Hz for the 16CP.

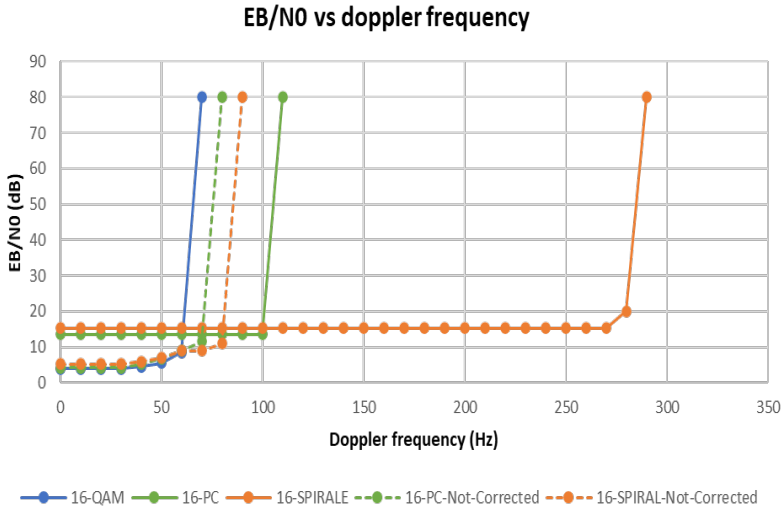

Figure 5-5: EB/N0 performance of 16QAM, 16-PC, 16 spiral versus Doppler shift @BER=10^{-3}.

As perspective, this study aims at:

- Evaluating the performance over 3GPP channel model affected by Doppler shift and phase noise, especially in sub-THz bands.
- Evaluating higher constellation order (typically 32 and 64 states).

5.1.4 Hardware-friendly waveforms

Problem statement: During the first phase of Hexa-X project it was observed that for single carrier frequency domain equalization (SC-FDE) transmissions, PAPR level can notably be reduced by selecting suitable constellation patterns and pulse shaping filter. This reduction in PAPR can be achieved with just moderate or even no losses in the BLER performance. For example, a large PAPR reduction of 1.8 dB can be achieved using 16-APSK pattern compared to NR 16QAM case. This improvement comes with a moderate loss of 0.2 dB in the BLER performance. In case of higher modulation order, the selected Amplitude Phase Shift Keying (APSK) constellation pattern exhibits a PAPR reduction of 0.6 dB in comparison to standard NR 64QAM, without any further penalty in BLER performance [HEX23-D23]. However, identifying the optimal waveforms, i.e., modulation and filtering is a challenging task, particularly for higher modulation order. The mutual dependency of modulation and filtering as well as the large number of possible combinations to pack the constellation points in various phase noise channel conditions requires solution approaches with high computational efforts. This challenge is partly addressed in [MNM+24]. In the context of Hexa-X-II the feasibility of these hardware friendly waveforms will undergo validation through transmission over the air using real-world sub-THz hardware setup.

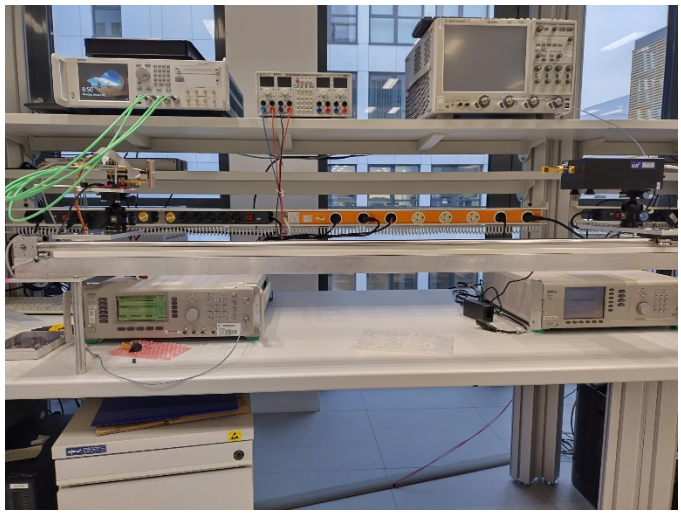

Figure 5-6: In-house sub-THz proof-of-concept setup.

Methodology: The hardware friendly constellations detailed in [HEX23-D23] and designed in [MNM+24] will undergo validation through over-the-air transmissions using an in-house demonstrator with 144 GHz hardware in the loop. Figure 5-6 shows the proof-of-concept (PoC) set-up utilized to validate the performance of the diverse optimized waveforms. The flexible PoC setup can support various waveform types and constellation designs. Test vectors of different designed waveforms can be pre-generated and uploaded to the arbitrary waveform generator (AWG) (upper left corner of figure). The base band signals are then directed to the transceiver board (TRX) (middle left side in the figure), directly upconverted to 144 GHz and transmitted over a horn antenna with 25 dBi gain. The TRX board is capable of transmitting signals with up to 5GHz signal bandwidth. For the investigations, RF output power is roughly 3 dBm for 64QAM case. Note that the purpose is to validate the performance of diverse designed waveforms, the power level setting is chosen such that the hardware setup operates in linear region. The test vectors are designed to occupy the entire 5 GHz bandwidth, fully exploiting the transmission bandwidth capability of the TRX board. Detailed setting parameters on the pre-generated waveforms can be found in [MNM+24]. At the receive side signal is collected by a horn antenna, down converted by a measurement module, and captured by an oscilloscope at a sampling frequency of 80 GHz. From transmit to receive antenna the received signal travers over 1 m distance and imposed by real-world hardware impairments. After transmission, the received signal is offline investigated using a MATLAB-based processing module. The following steps are performed: resampling, synchronization, filtering, and down

sampling to the original sampling frequency. Channel estimation and equalization are done in frequency domain utilizing common textbooks algorithms such as least squares and averaging over transmitted blocks.

Results: To ensure an understanding of the capabilities and limitations of the setup at sub-THz frequency, the initial focus is on transmissions of SC-FDE waveform type with NR standard square constellations. Once feasibility is confirmed, the investigation can proceed to explore other waveforms designed for sub-THz specific requirements.

Figure 5-7 shows the results of NR standard waveform transmissions deploying QPSK, 16QAM, 64QAM and 256QAM modulations. The observed EVM is well below the 3GPP recommended values for all modulation orders. Additionally, the coded BER performance over a transmission of 260 symbols is as follows: 0 for QPSK, 0 for 16QAM, $3.2*10^{-7}$ for 64QAM and $3.5*10^{-7}$ for 256QAM. These results serve to validate the feasibility of wireless transmission at 144 GHz using the implemented hardware setup. In the upcoming deliverables, the performance of APSK and other optimized waveforms candidates will be investigated and reported. Furthermore, a performance comparison to the NR standard will be conducted.

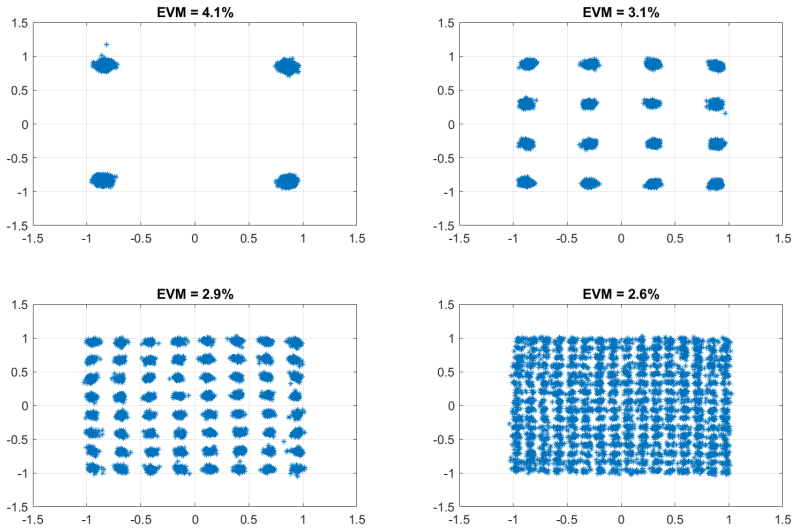

Figure 5-7: Received constellation pattern of the transmit signals in NR standard format.

5.2 Waveform and modulation enhancements

This section introduces enhancements to waveform and modulation schemes for wireless systems operating in all frequency bands. As known, waveforms and modulations schemes are an important asset to achieving higher rates and spectral efficiency. However, as new applications arise, other— now essential—aspects such as mobility and energy consumption must be considered. These new challenges demand low-complexity techniques capable of tackling known issues, including high Doppler shifts, PAPR, and out-of-band emissions. The following subsections address some of these issues by enhancing and optimizing known standardized solutions.

5.2.1 Adaptive multicarrier modulation

Problem statement: Multicarrier modulations (e.g., CP-OFDM) have established themselves in various standards thanks to their advantages compared to the single-carrier system: robustness against multiple paths, simple equalization, and natural association with MIMO systems, etc. But there are still areas for improvement such as resistance to Doppler, out-of-band radiation, PAPR, etc. In that sense, a new type of multicarrier modulation is proposed, flexible and robust in the face of the areas of improvement listed above. This section describes one new multicarrier scheme called adaptive multi-carrier modulation (AMCM) that is flexible in the sense it easily adapted to the radio environment (time and/or frequency selective channel). This study introduces this new waveform by analysing its power spectral density (PSD) and compare it to classical CP-OFDM.

Methodology: The block diagram with detailed description of the relevant blocks is depicted in Figure 5-8.

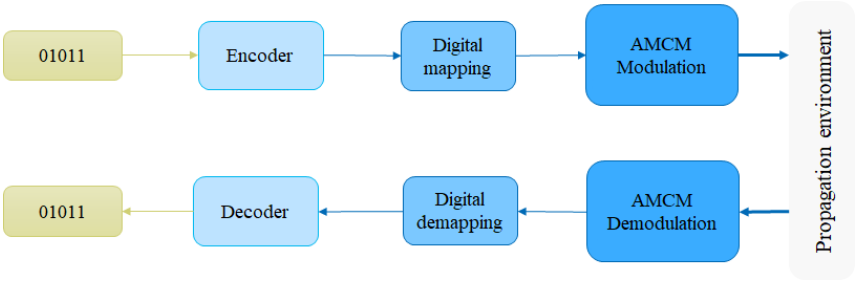

Figure 5-8: Block diagram with AMCM Modulation.

As illustrated in Figure 5-9, the AMCM modulation is based on the disjoint processing of the In-phase and Quadrature-Phase channels of the data symbols, i.e., I and Q. The inverse fast Fourier transform (IFFT) is applied separately at each of them. Moreover, the data processing in the frequency domain, i.e., before IFFT, includes a summation between real (imaginary) modulation symbols and the negative (positive) value of their quadrature in phase version delayed according to the delay factor $\boldsymbol{R}$, i.e., $\boldsymbol{R}$ being the delay between I and Q ways. Then, phase rotations $e^{-jk\frac{\pi}{2R}}$ and $e^{+jk\frac{\pi}{2R}}$ are applied on I and Q channels, respectively, to guarantee a quadrature between them to make exact restitution after demodulation at reception side. This generic scheme allows us to obtain classical CP-OFDM by applying $\boldsymbol{R} = \boldsymbol{0}$ in the formula showing the flexibility of the system. Z is the classical delay line introduced in the common "electronic circuit world".

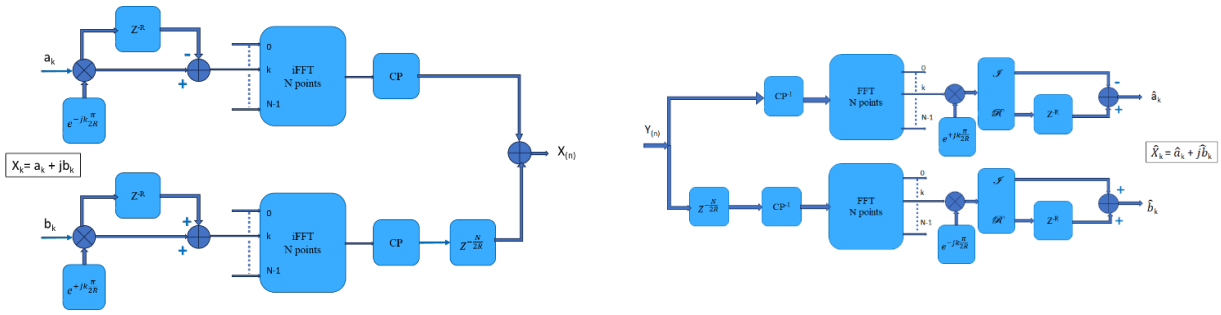

Figure 5-9: AMCM Modulation and Demodulation.

It can be seen that this architecture implements 2 FFTs that can be viewed as an increase in complexity compared to CP-OFDM. It is not the case as 2 real FFTs is used instead of one complex one in pure OFDM, leading to around the same.

Results: Figure 5-10 illustrates the difference between OFDM and AMCM modulations in PSD point of view.

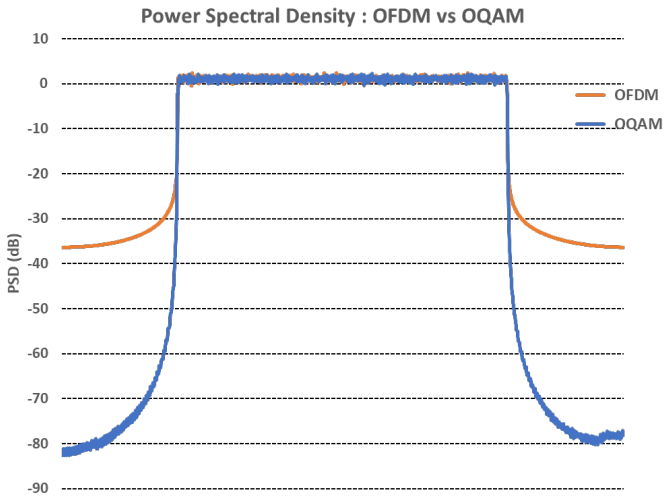

Figure 5-10: the PSD of OFDM (R=0) and OQAM (R=1).

It can be observed that a significant gain in favour of the AMCM compared to CP-OFDM that allows AMCM to fit better constraints due to spectrum mask imposed by the regulation instances, especially from ITU in THz bands.

In perspective, the objectives are to provide other type of performance results in terms of BLER vs SNR over frequency selective channels (3GPP model) and to evaluate the robustness in mobility environment (Doppler effect). Combining AMCM with polar constellations (Section 5.1.3) is also one objective to evaluate the whole system with phase noise and Doppler shift.

5.2.2 New LDPC code parity matrix design

Problem statement: Correction codes are one of the essential functions of the digital communication chain. LDPC codes have been selected by 3GPP for 5G, they offer a wide variety of size and code rate, called modulation and coding schemes (MCS). This work proposes a new parity matrix structure based on the structure of 3GPP (Figure 5-12) which improves the performance according to the number of iterations of the decoder allowing to decrease the energy consumption of the system.

In the first phase, a new design for the 5G LDPC matrix is proposed, which retains the constraints of the matrices defined by the 3GPP and which offers increased performance with a lower number of iterations. The second step defines a new matrix scheme that would be proposed for the design of 6G systems, improving performance while minimizing latency and reducing energy consumption (optimization of the number of decoding iterations). AI will be also introduced as an optimized tool to achieve these goals. Some first details are given in Chapter 7.

Methodology: To evaluate the gains of the new LDPC matrixes, link simulations are performed over AWGN channel and compute curves in terms of BLER versus SNR. The Block diagram in Figure 5-11 illustrates the relevant blocks to evaluate the LDPC codes.

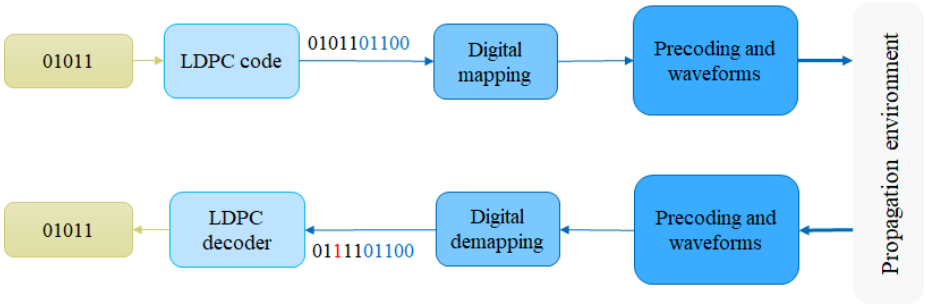

Figure 5-11: Block Diagram with LDPC code.

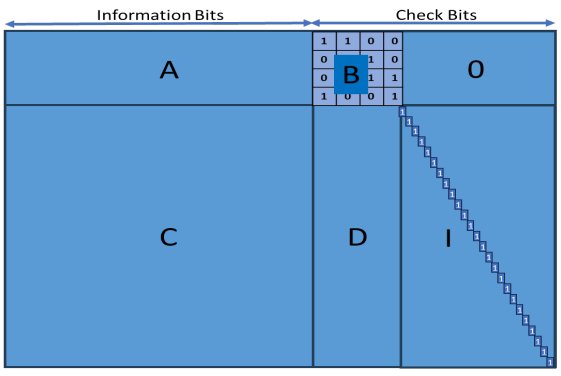

Figure 5-12: Structure of the parity matrix H.

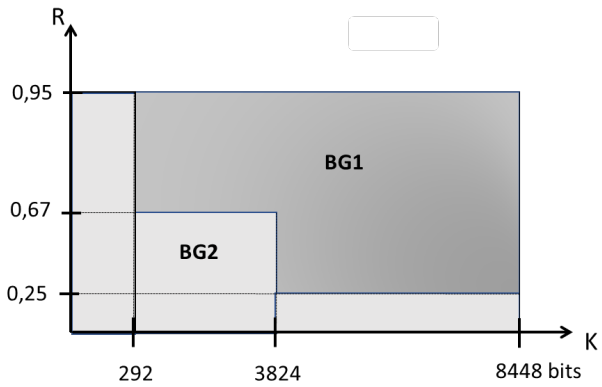

Figure 5-13: Definition of BG1 and BG2.

The parity matrix H is composed of 6 sub-matrices: A, B, C, D, O and I. The matrix A is the Kernel, C and D are extended matrices, B is a diagonal structure matrix, O an empty matrix and I a matrix identity. To evaluate

the LDPC at the receiver side, Normalized MinSum decoder [EE14] is used, which is the common decoder implemented in the hardware component.

3GPP defines 2 basic graphs (BGs), called BG1 and BG2, that are photograph matrices designed from 2 main parameters K, the number of bits of information, and Zc, the factor of expansion. The matrices obtained make it possible to code blocks of 12 à 8448 bits ($K'Zc\ K$). BG1 and BG2 are depending on the coding rate and the bit of information as illustrated in Figure 5-13, with the following definition:

Use BG2: if $K' < 292$ or $K' < 3824$ and $R < 2/3$ or $R < 0.25$ else BG1

Results: The performance results (BLER vs SNR) are given in AWGN channel for one BG1 and one BG2 matrixes. In the simulation campaign, the quasi totality of MCS is used to evaluate the new matrices designs. The results lead to the same conclusion as the performance presented below.

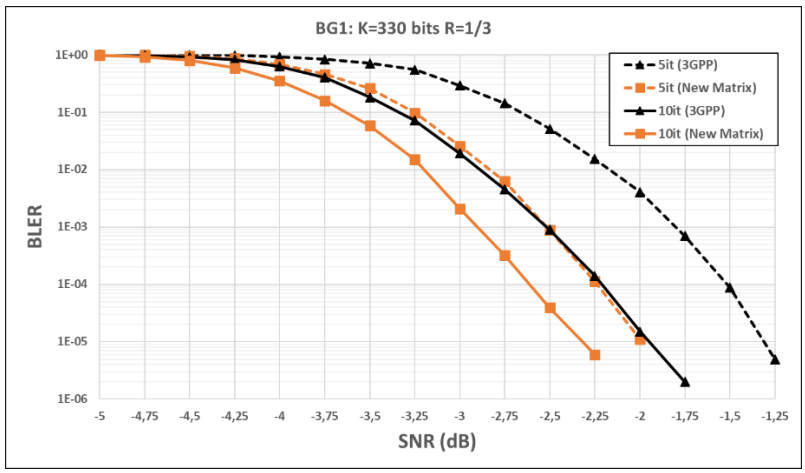

Figure 5-14: Performance for the new matrix (orange curves) BG1 K=330 bits R=1/3 for 5 and 10 iterations of decoding compared to 3GPP matrix (black curves).

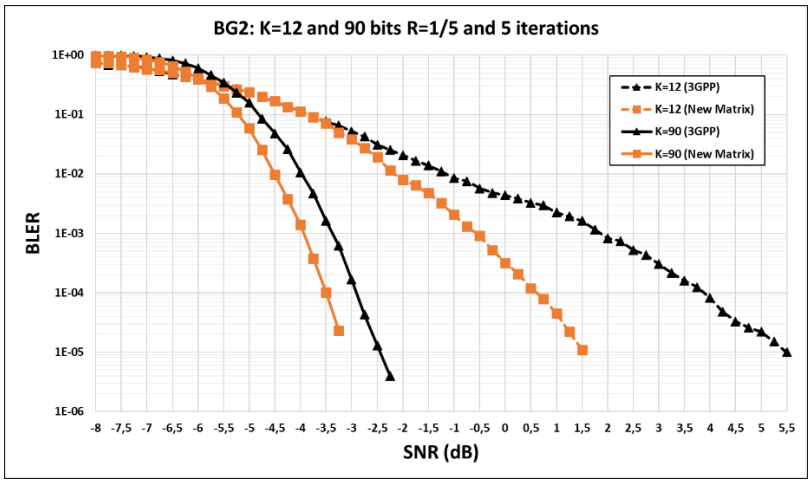

Figure 5-15: Performance for the new matrix BG2 (orange curves) K=12 to 90 bits, R=1/5 for 5 iterations of decoding compared to 3GPP matrix

Figure 5-14 shows that the matrix scheme gives the same performance as the matrix defined in 3GPP but with twice less iterations. This gain can be reduced by reducing complexity and thus energy consumption. At the same number of iterations (#10 iterations), this design has 0.4dB gain compared to 3GPP matrix and #5 iterations, one gain of 0.75 dB. Figure 5-15 illustrates the performance obtained with short packet sizes with 5 iterations of decoding. For the smallest packet size (12 bits), the achieved gain is 2.5 dBs at block error rate (BLER) $= 10^{-3}$, which corresponds to close a decrease of a factor of 2 of the signal's transmit power.

To conclude, it can be said that the new matrices design, based on the optimization of the matrices C and D, leads to better performance results when using 10 iterations at the decoder (gains between 0.2 dB and 1.5 dB depending on the MCS) compared to current 3GPP matrices and to the same performance when using 5

iterations with the matrices compared to 3GPP matrices with 10 iterations of decoding. In current 5G hardware (HW) implementation of transmitter, the most often, 10 iterations are carried out. Thus, this design allows in that case to achieve the same performance with twice less of iterations decoding that can be declined in power consumption gain. Is it possible to announce that a factor 2 of power consumption in the decoding processing is achieved? The analysis is made in that sense.

In perspective, this work is on new LDPC matrices designs for 6G (not background compatible with those defined in 3GPP) and also to the matrix A (the Kernel of H) optimization by using AI approach. One first strategy description about AI is described in Chapter 7.

5.2.3 Optimised delayed bit interleaved coded modulation

Problem statement: For achieving higher spectral efficiencies, coded modulation combines higher order modulation with channel coding. Bit interleaved coded modulation (BICM) [CTB98] creates code-diversity at individual bit level. Bit-wise interleaving at encoder output breaks the correlation induced by the modulation and adds additional redundancy against bit errors. DBICM [MLY+16], as a modified version of BICM, can decrease the achievable spectral efficiency gap between coded modulation (CM) and BICM. The capacity of DBICM depends on the specific delay schemes used in the bit delay module before modulation. For a given choice of constellation and bit labelling, the best delay scheme that maximizes the DBICM capacity can be obtained. The authors of [LQY21] have considered Gray labelled QAM constellations and analysed the effect of the delay scheme on the performance. The task of obtaining the best delay scheme for Gray labelled QAM constellations has been converted to a simpler problem of obtaining the best delay scheme of the constituent PAM constellation in [LQY21]. Authors of [Hos21] have considered APSK constellations of various sizes and analysed the effect of delay scheme on the performance. Bit delay scheme optimization requires calculation of the DBICM capacity using expensive numerical integration. A common approach involves employing Monte Carlo simulation and its complexity grows quadratically ($O(M^2)$) with the constellation size.

In this work, the aim is to optimise delay schemes for a given constellation using a low complexity algorithm compared to the conventional numerical integration method. For developing this algorithm, the problem is viewed as analogous to the bit labelling optimisation problem in BICM.

Methodology: The structure of a typical DBICM system is illustrated in Figure 5-16. The functionality of different blocks in the system model can be explained as follows. The encoder and interleaver module perform forward error correction (for example LDPC). Input bit stream $\boldsymbol{u}_t$ of length K received at time t. It is converted to coded and interleaved bit stream and $\boldsymbol{c}_t$ of length N. Serial to parallel module converts $\boldsymbol{c}_t$ into m parallel sub-blocks where the ith sub-block is $\boldsymbol{c}_t(i) = [c_t^0(i), \dots, c_t^{n-1}(i)]$, where $n = \frac{N}{m}$ and $i = 0, \dots, m-1$. The bit delay module then introduces delay T_i into the ith sub-block $\boldsymbol{c}_t(i)$ based on the given delay scheme $\mathbf{T} = [T_0, \dots, T_i, \dots, T_{m-1}]$, where $T_i \in \{0, .., \tau_{max}\}$. Finally, the mapper maps bit sequences output from the bit delay module into constellation symbols. The receiver side blocks have the opposite functionality. The demapper module can use the extrinsic information of delayed symbols from the decoder for symbol demapping in addition to received symbols.

Bit labelling optimisation using Chernoff bound [CTB98] based cost function minimisation along with binary switching algorithm (BSA) was introduced in [SFG+03]. A modified version of the Chernoff bound is used as a cost function to optimise delay schemes. The proposed method demonstrates strong performance only for Gray-labelled constellations, while the BICM performance on non-Gray labelled constellations is generally considered poor. Bit error rate and capacity curves are used to measure performance of the DBICM schemes. The best delay scheme has the highest capacity for a given SNR.

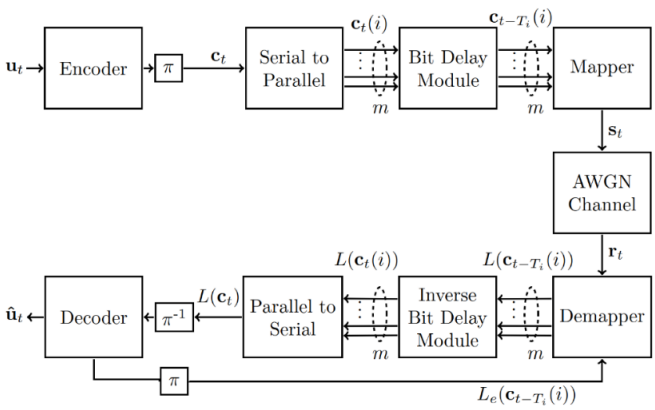

Figure 5-16: The structure of a delayed bit-interleaved coded modulation (DBICM) system.

Results: 64-QAM, 256-QAM, 1024-QAM and 16-APSK Gray labelled constellations are considered to initially obtain the capacity curves using numerical integration. The highlighted curves in Figure 5-17 are obtained as the best delay schemes using the proposed low complexity method. Maximum possible delay $T_{Max} = 1$ case is considered.

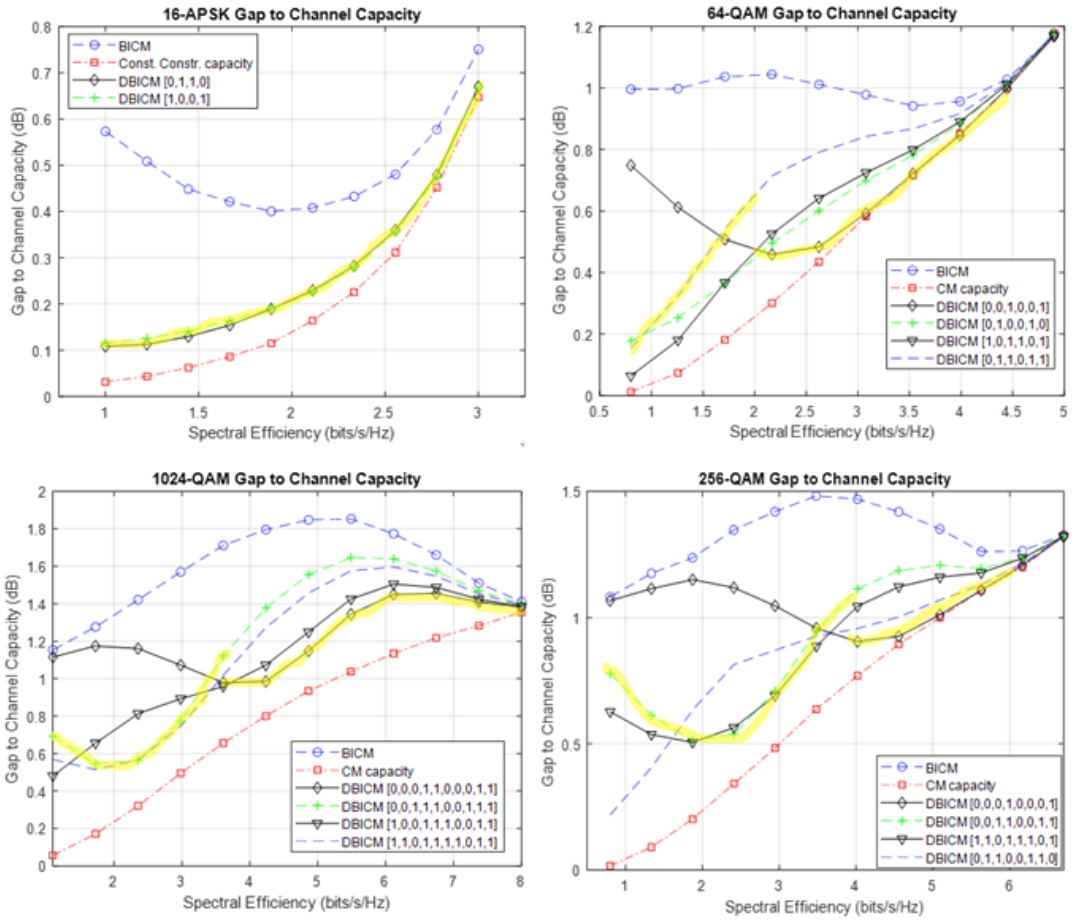

Figure 5-17: The performance comparison of the gap to Gaussian channel capacity for different DBICM delay schemes, BICM, and coded modulation focusing on specific constellations. The best delay scheme according to our proposed method is highlighted.

Similar performance was obtained for Gray labelled 16-QAM, 16-PSK and 32-PSK. It is evident that the proposed low-complexity method can identify the best delay scheme at a given spectral efficiency with reasonable accuracy, especially at high SNR. Future work includes developing an analytical explanation for the results.

6 Intelligent radio air interface design

In the last few years, the continuous evolution of wireless technologies has intersected with breakthroughs in machine learning, aiming to address the demands for spectral efficiency, reliability, and flexibility in modern telecommunication systems. This intersection is pushing for the creation of intelligent radio air interfaces, designed to enhance the performance and adaptability of wireless networks. This chapter delves into this dynamic area, exploring cutting-edge solutions leveraging artificial intelligence (AI) to optimize air interface design. Segmented into four main sections, each dedicated to a critical aspect of radio interface design, the chapter presents contributions ranging from the application of machine learning for modulation and coding to intelligent channel state information (CSI) acquisition, AI-based MIMO transmissions, and AI solutions for compensating hardware impairments.

The first section, "Learning for Waveform, Modulation, and Coding," investigates how AI can be utilized to enhance modulation and coding by optimizing MIMO waveforms, designing for both communication and also for joint communication and sensing (JCAS), and optimizing LDPC matrix structures for error correction. The second section, "AI-based CSI Acquisition," delves into AI-driven techniques for CSI compression and prediction to maximize spectral efficiency while minimizing overhead. The third section, "AI-Based MIMO Transmission," discusses innovative solutions for MIMO transmission, including beamforming with imperfect CSI, antenna muting, user pairing, and pilot assignment in D-MIMO scenarios. Finally, the fourth section, "AI Solutions for Hardware Impairments," focuses on how AI can mitigate the non-linearities of power amplifiers, highlighting AI's potential in compensating for hardware imperfections affecting transmission quality.

Overall, this chapter provides a comprehensive overview of how artificial intelligence is shaping the future of radio interface design, with profound implications for the development of more efficient, reliable, and intelligent wireless networks.

6.1 Learning for waveform, modulation, and coding

This section illuminates the potential of artificial intelligence in advancing modulation and coding techniques. By exploring optimized multiple-input and multiple-output (MIMO) waveforms for pilot-free channel communication, integrating sensing capabilities into waveform design, and optimizing LDPC matrix structures for error correction, the contributions presented here highlight how AI can overcome the limitations of traditional methodologies, promising significant improvements in spectral efficiency and transmission reliability.

6.1.1 MIMO waveform for communication

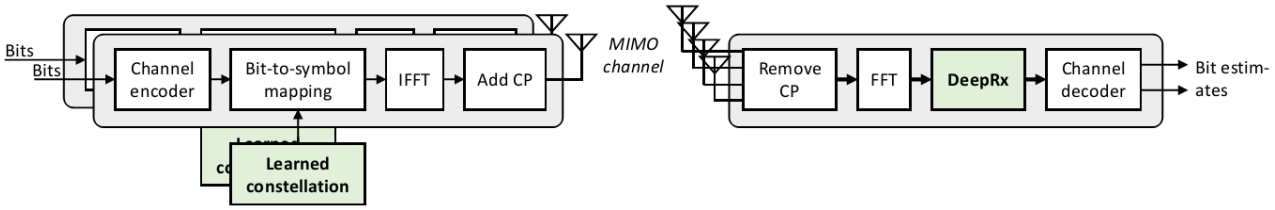

Figure 6-1: The considered system model for the ML-based pilotless scheme.

Problem statement: In this contribution, MIMO transmitter and receiver are trained end-to-end to communicate without any channel estimation pilots [KHH23]. This means that the link can perform spatial multiplexing without wasting any resources for pilot overhead, thereby improving the spectral efficiency. This is achieved by considering the transmitter and receiver as part of a single model, connected by a differentiable wireless channel. Such a system can be learned in a supervised manner by treating the channel and any required conventional functions as fixed neural network layers, which are not modified during the training. This results in a learned MIMO waveform and a compatible machine learning (ML) based receiver for detecting the information bits.

Methodology: As illustrated in Figure 6-1, an orthogonal frequency-division multiplexing (OFDM) system is considered, where a learned constellation shape is utilized to facilitate fully blind MIMO detection at the

receiver side using a DeepRx-type convolutional neural network (CNN)-based receiver [HKH21]. The detailed architecture of the considered ML-based receiver follows the MIMO DeepRx presented in [KHH21]. The ML receiver takes in the Fourier transformed received MIMO signal and outputs the log-likelihood ratios (LLRs) for each received spatial stream. With this, the input signal to the receiver can be expressed as:

$$\boldsymbol{y}_{ij} = \boldsymbol{H}_{ij}\boldsymbol{x}_{ij} + \boldsymbol{n}_{ij}, \quad \textbf{(6-1)}$$

where $\boldsymbol{H}_{ij}$ is the $N_R \times N_T$ MIMO channel matrix for the i-th subcarrier and j-th symbol, N_R is the number of receive antennas, N_T is the number of transmitted spatial streams, $\boldsymbol{x}_{ij}$ is the transmitted $N_T \times 1$ symbol vector, and $\boldsymbol{n}_{ij}$ is the $N_R \times 1$ additive noise signal.

In order to achieve pilotless spatial multiplexing, the transmit constellations are learned jointly with DeepRx. This means that, in the transmitter, the elements of $\boldsymbol{x}_{ij}$ are selected from learned constellation points. In this work, each MIMO stream is modulated with a different constellation, meaning that N_T different constellations are learned. Therefore, each element of $\boldsymbol{x}_{ij}$ is chosen from a different constellation, which allows the receiver to learn pilotless MIMO detection.

The input of the DeepRx is formed by collecting the received signal samples over one slot, consisting of N_F subcarriers and N_S OFDM symbols. Therefore, the input array has a size of $N_F \times N_S \times N_R$. This input is fed to a MIMO DeepRx model, as described in [KHH21], with the exception that now there is no separate input for the raw channel estimate as there are no pilots being transmitted. The output of the pilotless MIMO DeepRx model consists again of the log-likelihood ratios, which are fed to the low-density parity check (LDPC) decoder for extracting the information bits.

The system can be trained end-to-end assuming a differentiable implementation of the radio link (e.g., using [HCA+22]). In this work, the training is done similar to [HKH21] by using the binary cross entropy (BCE) between the detected and transmitted bits as the loss function. To facilitate more robust convergence, the loss function includes also a term which penalizes for constellation points which are too closely spaced [KHH23]. When the transmitter and DeepRx are trained jointly using the above loss function, DeepRx will learn to utilize the simultaneously learned constellations for detecting the data signals without any pilots.

The approach is evaluated with single-user MIMO (SU-MIMO) simulations, where two MIMO streams are multiplexed. The simulations are performed using the Sionna library [HCA+22]. In particular, the proposed approach is trained with both 16- and 64-point constellations, resulting in 4 and 6 bits per symbol, respectively. Different channels models are employed for the training and validation to avoid overfitting to the selected channel models. For training, each training sample is generated either from clustered delay line (CDL)-A and CDL-B channel profiles [38.901] (selected randomly for each training sample), while CDL-C is used for validation. More detailed simulation parameters are presented in the Appendix (Section A.4.1).

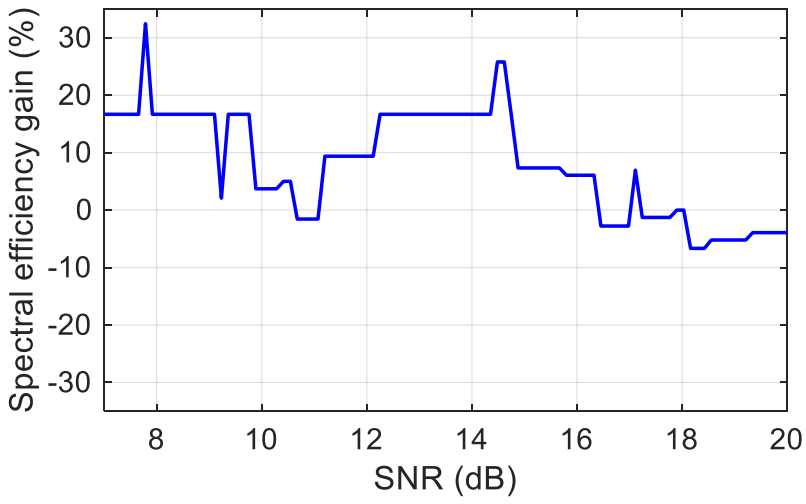

Figure 6-2: The spectral efficiency gain of the ML-based pilotless scheme over the conventional pilot-based scheme.

Results: The proposed learned pilotless scheme is compared to a conventional QAM-OFDM waveform and a nonlinear K-Best detector [FT15] which is utilizing a demodulation reference signal (DMRS) based channel estimate. The performance gain over the conventional DMRS-based scheme can be analysed from Figure 6-2. With signal to noise ratio (SNR) below 15 dB, a gain of 15-20% is typically achieved, with some exceptions. However, when the SNR goes above 15 dB, the ML-based pilotless scheme performs worse than the baseline. Since use of the 64-point constellations is required at these SNRs, the issue is most likely related to the higher-order constellation. It is likely that a larger DeepRx model would be required for detecting the high-order modulation symbols at high SNRs. Nevertheless, this result already shows that by learning jointly the constellation shapes used by individual spatial streams as well as a CNN-based receiver, it is possible to transmit several spatial MIMO streams successfully without any pilots.

6.1.2 Waveform and precoding for JCAS

Problem statement: JCAS combines sensing and communication resources to enhance system efficiency and develop new functionalities. While traditional JCAS designs use model-based algorithms, unexpected hardware impairments can impact their performance [CLM+23]. Deep neural networks (DNNs) address these challenges, with single-component DNNs optimizing individual operations [LYL+22] and end-to-end DNNs jointly optimizing transmit and receive tasks [MSW+22]. However, the black-box nature of DNNs limits interpretability and often requires significant labelled training data. In this work, an end-to-end model-based machine learning (MB-ML) approach is used to compensate for hardware impairments, while augmenting the interpretability of the results. A semi-supervised learning (SSL) method, which combined labelled and unlabelled data, is proposed to reduce labelled data acquisition. The goals are: (i) to compensate for hardware impairments, and (ii) to show that with a small fraction of the labelled data needed for supervised learning (SL), the SSL framework can achieve similar performance to SL.

Methodology: A JCAS scenario is simulated as follows; (i) a monostatic sensing transceiver is equipped with a ULA to sense a single target, and (ii) the same sensing transmitter is used to send messages to a single-antenna communication receiver in a different direction of the target. The JCAS transceiver is assumed to have a coarse knowledge of the target and the communication receiver positions. An OFDM signal is designed and sent over the physical channel. However, the JCAS transceiver is perturbed with inter-antenna spacing impairments in the ULA, affecting beamforming and the processing of the backscattered signal from the target. The communication receiver is fed with CSI, which already includes the effect of the impairments. Hence, the impairments are compensated using just sensing data for training, as depicted in Figure 6-3.

As a model-based baseline, a least-squares (LS) beamformer is adopted to steer the ULA energy into a particular direction, and the orthogonal matching pursuit (OMP) algorithm is used to estimate the target position. The MB-ML approach parameterises the LS beamformer and the OMP algorithm to learn the true inter-antenna spacing values from data. Nevertheless, model-based OMP is a nondifferentiable algorithm which does not allow for learning. A modified OMP algorithm is developed to enable end-to-end learning of the impairments. Reducing the amount of labelled data is achieved by a two-step SSL approach. Firstly, labelled data samples are used to learn the impairments (supervised), after which unlabelled received data samples are utilised to complete training (unsupervised). The received signal is pre-processed to compute the so-called *angle-range map*, a 2D matrix showing the angle and range of potential targets in the scene. The positions of the targets are computed in OMP by iteratively looking at the highest peak in the map and subtracting it from the map for the next iteration. This angle-range map is shown to be sensitive to hardware impairments, i.e., the peaks corresponding to targets are no longer in the correct positions under hardware impairments, and the magnitude of the peaks is reduced. Hence, this work proposes to maximize the magnitude of the highest peak in the angle-range map during the unsupervised stage. The position mean squared error is employed as the supervised loss function.

Results: In Figure 6-4, JCAS trade-offs are plotted for the model-based baseline, SL with different degrees of training data and SSL. When impairments appear in the JCAS transceiver, the baseline severely degrades in performance. SL can deal with the impairments and achieve a performance similar to the baseline with perfect knowledge of the impairments. Poor performance is shown by SL when fewer labelled data samples are used. However, the same performance as SL using all the labelled data is achieved by SSL with 1.18% of the labelled data, and 98.82% of unlabelled data.

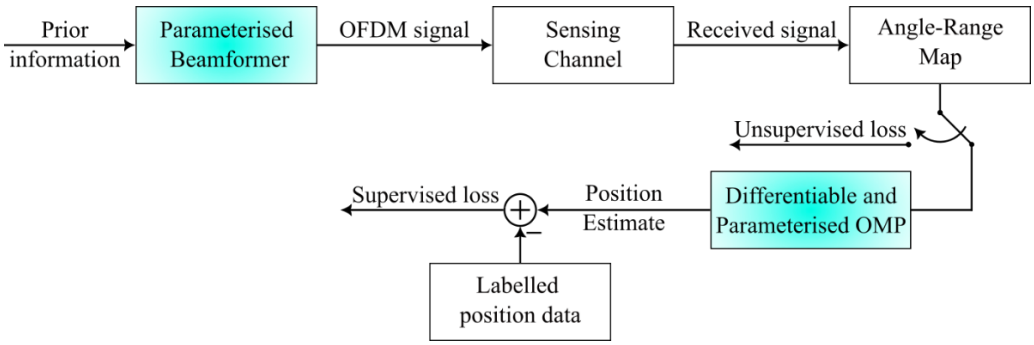

Figure 6-3: Forward pass of the learning algorithm.
Training only involves single-target sensing, as accounting for hardware impairments in sensing also accounts for the hardware impairments in the transmitter that affect communication performance. The supervised loss is replaced by the unsupervised loss after a fixed number of iterations. End-to-end learning is performed, where the coloured blocks contain the parameters to learn.

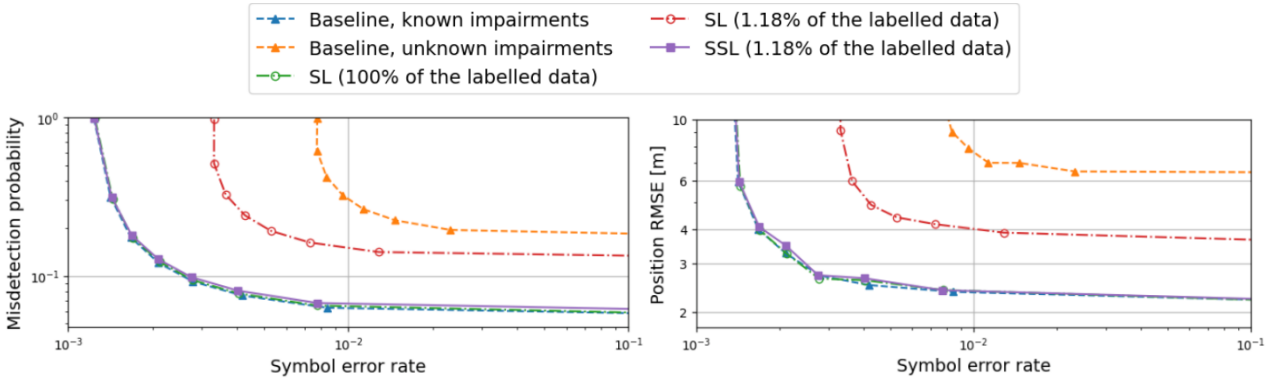

Figure 6-4: JCAS trade-off performance under hardware impairments for a false alarm probability of 1%. Only Pareto optimal points are shown for supervised learning (SL) and semi-supervised learning (SSL).

6.1.3 AI for LDPC matrix structure optimization

Problem statement: Low-density parity-check code (LDPC) is a type of error-correcting code used in digital communication systems to detect and correct errors that occur during transmission. It consists of adding redundancy bits to the message transmitted by the generator matrix G, and then solving equations at the receiver to recover the original message. These equations are called check equations and are given by the parity check matrix H. LDPC codes are currently used in the communication chain of 5G and may be continued for 6G. To ensure evolution and improvement of the communication chain, it is essential to improve the performance of error-correcting codes in this chain. This improvement could potentially be achieved through artificial intelligence where theoretical methods are limited. Artificial intelligence has proven its worth in many domains and could also be used for LDPC codes. This is why the topic of optimizing LDPC codes using artificial intelligence for 6G is being addressed.

Methodology: The 5G communication chain consists of several blocks, including the LDPC encoder and LDPC decoder (see Section 5.2.2). Recent research focuses on modelling the decoder using a recurrent neural network (RNN) to optimize the parity check matrix for a given codeword length [LDL+21]. The weights of this neural network are the coefficients of the parity check matrix as shown in the Figure 6-5. Since belief propagation (BP) decoding involves a recursive exchange of information, a recurrent neural network is used to calculate the decoding iterations. The output of each iteration is then used as input for the next iteration. The weights are updated automatically, and each new weight value undergoes a binary selection to ensure correspondence with the parity matrix structure.

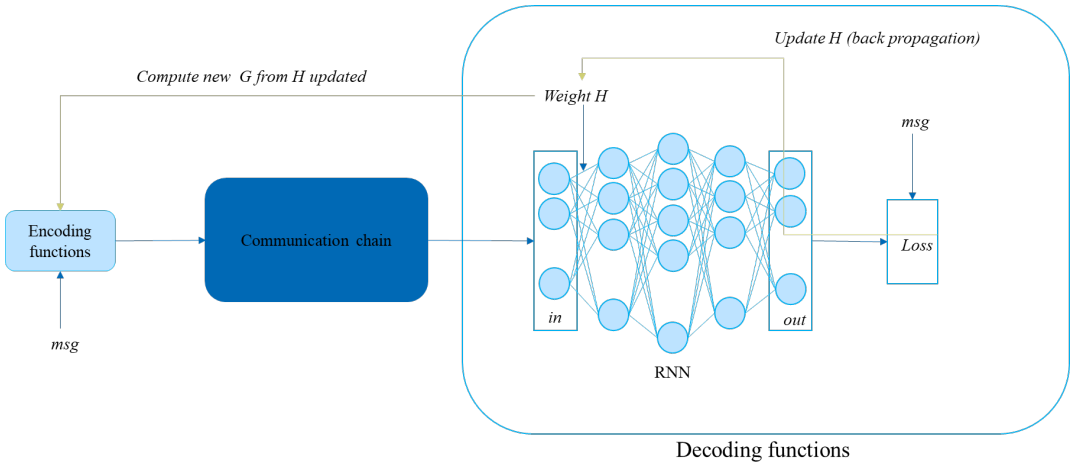

Figure 6-5: System architecture with RNN decoder.

After multiple decoding iterations, the proposed RNN tends to converge the weights, and thus the parity matrix, towards an optimal solution.

These works address a classical LDPC structure, but the 5G LDPC structure (see Section 5.2.2) presents several challenges:

- The structure - maintaining the structure after weight updates.
- Size diversity - finding an algorithm capable of improving all the BG1 and BG2 matrices, regardless of Zc (expansion parameter).
- Cycles - it is difficult to reduce cycles for small Zc.

Further studies are ongoing to solve these different problems with a particular neural network structure which will be added in future deliverables, as preliminary results seem promising.

6.2 AI-based CSI acquisition

The acquisition of accurate channel state information (CSI) is pivotal for the efficient operation of modern wireless systems. This section focuses on innovative AI-based strategies for CSI feedback compression in multi-vendor scenarios and intelligent CSI compression techniques. It presents research on enhancing CSI compression and prediction using artificial intelligence, aiming to reduce overhead and improve spectral efficiency without compromising the accuracy of channel information. The utilization of AI in this context demonstrates a significant step towards more adaptive and efficient wireless communication systems.

6.2.1 ML-based channel state feedback compression in a multi-vendor scenario

Problem statement: CSI feedback is a key element to enable MIMO and beamforming techniques and improve system performance. However, as the number of antenna elements increases the CSI overhead becomes significant. While codebook-based channel state feedback (CSF) can limit overhead, this is at the expense of a degraded CSI accuracy.

The target of this contribution is a demonstration that cooperative AI based techniques can improve the spectral efficiency and accuracy of CSF compared to legacy CSI schemes. In the considered demo, an AI/ML algorithm runs at the device to encode/compress the CSI to be sent. At the gNB a reciprocal AI-based technique decompresses the CSI. Together, those two AI algorithms can improve CSI resolution for a given number of bits, or equivalently reduce overhead for a fixed CSI resolution.

Methodology: The proof of concept is the over-the-air (OTA) demonstration of the feasibility of cross-vendor cooperation to enable joint AI solutions. The Section 10.3.1 provides an overview of the planned Lab and over-the-air tests.

As a step towards this goal, a simulation study of this scheme and the accuracy evaluation between the CSI at UE and the reconstructed CSI at the gNB is here proposed. This contribution details the scenario and simulation configuration and assumptions considered for this study.

In the considered setup, the gNB and UE cooperate to enable compressed CSF. The end-to-end joint training of the ML models (CSI decoder and CSI encoder, respectively, as shown in Figure 6-6) by sharing data set to a single entity that does the training is not a preferred solution as it requires sharing the proprietary models. Instead, the ML models are obtained through sequential and separate training of the UE and gNB models. That is, the model at UE and gNB sides are trained independently: the UE starts with training the UE encoder and UE reference decoder (both using UE-proprietary models) and then share the dataset so that the gNB would be able to learn a decoder (using gNB-proprietary model) capable of generating similar output as the one from the UE. This mechanism enables ML-based CSF without sharing the proprietary ML models at the UE and gNB. The process is detailed below.

1. The UE-side starts by collecting channel state measurement, these are the features and labels for training the models.
2. When enough channel measurements have been collected, the UE-side starts training the ML model encoder and the reference decoder for CSF compression.
3. UE-side shares a dataset to the gNB-side containing compressed CSF-samples and the channel state inputs, i.e., the ground truth.
4. With this dataset, the gNB-side trains a ML model capable of decoding the compressed CSF.
5. After training at the gNB-side, the UE-side and gNB-side ML models are deployed to the UE and the gNB, respectively.

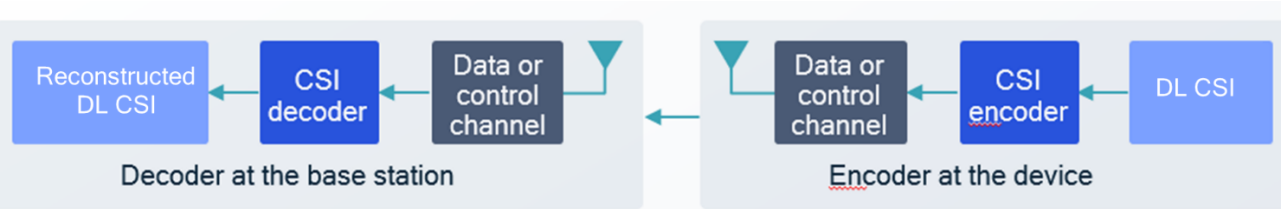

Figure 6-6: Diagram of the gNB and a UE processing block.

To evaluate the performance of ML-based CSF compression a system-level simulation will implement infra-vendor cooperation where the UE-side trains the encoder and decoder using UE AI/ML model and the gNB-side trains the decoder using network (NW) based ML model. The simulation will output reconstructed CSI samples that will be compared to ground truth CSI using the squared generalized cosine similarity (SGCS) metric. The simulation results will then evaluate the accuracy of the reconstructed CSI at the gNB versus the CSI at UE. Further details are provided in the Appendix (see Section A.4.2).

Results: The following table summarizes the sequential training performance based on 8 port 14 sub-band 3GPP TR 38.901-based Dense Urban channel model [38.901], dataset shared between the UE and the network. Two different encoder model designs have been considered: UE-side encoder type-1 (Qualcomm model) and UE-side encoder type-2 (Nokia model), to mimic different UE vendor scenarios in the network. Each encoder is trained following the steps 1-5 detailed above. For each encoder model, the SGCS performance have been looked with (a) UE-side decoder through joint end-to-end training, (b) Network-side encoder-specific decoder through UE-first training with individual encoder dataset, and (c) Network-side common decoder through UE-first training with mixed encoders: UE-side encoders type-1 and type-2 data sets.

With the current configuration each UE has 4 Rx antennas, providing a channel matrix of rank 4. The layer *i* in Table 6-1: SGCS performance with sequential training. denotes the eigenvector *i*, where layer 0 is for the best layer.

As it can be seen from the results, for each encoder, the UE-NW SGCS performance with UE-first sequential training is similar to UE-UE joint training performance, and NW common decoder gives similar performance as the NW encoder-specific decoders. This proves that sequential training through dataset sharing is an effective training method to deal with multi-vendor scenarios without disclosing the proprietary neural network

(NN) architectures. Furthermore, results show that a common NW decoder model can be trained through sequential training to deal with multi-UE vendor scenarios in the network.

Table 6-1: SGCS performance with sequential training.

Encoder	Decoder	Training	SGCS (lin) layer 0	SGCS (lin) layer 1	SGCS (lin) layer 2	SGCS (lin) layer 3
UE encoder type 1	UE decoder type 1	End-to-end	0.844	0.736	0.666	0.617
UE encoder type 1	NW decoder 1	UE-first, encoder-specific decoder	0.847	0.732	0.656	0.603
UE encoder type1	NW common decoder	UE-first, common decoder	0.842	0.725	0.648	0.595
UE encoder type 2	UE decoder type 2	End-to-end	0.852	0.757	0.705	0.673
UE encoder type 2	NW decoder 2	UE-first, encoder-specific decoder	0.856	0.756	0.698	0.663
UE encoder type 2	NW common decoder	UE-first, common decoder	0.854	0.753	0.695	0.659

6.2.2 Intelligent CSI compression

Problem statement: CSI compression is essential for communicating the channel characteristics between UE and base station (BS) when the channel matrix is too large to be transmitted back digitally via uplink, e.g., in the frequency division duplexing (FDD) of large MIMO systems. In turn, the fed-back compressed representation of the precoder matrix (or channel eigenvectors over sub-bands per layer) is of large importance to represent channel statistics adequately. Advanced precoding techniques at BS side (a must for enhancing UE signal strength in modern MIMO systems) allow to:

- change the original physical channel to the effective channel.
- improve the channel's gain (e.g., due to "synchronized" coherent addition of the signals from BS antennas towards UE).
- improve the no-fading statistics (known as "solidification" of the physical channel by a precoder).

This research work concentrates on the study of intelligent CSI compression techniques for multi-user MIMO (MU-MIMO), using AI-driven models or non NN-based approaches of smaller complexity.

Methodology: Initial study and evaluations have started from the SU-MIMO case, where a BS precoder treats a single UE, having relatively small number of receiving antennas, i.e., NRX UE << NTX BS. It is well known since early MIMO studies [T99] that capacity is maximized when precoder utilizes, per resource element (RE), the "best" eigenvectors (corresponding to the largest eigenvalues) of the channel correlation matrix. In the special case of study (NRX UE << NTX BS), advanced precoder is even more important as it essentially shifts the receiver (RX) diversity to the transmit (TX) side of the BS. The improvements from advanced precoding can be utilized for better UE performance (e.g., data rate) or to reduce power at the BS side. Figure 6-7 presents an example of SU-MIMO channel improvement via linear precoding under unit transmit power constraint. Intelligent compression of channel H information and precoder matrix W enables harnessing the full precoding gains in large MU-MIMO system since the accuracy is required for DL BS precoder construction. In practice, the channel matrix cannot be delivered back digitally in full per every RE due to its large size. Delivery of coefficients per sub-band may be considered (as in 5G standardised Type2 scheme) but it is still costly even with large coefficients quantization. Hence, there is great need for more advanced CSI compression and precoding schemes. In 5G new radio (NR), this is done with further frequency compression of the sub-band precoder via the so called standardised enhanced type 2 (eType2) scheme, or via AI-based schemes (studied from Rel.18 [FLV+23]). But how to "synchronize" different channels inside of a sub-band for the optimal result is an open question.

At the first stage of the study, a background analysis has been performed, where:

- the mathematical model of the eType2 advanced precoding scheme defined in 5G NR has been constructed.
- the performance of eType2 has been compared to the simpler 5G NR precoding scheme (termed as Type1) which is de-facto used currently in industry.
- the performance of outer bounds for the system have been constructed and compared.

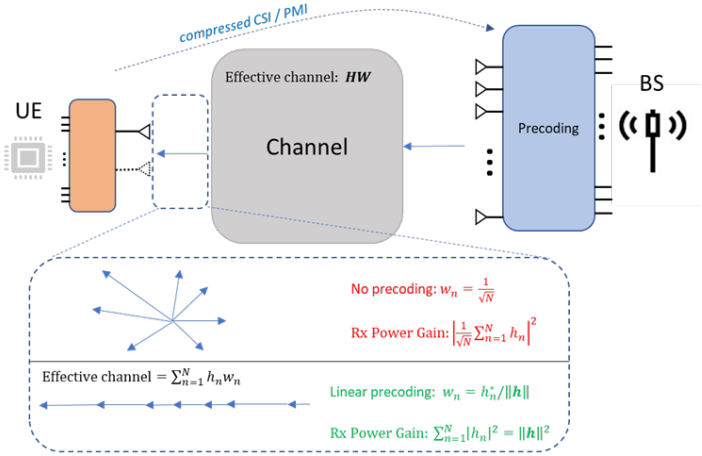

Figure 6-7: Example of SU-MIMO channel improvement via linear precoding under unit transmit power constraint.

Results: Numerical simulations have been complementing this analysis, providing initial observations and further research directions. For example, Figure 6-8 examines the capacity performance (in terms of bits per RE averaged by the number of information layers) of the Type 1 and eType2 precoders as well as the heuristic sub-band (SB) precoder (generalized from [T99] approach) and the singular value decomposition (SVD) bound for the case of 3-layers and 4 spatial beams (optimally selected from the full 16 beams basis, corresponding to 32 dual-polarized BS antennas). A performance gap between Type1 and eType2 precoders is observed, confirming the advantage and importance of the latter. However, it is also observed that eType2 is not well aligned with the heuristic SB precoder performing close to the bound, and a possibility for improvement will be investigated in future work. Also, the 4-beams precoder bound performs very far (~5 dB) from the bound with the full 16 beam basis. Hence, trade-offs delivering better compression and preserving a larger basis size (in 5G number of beams) may be essential. Further details are provided in the Appendix (see Section A.4.3).

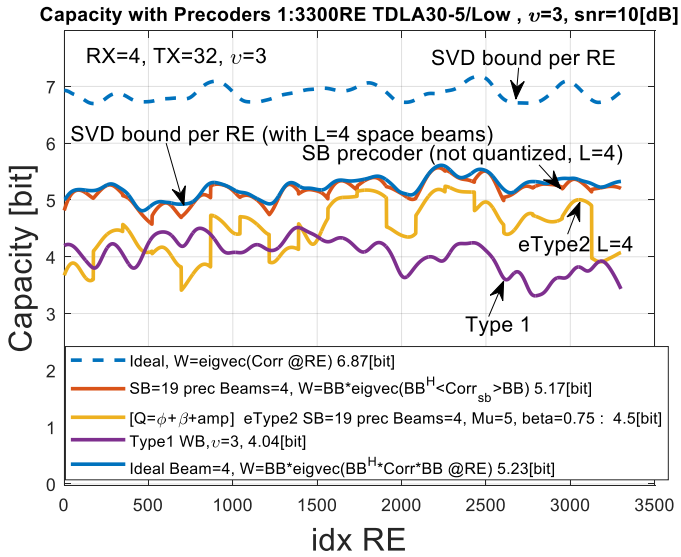

Figure 6-8: Performance of the eType2 precoder for TDLA-30-5/LOW channel [38.101], υ=3 information layers and use of L=4 spatial beams basis.

6.2.3 CSI prediction

Problem statement: In frequency division duplexing (FDD) systems, where channel reciprocity is not available, the downlink CSI is estimated at the UE and the estimated CSI is sent to the BS through a feedback report in uplink. In FDD systems, the CSI feedback incurs high overhead, motivating the study of ML-based CSI feedback enhancements in 3GPP. An autoencoder (AuE) can be used for dimensionality reduction and minimize feedback overhead, improving feedback accuracy at a maintained overhead compared to the conventional CSI feedback techniques. The AuE-based CSI compression has been studied for the ML-based CSI feedback enhancement in the Release-18 study [38.843]. The AuE-based CSI compression may suffer performance degradation due to channel aging in a dynamic network since the AuE model cannot capture the time-varying nature of the wireless channel.

Methodology: To avoid the channel aging issues, this study aims at developing a deep learning-based solution that allows the BS to accurately predict radio channel variations under the 3GPP CSI feedback mechanism. Aiming at multi-step-ahead prediction based on a single feedback information under the CSI feedback process, this study proposes an evolutional CSI neural network (evoCSINet), a CSI framework that learns latent dynamics of radio channel for prediction applications. The proposed evoCSINet, detailed in Section A.4.4, uses deep neural networks as a parameterized function approximator to identify the unknown true channel dynamics from data. A dynamicNet is introduced that learns the temporal evolution of radio channel in latent space. This model has the potential to enable a recursive multi-step prediction in the latent space. The proposed evoCSINet applies the combination of autoencoder and dynamicNet to identify latent-level representation of channel dynamics from radio channel images given by the current channel states. Through learning the latent dynamics representation, evoCSINet is optimized towards multi-step predictions. The proposed evoCSINet provides a factorized representation of radio channel dynamics that allows evoCSINet to fit into the 3GPP CSI feedback procedure. As a result, it has been shown that the evoCSINet can achieve an accurate multi-step-ahead prediction only based on the single feedback information of an encoded vector, called latent code.

The factorized decomposition of the proposed evoCSINet allows two different implementations, namely, BS-centric and UE-centric predictions. In this study, a BS-centric prediction is introduced with prediction depth D, where the BS acquires the encoded CSI of downlink channel state H_k at a slot k and wishes to accurately forecast the next D channel states $H_{k+1}, H_{k+2}, \ldots, H_{k+D}$ into the future. Figure 6-9 depicts a schematic diagram of a BS-centric CSI prediction with the proposed evoCSINet, where the evoCSINet is split into UE and BS sides: encoder φ at the UE side, and dynamicNet F and decoder φ^{-1} at the BS side. Note that the single CSI feedback $z_k = \phi(H_k)$ from the slot k is used for precoding-based data transmission over the following slots, until the next CSI update. Therefore, the prediction depth D is determined by the CSI feedback periodicity, which is specified in the 3GPP TS 38.213 [38.213]. Throughout this work, the CSI periodicity is assumed to be 10 slots, corresponding to the baseline time periodicity of 5ms being considered in the Release-18 study item on AI for the air interface, TR 38.843 [38.843]. This means that the BS should forecast the variation of CSI from H_{k+1} to H_{k+9} with the prediction depth D = 9 based on the single CSI feedback z_k.

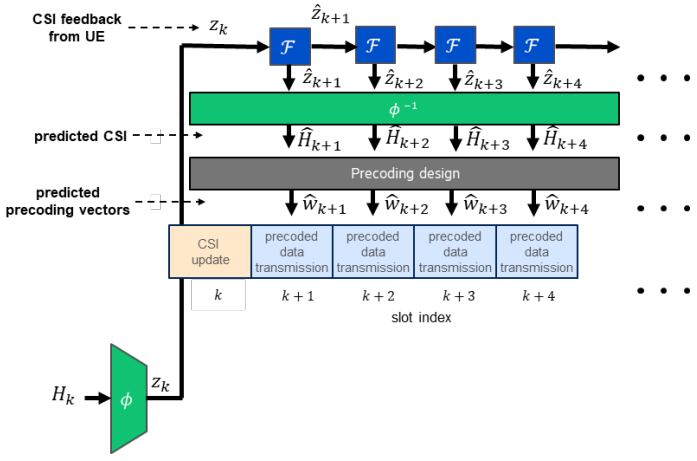

Figure 6-9: Schematic diagram of feedback-based precoding design based on the proposed evoCSINet.

For performance simulations and analysis of its impact on precoding performance, channel realizations have been generated using 3GPP 5G Urban Macro (Uma) channel models [38.901]. The data set are created with 15000 state sequences with length 12. Throughout this work, the new CSI-RS configuration with a comb-factor 6 in frequency domain is applied for T=4 OFDM symbols within slot time k, i.e., with CSI-RS every 6 of the 12 subcarriers of a PRB, and the number of available physical resource blocks (PRB) is assumed to be 64, i.e., the number of subcarriers carrying CSI-RS in each of the T OFSM symbols is N = 64 × (12 / 6) = 128. Then, the corresponding channel states can be represented by the channel matrices of size T × N = 4 × 128, i.e., $H_k \in C^{4\times128}$.

Results: The performance metric considered is ϵ-outage capacity, which is defined as maximum rate below which reliable transmission is possible at outage probability ϵ. In Figure 6-10, the 10% outage capacity (ϵ=10%) performance has been evaluated under three different CSI assumptions, perfect CSI, compressed CSI, and predicted CSI by evoCSINet, and it has been normalized by the upper capacity bound with perfect CSI in order to quantify prediction performance loss relative to the upper bound. The prediction time grids generate a specific set of time points with the same initial point k. Maximum ratio transmission (MRT) precoding method is used in this evaluation. MRT is known as optimal for this MISO setup by maximizing the signal gain, and CSI at the transmitter is required to enable the precoding.

Notice that the MRT precoding with the compressed CSI suffers from a severe performance loss due to channel aging. For instance, the performance loss reaches 23% at the CSI aging of 9 slots, compared to the ideal CSI. The plot shows that evoCSINet achieves performance improvement compared to AuE-based CSI compression as the number of CSI aging slots increases. The performance loss of evoCSINet is reduced to 11% at the CSI aging of 9 slots. Further details are available in the Appendix A.4.4.

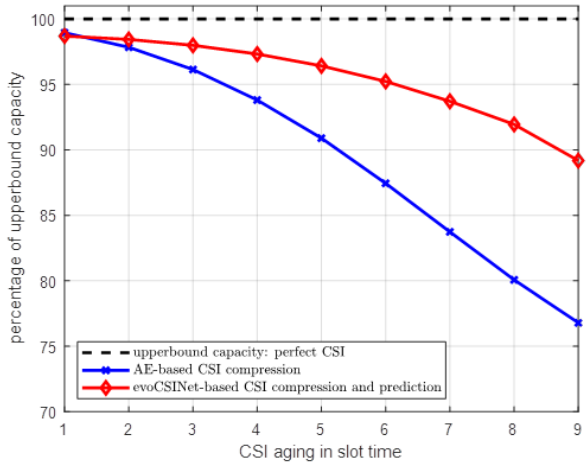

Figure 6-10: Performance comparison between AuE-based CSI compression and evoCSINet-based CSI prediction in percentage capacity, compared to ideal CSI.

6.3 AI-based MIMO transmission

MIMO transmissions represent a cornerstone for achieving high data rates and reliability in wireless networks. This section discusses the role of AI in enhancing MIMO transmission techniques, covering topics such as beamforming with imperfect CSI, antenna muting strategies for power conservation, user pairing optimization, and pilot assignment for distributed MIMO systems. Each contribution underscores the application of AI to address specific challenges in MIMO transmission, showcasing the potential for improved network performance through intelligent algorithm design and implementation.

6.3.1 Beamforming with imperfect CSI

Problem statement: This work focuses on beamforming for downlink MU-MIMO transmission. MU-MIMO can significantly improve capacity in high-load scenarios but suffers from performance degradation when the channel state information is not perfectly known in the transmitter. Such imperfections could be caused by

channel aging, noise and compression artifacts from CSI Type II reporting schemes and others, as well as combinations of these.

To reduce these detrimental effects, it is possible to train an ML model to compute precoders for a set of users given the estimated channels and the corresponding uncertainties.

Methodology: The model is trained offline in a simulator, which means that it has access to the true channels. During training the ML model is trained by gradient ascent to maximize certain performance objective. Due to its simplicity, spectral efficiency was chosen as maximization objective.

Let $s_k \in \mathbb{C}^K$ be the transmitted symbols in the downlink. The received signal for user k can be expressed as

$$y_k = H_k W_k s_k + \sum_{i=1, i\neq k}^{N_{user}} H_k W_i s_i + n_k, \quad \textbf{(6-2)}$$

where $W_k \in \mathbb{C}^{N_{tx} \times N_{rx}}$ is the precoding matrix for user k, $H_k \in \mathbb{C}^{N_{rx} \times N_{tx}}$ is the *true* downlink channel matrix for user k, and $n_k \sim \mathbb{CN}(0, \sigma_k^2) \in \mathbb{C}^{N_{rx} \times 1}$ is additive white gaussian noise for user k with noise variance σ_k^2. Furthermore, N_{user} is the number of users, N_{tx} is the number of transmit antennas at the base station and N_{rx} is the number of receive antennas at the UE. Precoders are assumed to be normalized to unit power per user, i.e., $W_k W_k^H = 1$ and N_{rx} is assumed to be equal to 1.

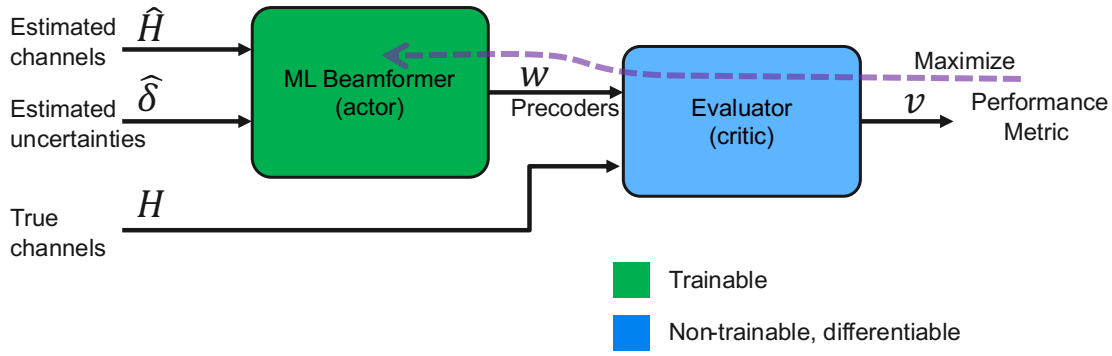

Figure 6-11: Block diagram for training of the proposed solution. Estimated channels ($\hat{H}$) together with estimates of various CSI imperfections ($\hat{\delta}$) are fed to an ML beamformer that outputs precoders (W).

In the proposed method (see Figure 6-11), a trainable block (ML Beamformer) calculates precoders ($\widehat{W}$) based on imperfect CSI (estimated channels, $\widehat{H}$) and associated uncertainties (estimated uncertainties, $\hat{\delta}$). Training is done using gradient ascent through a differentiable critic (Evaluator) to maximize a given performance metric (v). With this solution the performance metric needs to be a known and differentiable function of the selected precoders (W) and the true channels (H).

Results: The approach has been evaluated for varying levels of channel aging and downlink SNR, and the results are shown in Figure 6-12. The UE speed is fixed to 10 m/s and the channel estimate delay is swept from 0 to 4 ms. Here the channel estimate delay is defined as the delay from SRS transmission (uplink) to payload transmission (downlink).

Except from the aging, channel estimates are ideal, i.e., there is no noise, hardware impairments or any other type of imperfections in the channel estimates. Performance obtained with the baseline signal to leakage and noise ratio (SLNR) precoder (dotted lines in Figure 6-12) are compared with the performance achieved using the ML beamformer (solid lines) in terms of spectral efficiency. It can be observed that when there is no channel aging (i.e., when the channel estimate delay is zero resulting in perfect channel estimates) the performance for the SLNR precoder and the ML approach are identical. As the amount of channel aging increases, the spectral efficiency decreases for both the ML and the SLNR solutions, but the performance of the SLNR solution drops off quicker resulting in a significant performance gap for high SNR when the channel aging exceeds ~2 ms. This performance improvement by the ML beamformer is due to its ability to form beams that are more robust to channel aging, for example by creating wider nulls for interfered UEs. It should be

noted that this gain is not due to any form of channel prediction since the ML beamformer does not have access to historical channel estimates or similar that would be required for such predictions. Hence, a full solution would benefit from both a prediction function that aims to predict future channel realisations, and where these predictions are fed to an ML beamformer together with associated uncertainty estimates that can help the ML beamformer to form robust beams when needed.

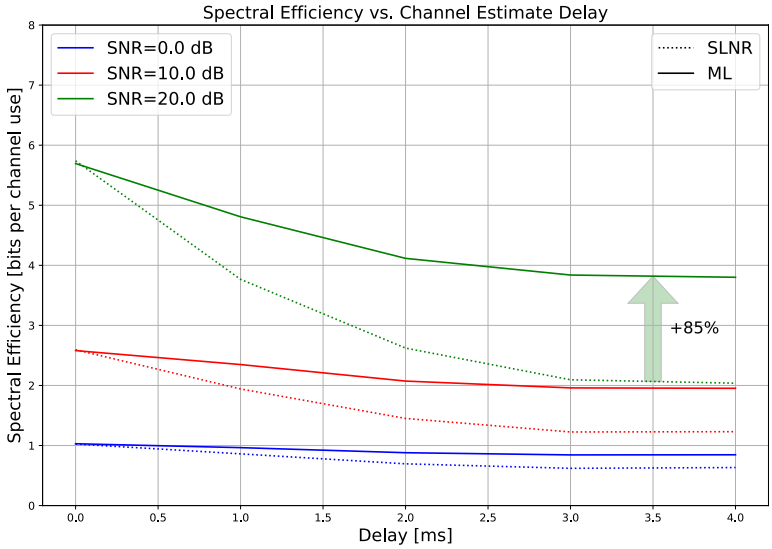

Figure 6-12: Spectral efficiency comparison between the SLNR and ML beamformers. The ML beamformer shows improved robustness to channel aging and significantly outperforms the SLNR solution when the SNR is high.

It should be noted that in Figure 6-12 no generalization over the channel estimate age was done. Instead, different models have been trained for the different channel estimate delays. In a practical solution a generalized model would be required. Further details can be found in the Appendix A.4.5.

6.3.2 Antenna muting

Problem statement: In this contribution, a transmit antenna muting (TAM) problem is formulated in the downlink (DL) transmission of a MU-MIMO setting. The TAM problem allows to reduce a base station's power consumption (PC) by efficiently utilizing only a subset of antennas available at the BS (see Figure 6-13). To this extent, an optimization problem is formulated to minimize the number of active antennas at the BS, subject to per-user equipment (UE) throughput requirements. Prior to presenting the optimization problem, the system model and relevant assumptions are described here.

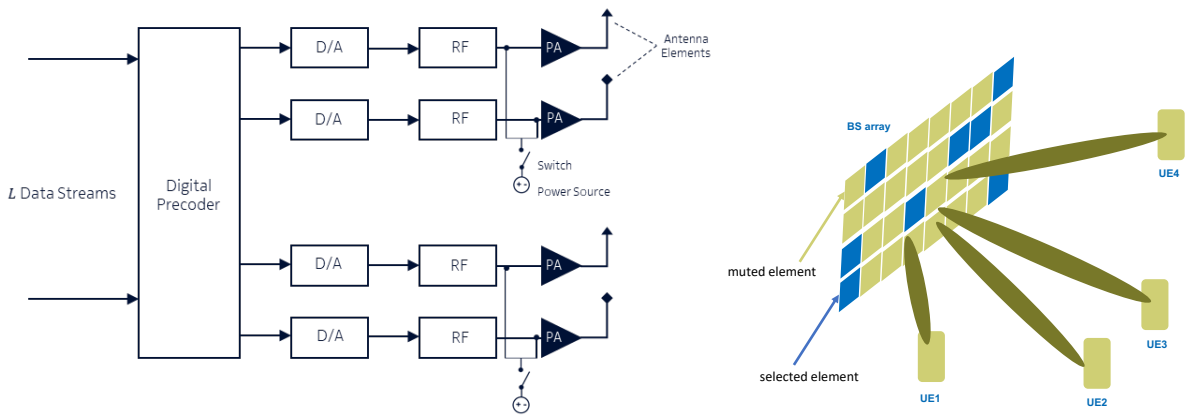

Figure 6-13: (a) Fully Digital Antenna Array (b) TAM Conceptual Diagram.

Antenna panel assumptions: In the BS's antenna panel, it is assumed that each antenna element (AE) is co-located with its cross-polarized counterpart, thus demonstrating spatial correlation. The BS's cross-polarized AEs are arranged into M_{col} vertical columns and M_{row} horizontal rows such that $M = 2 \times M_{col} \times M_{row}$. Each AE is assumed to be driven by an RF chain and the co-located AEs are controlled by a single switch (refer to the Figure 7-18(a)). Therefore, for a given set of antenna indices $\mathcal{M}_{pol} := \left\{1, \dots, \frac{M}{2}\right\}$, let $H_{k,\mathcal{A}} := \boldsymbol{H}_k \boldsymbol{A}_{\mathcal{A}}, \boldsymbol{H}_{k,\mathcal{A}} \in \mathbb{C}^{K \times M}$ be the channel matrix of UE k, where $\mathcal{A} \subseteq \mathcal{M}_{pol}$ is the active antenna element subset. Furthermore, $A_{\mathcal{A}} := diag([\boldsymbol{a}_{\mathcal{A}}^T, \boldsymbol{a}_{\mathcal{A}}^T])$ is the diagonal antenna activation matrix with BS antenna activation vector $\boldsymbol{a}_{\mathcal{A}} := \left[a_1, \dots a_{\frac{M}{2}}\right]^T \in \{0,1\}^{\frac{M}{2} \times 1}$ and the binary antenna element activation indicator is defined by:

$$a_i := \begin{cases} 1, i \in \mathcal{A} \\ 0, i \notin \mathcal{A} \end{cases} \quad \textbf{(6-3)}$$

for a given transmitter matrix $\boldsymbol{W}_{k,\mathcal{A}}$ and the channel matrix $\boldsymbol{H}_{k,\mathcal{A}}$, the error covariance matrices, per-UE SINR γ_k and subsequently the per-UE rate, $r_k\left(\boldsymbol{H}_{k,\mathcal{A}}, \boldsymbol{W}_{k,\mathcal{A}}\right)$ can be computed using the analytical expressions provided in Section II of [RMW+23].

TAM optimization problem: The TAM problem of minimizing the number of active antenna elements subject to per-UE rate constraints capturing the QoS guarantees can be formally written as:

$$\begin{aligned} &minimize_{a_i \in \{0,1\}} \ \left|\left|\boldsymbol{a}_{\mathcal{A}}\right|\right|_0 \\ &subject\ to \quad r_k\left(\boldsymbol{H}_{k,\mathcal{A}}, \boldsymbol{W}_{k,\mathcal{A}}\right) \geq r_{min}, \forall k, \\ &\qquad\qquad \left|\left|\boldsymbol{a}_{\mathcal{A}}\right|\right|_0 \leq M - M_{min}, \end{aligned} \quad \textbf{(6-4)}$$

$r_k\left(\boldsymbol{H}_{k,\mathcal{A}}, \boldsymbol{W}_{k,\mathcal{A}}\right)$ is the per-UE rate, r_{min} is a predetermined value indicating the minimum allowed per-UE rate to guarantee the QoS requirements and M_{min} is the minimum number of active antennas (per-polarization) in the BS which is also a predetermined value. The above formulation is targeted to primarily satisfy UEs' QoS requirements while implicitly and opportunistically reducing the PC by selecting only a subset of antennas at the BS.

Methodology: the above optimization problem (henceforth referred to as **P1**) is a constrained cardinality optimization (CCO) problem and non-convex in nature. On top of being non-convex, CCO problems in general also happen to be combinatorial in nature (NP-hard in this case) w.r.t the optimization variables. For instance, the processing runtime scales exponentially as the number of antennas increase at the BS in **P1**. To overcome the computational complexity issues posed by hand-tuned heuristic algorithms, which are typically used for solving CCO problems resembling **P1,** this work follows a data-driven approach. More specifically, a neural antenna muting (NAM) approach is proposed, where a feed-forward neural network architecture comprising of a single CNN layer followed by 2 dense layers is trained offline to solve the optimization problem in **P1**. Training is performed following the supervised learning approach, where the training inputs are given by $\boldsymbol{X}_k = [Re\left(\boldsymbol{W}_{k,pol}\right), Im\left(\boldsymbol{W}_{k,pol}\right), Re\left(\boldsymbol{H}_{k,pol}\right), Im(\boldsymbol{H}_{k,pol})]$ and the corresponding labels are given by one-hot vectors $\boldsymbol{y} = \boldsymbol{1}_y \in \mathbb{R}^N$. Here, $\boldsymbol{1}_y$ denotes an N-dimensional vector where the y^{th} element is one and zero otherwise, with N being the number of array configuration classes (considered to be in [RMW+23]).

The proposed NAM approach is compared with greedy heuristics as described in Section V of [RMW+23]. The proposed approach is evaluated w.r.t the spectral efficiency (SE) and power consumption, where SE is defined in terms of UEs' throughput and the expression for PC is modelled after the radio frequency (RF) frontend power model provided in [HWW+18]:

$$\tilde{P}_{tot} := \sum_{n=1}^{N_{RF}} (\tilde{P}_n^{PA} + \ + \tilde{P}_n^{LNA} + \tilde{P}_n^{TXconv} + \tilde{P}_n^{RXconv}) \quad \textbf{(6-5)}$$

Where, $\tilde{P}_n^{PA}$ and $\tilde{P}_n^{LNA}$ denote the PC of power amplifier (PA) associated with n^{th} ($n \in \mathcal{N}_{RF}$) RF chain and low-noise amplifier (LNA) respectively. Similarly, $\tilde{P}_n^{TXconv}$ and $\tilde{P}_n^{RXconv}$ denote the conversion unit PC of the n^{th} RF chain, in the DL and uplink (UL) respectively.

6.3.3 User pairing for MU-MIMO

Problem statement: In modern wireless communication systems, optimizing resource allocation in multi user multiple-input multiple output (MU-MIMO) environments is crucial. A key challenge in MU-MIMO is user pairing and precoding, particularly under the constraint of limited channel state information. Traditional methods relying on full CSI are infeasible due to high overheads in data exchange. This challenge is evident in scenarios like the O-RAN Use Case 22 [ORAN23], where only partial CSI, including channel quality indicator (CQI), precoding matrix indicator (PMI), and buffer status, is available.

This study aims to design a machine learning algorithm to efficiently select UEs for co-scheduling in MU-MIMO using only partial CSI.

Methodology: The focus is on leveraging reinforcement learning (RL), specifically the deep Q-network (DQN) algorithm [MKS+13], to address the challenges posed by limited channel information. The proposed algorithm aims to optimize the pairing and scheduling of UEs in a way that maximizes network efficiency and data throughput.

The methodology involves modelling the MU-MIMO optimization problem as a Markov decision process (MDP), where states represent the environment's status (described in terms of users' CQI, PMI and buffer status), actions are the selection of UEs for scheduling, and rewards reflect the efficiency of data transmission. The DQN algorithm exploits a deep neural network, shown in Figure 6-14, which takes in input the current state and provides as output the value of the possible actions, and it iteratively learns the action-state value function Q using the Bellman equation [JKH+19], thus guiding the agent (base station) to make optimal scheduling decisions.

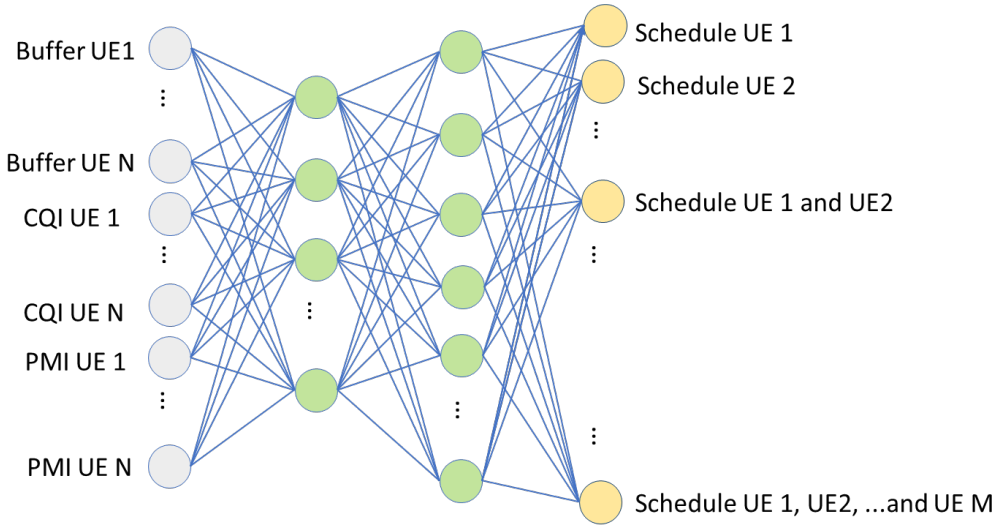

Figure 6-14: Neural Network model defined for DQN application to MU-MIMO pairing.

A simulated MU-MIMO environment is used for training and testing the DQN model. The simulation includes factors like path loss, fast fading channels, spatial correlation, and a predefined set of UEs with data buffers. The DQN model is compared with traditional round robin (RR) scheduling and a greedy genie (GG) algorithm that uses full CSI for decision-making, as further explained in the Appendix (see Section A.4.6).

Results: As shown in Table 6-2, the DQN algorithm significantly outperformed the RR method and closely matched the performance of the GG approach, which is considered an upper bound due to its access to full CSI. Specifically, the DQN solution was approximately 38% faster than RR in emptying UE buffers and only marginally slower than GG. Additionally, DQN achieved higher user and cell data rates compared to RR and

nearly matched those of GG. This improvement in efficiency is attributed to the intelligent pairing and scheduling of UEs by the DQN algorithm, even with limited CSI.

It should be noted that the current study has some limitations, including the idealized simulation environment and the potential for further optimization of the network in more complex scenarios. Future work is suggested to involve more advanced deep reinforcement learning techniques and comprehensive evaluations in realistic channel conditions. Still, results indicate that DQN, with its ability to make efficient decisions with limited information, is a promising approach for optimizing MU-MIMO in practical wireless networks. Further results are available in the Appendix (Section A.4.6).

Table 6-2: Summary of simulation results of DQN application to MU-MIMO pairing.

	Round Robin	DQN	Greedy Genie	DQN vs RR	DQN vs GG
Average # of steps to empty all buffers	29,38	19,105	18	38,7%	-8,3%
Average user data rate [Mbps]	6,64	15,21	18,47	129%	-17,6%
Average cell data rate [Mbps]	20,2	36,4	38,7	81,7%	-5,9%
Corresponding Spectral Efficiency [bps/Hz]	2,02	3,64	3,87	81,7%	-5,9%

6.3.4 Pilot assignment for D-MIMO

Problem statement: Channel estimation is a critical component in distributed MIMO (D-MIMO), as well as in almost every other communication technique. An estimated channel with high precision and minimal overloading may assist in the development of beamformers and precoders, as well as in localization and positioning. To estimate the channel, the UE send the pilot sequences to the AP, so that the pilot assignment becomes the crucial steps for estimating channel.

In this work, the channel estimation phase is investigated in a model of a large-scale D-MIMO system, where the number of UE, M, and APs, K, could reach a significant amount. On behalf of the channel reciprocity characteristic of the time division duplex (TDD), the uplink and downlink channels can be regarded as identical. The UE and AP that are generated at random with the uniform distribution and spread over a large area in this work, and each AP is connected to a CPU via an error-free backhaul link. Due to applying mmWave channel, the blocker problem exists, and severe channel strength degradation occurs along the distance between the AP and UE, thus a considerable number of channels in D-MIMO can be ignored for each UE and AP. This work proposes a method for representing the pilot assignment as a colouring problem in a sparse graph, which is an NP-completed problem, and graph neural network (GNN) assisted reinforcement learning method will be used to solve the represented colouring problem. The graph representation method can be applied to nearly all D-MIMO systems, as its rules and objective function can be tailored to the communication problems at hand.

Methodology: The work is divided into three stages: a) graphical representation; b) resolution of the corresponding graph problem; and c) communication performance evaluation of the result.

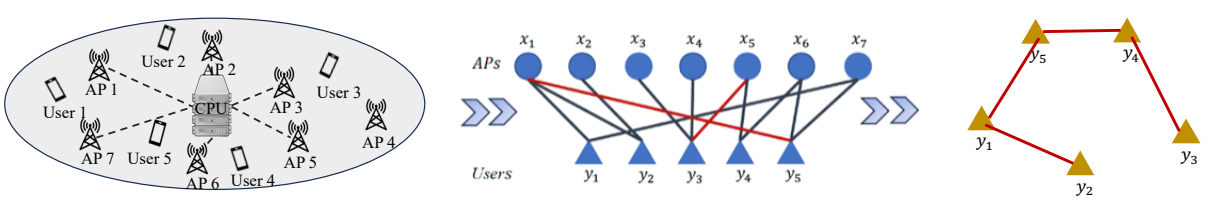

(a) D-MIMO system **(b) bipartite graph** **(c) conflict graph**

Figure 6-15: From D-MIMO system model to graph representation.

Before proceeding into the details of the scheduling strategy, it is possible to represent the connection structure of the D-MIMO system as a bipartite graph, as shown in Figure 6-15. Initially, a D-MIMO system (Figure 6-15 (a)) is converted into a bipartite graph (Figure 6-15 (b)), with the nodes at the bottom representing the UE and the upper nodes representing the AP. If an edge connects two nodes, $x_m \in [M]$, $y_k \in [K]$, it indicates that the channel strength g_{mk} is greater than the threshold that is implemented. A bipartite graph can effectively illustrate the connection structures of D-MIMO. The purpose of this communication problem is to solve a pilot assignment problem considering the interference between the UEs. Therefore, the bipartite graph is utilized to generate the conflict graph as Figure 6-15 (c) according to the rules:

1. Each UE represents the node in the conflict graph.
2. Only the interference channel that cannot be disregarded is considered.
3. The edge in the conflict graph should be connected, if and only if two UEs have overlapped connection in one AP.

The conflict graph has effectively transformed the interference information. Figure 6-15 (c) is the conflict graph representation that corresponds to Figure 6-15 (b). Evidently, this enables the development of a visible scheduling strategy, as no two adjacency nodes may designate the identical assigned sequence. The graph colouring rule is identical to such a schedule rule [BM82]. In this work, the UE scheduling uses a rapid AI-based graph colouring method [SYH+23]. This method is applicable to dynamic scenarios with moderately fast and can also be used to coordinate parallel UE scheduling strategies across multiple clusters. The learn-to-code on graph (LCG) colouring method is illustrated in the Appendix in Section A.4.7. Consequently, the edges ought to be assigned orthogonal pilot sequences. Such a rule corresponds to the graph colouring problem. Then, based on the bipartite graph, a conflict graph can be generated to display interference information between UEs. Following the resolution in this part, the coloured graph result should be transferred to the specified pilot assignment strategy. In the simulation section, the desired channel is estimated using the pilot assignment strategy and evaluate the uplink user rate as the metric.

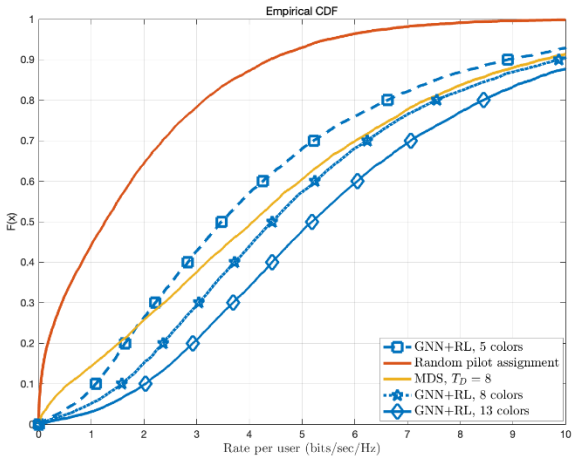

Figure 6-16: Cumulative Distribution Function plot of user's rate.

Results: With respect to the D-MIMO model, the mmWave frequency band, 28 GHz is adopted, the bandwidth is 100 MHz, a 1 km×1 km region is generated utilizing 100 UEs and 200 APs each with a single antenna. As robust connections, the greatest N=8 APs are chosen by each user, and the number of pilot dimension $T_D = 8$. With respect to the training of LCG, the Erdős–Rényi (ER) random graph is utilized as the data set. This work utilizes a random dataset consisting of four colours (T=7,8,13,14). The number of colours is denoted by T, which is also the number of pilot dimensions in training phase. In order to facilitate comparisons with alternative methodologies, both random assignment and a previously proposed pilot assignment method are considered; the latter is a maximum distance separable (MDS)-code based pilot sequence presented in [YGY+23]. The simulation result is illustrated in Figure 6-16. Evidently, the LCG-based colouring method exhibits superior performance to the MDS method, even when applied to the same pilot dimension. This is due to the fact that the LCG-based colouring technique employs the orthogonal pilot sequence in UEs, whereas the MDS-based method generates non-orthogonal pilot sequences. It should be noted that the number of pilot

dimensions also should be selected properly as shown in the plot with 5 colours in Figure 6-16. Because a small pilot dimension incurs considerable interference that cannot be mitigated.

6.3.5 Access point selection and uplink power control for D-MIMO

Problem statement: distributed massive MIMO, or cell-free MIMO allows serving a set of users in a given area using same time-frequency resources via a set of distributed access points which are connected to a CPU, without traditional cells or cell-boundaries. These architectures provide more uniform service performance for the users in terms of spectral efficiency and improve connection robustness due to the additional spatial diversity. Proper resource allocation such as power control, fronthaul link management etc. can further improve the network performance, however, the traditional optimisation techniques could be practically infeasible due to their computational complexity and lack of flexibility. Machine learning techniques can be exploited to solve these resource allocation problems in a data-driven way with a reduced complexity, instead of using optimisation-based solutions.

In [RMR+21], unsupervised learning-based uplink power control is proposed to maximise the minimum user rate in a cell-free network. It is extended in [RMR+23] to learn the joint uplink power control and fronthaul capacity allocation by directly training a deep neural network to maximise the sum rate objective. Although they have shown similar or better performance compared to the conventional optimisation-based solutions and a significantly lower computational complexity, both studies considered a full cell-free architecture where all the users are served by all the access points in the network which is not scalable in practice. In this work, an AP selection approach is proposed to enable scalable D-MIMO implementation where each user is served by only a fraction of the APs in the network. Uplink power control is also utilised to further improve the sum rate performance.

Methodology: A D-MIMO system which consists of M single-antenna APs and K single-antenna users randomly distributed in a $D \times D$ geographic area is considered. The APs are connected to a CPU via backhaul connections. Each user is connected to a set of APs $\mathcal{M}_k$, where $\mathcal{M}_k \subset \mathcal{M}$ where $\mathcal{M} = \{1,2,\dots,M\}$ is the full set of APs in the network. Initially, all the users undergo a pilot transmission phase to estimate the uplink channel coefficients. The minimum mean square error (MMSE) channel estimation is done at each AP after the pilot transmission. Then, during the uplink data transmission phase, all the users simultaneously send their transmit signals to all the APs. Match filtering is done at each AP using the estimated channels, and the scaled received signals are sent to the CPU for joint detection. The aggregated received signal at the CPU is used to detect the transmit signals. The uplink rate for the kth user, R_k^{uplink}, can be derived using the channel statistics, which is a function of user power allocations η_k and the serving AP set $\mathcal{M}_k, k = 1,2,\dots,K$. The following sum rate maximisation problem is then formed to select the best set of APs to serve each user and to determine the user power levels to maximise the system sum rate subject to the throughput constraints for the minimum user rates.

$$\begin{aligned} \text{P1:} \max_{\eta_k, \mathcal{M}_k} \quad & \sum_{k=1}^{K} R_k^{uplink} \\ \text{subject to} \quad & R_{min} \leq R_k^{uplink}, \ k = 1,2,\dots K, \\ & |\mathcal{M}_k| \leq a\,|\mathcal{M}|, \ k = 1,2,\dots K, \text{ with } 0 < a \leq 1 \text{ a fixed design parameter.} \\ & 0 \leq \eta_k \leq 1, \ k = 1,2,\dots K. \end{aligned} \tag{6-6}$$

Problem P1 is a non-convex multi variable optimisation problem which needs convex approximations and iterative algorithms to obtain solutions. To overcome this challenge, an ML model is trained to predict the outputs without directly solving the sum rate optimisation problem. Specifically, a DNN which takes in large-scale channel coefficients between the users and the APs is trained to learn the AP selection and power control outputs by taking the negative Lagrangian of the optimisation problem as the loss function. It is assumed that the large-scale channel statistics are available, and that the control signalling and other required D-MIMO architectural components are in place, providing centralised processing and ideal synchronisation between APs.

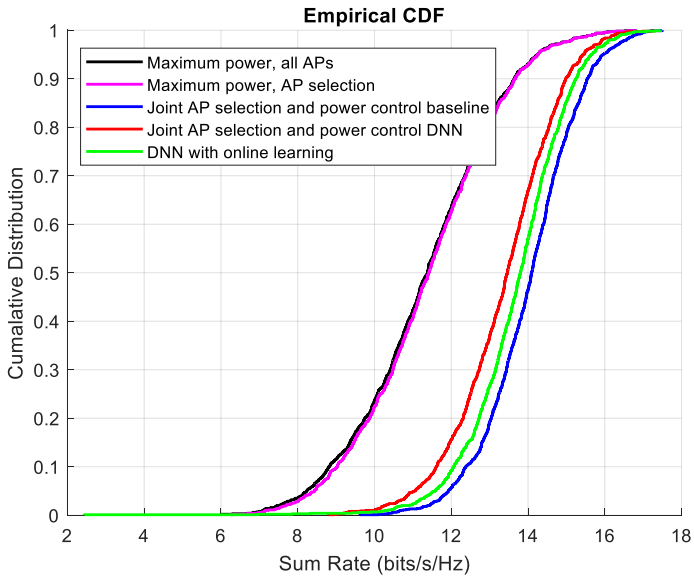

Figure 6-17: Sum rate performance with AP selection and power control for a cell-free network with 50 APs and 10 users.

Results: Some initial results for a system configuration of 50 APs and 10 users are shown in Figure 6-17, where the sum rate performance is evaluated for different algorithms including the DNN for AP selection and power control. For the AP selection procedure, the parameter is set to $a = 0.4$, so that each user is served by 40% of the APs in the network. Further improvements to the DNN model architecture, hyperparameter tuning and dual variable optimisation are ongoing, especially to optimise the dual variables or Lagrangian parameters in the loss function to enable improved model convergence.

6.4 AI solutions for hardware impairments

Hardware impairments, particularly in the power amplifier, can significantly affect the performance of wireless communication systems. This section explores an AI-driven approach to compensate for such non-linearities, offering insights into how artificial neural networks can be deployed to improve transmission quality by mitigating hardware-induced distortions. Highlighting the adaptability and effectiveness of AI in addressing physical layer challenges, the contributions illustrate the growing importance of artificial intelligence in overcoming inherent limitations of wireless hardware components.

6.4.1 AI-based PA-nonlinearity compensation

Problem statement: Non-linearity of wireless transceivers, specifically power amplifier (PA) hardware imperfections, introduces in-band and out-of-band distortion. These distortions could pose major limitations towards having high throughput, and cost and energy efficient wireless communication systems. Such limitations from PA are typically compensated in the transmitter, e.g., by applying power back-off or performing digital predistortion (DPD) aiming to linearize the transmitter. However, applying PA power back-off leads to lower energy efficiency, and lower output power, and hence lower coverage; and performing DPD results in higher complexity of the transmitters.

To this end, a receiver technique using artificial neural networks (ANN) de-mapper was proposed in [FHS23] to compensate for the PA non-linearity in the receiver side, when DFT-s-OFDM (Discrete Fourier Transform – spread-OFDM) signal transmission was considered, with performance evaluations performed in FR1, in the presence of memoryless PA for a single antenna setup. This work extends the work in [FHS23] to FR2, in the presence of memory PA, and for multi-antenna setting.

Methodology: This study proposes an AI-driven receiver for PA post distortion compensation. The proposed method uses an ANN de-mapper to compensate for the PA memory impacts in the receiver side, when DFT-s-OFDM signal transmission is considered. The receiver performs channel estimation using reference signals and conducts equalization using the estimated channel state information. The proposed ANN de-mapper performs per

resource element soft bit de-mapping of received signal before channel decoder. The block diagram of such an AI-driven receiver is shown in Figure 6-18.

Figure 6-18: AI-empowered receiver for PA compensation.

ANN de-mapper is a fully connected neural network (FCNN) where the inputs are real and imaginary part of the equalized received symbol and the SNR estimates in the receiver. The outputs are log likelihood ratio values corresponding to the transmitted coded bits.

Results: A fixed throughput scenario is considered; in this case, given that the system is not power limited, the UE operates at an as efficient operating point as possible in the network to reach a given throughput level. The intention is to investigate with a new standard specification how energy efficient the UE can operate leveraging on this new feature.

In this scenario, the gain in energy efficiency is dependent on the power efficiency profile of the PA and the operated throughput level. For the considered class A PA model, as shown in Figure 6-19, energy reduction gains in the range of 35%-45% are observed at throughput levels in the range of 1.6-2.0 Gbps. In this figure, the x-axis shows the fixed/assumed throughput, and the y-axis show the relative energy consumption needed to reach the assumed throughput for the legacy receiver (no ML) and the AI-driven receiver subject to different PA back-off levels.

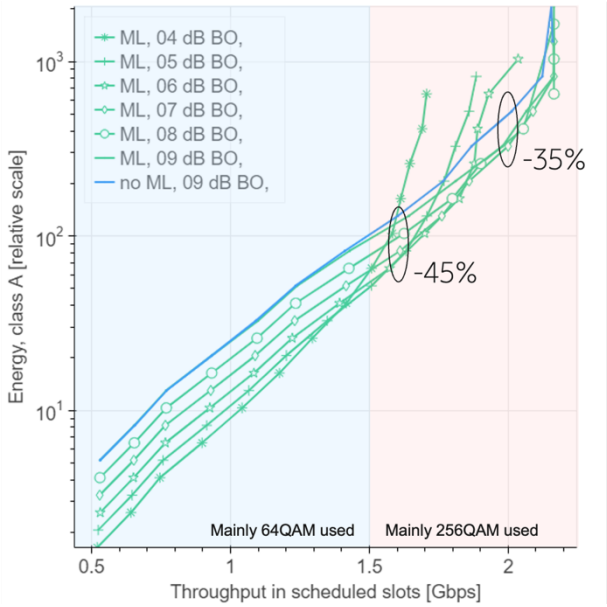

Figure 6-19: Energy efficiency versus throughput performance for different operating points.

The AI-driven receiver for PA post distortion feature has been evaluated in an UL FR2 scenario using up to 256QAM modulation and 400 MHz allocation to trigger memory effects from the PA model. The findings are as follows: throughput can be improved, up to ~15%, both with and without standard changes in both non-power limited and power limited scenarios; UE energy efficiency can be improved 11-45% when transmitting with higher order modulations; Coverage throughput for higher order modulations can be improved 2-3 dB. It should be noted that these evaluations are carried out without UE PA model known to be representative of current UEs, and conclusions will be impacted by the UE implementation.

7 Joint communications and sensing

In recent years, there has been an unprecedented surge in the demand for precise sensing and localization services, driven by the emergence of innovative use cases and applications. From the advent of self-driving cars and unmanned aerial vehicles to the intricacies of controlling indoor robotics, virtual and augmented reality environments, and the development of digital twins, diverse sectors are now reliant on sensing services. Each application presents its own distinct criteria for sensing and localization accuracy, availability, and reliability. Responding to this burgeoning need, the International Telecommunications Union (ITU) has identified joint communication and sensing (JCAS), also referred to as integrated sensing and communications (ISAC), as a cornerstone of the upcoming 6th generation (6G) of cellular communications. The pursuit of 6G JCAS entails a multifaceted exploration within the research community. This involves delving into various deployment scenarios and their corresponding sensing and localization performance, while also devising optimization strategies to fulfil both the sensing and communication requirements. This section presents the preliminary results of exploring these two paths. Hence, the section is divided into two parts, JCAS deployments and JCAS resource optimization. The works included herein encompass a wide range of assumptions regarding the employed 6G radio. These assumptions encompass a spectrum of factors, ranging from hardware impairments to the availability of diverse radio resources. They also account for different deployment scenarios, such as the quantity and capabilities of both user equipment and base stations. By considering these multifaceted aspects, researchers aim to construct a comprehensive understanding of the challenges and opportunities inherent in the integration of sensing and communication technologies within the framework of 6G JCAS.

7.1 JCAS deployments

In this subsection, three sensing and localization deployment scenarios are investigated. Namely, the section investigates non-terrestrial networks (NTN) and reconfigurable intelligent surfaces (RIS)-aided localization, integrated monostatic and bistatic sensing, and multistatic sensing.

7.1.1 NTN and RIS-aided localization

Problem statement: The goal is to optimize the estimation of the 3D position, velocity, and orientation of a single user equipment (UE) in an outdoor environment (urban and sub-urban). Optimization in this context means minimizing both the Crámer-Rao bound (CRB) and the actual variance of the estimated states as well as increasing the availability of the positioning solution. The positioning setup incorporates a single base station (BS), a low-earth orbit (LEO) satellite, and a RIS. The study utilizes downlink (DL) orthogonal frequency division multiplexing (OFDM)-based positioning reference signals (PRS) at both FR1 (2 GHz) and FR3 (10 GHz). The available bandwidth for FR1 and FR3 is100 MHz (30 KHz sub-spacing) and 400 MHz (120 kHz sub-spacing), respectively. The terrestrial BS has access to a uniform rectangular array (URA) while the satellite has access to a directive dish antenna. The UE, on the other hand, has two setups, one of which has access to a single omnidirectional antenna, while the other has access to an URA. In the first case, UE orientation is not estimated. As the setup utilizes DL signals, localization takes place at the UE side. Hence, the UE is expected to conduct channel estimation from raw I/Q samples. Here, channel estimation includes the estimation of the delays, Doppler shifts, and complex channel gains for each path. Ultimately, the UE has access to four line-of-sight (LoS) time of arrival (TOA) measurements from the direct terrestrial network (TN) and NTN paths and the TN-RIS and NTN-RIS paths, two angle of departure (AOD) measurements from the RIS (vertical and horizontal) paths, two angle of arrival (AOA) measurements (in case of 2D array at UE side), as well as three Doppler measurements from each technology. In this study, three problems are considered, a long-term deployment optimization problem, a short-term resource optimization problem, and a positioning estimation problem. The long-term optimization of the setup includes optimizing the placement of the BS and RIS and the orbit of the LEO satellite. On the other hand, short term optimization includes precoding, resource allocation, and RIS configurations. Finally, the estimation problem includes optimizing localization algorithms and methodologies to fuse the measurements provided by the setup. Here, both the snapshot estimation problem (i.e., the states are not dynamic) and the tracking problem are considered. This work considers the following assumptions: LEO altitude is 600 km; RIS is controlled by the network; BS and LEO are time synchronized; UE has time bias and carrier frequency offset (CFO) (to be estimated); LoS between UE and

the BS, LEO, and RIS; LoS paths are resolvable (due to the high bandwidth); constrained LEO-UE link budget and atmospheric effects (effects of scintillation, gases, and clouds); and the UE is installed in an autonomous vehicle (vehicular motion models, 100 km/h max speed).

Methodology: As the problem is complex, a simplified scenario is considered first and then complexities will be added at later stages to achieve the scenario highlighted above. In this report, the focus is directed to an NTN-RIS scenario only with a static UE that has access to a single antenna element. Here, the goal is to estimate the position of the UE only (i.e., velocity and orientation are not estimated). Additionally, it is assumed that the UE receives two paths only (i.e., NTN-UE and NTN-RIS-UE paths with multipath components resolved and discarded). A raytracing-based channel model was derived for each path and was then used to compute the channel fisher information matrix (FIM). The channel FIM incorporates information on the four channel gains (real and imaginary components for each path), two delays, two Doppler coefficients, and two RIS AODs. It is worth noting that the derivation assumes random RIS configurations. Next, a transformed FIM was derived for positioning estimates which included the four channel gains, the 3D position of the UE, the time bias, and the CFO. Finally, a maximum likelihood estimator (MLE) was implemented to estimate the delay and the Doppler coefficient for both paths. The MLE utilized a simple iterative linear search algorithm with a dynamic grid size to find the estimates. The next step is to implement a second MLE to estimate the 3D position of the UE given the estimated delays, Dopplers, and the RIS AOD measurements.

Results: A MATLAB-based simulation setup was developed where the position and orientation of the RIS can be chosen in a global coordinate system and the UE is placed in a study grid. Additionally, a simple script was developed to compute the position and velocity of the LEO satellite based on the given angle of ascension, elevation angle, and altitude. Such computation enhances the credibility of the results generated. The deployment information of the UE, RIS, and LEO are then passed to a script that computes the channel and position FIM and CRB as well as the MLE estimates. Finally, the CRB is used as a benchmark to assess the performance of the investigated algorithms. The parameters utilized in these experiments shown in Table 7-1.

Table 7-1: Simulation parameters of RIS and NTN-aided localization scenario.

Parameter	Value	Parameter	Value
Carrier frequency	2 GHz	Sync. bias	~1 ns
Sub-carrier spacing	30 kHz	CFO coefficient	~1 ppm
Bandwidth	100 MHz (3300 SC)	Modulation	QPSK
RIS # elements	100 (10x10)	RIS element spacing	$\lambda/2$
UE noise figure	7 dB	UE noise PSD	-174 dBm
UE gain	1 dB	Satellite gain	30 dB
Atmospheric gasses loss	0.1 dB	LEO EIRP density	34 dBW/MHz
Scintillation loss	2.2 dB	Shadow fading loss	3 dB
UE position (in meters)	$x = 0, y = 5, z = 1.5$	RIS position (in meters)	$x = 0, y = 0, z = 10$
LEO position/velocity	Variable	RIS orientation	Towards y-axis (north)

In this study, the effect of the satellite orbit settings on the various channel parameters are investigated. The elevation angle and the ascension node (AN) (also known as the azimuth angle) of the satellite were swept from 0 to 90 degrees and 0 to 180 degrees, respectively. The effect of these angles on the signal-to-noise-ratio (SNR) for each path is shown in Figure 7-1. The corresponding CRBs of the respective TOA and position estimates are shown in Figure 7-2. It can be seen that the AN does not have any effect on the SNR of the direct NTN-UE path. On the other hand, the SNR increased quadratically as the elevation increased, which can be attributed to the linear decrease in the NTN-UE distance. The NTN-RIS-UE path, however, was affected by both the AN and the elevation angle. To be specific, the SNR reached a maximum around AN = 90 degrees (i.e., when the LEO was directly in front of the RIS) and rapidly decreased as the LEO ascended from angles that are further away from the boresight of the RIS. This decrease in SNR can be attributed to the decrease of the effective area or the radar cross-section of the RIS. Contrary to the previous effects, the effect of the elevation angle on the SNR of the NTN-RIS-UE path is non-monotonic as it affects the SNR in two opposite ways. First, as is the case with the NTN-UE path, the SNR is directly proportional to the elevation angle due to the decrease in NTN-RIS distance. Second, the SNR is inversely proportional to the elevation angle due to the decrease of the effective area of the RIS as the LEO elevates higher in the sky. The effect of the SNR is

directly reflected in the CRB of the TOA estimates of both paths and the positioning estimate. Finally, it is noteworthy to comment on high discrepancy between the average SNR of the NTN-UE and the NTN-RIS-UE paths. It can be seen that, on average, the NTN-RIS-UE path is 35 dB less than the direct NTN-UE counterpart. This is mainly attributed to the well-known double distance effect that RIS suffers from. Hence, it is advised to investigate active RIS elements for such scenarios in future works.

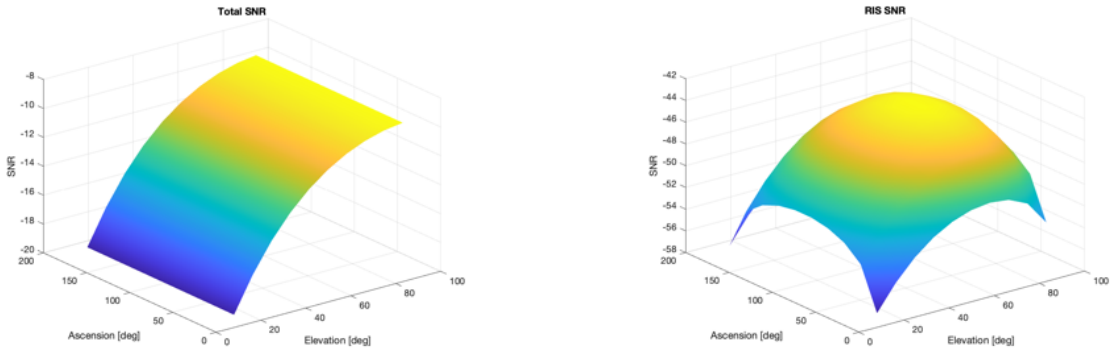

(a) NTN-UE **(b) NTN-RIS-UE**

Figure 7-1: SNR of the NTN-UE and NTN-RIS-UE path.

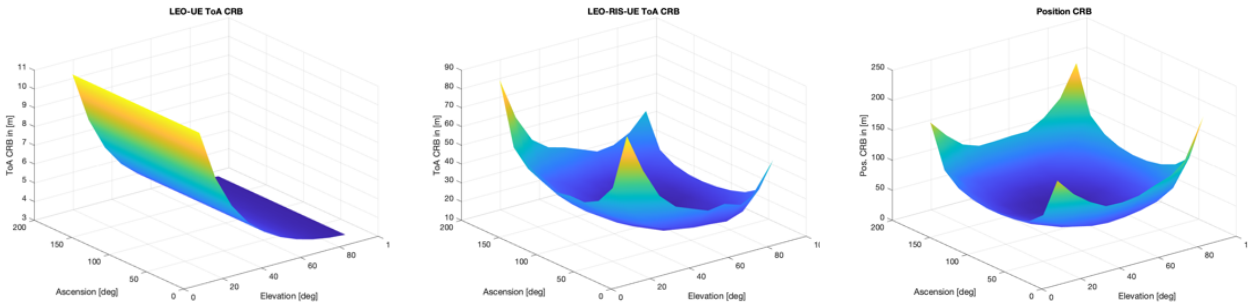

(a) NTN-UE **(b) NTN-RIS-UE** **(c) Position**

Figure 7-2: CRB of TOA of NTN-UE, NTN-RIS-UE, and position.

7.1.2 Integrated monostatic and bistatic sensing

Problem Statement: Two common modalities used in mmWave sensing are monostatic and bistatic sensing, which are usually considered separately. However, the two modalities can be employed simultaneously. The goal of this study is to integrate monostatic and bistatic sensing to improve the sensing performances. In the considered scenario, the BS sends out downlink signals, and those signals can reach the UE via LoS and non-LoS (NLoS) paths. The UE performs the channel estimation to get the AOA, AOD and TOA estimates of the paths, and then performs bistatic sensing to estimate the UE position, heading, clock bias with the BS, and the map of the surrounding environment. The downlink signals can also be bounced by the landmarks in the environment back to the BS. The BS performs channel estimation on the received signals to get the AOA and TOA estimates and perform monostatic sensing to map the surrounding environment. Since both bistatic sensing and monostatic results contain the information on the UE and the map, by integrating these two modalities, information can be shared between them, leading to improved sensing performance. This work considers the following assumptions: a single BS and a single UE; BS position is known; channel estimation is implemented; and only LoS or single-bounce NLoS signals are received.

Methodology: The main components of the block diagram shown in Figure 7-3 include the simultaneous localization and mapping (SLAM) filter at the UE side for bistatic sensing, the mapping filter at the BS side for monostatic sensing, and the periodic fusion at the fusion centre. For bistatic sensing, given the received signals at the UE side and the knowledge of the sent signals and combiner, the channel estimator can recover the geometric information of the multi-path components (MPCs), like the delays, angles of arrival, and angles

of departure, which are a function of the UE state and the map. Then an extended Kalman-Poisson multi-Bernoulli (EK-PMB) SLAM filter is implemented to map the landmarks and also localize the UE. For monostatic sensing, a channel estimator can be applied on the received signals at the BS side to estimate delays and angle of arrivals. Then, a PMB mapping filter is implemented to map the landmarks and also the moving UE. Once these two sensing results are available, they fused together. This can be done by firstly matching two maps, which would tell whether a given landmark should be fused with a corresponding landmark in another map or should it be fused with the background. Then, components in two maps should be fused accordingly.

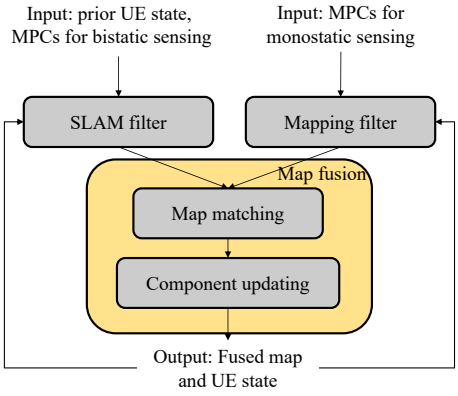

Figure 7-3: The framework of integrated monostatic and bistatic sensing.

Results: The proposed framework is evaluated by simulation. The simulated scenario contains a single BS and a single UE which does a constant turn-rate movement around the BS. There are 4 virtual anchors (VAs) and 4 scatter points (SPs), which represent reflecting surfaces and small objects, respectively. Every time step, the BS sends out downlink signals. The simulation parameters are listed in Table 7-2.

Table 7-2: **Simulation parameters for integrated monostatic and bistatic scenario.**

Parameter	Value	Parameter	Value
Carrier frequency	28 GHz	Reflection coefficient	0.7
Number of symbols	16	Radar cross section	50 m^2
Bandwidth	200 MHz	Range of view	50 m
Number of subcarriers	64	Detection probability	0.9
UE Noise figure	20 dBm	Fusion frequency	Every 5 time step
Transmitter power	35 dBm	Monte Carlo simulations	100

The implementation of the EK-PMB (SLAM) filters can map the VAs and SPs in the environment and position the UE state simultaneously in bistatic sensing and map the incidence points (IPs) in the environment as well as the passive UE in monostatic sensing. The results also indicate that periodic fusion of monostatic and bistatic sensing helps the filters to acquire better mapping and SLAM performances in monostatic and bistatic sensing, respectively, as the generalized optimal sub-pattern assignment (GOSPA) distances in Figure 7-4 and root mean square errors (RMSEs) in Figure 7-5 are lower. The bistatic map introduces the landmark types to the monostatic map, as GOSPA distances for VA and SP in monostatic sensing drops after fusion while they remain unchanged without fusion. The monostatic map also introduces the unseen landmarks to the bistatic map, as the GOSPA distance for SP in bistatic sensing directly drops after the first fusion.

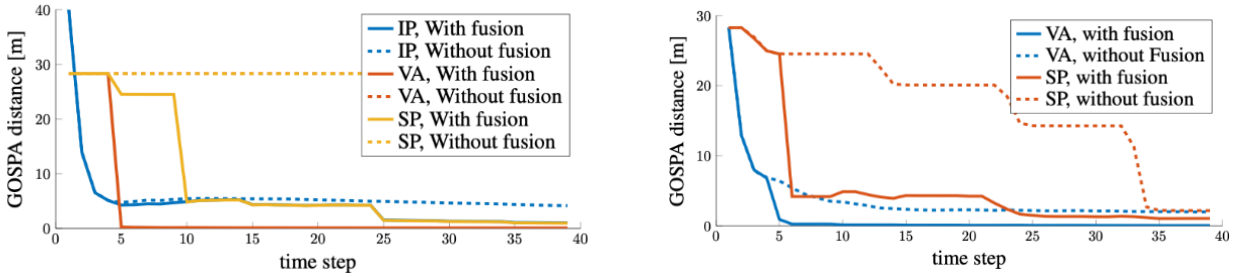

(a) **(b)**

Figure 7-4: Comparison of mapping performance of a) bistatic sensing and b) monostatic sensing for cases with and without periodic sensing.

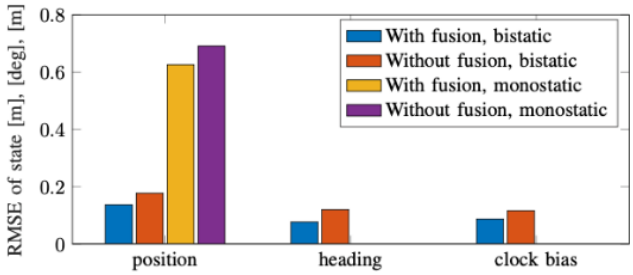

Figure 7-5: Comparison of UE state estimation in bistatic and monostatic sensing between two cases: with and without fusion.

7.1.3 Multistatic sensing

Problem Statement: Section 7.2.1 establishes the rationale behind the use of bistatic sensing when combined with the legacy 5G OFDM-based waveforms as the sensing waveform. Even though such a solution presents itself as a strong candidate for the JCAS functionality in the forthcoming 6G networks, its performance is limited by the fundamental limits of bistatic sensing. A possible way to improve the performance of a sensing procedure in a cellular JCAS network is to leverage the redundancy of the existing nodes. The use of multiple sensing nodes for sensing a space of interest promises performance improvement via diversity. In particular, the sensing of a space from different directions using different nodes is expected to have a better performance. This is because, even though a portion of the undertaken sensing measurements might be of poor quality, with the sophisticated fusion of the separate measurements, the performance can be significantly improved. Thus, in this study, the aim is to explore the performance of multistatic sensing when it is composed by multiple bistatic sensing measurements. This work has the following assumptions: 1) multistatic sensing composed by multiple separate bistatic radar sensing measurements; 2) omni-directional or directional transmission and directional reception; 3) plethora of transmit and receive nodes; 4) possibility of central processing; 5) perfect synchronization between involved nodes; and 6) realistic channel modelling (LoS and NLoS propagation paths).

Methodology: The block diagram of the multistatic sensing considered in this study is given in Figure 7-6. As shown in this figure, a sensing node transmits radar signals which after being reflected by a target of interest are collected by a number of nodes distributed in the surrounding space. Under the assumption that all $\boldsymbol{N_m}$ reception nodes are synchronized with the transmitting node, each reception node undertakes its own bistatic sensing measurement. Note that the receiving nodes do not have to be synchronized to each other. The result of the $\boldsymbol{i}$-th, $\boldsymbol{i = 1, \dots, N_m}$, bistatic radar sensing is then conveyed to the sensing processing unit (SPU). The $\boldsymbol{i}$-th reception node is able to provide the following measurements/estimates, $\boldsymbol{m_i} = \{\boldsymbol{\theta_i}, \boldsymbol{\phi_i}, \mathbf{S_i}, \mathbf{D_t^{(i)}}, \mathbf{D_r^{(i)}}, \mathbf{r_i}\}$, to the SPU. With reference to the implementation of bistatic sensing in Figure 7-8. $\boldsymbol{\theta_i}$ and $\boldsymbol{\phi_i}$ are the estimated vertical and horizontal AOAs, respectively, of the incoming signal, reflect by the target of interest, in the local coordinate system (LCS) of the $\boldsymbol{i}$ −th reception node; $\boldsymbol{S_i}, \boldsymbol{D_t^{(i)}}$, and $\boldsymbol{D_r^{(i)}}$ are the estimated distance of flight between the transmit node-target-receive node, transmit node to target distance, and the target to receive node

distance, respectively; and $\mathbf{r_i}$ is the estimated position of the target in the network global coordinated system (GCS). In the final step, the SPU fuse the $\boldsymbol{N_m}$ separate bistatic sensing in order to measure the quantities of interest. Thus, the estimate of the 3D position of target of interest can be obtained as $\hat{\mathbf{r}} = \boldsymbol{f}(\boldsymbol{m_1}, \ldots, \boldsymbol{m_{N_m}})$, where $\boldsymbol{f}(\cdot, \ldots, \cdot)$ is the used fusion function. In this work, the aim is to explore the performance improvements of the 3D positioning of the multistatic sensing of Figure 7-6, when each separated bistatic sensing is implemented as the bistatic radar sensing described in Figure 7-8. The evaluation of each bistatic sensing is done using either a theoretical analysis or using simulation results.

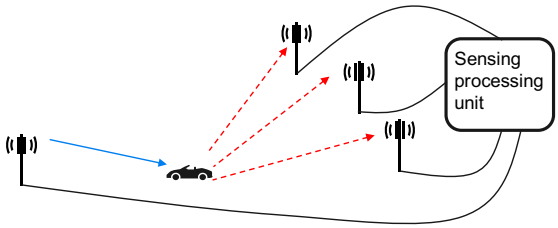

Figure 7-6: Multistatic sensing composed by a number of N_m independent bistatic measurements.

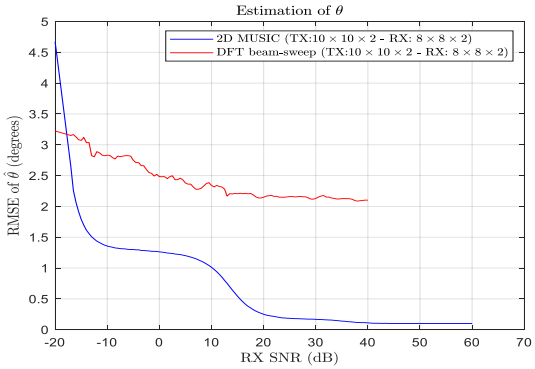

(a) RMSE of the estimate of θ

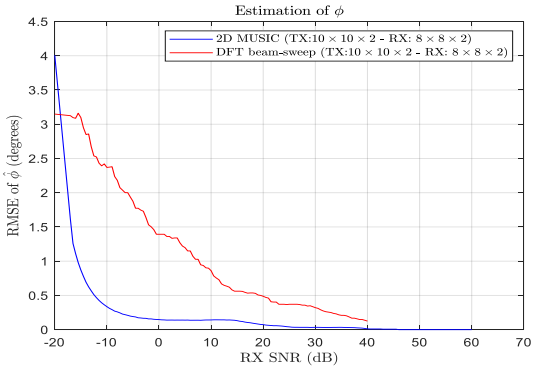

(b) RMSE of the estimate of ϕ

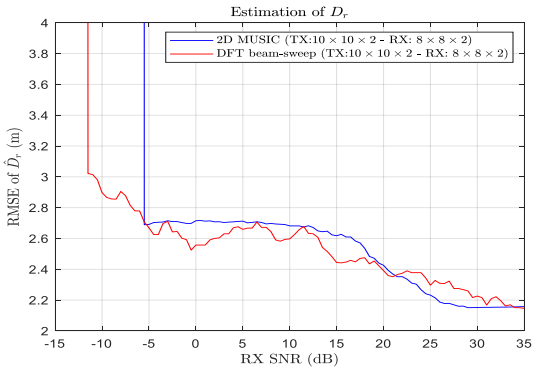

(c) RMSE of the estimate of D_r (RX to target distance)

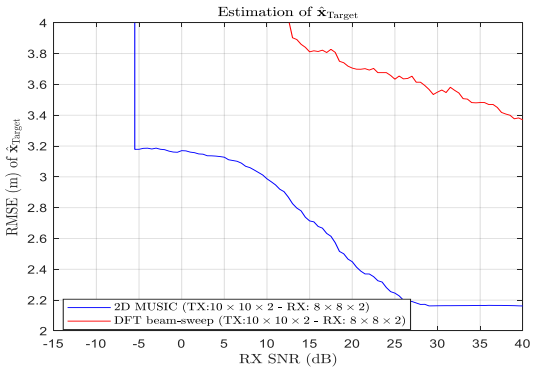

(d) RMSE of the estimate of $\hat{x}_{target}$

Figure 7-7: RMSE performance of a typical underlying bistatic sensing of the type of multistatic sensing considered in this study.

Results: In this study, as the fusion of the N_m independent measurements, $m_i = \{\theta_i, \phi_i, S_i, D_t^{(i)}, D_r^{(i)}, \mathbf{r}_i\}, i = 1, \ldots, N_m$, is done in a non-coherent way in the SPU, one approach for improving the performance of the multistatic radar sensing described before is to improve the performance of the N_m underlying bistatic sensing procedures undertaken separately in each sensing node. For a given deployment and provided sufficient synchronization between the transmitting node and each receiving node, the performance of each bistatic sensing is improved via the use of more sophisticated radar signal processing techniques. This is illustrated in

Figure 7-7 where the performance of a typical bistatic is evaluated, composing radar sensing in terms of ranging, AOA estimation, and 3D positioning. This is done for the cases when the AOA is done using the non-parametric method of DFT beam-sweeping and the parametric method of 2D MUltiple SIgnal Classification (MUSIC). In this figure, the RMSE performance is undertaken using a bistatic deployment where the channel model is based on ray tracing in 3.5 GHz. The transmitting and the receiving nodes are equipped with a dual-polarized 10×10 and 8×8 rectangular antenna panels, respectively. For capturing the optimal possible performance, the antenna panels are oriented, in a genie way, towards the target of interest. Note that the parameterization of MUSIC is set to be correct in a genie way. Finally, the used waveform is OFDM with reference signal generated using a Zadoff–Chu sequences. The observation of Figure 7-7 a) and b) shows that the MUSIC AOA estimated outperform the DFT beam-sweeping, as expected, despite the presence of clutter. In Figure 7-7 c) it can be seen that both methods have a similar ranging performance in the SNRs of interest. However, as shown in Figure 7-7 d), the MUSIC based processing outperforms the DFT beam-sweeping approach in terms of 3D positioning of the target of interest. This is due to the better estimation of the AOA of the received signal reflected by the target of interest. Finally, in all subfigures of Figure 7-7, a performance saturation is observed in high SNRs. This saturation is the result of clutter that needs to be treated.

7.2 JCAS resource optimization

In this subsection, three optimization scenarios are considered. Namely, the subsection investigates the optimization of OFDM-based bistatic systems, resource allocation for multi-band systems, resource allocation of 6D (position and orientation) tracking in JCAS systems, and resource allocation and protocols for inter-UE JCAS systems.

7.2.1 Optimization of OFDM-based bistatic sensing

Problem Statement: Cost and implementation reasons dictate that the legacy of the previous generations of cellular communications, i.e., 4G and 5G, will have, up to an extent, an impact in the forthcoming 6G wireless communication networks. One of the elements of 4G that influenced the development of 5G is the used OFDM waveform and its adopted numerologies. The projection of this trend indicates that OFDM and its variant discrete Fourier transform (DFT) spread-OFDM (DFTS-OFDM) are strong candidates, at least for the most common bands. This rationale is further enforced by the expected coexistence of 5G and 6G for the initial stages of the 6G deployment. Consequently, OFDM and its variants pose also as strong candidates for future JCAS functionality of 6G. Conceptually, the simplest form of sensing is monostatic sensing. However, monostatic sensing requires the transmitter and the receiver to be collocated. Therefore, a monostatic transceiver faces implementation challenges originating mainly from the requirement of the full duplex operation. An alternative that does not require full duplex operation is bistatic sensing, where the transmitter and the receiver are geographically separated. Furthermore, the plethora of nodes (base stations and UEs) in a cellular network, which can act as candidate sensing nodes, indicates a performance robustness. This can be achieved via the appropriate selection of the two involved sensing nodes. Based on the previous short analysis, it becomes clear that bistatic sensing using the OFDM waveform, with a parameterization that closely follows the corresponding communication parameterization, presents as an attractive solution for the JCAS functionality in 6G. Thus, the aim of this study is to explore the fundamental performance of bistatic sensing when the used waveform is the communication based OFDM. This work assumes the following: 1) perfectly synchronized transmit and receive nodes; 2) omni-directional or directional transmission using the required transmit antenna setup and beamforming (for the directional case); 3) directional reception using the required receive antenna array and (DFT) beamforming; 4) realistic channel modelling where both the useful propagation paths and clutter are present; 5) OFDM parameterization that closely follows the 5G parametrization and variations of it.

Methodology: The block diagram of the bistatic sensing of interest based on the OFDM waveform is given in Figure 7-8. In more detail, it is assumed that the bistatic sensing of interest is undertaken using a train of N_s periodic OFDM symbols. Each symbol is generated assuming an allocation of N_{sc} subcarriers and a given numerology. The allocation of the sensing subcarriers is done either using dedicated sensing signals or other existing reference signals. In the transmitter, once the signal is transformed in the time domain and before its transmission a cyclic prefix (CP) is added, or a guard interval (GI), or a unique codeword (UCW). The duration of the CP (or GI or UCW) is selected such that its duration is longer than the longest time of flight (TOF) of

interest. At the receiver side, upon the reception of an OFDM symbol, the CP (or GI, or UCW) is removed before the received signal is transformed to the frequency domain. The following step includes matched filtering in the frequency domain. Upon the reception of the N_s OFDM symbols of interest, for the estimation of the quantities of interest (range, 3D positioning, and velocity), additional radar signal processing is undertaken, such as the calculation of the Doppler-delay representation of the N_s OFDM symbols and the corresponding peak finding.

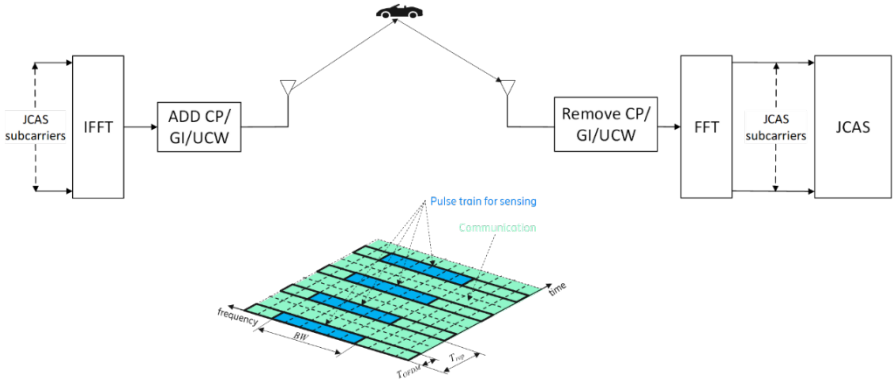

Figure 7-8: Bistatic sensing using OFDM.

Results: In this study, the aim is to characterize the limitations set by the duration of the CP on the maximum permissible distance between the receiving node and a target that can be sensed. For this reason, it is assumed that the bistatic sensing of interest is implemented as shown in Figure 7-9. More specifically, the operating principle for estimating the Target-to-RX distance D_r, the TX-to-Target distance D_t, and the position of the target, $\mathbf{r}$, rely on the measurement of the time of flight (ToF) of the propagation path between the TX-Target-RX and the knowledge of the angel ψ_r, which is the AoA in the RX. From the measured ToF, the distance of flight, $S = D_t + D_r$, can be obtained. Also, the TX-to-Target distance is expressed as, $D_t = \left[S^2 + D_b^2 + 2SD_b\cos\psi_r\right]\left[2(S - D_b\cos\psi_r)\right]^{-1}$, where, D_b is the TX-to-RX distance; the distance D_r is given as,

$$D_r = \left[S^2 - {D_b}^2\right]\left[2(S - D_b\cos\psi_r)\right]^{-1}, \quad \textbf{(7-1)}$$

while, the position of the target is expressed as, $\boldsymbol{r} = D_r[\sin\theta\cos\phi \quad \sin\theta\sin\phi \quad \cos\theta]^T$. Note that the angle ψ_r can be expressed in terms of the angle θ and ϕ, the TX-RX distance D_b, and the position of the TX $\mathbf{t} = [t_1, t_2, t_3]^T$ as:

$$\cos\psi_r = \frac{t_1\sin\theta\cos\phi + t_2\sin\theta\sin\phi + t_3\cos\theta}{D_b\sqrt{(\sin\theta\cos\phi)^2 + (\sin\theta\sin\phi)^2 + (\cos\theta)^2}} \quad \textbf{(7-2)}$$

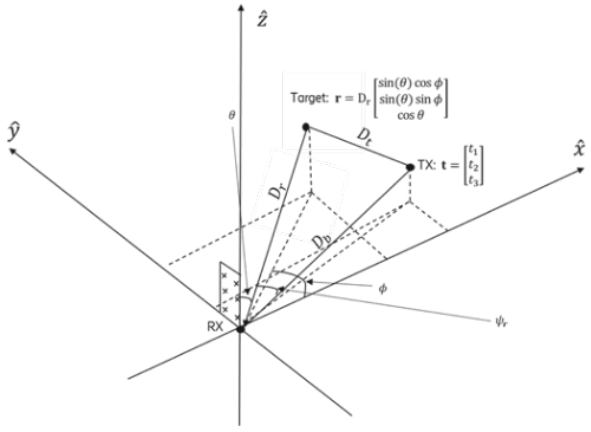

Figure 7-9: Bistatic radar range sensing and positioning in the RX LCS using an estimate of the angle ψ_r which is connected with the zenith and azimuth AoA θ and ϕ.

In Figure 7-9, the angles θ and ϕ, and consequently the angle ψ_r, need to be estimated using the appropriate procedure. Note that, the previous derivations are based on the use of the LCS of the RX. However, the efficient representation of bistatic radar sensing involves the use of the LCSs of all nodes and of the system Global Coordinate System (GCS).

Figure 7-10 presents the maximum target-to-RX distance, D_r, that can be sensed for a pair of angles of (θ, ϕ), when the CP duration is the one adopted by New Radio (NR) for a normal CP duration for the numerologies with $\mu = \{0, 1, 2, 3\}$, defined in the 3GPP technical report 38.211, i.e., CP duration of 4.69, 2.34, 1.17, and 0.57 μs which correspond to a numerology of μ, 0, 1, 2, and 3, respectively. Note that, as shown above, the distance D_r depends on the pair (θ, ϕ) through the angle ψ_r. Also, this figure provides results for a pair of angles, $\theta, \phi \in [0, 85]$, as the rest of the angles are either not of interest (correspond to back lobe angles or to the LoS path where the performance of bistatic sensing is poor) or the corresponding maximum distance is readily available due to the symmetry of the maximum sensed ellipsoid. The observation of Figure 7-10 shows that, as expected, longer durations of CPs provide longer maximum sensed distances D_r. In addition, irrespective of the CP length, the maximum distance that can be sensed corresponds to θ and ϕ equal to 85 degrees. This is because this direction points towards the outer ellipsoid that can be sensed for a given CP duration.

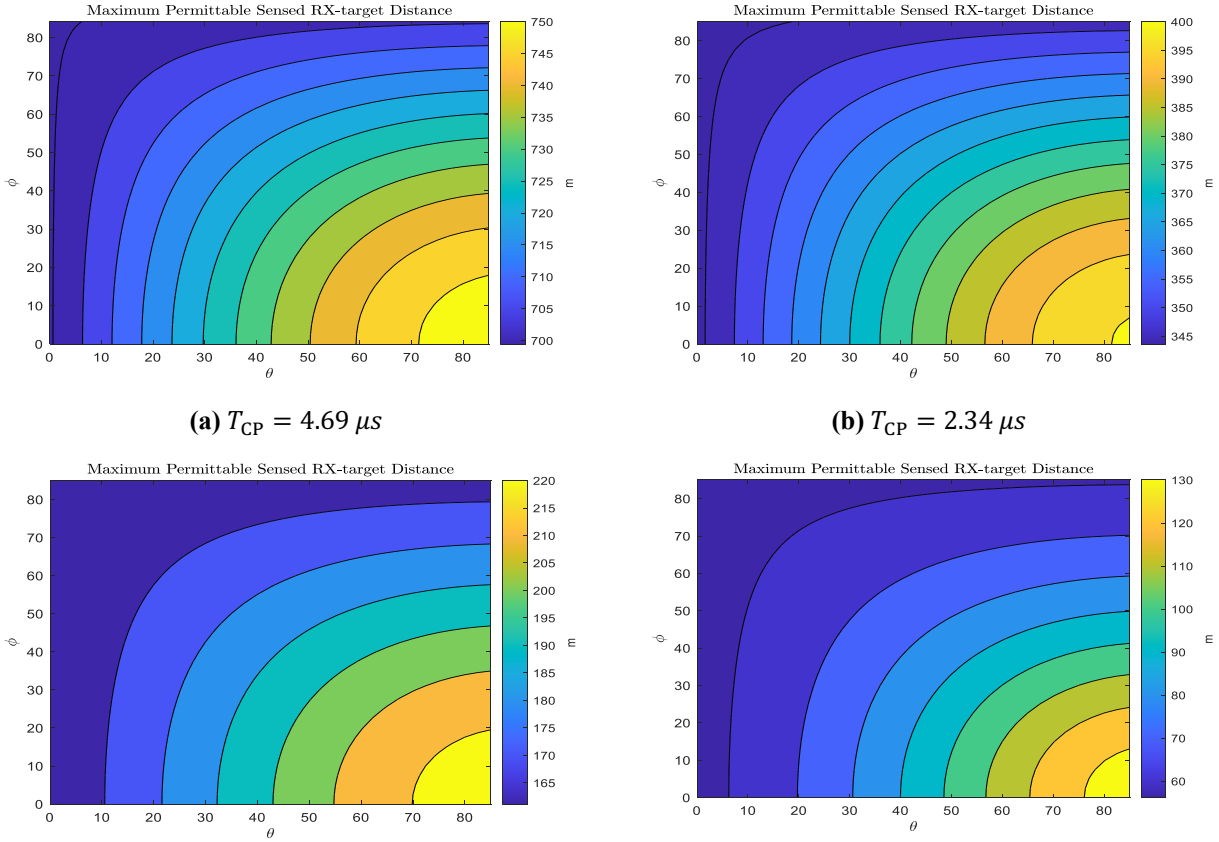

(a) $T_{\mathrm{CP}} = 4.69\ \mu s$ **(b)** $T_{\mathrm{CP}} = 2.34\ \mu s$

(c) $T_{\mathrm{CP}} = 1.17\ \mu s$ **(d)** $T_{\mathrm{CP}} = 0.57\ \mu s$

Figure 7-10: Maximum permittable sensed Target-to-RX distance D_r .
For a CP duration, T_{CP}, 4.69, 2.34, 1,17, and 0.57 μs, when the receiving and the transmitting nodes are placed in the $[100, 0, 0]^T$ and $[0, 0, 0]^T$ positions in the LCS of the receiving node (measured in m).

7.2.2 Resource allocation for 6DoF tracking in RIS-aided JCAS scenarios

Problem Statement: This work considers a RIS-aided multiple-input-multiple-output (MIMO) system operating in FR2 where a UE (e.g., a VR headset or a multi-antenna UAV is communicating with a BS. In order to achieve certain communication KPIs at the UE side, beamforming at the BS, RIS, and UE needs to be optimized, which requires the 6DoF state (i.e., 3D position and 3D orientation) of the UE. For 6D localization, this work assumes that the LoS path and RIS path are available to UE. In addition, the BS is the localization coordinator that allocates resources and configures system parameters (e.g., beamformer and RIS profile) for

localization. After localization and tracking algorithms are performed at the UE, the results are sent to the BS for future transmissions. More specifically, the BS sends localization pilot signals to the UE at each time slot using DFT beams (without prior information) or optimized beams (with prior information). The 6DoF state of the UE can be estimated at each time slot, and tracking algorithms can be implemented. Based on the predicted states, BS/RIS/UE beams can further be optimized for better communication and localization performance. This work has the following assumptions: the LoS path and RIS path are available to UE; the channel state information (CSI) is available; and the pilot signals are known to UE for 6DoF state estimation.

Methodology: In this work, it is assumed that the state (3D position and 3D orientation) of UE $\mathbf{P}_{\mathrm{U},t}$, $\mathbf{R}_{\mathrm{U},t}$ and the prior information (covariance matrix of the state $\mathbf{\Sigma}_{\mathrm{U},t}$) from $t = 1$ to $t = T - 1$ can be estimated via certain localization algorithms. Based on the developed 6DoF tracking algorithm, the UE state $\mathrm{P}_{\mathrm{U},T}$, $\mathrm{R}_{\mathrm{U},T}$ and the updated covariance matrix $\mathbf{\Sigma}_{\mathrm{U},T}$ at $t = T$ can be estimated. Based on the predicted state and covariance matrix, the BS/UE/RIS beamformers ($W_{\mathrm{B},T}$, $W_{\mathrm{U},T}$, $W_{\mathrm{R},T}$) are optimized for better communication performance for the next step at $t = T + 1$. The block diagram of the 6DoF tracking can be found in Figure 7-11. More details about the signal model can be found in [WS22a] and [WS22b] and the geometry model can be found in [ZCB+23]. The beam optimization for localization is also considered. Different from communication where a single beam codeword is sufficient, localization requires a beamforming matrix containing the beamformers at G transmissions (e.g., $\boldsymbol{W}_{\mathrm{B},T} = [\boldsymbol{w}_{B,T,1}, \ldots, \boldsymbol{w}_{\mathrm{B},T,G}]$). Note that if multiple BSs ($L_{\mathrm{B}} > 1$) are adopted instead of an RIS-aided system, power allocation at the BSs ($P_1, P_2, \ldots, P_{L_{\mathrm{B}}}$) is also needed. In this JCAS system, channel capacity is used to gauge the communication performance, and the position/orientation error bound is used to gauge the localization performance.

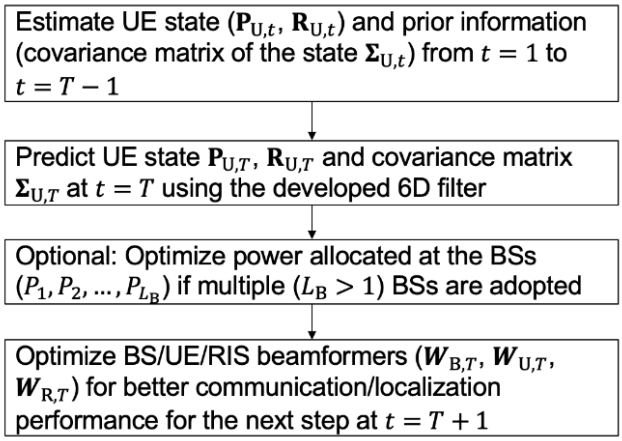

Figure 7-11: Block diagram of the 6DoF tracking.

Results: In Figure 7-12, the RMSE of the estimated orientation with a known UE position is evaluated. The BSs are located at [0, 0, 0] and [0, 5, 0], while the UE is located at [5, 3, 0]. Each BS can provide an angle pair (azimuth and elevation) estimation. Next, 1000 angle estimation samples were randomly generated with covariance matrices of diag ([0.88, 1.50]) and diag ([0.05, 0.65]). The RMSEs are in the form of Euler angles, rotation matrix, and the matrix error in the tangent space are compared with the derived CRB, constrained CRB (CCRB), and intrinsic CRB (ICRB). It can be seen that for certain UE orientations, the estimated Euler angles have large errors.

This is due to the non-unique mapping from the rotation matrix to Euler angles. The estimated rotation matrix at high SNR matches CCRB well. However, the CCRB cannot be directly used in the filter due to the low rank of the matrix. Alternatively, ICRB that can reflect the intrinsic error of the rotation matrix is used in the 6DoF filter design.

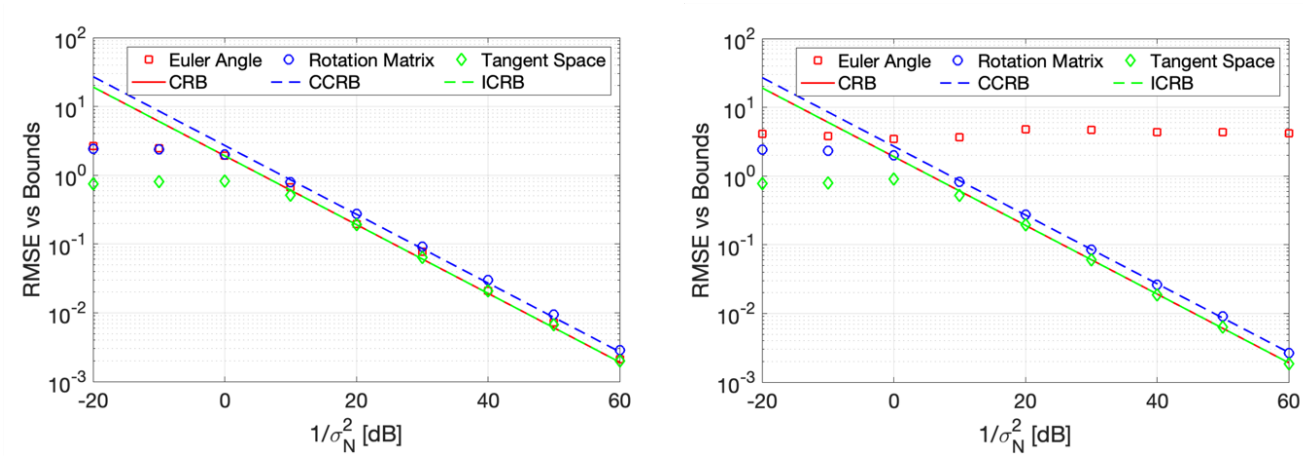

(a) UE orientation [0, 0, 0] **(b) UE orientation [180, 0, 0]**

Figure 7-12: Comparison between different orientation errors (Euler angles errors, rotation matrix errors, and rotation matrix errors in the tangent space) and corresponding bounds (CRB, CCRB, ICRB).

In Figure 7-13, the direction vectors of the UE-BS link are visualised, e.g., the BS seen at the UE's local coordinate system. The BS is located at [5 0 0], and the UE is located at [0 0 0]. The orientation of the UE in terms of the Euler angle is [-20, 30, 0]. Due to the uncertainty of UE state estimation, beamforming at the UE is crucial for a stable link. By setting the covariance matrix of the UE position as diag ([0.02, 0.02, 0.2]), and UE orientation tangent space error as diag ([0.2, 0.01, 0.01]), 1000 realizations are visualized for three scenarios: (a) only position uncertainty is considered with a known UE orientation; (b) only orientation uncertainty is considered with a known UE position; (c) both position and orientation uncertainties are considered. The visualization indicates that different uncertainty levels require different beamforming strategies.

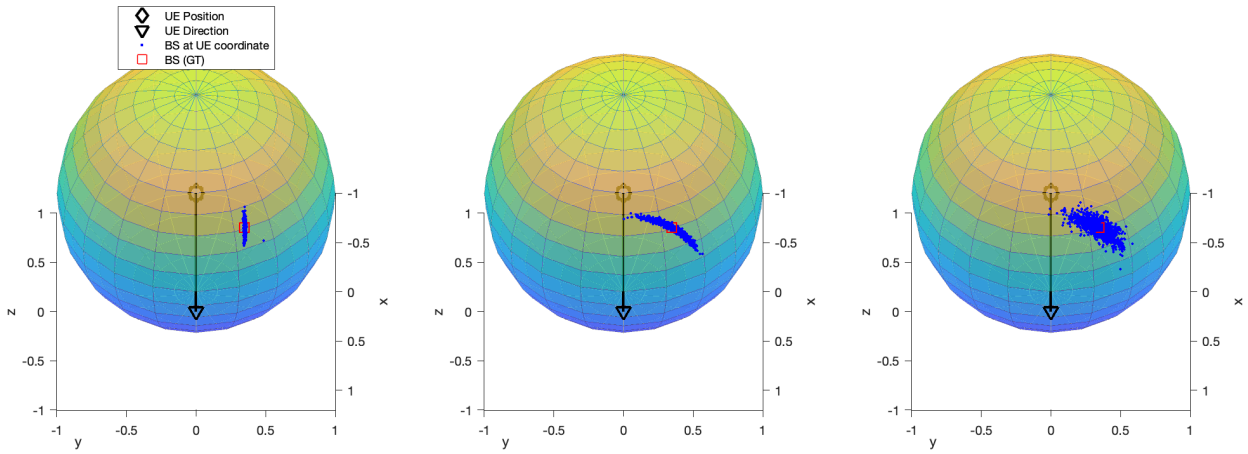

Figure 7-13: Visualization of the BS direction at the UE's local coordinate system under different uncertainties.

7.2.3 Resource allocation and protocols for inter-UE sensing

Problem Statement: Bistatic sensing refers to the sensing mode where one node transmits a sensing signal that is received by another node. While it is simple to utilize such a signal in theory, it is quite complex due to various practical constraints. Various signal processing techniques have been developed, often in the field of "passive radar" [LKR21] to utilize such signals in an optimal way. Key problems are linked to missing, or weak time and frequency synchronization, clock drift, phase noise to name a few key challenges. Consequently, research was focusing on setups that leverage specific properties of the environment or of the participating nodes. For example, scenarios were limited to air surveillance with few targets, or multistatic sensing was realized using multiple well-synchronized transmitters. In this work, the intention is to develop the foundation for bistatic sensing between UEs. Due to their mobility and limited synchronization, such a setup can be considered the most challenging one. Multiple tasks need to be handled to allow useful sensing

signal exchanges between the UEs. The goal is to leverage the 6G standard to enable such functionalities by deeply integrating required protocols and procedures into the standard to solve problems such as coordination and orchestration of air interface resources, and the sensing task itself. Air interface resource allocations could be defined in time, frequency, space, code and polarization domain. Suitable device to device sensing may be performed in licensed or unlicensed band under the regulations and rules in the specific band. The choice may depend on the frequency. Here, the focus is on bands around 60 GHz and Sub-THz frequencies. Each device is assumed to be connected via cellular technology to a central controller (CC) for sensing administration and orchestration. In order to allow the two devices to hear each other, a minimum set of resource parameters have to be met. The corresponding PHY-layer procedures are assumed to be available for this purpose. These sensing procedures define the waveforms, synchronization aspects in time and frequency and the "message content" of the sensing signal itself. In case of directional transmission, a notion of relative orientation is required. This could be achieved by pointing the transmitter and receiver at the sensed object. For directional channels it is further assumed that the line-of-sight components between transmitter, sensed object and receiver are dominant. Exchange of information, capabilities and control can be handled via CC. In the following, an OFDM based waveform is assumed to be transmitted for sensing purpose.

Methodology: Given inter-UE sensing between at least two devices, where the presence of another device in the vicinity must be detected. This discovery could be done via low non-3GPP technologies like Bluetooth or ultrawideband (UWB). Once a suitable device is found, relative orientation of the two devices must be established. To receive a sensing signal proper synchronization is required. Synchronization in time and frequency could be achieved via 3GPP or IEEE based technology. Here 3GPP technology is assumed. Initial timing synchronization is assumed to be down to a fraction of the CP of the OFDM symbol as this is required for transmission and reception in communication. In addition, a minimum synchronization accuracy of the carrier frequency has to be met, e.g., 0.1 ppm.

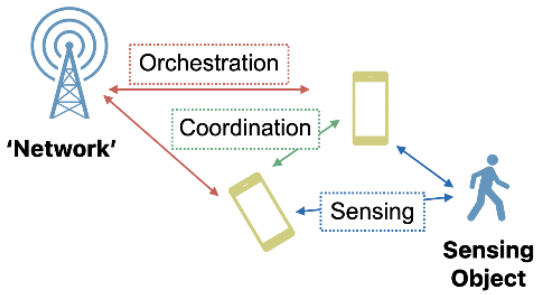

Figure 7-14: Block Diagram for Bistatic Sensing at UE.

Results: An exemplary solution for inter-UE sensing is shown in Figure 7-15. Leveraging today's 5G positioning protocol, a first solution for inter-UE sensing is provided. It is agnostic to frequency bands and utilizes licensed band for coordination and sensing. This can be considered an ideal solution from resource allocation point of view since additional delay due to required listen-before-talk in unlicensed band is avoided. Listen-before-talk could potentially result in multiple iterations of coordination until the unlicensed channel is available for sensing. The coordination task is mostly realized by a network function (SeMF) and may be assisted by the serving Transmission Point(s) (TRP). Sensing operation may be requested either by a network entity or by one of the participating UEs. While reporting of results is likely required in the first case, it may be obsolete in the latter, therefore this step needs to be optional. To avoid interference, the SeMF needs to assign resources such that the assigned sensing signals are orthogonal to any other signal that is transmitted in the vicinity of the participating UEs. Such orthogonality may be realized in any domain. Such scheme can be straightforwardly adapted to other modes such as monostatic UE, monostatic TRP, as well as bistatic and multistatic sensing between UE-TRP.

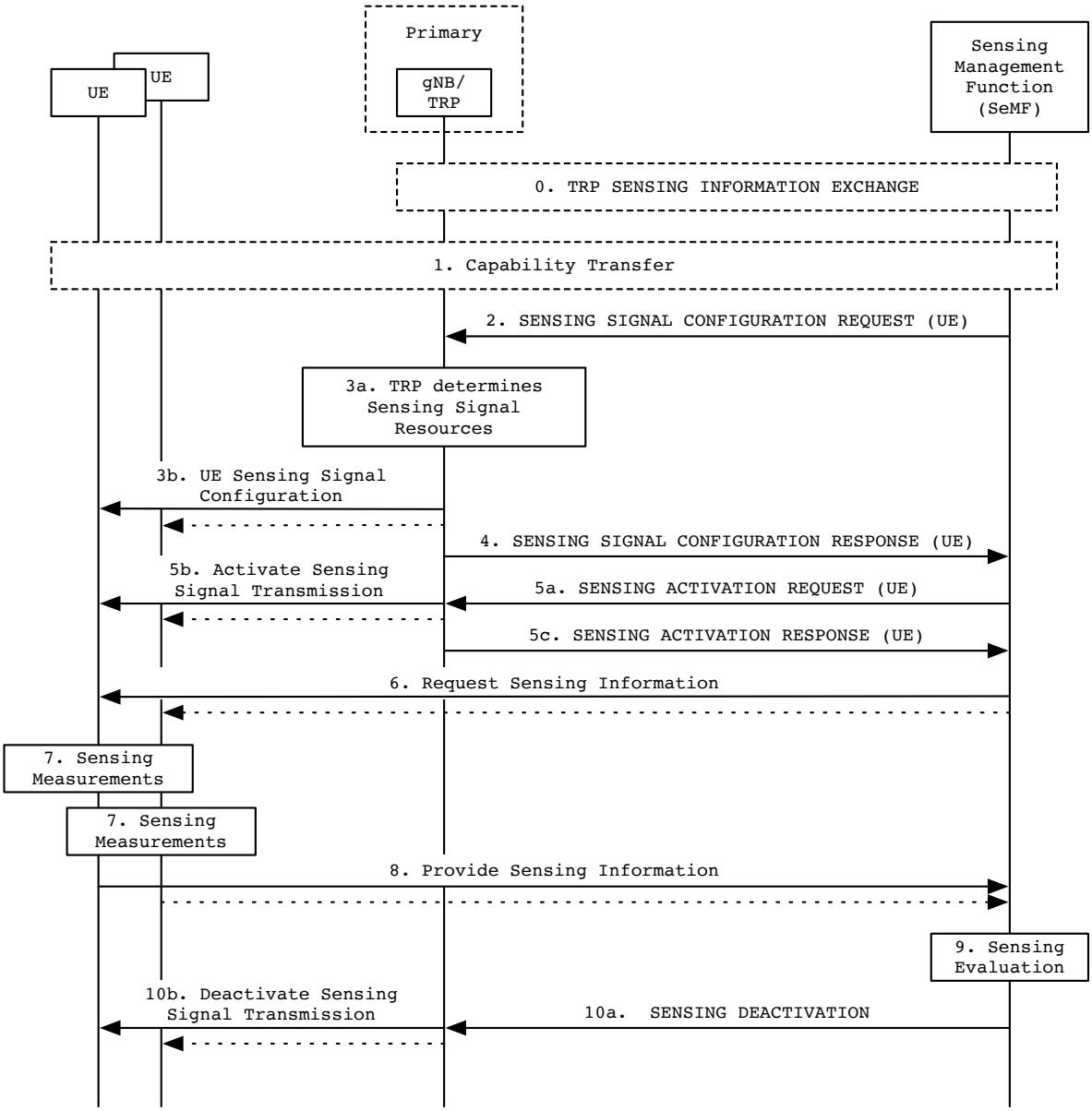

Figure 7-15: Protocol for Bistatic Sensing between UEs.

8 Flexible spectrum access solutions

This chapter covers spectrum access related topics including spectrum sharing with non-terrestrial networks (NTN) and 5G as well as approaches for low latency spectrum access: Section 8.1 discusses spectrum sharing and required coexistence mechanisms with NTN as well as multi-radio access technology (RAT) spectrum sharing (MRSS) with 5G. Related representative use cases (UC) from [HEX223-D12] include *ubiquitous networks* and *network-assisted mobility* due to high service coverage requirements that can be achieved by NTN to augment terrestrial network (TN) coverage. Section 8.2 covers low-latency spectrum access solutions for higher frequency ranges as well as risk-aware access protocols. Low-latency access is important for UC with stringent latency and reliability requirements like *real-time digital twins* or *cooperating mobile robots*. Two related aspects are further detailed in this chapter: Section 8.3 addresses handover (HO) challenges and associated overheads within NTN. Section 8.4 proposes a method to predict interference levels to assist radio resource management.

8.1 Spectrum sharing and coexistence

Spectrum is a valuable and scarce resource. The success of 6G will rely on the existence of new spectrum to satisfy the requirements of the new use cases, and, therefore, the ability to leverage spectrum that is already allocated to existing services is essential. It is necessary that coexistence mechanisms are in place for efficient spectrum sharing, which is the focus of this chapter. Therefore, the emerging non-terrestrial connectivity leading to new interference scenarios is investigated. First, improvements on the assumptions and models in sharing studies are proposed for the case of co-channel coexistence of international mobile telecommunications (IMT) and fixed satellite service (FSS) ground stations. Next, spectrum sharing possibilities between 6G and FSS uplink (UL) in the centimetric range are shown, giving hints on how to improve antenna design to make the coexistence possible. This is followed by a study on TN-NTN spectrum sharing in S-band (2 GHz) using stochastic geometry, which gives insights on how to optimize the integrated network performance in complex systems. The chapter ends with a section on MRSS between 5G new radio (NR) and 6G, focusing on TN, which will allow a smooth spectrum migration between the two generations.

8.1.1 Assumptions and models to determine sharing possibilities with fixed-satellite service Earth stations

Problem statement, scope: The assumptions and models of spectrum sharing and related compatibility studies are crucial in understanding how mobile networks coexist with other radio services. The focus of this section is to determine how additional assumptions on antenna models and deployment related parameters can improve conditions to prevent interference between radio services, e.g., shorter separation distances between terrestrial stations operating in the same frequency band. This aims to enhance efficiency and compatibility in wireless communication systems.

Methodology, deployment considerations: This assessment evaluates co-channel separation distance to prevent interference from a mobile network base station (BS) using active antenna systems (AAS) to FSS earth stations (ES). It compares factors, including refined assumptions on radiation patterns and user equipment (UE) deployments, using Monte Carlo simulations to determine separation distances. Focus is on C-Band (3.4-4.2 GHz), as both 5G and FSS heavily utilize this frequency band. The relevant system parameters for deployments in Fuchsstadt [Int23] and DLR (Deutsches Zentrum für Luft- und Raumfahrt; German Aerospace Centre) [DLR23] for both mobile networks BS with AAS and FSS ES are detailed in Appendix Section A.5.1.

Results: For different ground distances between the BS and FSS ES, the following results correspond to the case when the BS is always facing the FSS ES around it (worst-case). Additionally, it is assumed that the BS is active either 100% or 50% of the time, accounting for varying network loading factors, and that the time division duplexing (TDD) ratio for downlink (DL) is 75%. Table 8-1 summarizes the separation distances considering clutter losses only on one end of the propagation path, FSS antenna model S.465 [ITU-S.465], and a uniform UE distribution. These distances are detailed for the instances where the BS is facing the main-lobe and the back-lobe of the FSS ES.

Table 8-1: Separation distances for a FSS with S.465 antenna model and a UE uniform distribution

BS Size	FSS ES	FSS ES Pattern	Activity factor	Main-lobe (km)	Back-lobe (km)
8×8 AAS	DLR	S.465	100%	< 10.8	< 2.8
8×8 AAS	DLR	S.465	50%	< 5.6	< 1.4
8×8 AAS	Fuchsstadt	S.465	100%	< 19.6	< 2.8
8×8 AAS	Fuchsstadt	S.465	50%	< 12.8	< 1.4
4×4 AAS	DLR	S.465	100%	< 15.8	< 4.6
4×4 AAS	DLR	S.465	50%	< 14.6	< 3.8
4×4 AAS	Fuchsstadt	S.465	100%	< 23	< 4.6
4×4 AAS	Fuchsstadt	S.465	50%	< 21.4	< 3.8

For instance, interference-to-noise (I/N) values for a 20% probability around the DLR ES with a 37.5% activity factor are shown for an 8x8 BS in Figure 8-1. The darkened area indicates locations where the I/N protection criterion is exceeded.

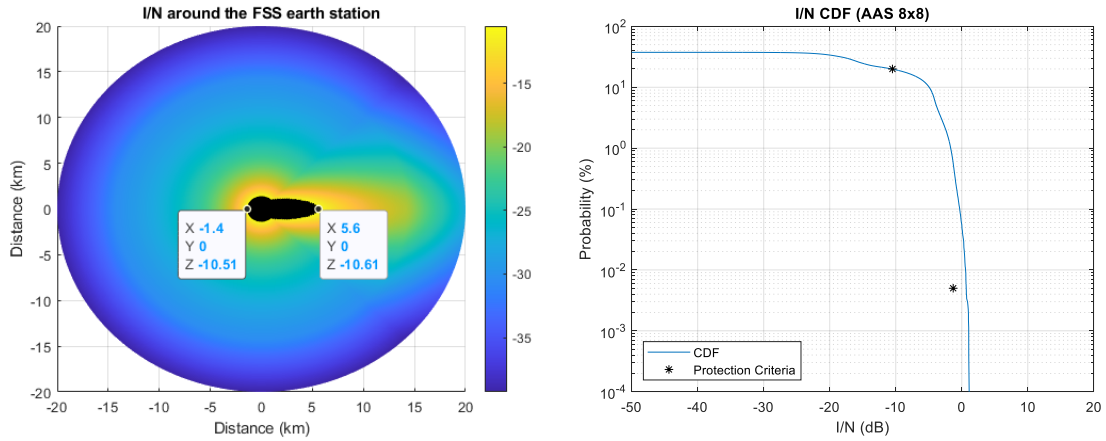

(a) (b)

Figure 8-1: (a) I/N around DLR earth station and (b) I/N CDF at 5.6 km from FSS ES (facing main-lobe).

Table 8-2 summarizes the separation distances considering clutter losses only on one end of the propagation path, FSS antenna model based on Bessel functions, and a UE Rayleigh distribution. These distances are detailed for the instances where the BS is facing the main-lobe and the back-lobe of the FSS ES.

Table 8-2: Separation distances for a FSS with Bessel antenna model and a UE Rayleigh distribution.

BS Size	FSS ES	FSS ES Pattern	Activity factor	Main-lobe (km)	Back-lobe (km)
8×8 AAS	DLR	Bessel	100%	< 2	< 0.6
8×8 AAS	DLR	Bessel	50%	< 1	< 0.4
8×8 AAS	Fuchsstadt	Bessel	100%	< 2	< 0.6
8×8 AAS	Fuchsstadt	Bessel	50%	< 0.8	< 0.4
4×4 AAS	DLR	Bessel	100%	< 7.2	< 1.2
4×4 AAS	DLR	Bessel	50%	< 4.8	< 0.8
4×4 AAS	Fuchsstadt	Bessel	100%	< 7.4	< 1.2
4×4 AAS	Fuchsstadt	Bessel	50%	< 4.8	< 0.8

For instance, in Figure 8-2, I/N values for a 20% probability around the DLR ES with a 37.5% activity factor are shown for an 8x8 BS, FSS ES radiation pattern based on Bessel functions, and UE Rayleigh distribution.

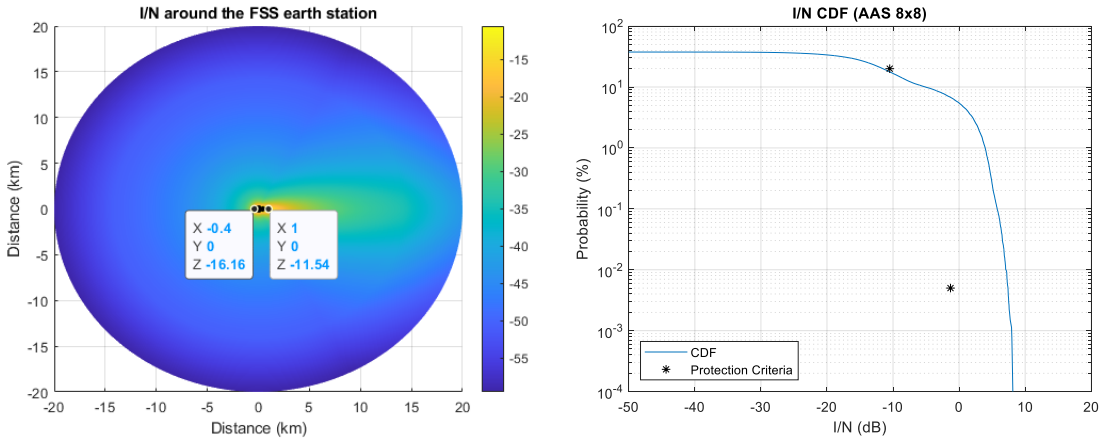

Figure 8-2: (a) I/N around DLR earth station and (b) I/N CDF at 1 km from FSS ES (facing main-lobe).

In conclusion, additional assumptions including more accurate FSS ES radiation patterns, UE deployments, and the BS activity factor are considered to determine their impact on the required separation distances to prevent harmful interference:

- Bessel functions provide a mathematical description of the electromagnetic fields within parabolic reflectors, enabling accurate predictions of radiation patterns.
- A Rayleigh distribution for the UE ground distance from its BS is deemed more appropriate for scenarios like local networks provided that these networks are deployed where users are expected to remain in the local cell rather than moving between different cells as in public mobile networks.
- It is reasonable to assume that a BS is active either 100% or 50% of the time, accounting for varying network loading factors. Considering a TDD activity factor of 75% for DL (3:1), the equivalent activity factors become 75% and 37.5% respectively.

This analysis shows that taking into account the mentioned factors lead to a reduction in distances from tens of kilometres to just few kilometres in some cases. This highlights that utilizing more accurate models and assumptions, when available, can provide results that can be closer to reality. Additionally, note that for larger AAS antenna arrays, the separation distances decrease due to the enhanced directivity of such larger arrays.

8.1.2 TN-NTN spectrum coexistence and sharing frameworks

Coexistence of TN and NTN is foreseen as an important component to fulfil the global coverage promised for 6G. Due to ever rising spectrum demand, certain frequency bands allocated by radio regulations to NTN and satellite networks may overlap with those already utilized by cellular TN, leading to performance degradation due to the potential co-channel interference. In this section two studies on this issue are presented.

8.1.2.1 Spectrum sharing between 6G and FSS UL in the centimetric range

Problem statement, scope: Additional spectrum from the centimetric range (7-15 GHz) is identified as essential for realizing the high demanding use cases envisioned in future 6G networks [STK+23]. In the following the coexistence and sharing possibilities in this frequency range focusing on spectrum sharing between 6G IMT and satellite networks, namely FSS UL, are investigated.

In case of coexistence with satellites the goal is to protect the feeder UL or the service UL. In the following the latter is considered. The interfering terrestrial node can be either the BS (transmitting in DL) or the UE (transmitting in UL). For this study, the impact from the UE is disregarded, since the transmit power is lower. Figure 8-3 includes a sketch of the described scenario. In this situation, the level of interference will depend, among others, on the transmit power of the interferer, directivity of the antennas, the spectrum arrangement between the networks, and the density of interfering nodes. In fact, since in this case a) the propagation between the interfering terrestrial node and the victim satellite node is mostly in the “vertical” direction, b) a single satellite beam can have a large footprint and c) the orientation of the interferer antennas has a smaller impact

(most of the interference is transmitted via the sidelobes and back lobes), there can potentially be a large number of meaningful interferers that should be taken into account when calculating the level of the total interference. Furthermore, the distance between the victim satellite receiver and the interfering terrestrial transmitter (i.e., the altitude of the satellite orbit and the elevation angle) has only a minor impact, partially due to the "vertical" (line-of-sight) propagation, but mostly due to the relationship between the path loss and the size of the footprint affecting the number of interfering nodes (as the altitude increases, the path loss increases quadratically with distance, but at the same time the size of the footprint is equally increased). Hence, for this scenario, the problem is not so much the impact of a few strong interferers, but the potentially high level of the average interference. In practice, what will matter is how much power per area unit (km^2) is used on earth (i.e., the output power of the base stations and the site density within the satellite beam coverage area), how much the antennas can attenuate the transmitted power towards the satellite and what frequency is being used.

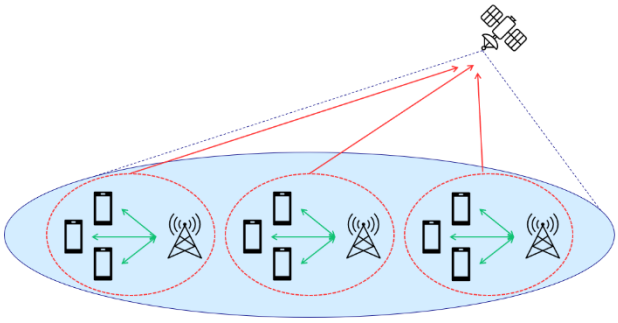

Figure 8-3: Schematic overview of the coexistence scenario, where the victim is the satellite. Several IMT base stations serve UEs in the footprint of the satellite (in blue). The green lines represent the communication between the BS and UE, and the red solid lines represent the interference that those induce in the satellite.

Methodology, deployment considerations: To study the impact of a mobile system on the FSS UL in the centimetric range, the following frequency ranges are of interest: 12.75-13.25 GHz (UL for SpaceX Starlink Gen 2 and OneWeb Phase 1) and 14-14.5 GHz (UL for SpaceX Starlink and OneWeb Phases 1 and 2). After the recent outcome of WRC23, these frequency bands are not of immediate interest for 6G, but the conclusions remain valid and useful for an eventual further future IMT identification.

The simulation methodology used can be described in the following steps:

1. An IMT network is created with a set of BSs in a hexagonal grid. UEs are distributed uniformly in the cell. At a given instant, each BS serves three random UEs simultaneously.
2. Multiple IMT networks are distributed randomly in the satellite footprint on the earth surface. The total number of BS is calculated based on the Ra/Rb method [ITU-5D716] for large area aggregation and the deployment density for the specific scenario.
3. The average antenna gain from all BS to the satellite is calculated for different elevation angles.
4. An estimate of the cumulative interference to a satellite is calculated.

Table A.5-26 includes the IMT assumptions, which are aligned with ITU-R WP 5D [ITU-RA4.17, ITU-RTG5]. In contrast to the previous Section 8.1.1, in which new assumptions are used to improve future coexistence studies, this section uses the current recommendations. However, since there are currently no ITU recommendations for antenna characteristics in the frequency ranges in focus, two different sets of parameters have been used in the sharing studies, belonging to the closest frequency ranges: 6425-10500 MHz [ITU-RA4.17] and 24.25-33.4 GHz [ITU-RTG5].
The resulting antenna gains are included in Figure 8-4 a). On the satellite side, assumptions for the two constellations present at the studied frequency ranges are included in Table A.5-27. However, given that the main difference between Starlink and One Web in this set-up is the orbit height, the results have been produced only for the worst-case-scenario, which corresponds to the closest-lying constellation, Starlink.

Results: Figure 8-4 shows the main results. The I/N ratio in Figure 8-4 b) follows the trend of the antenna pattern, being lower where the BS transmit powers are lower and vice versa. It is important to note that angles

below 20-25 degrees are not interesting because they are not used by the satellite system. It can be seen that coexistence is not possible using the ITU recommendations for the 6450-10500 MHz frequency bands, unless the BS power spectral density is reduced below 6 W/200 MHz. However, delivering a service capable of satisfying the requirements of the future 6G network will be challenging at these low output powers in an urban macro network. On the other side, Figure 8-4 b) shows that coexistence is indeed possible using the recommendations for the 24.25-33.4 GHz frequency bands. This is very clear at the very low power included in the recommendation (10 dBm/element, which corresponds to ca. 1 W/200 MHz in an 8x8 antenna setup), whereas Figure 8-4 c) shows that the power in this configuration can indeed be increased to ca. 22 W/200 MHz, most likely because the BS are more shielded behind buildings when the BS are placed at a lower height.

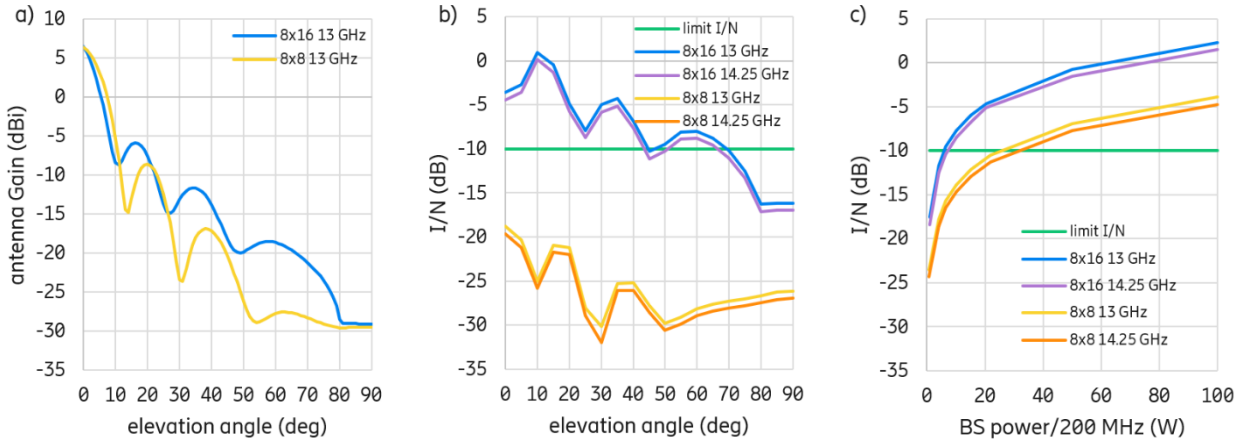

Figure 8-4: a) Antenna gain vs elevation angle generated for 13 GHz for the two sets of assumptions, b) I/N for both sets of assumptions and frequencies, c) I/N for different BS power at 35 degrees of elevation angle. The blue (8x16) and yellow (8x8) lines correspond to the ITU recommendations for 6450-10500 MHz and 24.25-33.4 GHz, respectively. The green horizontal line is the typical level for an acceptable I/N in coexistence studies..

If the studied frequencies are to be used in a typical urban macro deployment, sharing solutions need to address the high interference levels shown for the upper set of data in Figure 8-4, especially if higher output powers are to be used as expected in 6G. Different approaches can be explored: use of databases, improvement of the IMT antenna to reduce emissions towards the sky via mechanisms that control side lobes, and increase of the victim resilience making sure that satellite antennas can be made to tolerate more interference.

8.1.2.2 TN-NTN Spectrum Sharing in S-Band using stochastic geometry

Problem statement: Simulation-based studies on different co-existence scenarios may fail to offer a comprehensive and insightful understanding of these networks' overall performance, in particular because the complexity of a brute force performance evaluation increases exponentially with the number of nodes and their possible combinations in the network.

Methodology, deployment considerations: Stochastic geometry is utilized to analytically derive the performance of TN-NTN integrated networks in terms of the probability of coverage and average achievable data rate for two co-existence scenarios. From the numerical results, it can be observed that, depending on the network parameters, TN and NTN users' distributions, and traffic load, one co-existence case may outperform the other, resulting in optimal performance of the integrated network. The analytical results presented herein pave the way for designing state-of-the-art methods for spectrum sharing between TN and NTN and optimizing the integrated network performance.

The coexistence scenario is depicted in Figure 8-5. An NTN and a TN share the same spectrum, and the NTN is used to provide services to the UEs located outside the TN coverage area. The NTN generates interference on the TN UEs, arising both from the earth-to-satellite and satellite-to-earth links.

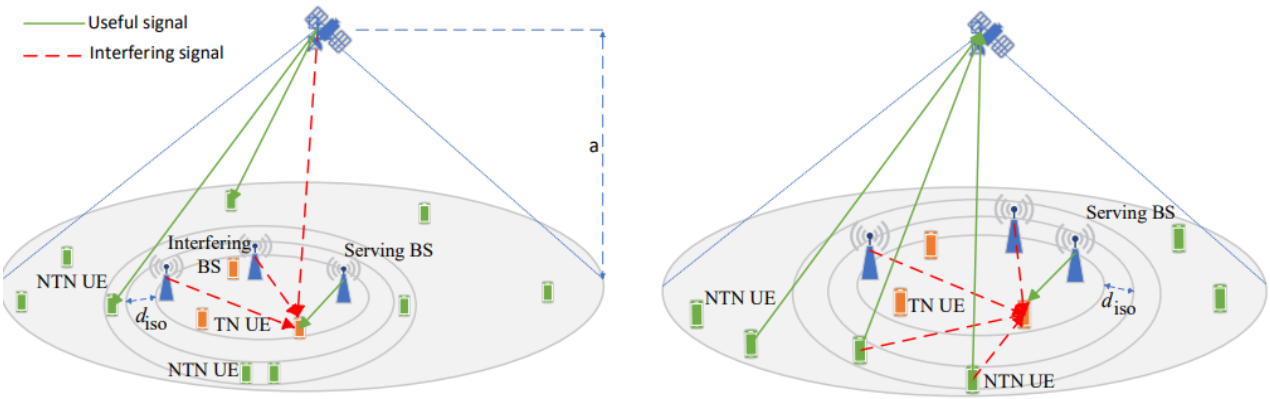

(a) NTN DL interferes with TN DL. (b) NTN UL interferes with TN DL.

Figure 8-5: Coexistence Model.

The satellites are located at a height a. All UEs and TN base stations are randomly located inside the coverage area. An isolation distance d_{iso} between the edge of the TN coverage area and the NTN UEs may be ensured to minimize the interference on the TN UEs located at the cell edge.

Results: In Figure 8-6 the distribution of the signal-to-interference-plus-noise ratio (SINR) caused by the NTN in the space-to-earth link is shown, and a performance penalty on the TN can be observed, which increases with lower-orbit satellites. It can also be seen that simulation and theoretical results are very close, indicating the correctness of the analysis. Results when the NTN UEs generate the interference are shown in Figure 8-7, where it can be seen that UEs close to the border can suffer a lot from interference if the isolation distance is not large enough.

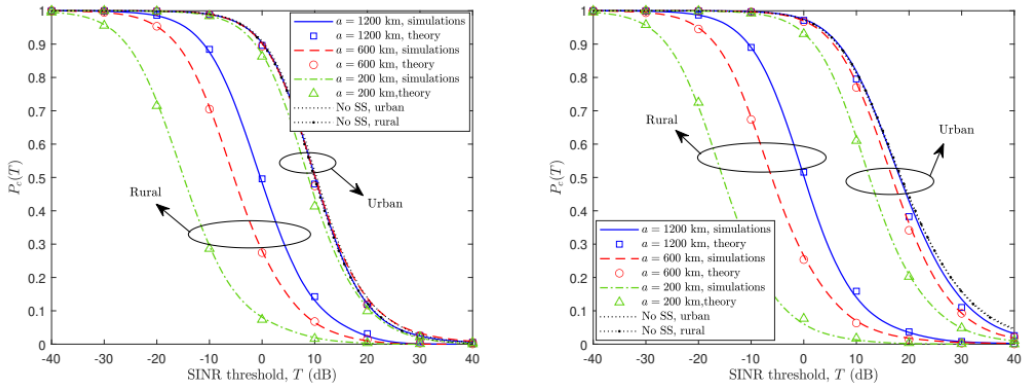

(a) 100% load. (b) 25% load.

Figure 8-6: SINR distribution at the TN for different satellite altitudes – space-to-earth link as aggressor.

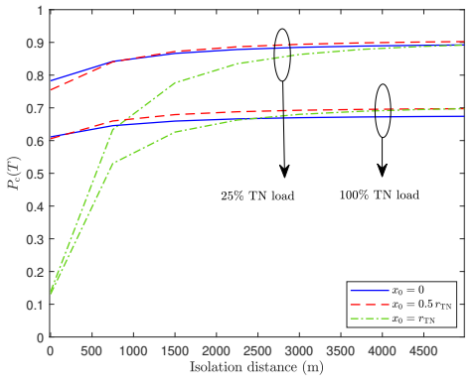

Figure 8-7: Effect of isolation distance on different users – earth-to-space link as aggressor.

8.1.3 Multi-RAT Spectrum Sharing

Problem statement, scope: MRSS will allow 5G-NR and 6G to share a single frequency band, especially in frequency range (FR) 1. This will enable network operators to smoothly migrate their networks from 5G to 6G as the traffic demands for the latter increase. At the beginning of 6G deployment, however, the penetration of 6G UEs is likely to be low, evolving over time. A static refarming of 5G frequency bands is not efficient and flexible enough to accommodate the different traffic profiles and the rapidly evolving 6G adaptation. Therefore, a framework that allows an incremental and dynamic allocation of resources to the 6G network is required. An initial blueprint for this approach was already provided with dynamic spectrum sharing (DSS), which enabled the transition from 4G to 5G, and one can learn from the experience with that framework, albeit with improved efficiency and flexibility. The MRSS solution will have to dynamically allocate radio resources in time, frequency and space, depending on the traffic demands from both 5G and 6G networks. As it can be seen in Figure 8-8 it is expected that 6G will provide a better spectral efficiency and capacity than NR. As the penetration of 6G UEs increases over time, the overall system efficiency should also increase, eventually reaching the full 6G potential when it is universally adopted. A certain overhead loss is to be expected when two different RATs share the same spectrum, which may decrease the efficiency slightly at the beginning of 6G operation, when only few terminals will be 6G-capable.

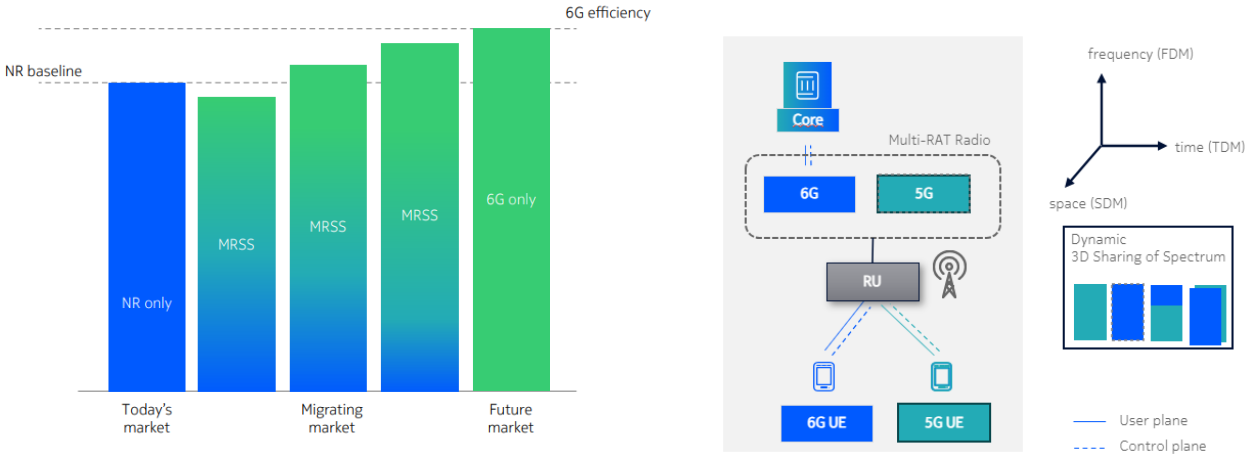

a) G/radual Deployment of 6G. **b) MRSS Architecture and 3D-Sharing.**

Figure 8-8: 6G Deployment.

Requirements and recommendations: In the development of MRSS some technical requirements should be observed as follows

- The solution must be transparent to legacy 5G UEs, which must not require any changes.
- The overhead associated with a hybrid NR/6G network must be minimized.
- Capabilities of 5G legacy devices and by day-1 6G features must be supported, including carrier aggregation configurations (DL and UL) on 6G UEs.
- Grant network operators the capability to alter their prioritized air interface as needed over time.

Further recommendations can be provided deriving from previous experience with DSS.

- 6G physical layer (PHY) should be compatible with NR waveforms and numerologies, avoiding additional guards and facilitating spectrally efficient sharing.
- Physical layer overhead must be kept as low as possible. Due to the lean and future-proof design of NR, the potential for overhead reduction in MRSS is high when compared with DSS.
- MRSS deployments should not prevent the utilization of energy saving gains introduced by 5G-Advanced. The framework should also be flexible enough to accommodate new 6G-specific energy-saving features.
- The Xn interface would fall short of expectations. The standardization of new interfaces between schedulers comes with realization and implementation challenges.

- Avoid 4G-6G MRSS due to fixed 4G long-term evolution (LTE) overheads. Sharing with LTE-M and narrowband Internet of things (NB-IoT) can be handled in a less optimized / more static way, when needed.

RAN Architecture and Sharing: Although MRSS deployments are expected to share a common radio unit (RU), the baseband unit could be shared or be independent for both RATs, as depicted in Figure 8-8. The former would facilitate coordination across packet schedulers, but the latter case would, for example, entail a high-speed low-latency interface. For DSS, no such interface was standardised and the existing network interface (Xn) would fall short of expectations given the additional delay introduced by the higher layers and the potential routing delays, but this new interface may be challenging to realize and implement. Avoiding new interfaces is preferable, given the associated standardization, implementation, testing, and integration costs. In Figure 8-8b it is also shown that MRSS is a form of spectrum sharing in time, frequency and space (beams) between two different RATs.

Methodology, system model and simulations: A system-level simulation framework allowing a joint investigation of NR and 6G is under development. The studies will be confined to the air interface performance of MRSS, with layers from PHY to radio link control (RLC) being modelled. Higher-layer and architectural issues will not be directly considered in this study, particularly at core network level. Different radio access network (RAN) architecture setups can however be modelled considering for instance different latencies for the communication between NR and 6G networks, as described in the previous subsection.

The system will consist of a regular hexagonal grid of 3-sector gNodeBs, both with and without beamforming. NR and 6G networks will share the same radio front-ends (RUs). The simulations will allow us to obtain an estimate of MRSS efficiency, in which a comparative analysis in the following domains will be performed:

- Different scheduler configurations, from a joint NR/6G scheduler to independent schedulers with minimum communication.
- Different RAN architectures
- Different adaptation timeframes, from long-term traffic trends to real-time (slot-level) adaptation.
- Efficiency of solutions in time, frequency, and spatial domain.

8.2 Low-latency spectrum access

Many services require low-latency access to spectrum for a good and reliable user experience. Low-latency access in this context covers initial access (sharing of basic access parameters and first-time access) as well as shared access for UL and DL resources with associated resource sharing and conflict handling. Especially for sub-THz communications highly directed beams are required to mitigate pathloss, which complicates beam search, alignment, and tracking procedures. Combined with standard listen-before-talk (LBT) requirements it is thus challenging to achieve a low access latency. In the following a further look on sub-THz spectrum access methods will be given. Options to achieve low latency will be presented and related simulation assumptions and evaluation methods will be discussed. The proposed access techniques are not limited to sub-THz frequency ranges; they could also be applied to lower frequency ranges like FR 2.

An additional technology that is covered in this section is a probabilistic approach to access spectrum. Risk-informed random access for local communication considers risks by creating extra interference for other users. It can be seen as a new paradigm that borrows ideas from random access concurrently with scheduled access.

8.2.1 Sub-THz access methods

Problem statement, scope: The different parts of spectrum access are described and tailored to sub-THz frequency range, covering initial search, initial access, idle, and connected mode access. At first, a general overview on basic ingredients of the access scheme is given, followed by an example implementation and simulation.
Methodology, deployment considerations: A two-step spectrum access including an omni-directional anchor RAT (e.g., FR 1) and a directed low-latency high-data-rate sub-THz booster RAT is assumed.

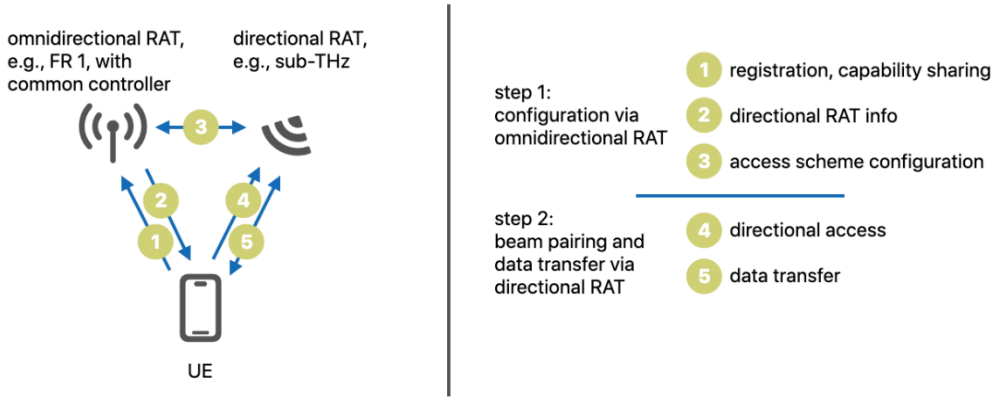

Figure 8-9: Overview of the two-step access and directional/omni-directional access.

In a first step, registration and initial access control are done via the omni-directional RAT to relieve the sub-THz access point (AP) from registration and sharing of basic connection parameters. Based on this registration the AP configures the associated directed sub-THz access for both UE and AP.

In a second step the UE, knowing the sub-THz AP timing and parameters, handles the additional sub-THz related procedures including synchronization, beam finding, and data transfer. See also the following list and Figure 8-10 for additional details on the repeated set of procedures.

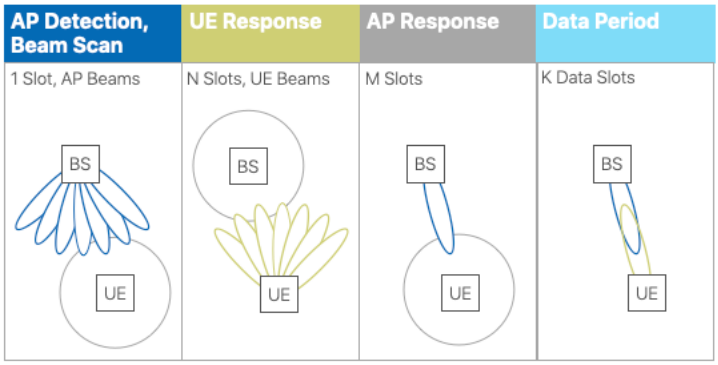

Figure 8-10: Sub-THz access scheme.

- *AP detection and beam finding*: The AP sends a set of beacon beams in a pre-defined pattern that are measured by the UE to find the current best AP Tx beam.
- *UE detection and beam finding*: After selecting the AP Tx beam the roles are changed and the UE sends a set of beacon beams towards the sub-THz AP with a pre-configured timing. The AP measures the beams and detects the best UE Tx beam.
- *AP response slots*: The AP sends a response at a pre-defined time to tell the UE that it is allowed to use the subsequent data period. Further assignment of slots and UL/DL resources will be done dynamically during that data period.
- *Data period*: The previously selected beam pair is used. The assignment of slots within the data period to a certain UE is done via a physical DL control channel (PDCCH) sent by the AP.

In shared unlicensed spectrum, fair access between several UE (not registered to the same AP) for this scheme can be ensured via a limited channel occupancy time combined with a minimum Tx and Rx directivity. This approach avoids time consuming LBT procedures and keeps interference low.

Results: Pre-configuration of the directed access avoids conflicts between multiple registered UE and allows a tailoring of the sub-THz access point parameters to the targeted access latency. For a bandwidth of 10 GHz and a set of optimized parameters a data latency in the range of 100–150 µs can be achieved. While the latency within the data period could be further reduced, the limiting factor for the worst-case latency is the repetition and duration of the detection and response period. A frequency-domain decoupling of beam search and refinement from the data period can further reduce latencies, see Figure 8-11.

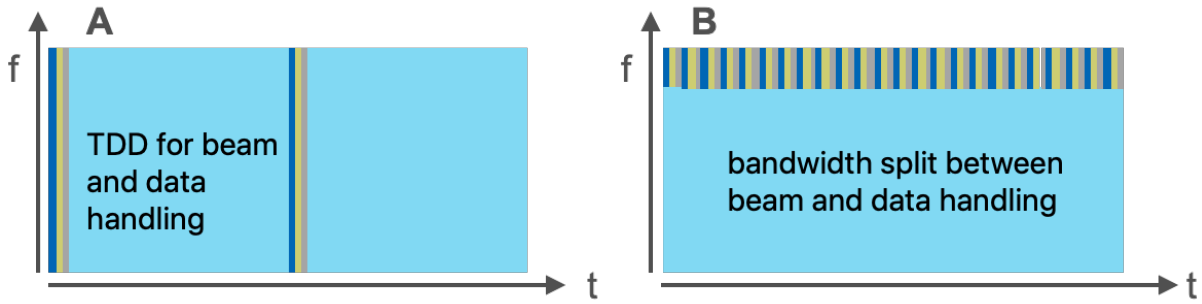

Figure 8-11: A) same frequency range, B) decoupled frequency range for beam search and data period.

The beam search and response part of the access scheme are put into a dedicated bandwidth part with a bandwidth of, e.g., 100–500 MHz. This bandwidth still allows very short beam durations, reasonable feedback message sizes, and an acceptable control overhead compared to the overall used bandwidth. This approach decouples beam pairing from data period handling and reduces latency. The beam search and alignment can be tailored to the UE velocity and environment while the data period can be tailored to achieve required latency and throughput. Assuming a similar structure of the data period (like in the previous time-multiplexed scheme) into data slots combined with PDCCH and reception acknowledgement feedback, a latency of down to 20 µs can be reached. The control overhead is increased to around 10–20 % (PDCCH and reserved bandwidth part for the beam alignment). Due to the large available bandwidth this trade-off is deemed acceptable.

An overview on the general simulation setup with a few used assumptions can be found in Section A.5.4.

8.2.2 Risk-informed random access

Problem statement, scope: Non-coordinated risk-informed random access to localized communication can augment scheduled access, if the risk for interference is expected to be low. Interference assessment is central as it helps in understanding potential risks and their occurrences during sharing.

Methodology, system model: In this study interference assessment for Aloha and carrier-sense multiple access (CSMA) based device-to-device communication for a shared frequency band is performed in a simulation environment. The key objective of this simulation is to understand the dynamic spectrum access with the consideration of risk-based interference management. A ray tracing simulation tool 'Wireless InSite' is used which is mainly dedicated for measuring the propagation loss paths of the signals between the base station and the devices and for modelling the channel access python is used. Signal strengths details are vital in modelling the behaviour of the UEs in the channel simulation of the Aloha and CSMA and allows to measure the interference for UEs at various timestamps. For the antenna modelling of the UEs and base stations, the built-in characteristics of the simulation tool are used, for example, a directive antenna model for the base stations and the omnidirectional antennas for UEs are used.

This simulation study comprised of six steps. The starting step defines the details about various involved devices and their properties in the Wireless InSite tool such as UEs, base stations and device implementation. The second step calculates the path loss between the UEs and the base station. Step three determines the potential destinations for UEs and measures the SINR. The modelling for communication channel for ALOHA and CSMA at specific timestamps is performed in step four (4a and 4b). In the final two steps of the simulation, interference is measured, and respective results are generated.

Initial results: The results of this study are assessed from different perspectives. The first one is to define the tolerable level of interference. Thermal noise radiation is also used to define the tolerable level of interference. For this simulation environment, Aloha and CSMA protocols have been used and both indoor and outdoor scenarios (City and Harbour) are considered. Figure 8-12 presents comparison of mean aggregate interference and throughput against the channel load. It can be analysed that for Aloha interference and throughput do not depend on each other while there is an exponential increase in interference against the throughput for CSMA.

The occurrence of potential interference risks can be defined when the particular threshold is exceeded and the details regarding how usual it occurs. Figure 8-13 presents the information about the time of maximum

interference against the channel load. It can be seen from the figure that there are different reasons for both Aloha and CSMA.

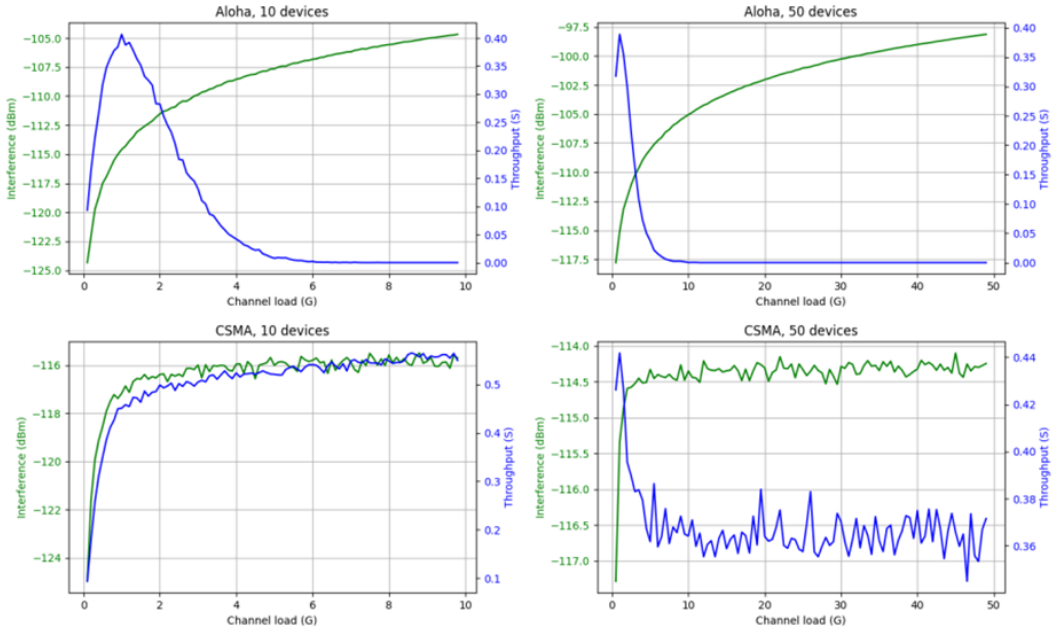

Figure 8-12: Channel load and mean aggregate interference plotted against channel load.

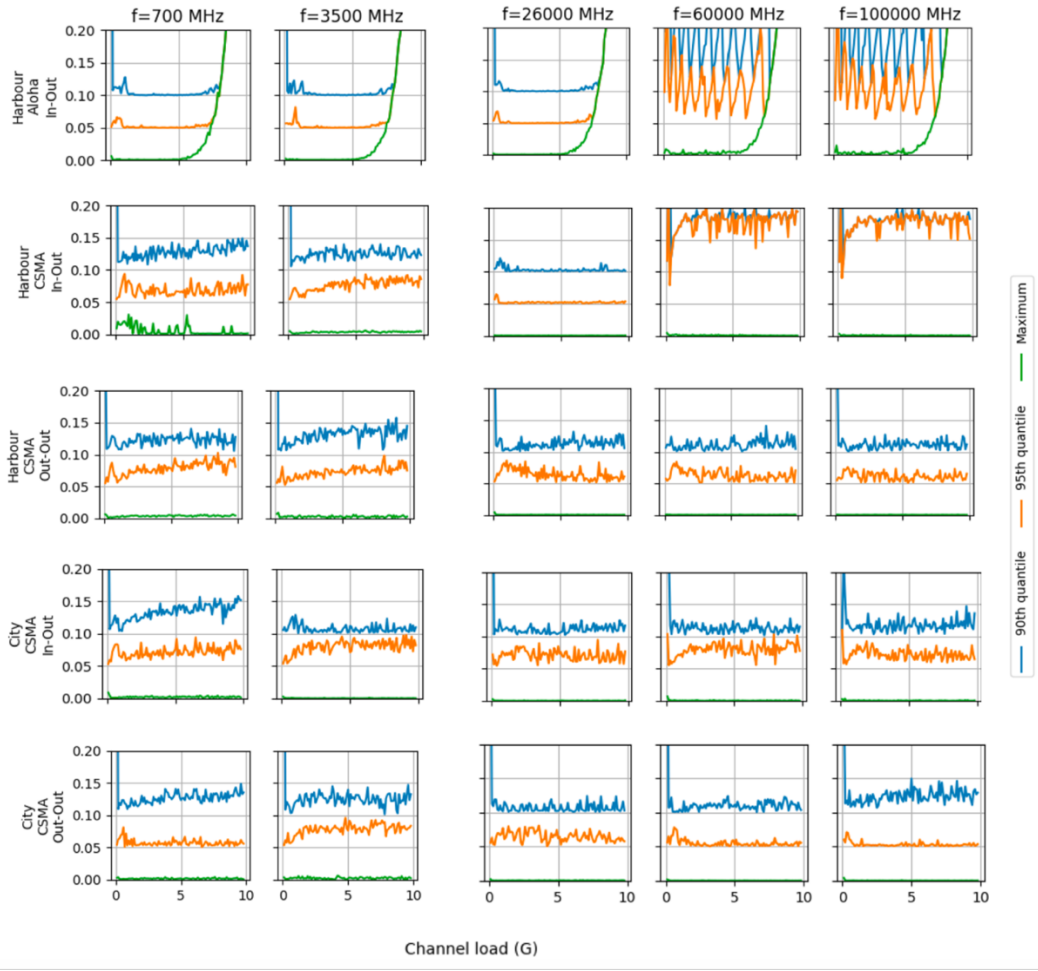

Figure 8-13: Proportion of observations exceeding indicated limits for aggregate interference.

8.3 Inclusive radio interface via TN/NTN enhancements

Problem statement, scope: In future 6G and beyond systems, NTN is envisioned as an essential supplement to the cellular TN to deliver ubiquitous coverage, unrestricted by landscape and infrastructure building limitations. The seamless integration of NTN (including communication through satellites, drones, etc.) and TN will connect the entire environment (sky, sea, remote terrain, etc.) of human activity. Various research and development activities are ongoing to address specific NTN challenges such as latency, Doppler effects, and TN interoperability. In 5G era, 3GPP has been working from Rel. 17 on standards to enable NTN within the NR and LTE internet-of-things framework [28.841]. Rel. 18 work introduced enhancements for optimizing satellite access performance, addressing new frequency bands, and supporting new capabilities and services [RP-234011, RP-234073]. Rel. 19 targets to further improve the service experience (coverage enhancements, support of reduced capability UE) and add new capabilities (support of regenerative payloads, multicast and broadcast services) [RP-234078].

A very critical aspect for TN and NTN integration, and key topic for specified NTN enhancements in 3GPP Rel. 18, is the HO of users between cells, i.e., the process of transferring an ongoing communication session from one cell (or node) to another, to maintain continuous and reliable connectivity. Figure 8-14 depicts such example HO cases in an TN-NTN integrated system. When it comes to NTN, and especially the satellite case, frequent HO (as perceived in legacy TN) become unavoidable. With earth-moving and quasi earth-fixed scenarios, the serving cell will regularly change (intra-satellite or inter-satellite cell change) independently of UE mobility, implying HO of all connected UE. In addition, feeder link change would also result in HO of all connected UE. So, even stationary users may need to perform HO procedures in seconds timescale when considering the very high-speed movement of satellites. This will result in significantly increased signalling overheads, service interruption from such signalling latency leading to degradation of overall service performance, as well as energy consumption at the device side. Current work on this area considers solutions for enhancing NTN HO procedures. The main assumptions and HO concepts considered in 3GPP Rel. 17/18 work for NTN are adopted, including sub-6 GHz bands, network scenarios include satellites on geostationary and non-geostationary orbits, transparent payload, 3GPP power class 3 UE with navigation satellite reception capability, earth-fixed or earth-moving cell NTN configurations.

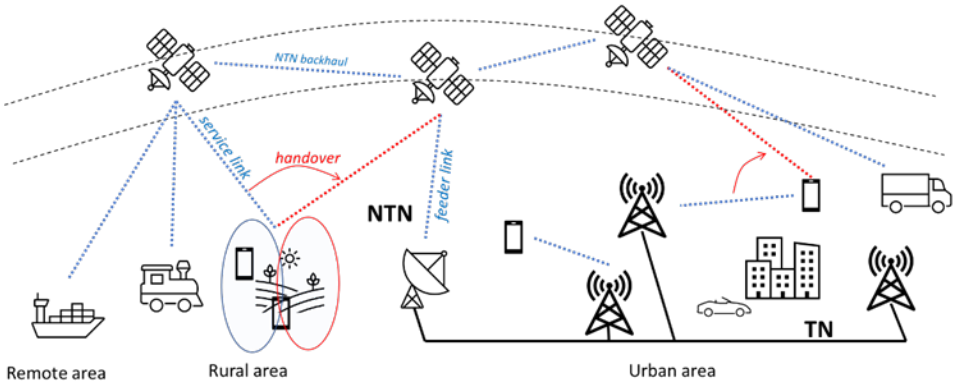

Figure 8-14: Handover in TN-NTN integrated system.

8.3.1 Reduction of NTN handover signalling overhead

The HO signalling overhead issue is twofold: a) during HO preparation time, network needs to send HO command to all UE in the cell; b) during HO execution, random access is performed by all UE in the cell. Regarding HO commands, one solution (also considered in 3GPP Rel. 18) is to include in those messages information that can be common to all UEs (in a cell or for subset groups of UEs). The question is if there is really benefit in terms of overhead reduction with such common signalling approach. To examine this, the evaluation considers a simplified model of the two possible ways of delivering the common information and it can be seen that there exists a trade-off when using dedicated versus common signalling (CS) and it is questionable whether CS is always a good solution for HO signalling overhead reduction (see Appendix A.5.6). For this reason, this work proposes an approach of ***Quality-of-Service (QoS) aware omission of HO common information***. More specifically, based on the knowledge of the QoS or traffic pattern the network could:

- Keep including HO common information in the HO command message (legacy behaviour), e.g., for UE with on-going voice calls.
- Omit (all or most) HO common information in the HO message, e.g., for UE with sporadic data or delay tolerant traffic. In that case instead, the UE will need to acquire the required parameters (e.g., from synchronization signal block (SSB), master or system information blocks (SIB) in current NR system) from the target cell. This approach incurs further HO interruption; however, this could be acceptable depending on the QoS or traffic pattern of the UE. A main advantage of the proposed scheme is that there are clear gains in terms of signalling overhead (with a compromise on HO interruption time, but only for UE that would tolerate it).
- It is also possible to omit HO common information in HO command message and UE acquires some of the required parameters while in source cell, during source and target overlap time. This is beneficial to reduce interruption time in case parameters can be available (within valid duration) from source cell through other signalling during overlap time (see Section A.5.6).

Regarding the second aspect of signalling, a problem identified in NTN has to do with the simultaneous mass random access messages during HO execution. To smooth out these HO, the network must configure different time periods for each UE, within the overlapping time of source and target cells. Hence, time-based conditional HO (CHO), a HO procedure introduced in early 5G allowing UE to decide HO when certain conditions are met, can be used to spread the HO messages load. However, this will involve very dense signalling within a usually short overlapping time while it is also possible that this time might prove not enough to perform HO execution for all UEs. To solve this, this work proposes a *random time-based CHO* approach including the following steps:

a) first, network (via source cell) broadcasts the overlapping time to UE.

b) then, the UE are configured to perform time-based CHO at a random time during the overlapping time.

Future work plan to quantify the potential gains of the proposed approaches under common practical scenarios.

8.3.2 Cell change without handover

The interruption time due to HO depends, in general, to a great extent on system configuration as well as on processing implementations at UE and network side. In NR TN scenarios, one can expect a minimum of 25 ms radio access latency during HO [R2-2301269], i.e., from HO command to HO complete transmission. In NTN scenarios, this HO latency will be inherited and may be larger, e.g., considering extra processing for beam management in higher frequency bands or non-regenerative payload processing at satellite. The main problem however in NTN scenarios is the frequency and the amount of HO, especially in low earth orbit scenarios involving high-speed satellite (e.g., 7.5 km/s). The time to HO in that case, even for static UE, can vary between 6 and 140 seconds, depending on cell size, while a large number of UE (up to twenty thousand per second) may need to perform HO concurrently [38.821]. A feature that could help dealing with the above extreme numbers in NTN cases is dual active protocol stack (DAPS), specified in 3GPP Rel. 16 of NR [21.916]. DAPS is essentially a HO procedure maintaining the source cell connect after reception of HO command and until releasing the source cell after successful random access to target cell. However, this feature is complex for implementation at UE (preventing wide adoption in the market so far) and can prove especially problematic to be supported by low capability UE, e.g., employing a single Tx/Rx chain. Instead, an alternative solution has been devised in Rel. 18 for NTN, considered for the case of hard satellite switch, where the main concept has been to perform satellite switching with physical cell indicator (PCI) unchanged. In that case, the expected benefit will come from the fact that the HO procedure is avoided altogether. There is no HO command, and the same cell appears projected to the same area by the next satellite. However, it can be observed that this solution comes with drawbacks (see Appendix A.5.6 for more information): a) questionable interruption time reduction, as target cell needs to be synchronized after leaving source cell; b) impact on other (legacy) UE; c) additional ephemeris and common timing advance (TA) provisioning. To solve these issues, this work instead proposes to adopt a *"PCI change only"* approach whereby:

- there is again no HO procedure involved,
- the cell configuration remains the same (except from parameters related to NTN (e.g., parameters included traditionally in SIB 19 in Rel. 17/18 NTN)

- only the identifier (ID) of the target cell is changed (compared to source cell ID) and needs to be broadcasted with existing signalling (introducing negligible additional overhead).

With the proposed approach, the following benefits are expected:

- Soft switch is possible (if desired). This allows to minimize interruption time as UE can be synchronised to target cell and have its NTN configuration parameters broadcasted while in the source cell.
- Legacy NTN UE can be handled as per legacy specification (approach would be fully backward compatible for them).
- There is no need to specify a new mechanism to broadcast at the source cell configuration parameters that are changed at the time of the switch. The legacy mechanism can be reused.
- There are no risks and constraints in synchronising target cell with same PCI for legacy UE.

HO command is still not needed, i.e., any benefit of Rel-18 NTN "unchanged PCI" solution is present.

8.4 Interference prediction-based proactive resource management

Problem statement: Efficient management of inter-cell interference is among the major challenges in guaranteeing the stringent reliability and latency requirement of ultra-reliable low-latency communications (URLLC). Conventional approaches such as hybrid automatic repeat request (HARQ) are not well suited for low latency applications. Instead, solutions that can predict the interference conditions and allocate resources proactively are found to be more effective. Existing works considered interference prediction in wireless networks using a non-linear auto-regressive neural network [PHM+21] and modelling the variation of interference as a discrete state space discrete-time Markov chain [MLA+21] for URLLC purposes.

Methodology: This proposes to pre-process the interference signal before prediction, with the aim of improving the prediction accuracy. More precisely, it proposes to decompose the interference signal using the empirical mode decomposition (EMD) algorithm. This decomposes the interference signal into several component signals called intrinsic mode functions (IMF), each having different frequency components [JSM+23]. Each component IMFs are then predicted using the transformer model, which is a deep neural network algorithm, as illustrated in Figure 8-15.

Results – Since each IMF has different frequency components, the proposed approach allows optimizing the transformer model for different IMF separately, thereby resulting in higher prediction accuracy, as shown in Table 8-3. The prediction is then applied to the resource management algorithm proposed in [MLA+21]. The resulting outage performance presented in [GSM+23] is found to outperform conventional resource allocation approaches presented in existing literature. It is planned to expand this work by considering a multi-antenna scenario with improved interference management approaches.

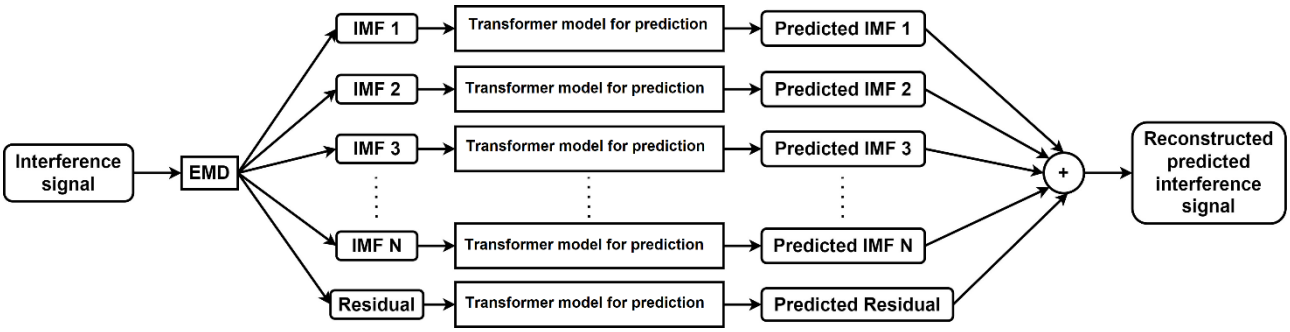

Figure 8-15: Schematic diagram of the proposed decomposition-based interference prediction framework.

Table 8-3: Summary of the RMSE values of conventional and proposed interference prediction methods.

Algorithm	Root mean squared error (RMSE) without EMD	RMSE of proposed EMD based approach
transformer (proposed)	0.77	0.54
long short-term memory (LSTM)	1.53	1.71
auto-regressive integrated moving average (ARIMA)	1.00	0.57

9 Trustworthiness

Trustworthiness is one the three core values targeted by Hexa-X-II. Different aspects of a trustworthy 6G radio design are explored in this chapter. These include, solutions for exploiting the physical properties of wireless channel and device hardware to ensure security against eavesdropping attack; investigating methods to assess the impact of jamming against and localize a jammer; and analysing the security and privacy analysis of a general cellular JCAS system, including the UE related aspects.

9.1 Secret key generation for D2D communication

Problem statement: Physical layer security (PLS) exploits the physical properties of the wireless channel and device hardware as sources of randomness to implement security solutions. PLS-based secret key generation (SKG) is a promising approach that can be used in hybrid crypto-PLS systems to achieve confidentiality at the physical layer. SKG uses the reciprocity and randomness of the wireless channel as a source of entropy and hence provides a quantum resistant solution to increase the trustworthiness in sixth generation (6G) communication systems. This work implements SKG in the presence of passive eavesdropping attack for device to device (D2D) communication systems. It provides a proof of concept (PoC) for SKG which can be a viable solution to use cases requiring low computation power, memory consumption.

While different studies have focused on specific parts of the protocol, there are only few that have implemented the full SKG chain [ZLM+20]. A typical assumption in the SKG literature, based on Jake's model [JC94], is that the channel decorrelates at half- wavelength. However, this assumption holds only when the environment has infinite uniformly distributed scattering [HDS+16]. Thus, in practice, it is important to account for the correlations between legitimate nodes and eavesdropper's observations. To address this point, a SKG protocol is implemented in the presence of passive eavesdropping attack in this work.

Methodology: For this experiment, three universal software radio peripherals (USRP) are configured, each equipped with a single antenna, representing two legitimate users, Alice and Bob, and an eavesdropper, Eve. The experiments were done in four scenarios: line-of-sight (LoS) static, LoS dynamic, non-line-of-sight (NLoS) static, and NLoS dynamic. The received in-phase and quadrature (IQ) samples at Alice, Bob and Eve are used to distil secret keys following the protocol in Figure 9-1.

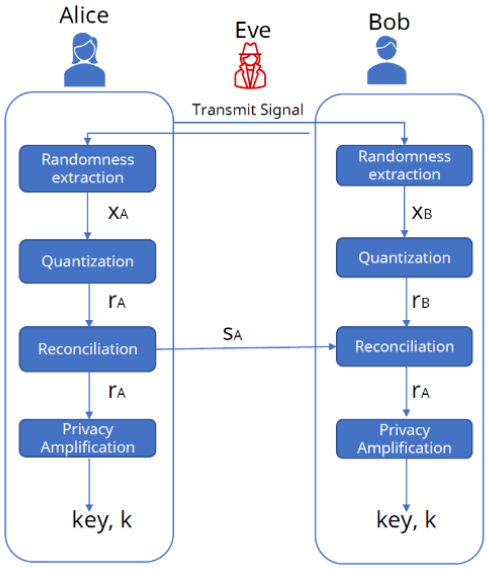

Figure 9-1: SKG protocol with Alice, Bob and Eve.

In the randomness extraction phase, legitimate users extract correlated channel observations using a filter bank, which are then converted into bits during the quantization step. Mismatches arising from receiver noise and imperfect channel estimations are corrected in the reconciliation phase using distributed source coding techniques. Evaluation of potential leakage occurs during the privacy amplification stage, ensuring the generation of secure confidential keys. In this setup, Alice, Bob, and Eve apply the protocol consistently (same

design parameters) using the respective received IQ samples in order to analyse and evaluate the feasible SKG rates. In this work, the design parameters are: (1) number of filters in filter bank, K; (2) number of quantization levels, Q; and (3) code rates during reconciliation, r. The achievable secret key rates are given by,

$$R = K * \log_2 Q * (1 - FER) * H_\infty(r_A|r_E, s_A) \quad \textbf{(9-1)}$$

where, FER is the frame error rates after reconciliation and $H_\infty(r_A|r_E, s_A)$ is the min-entropy of Alice's observations conditioned to Eve's observations and leakage during the reconciliation phase [MMC+23]

Results: In a TDD setup, Alice and Bob exchanged complex chirp signals. The passband frequency considered for the experiment was, $f_c = 3.75$ GHz, corresponding to a wavelength $\lambda \approx 8$ cm. Eve, acting as a passive eavesdropper, was positioned at five different locations relative to Bob, with distances of 2λ, 3λ, 4λ, 5λ, and 6λ. This translates to distances of 16, 24, 32, etc. in cm, to mount an on-the-shoulder eavesdropping attack. Eve recorded all communication exchanges between the legitimate users at each of her positions. To ensure the convergence of statistical min-entropy and leakage estimations, a total of 10^5 chirp signals were exchanged for each of Eve's positions. The signal bandwidth was set at $B = 70\,MHz$, the sampling rate at $f_s = 140\,MHz$, and the symbol duration at $T_s = 17.1875\,\mu s$. A detailed explanation can be found in [MMC+23].

Figure 9-2 represent the achieved SKG rates for the different positions of the eavesdropper given $K = 16, Q = 16$ from **(9-1)**. In case of on-the-shoulder eavesdropping attacks, there is no direct correlation between the distance of the eavesdropper to the SKG rates achieved, rather this depends on the multipath interference patterns at the eavesdropper which is highly specific to the environment.

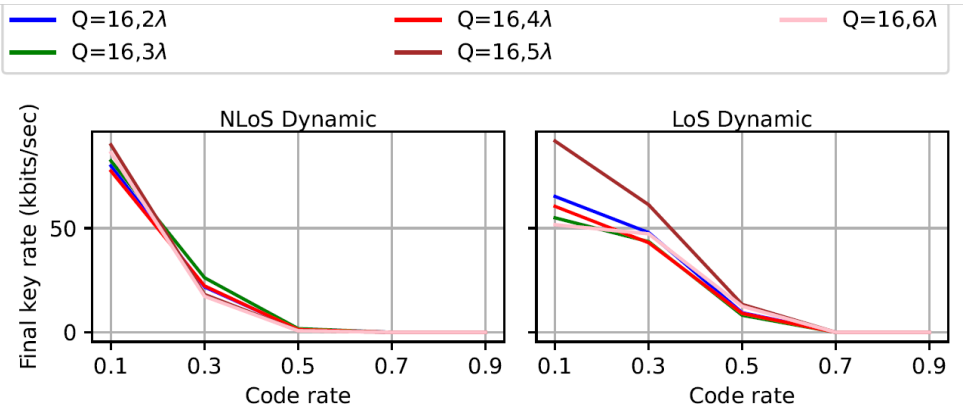

Figure 9-2: SKG rates achieved for K=16, Q=16 at different positions of Eve.

9.2 Impact of jamming as a foundation towards resilience

Problem statement: With the envisioned support of critical use cases and the broader availability of software defined radio (SDR) devices, not only the motivation for jamming is higher, but also the ease has been increased, making jamming a relevant threat for modern wireless communications [PZ22]. To develop effective countermeasures, it is essential to investigate jamming models.

Hence, as part of the threat analysis, in this deliverable on early results, different jamming models are defined and their impact on the performance is evaluated, which is often neglected in related work. However, the jamming impact is important, as there exists a trade-off between the damage a jammer creates and its detectability. For instance, a weak jammer is hard to detect, but is also a lesser threat and easier to cope with [GLQ14]. As a performance measure, the bit error rate (BER) at the physical layer (PHY) is considered. The presence of jamming at the PHY impairs the transmission and hence is expected to increase the BER.

Methodology: For the initial analysis a general single-input single-output (SISO) orthogonal frequency division multiplexing (OFDM) system in an additive white Gaussian noise (AWGN) channel with fixed signal-to-noise ratio (SNR) is considered.

For the jammer, different models are assumed, which are summarized in Table 9-1. They can be classified into modulated (single/multi tone, chirp) and noise jammers (narrowband, pulse noise). The defined models serve as prototypes, which in principle could also be combined to derive more complex patterns. All models are

normalized such that the total energy is the same, which is than reflected in the jamming-to-signal ratio (JSR). For instance, a three-tone multi tone jammer would have only a third of the signal power at each tone compared to a single tone jammer at the same JSR.

Table 9-1: Applied jammer models (modulated & noise jammers).

Model	Description	Configuration
Single tone	A single tone, i.e., a sinusoid, is transmitted by the jammer on a random frequency.	Random carrier frequency from the interval [0.1, 10] MHz
Multi tone	The multi-tone jammer is the sum of several single tones. Here the total power is distributed over all tones in order to yield the same JSR.	Number of tones uniformly chosen from {2,3,4,5}
Chirp (sweep)	Instead of emitting a single tone, the frequency here sweeps around a certain frequency within a given duration, after which it starts again.	Random frequency ranges from [5,15] MHz Random duration from [5,15] µs
Narrowband	This jammer emits white Gaussian noise on a limited narrow band.	Randomly chosen bandwidth from [0.2, 2] MHz
Pulse noise	Similar to the narrowband jammer, white Gaussian noise is generated and transmitted. However, now the entire observed spectrum is jammed but only for limited durations.	Randomly chosen pulse period from [20, 100] µs Randomly chosen duty cycle from [0.1, 1].
Unjammed (reference)	For reference, the system is also considered without any jammer	NA

Results: The settings of the simulation are summarized in Table 9-2, where the five jamming models are investigated. The simulation results are depicted in Figure 9-3. The baseline of the unjammed signal does not change for different JSR values, whereas the BER increases for stronger jammers as expected. The pulse noise and chirp jammer turn out to be the most efficient of the considered jammers even for lower JSR values. The reduction of the modulation order is not an effective strategy against jamming.

Future work will include more sophisticated modelling and the investigation of further transmission schemes with the aim of having more robust transmission in the presence of a jammer. Also, the jamming models may be extended to smarter strategies than static patterns.

Table 9-2: Simulation parameters.

Parameter	Value
Data subcarrier modulation order (QAM)	16, 64
Signal-to-noise ratio (SNR)	10 dB
Jamming-to-signal ratio (JSR)	-10:1:10 dB
Bandwidth	20 MHz
Total number of subcarriers	64
Number of simulated OFDM symbols	25000

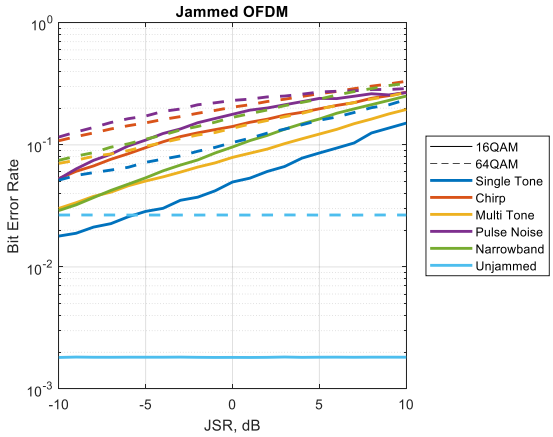

Figure 9-3: Bit error rate (BER) of a jammed OFDM system for two different modulations.

9.3 Indoor jammer localisation

Problem statement: In this section focuses on the process of determining the location of a blind transmitter or jammer without using any prior information about its location or the environment. The study of jammer localization is considered as this can be useful and essential for maintaining communication integrity,

enhancing network security, optimizing resource allocation, ensuring regulatory compliance, supporting spectrum management, and monitoring unauthorized interference.

It is considered that a jammer in an indoor space environment using four to six receivers. The jammer will transmit various waveforms, not aimed at compliance but aimed at disrupting communication. The question is whether the jammer can be accurately located by only the received signal strength.

Methodology: In the system model considered and the block diagram illustrated by Figure 9-4 [ACN+21], there are six sensing units (SUs) and one transmitter Tx1 with known positions. In addition, a jammer with an unknown location Tx2 is assumed. It is further assumed the nodes are synchronised using just network synchronization.

The received signal strength indicator (RSSI) is measured in a band of interest (sub-6GHz and millimetre wave for future testing) at the SUs assuming that there is receiving power from Tx1. For the current ongoing analyses, a log-normal path-loss model is calculated to obtain the respective distances between SUs and Tx1. Considering the distances and the present Gaussian noise, the presence and location of Tx1 can be identified and estimated. RSSI distance estimation is particularly affected by distance, frequency, multipath propagation, shadowing noise, and hardware nonlinearities which are already taken into consideration. However, if this value is further affected by the presence of a jammer, this can be identified. In the initial phase of the analysis, simulations on Dilution of Precision (DoP) are conducted to optimize the geometric placement of the SUs, aiming to minimize the Tx1 position estimation error. Subsequently, in the latter part of the investigation, practical experimentation will be performed utilizing the testbed available at IDLAB IMEC [IDLAB-01]. This real-world scenario evaluation aims to assess parameters such as data rate, reliability, latency, connection density, coverage, sensing accuracy, and jammer localization accuracy.

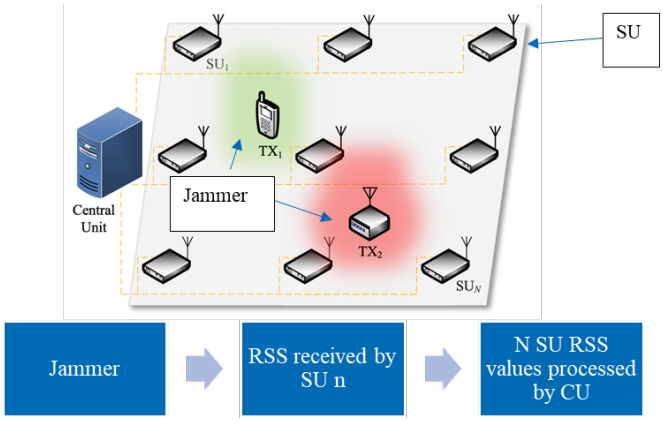

Figure 9-4: System model of indoor jammer localization [ACN+21].

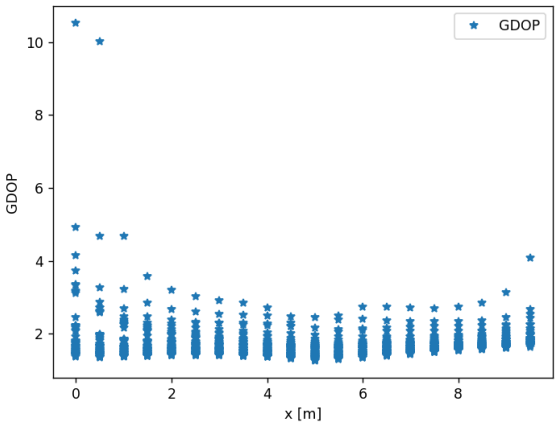

Figure 9-5: Geometric DOP results for the system model.

Results: The high values of DoP indicate that the current placement of the SUs is not feasible, making it impractical to conduct the planned experiments. To further investigate, it is required to change the placement of SUs or if not possible, change the experiment lab. The best DoP obtained results were when placing three SUs in parallel with the other three SUs, far enough to still ensure the coverage of six. The DoP in this case resulted be bounded by 10 as a maximum value, an average of 1.71 with a standard deviation of 0.50, and a minimum value of 1.25 as illustrated in Figure 9-5.

9.4 Security and privacy analysis of a general cellular JCAS system

Problem statement: JCAS gives the opportunity to the sensing participants, such as the network infrastructure or UEs, supplied with the required functionality, to acquire knowledge regarding the surrounding physical environment and the entities inside this environment. In general, this information may be public, or it may be private. In addition, due to the advent of automation, there are several use cases, such as automatic driving,

where information generated by a JCAS system is envisioned to be used for changing the physical state of manned or unmanned objects. Thus, new privacy and security requirement, beyond the existing ones connected to communication, need to be introduced to the future communication networks that support JCAS.

Methodology: Figure 9-6 presents the abstracted block diagram of a cellular JCAS system. As shown in this figure, upon the request of an application, called consumer, the physical environment of interest is sensed. The consuming application may be hosted in a sensing node (base station (BS) and UE), in the network, or in an external infrastructure or node. Possible sensing nodes which undertake the raw sensing measurements are the network infrastructure, UEs, or a combination of the network infrastructure and UEs. In general, the sensing nodes are expected to produce raw sensing measurements, compressed raw data, or lightly processed data, such as matched filtering and peak detection.

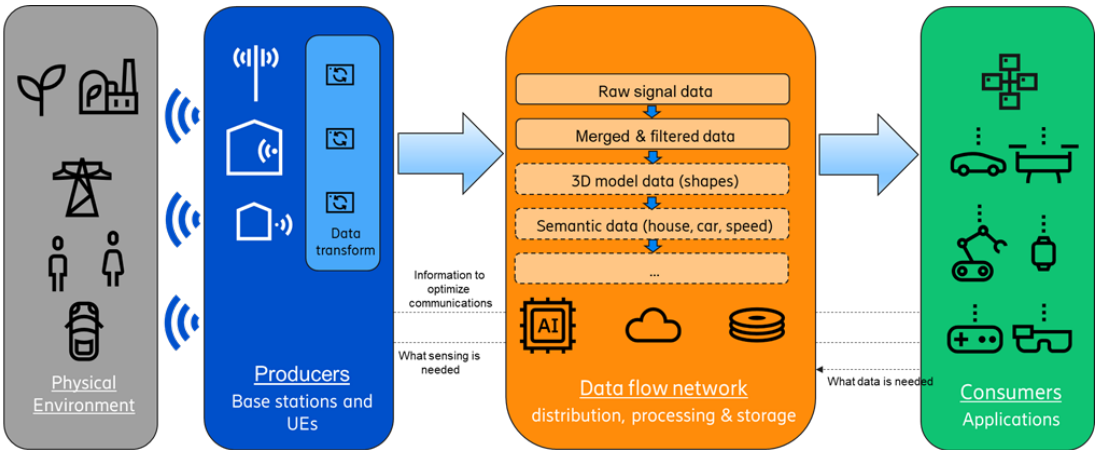

Figure 9-6: Abstract architecture of a cellular JCAS system.

In some use cases, for example optimization of beam-sweeping in sensing-aided communication, the collected data may be used locally. However, in the general case, the previous data will have to be forwarded to a central processing unit, here called data flow network, where they undergo advanced processing, under given privacy and security constraints, and acquire semantic meaning. Finally, the processed data are given to the consumer application following all the required security and privacy requirements.

A secure and privacy aware JCAS system, such the one presented in Figure 9-6, needs to satisfy that no security and privacy breach is possible to happen from the moment that raw measurements are generated up to the point where they are either used locally, or are given to the consumer application. This study focuses on the Spoofing, Tampering, Repudiation, Information disclosure (breach or leak), Denial of service, and Elevation of privilege (STRIDE) framework [MSFT-01] to identify the security threats encounter by a JCAS cellular ecosystem. Furthermore, the study utilizes the well-known Linking, Identifying, Non-repudiation, Detecting, Data Disclosure, Unawareness, and Non-compliance) LINDDUN privacy threat analysis framework [DWS+11] for identifying possible privacy threats faced by a JCAS system.

Security Analysis: Using the STRIDE framework for identifying the security threat faced by a cellular JCAS system, the following security risk are highlighted. *Spoofing*: 1) synchronization attacks, 2) raw data spoofing, 3) confusion, 4) ghost objects, 5) system information, 6) AI theft, 7) information disclosure, and 8) feed of false data to the consumer application; *Tampering*: 1) beamforming tampering, 2) request tampering, 3) timing tampering, 4) data tampering, 5) hide object, 6) ghost object, 7) blinding, 8) miss-classification, and 9) object modification; *Repudiation*: 1) false claim and 2) miss-correlation; *Information Disclosure*: 1) raw and semantic data, 2) detection and correlation results, 3) (non) detected objects, and 4) object reveal; *Denial of Service*: 1) physical denial of service and 2) noise addition; *Elevation of privilege*: 1) sensing of unintended or prohibited areas and 2) object reveal.

Note that the previous lists of risks for each security thread of the STRIDE is non-exhaustive. An exhaustive list requires to consider all possible use cases of JCAS in a cellular network. This is beyond of the scope of this study.

Privacy Analysis: In this study, the privacy analysis is done using the LINDDUN privacy threat modelling framework. In particular, the following privacy threats are highlighted.

- *Linking*: the unauthorized connection of processed or unprocessed sensing data with a private entity or other data of a private entity;
- *Identifiability*: the unauthorized use of processed or unprocessed sensing data for the extraction of the identity of a private entity;
- *Non-Repudiation*: the false attribution of an action or state to an entity using processed or unprocessed sensing data;
- *Detection*: the unauthorized extraction of private information (action or state) or insights about private information via the observation of the processing and/or transportation of sensing data;
- *Data Disclosure*: the unauthorized collection, processing, storage, and sharing of private sensed data extracted from processed or unprocessed sensing data (usually provided by the STRIDE framework);
- *Unawareness*: the unauthorized collection and processing of processed or unprocessed sensing data of private entities without their consent or with insufficient disclosure of the resulting privacy implications, the failure of allowing private sensed entities to access and manage their private data, and the failure to informs the consumer applications about the privacy implications of using the sensing infrastructure;
- *Non-Compliance*: the use and processing of processed or unprocessed sensing data and the use of sensing infrastructure that violate the industry practices and standards, and the local legislations and regulations.

Note that, due to space limitation, the detailed LINDDUN analysis of the general JCAS system of Figure 9-6 is beyond the scope of this study.

9.5 UE-related security aspects of JCAS

Problem statement and assumptions: Technological advances not only enable new functionalities such as bi- and multistatic sensing but also provide attackers with more powerful tools to perform malicious attacks. While the threats to communication systems are generally well-understood, introducing sensing capabilities adds a whole new attack surface that needs to be studied thoroughly to avoid potential risks, to establish trust and to prevent privacy incidents.

The value related requirements for trustworthiness, security, and privacy are especially important for sensing in the vicinity of users that utilize their mobile devices to perform sensing since the sensing results contain sensitive data of the user that may straightforwardly be linked to specific devices and individuals, if no precautions are taken. What follows describes potential threats to such user equipment (UE)-centric sensing by evaluating and adopting attack schemes from ranging and sensing.

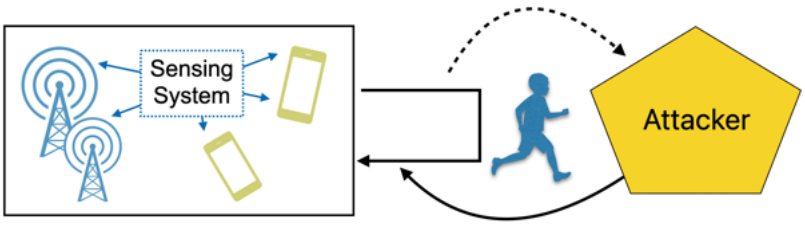

Figure 9-7: System model of UE security in JCAS.

This study assumes a sensing system that may be comprised of one or more UEs that perform monostatic or bistatic sensing, potentially with active involvement of a transmission point (TRP), as shown in Figure . The sensing system performs sensing by transmitting and receiving some sensing signal that is reflected by targets. It is assumed that all nodes of the sensing system are trustworthy. The malicious agent is placed in the sensing channel. It can receive the transmitted sensing signal and to transmit is back to the sensing system.

Attack models for Ranging and Sensing: In ranging, the purpose of an attack usually is to present a different distance between two devices to the ranging initiator, usually a shorter one as often specific action such as unlocking a car are triggered if the distance between two devices falls below a specific threshold. Multiple

attack schemes are known for this purpose, e.g., replay attack, early detect/ late commit [LKR+21], or the Cicada attack [SRZ+21] that exploits cross-correlation properties. Early detect/late commit (ED/LC) is especially suited for multi carrier waveforms such as OFDM due to deterministic signal properties. In the case a cyclic prefix is used, the attack becomes trivial since the signal may be recorded and delayed.

For sensing, the attack scheme is not that trivial. Compared to ranging, it is not sufficient to generate one additional shorter path. Instead, a consistent environment has to be presented to the victim. This requires a detailed knowledge of signal parameters and the relation between victim and attacker. Furthermore, it is important that the attacker cannot 'block' the actual channel of the victim and only add targets to the real channel. Sensing usually relies on angular estimation as a key functionality which is difficult to manipulate in real world scenarios. Yet, the area of '*radar target simulators*' demonstrates that it is at least in a static lab environment nicely possible to inject over the air signals to a radar to 'simulate' an arbitrary environment [SJM+21]. They are commonly realized with analogue or digital delay lines and frequency modulation for Doppler, or based on signal and evaluation properties that are specific for frequency modulated continuous wave (FMCW) radars.

ED/LC Attack for Sensing: Simulations are carried out to demonstrate the applicability of ED/LC attacks to sensing. This work assumes a monostatic SISO joint communication and sensing (JCAS) 'Radar' with double use of communication data using quadrature phase-shift keying (QPSK) modulation. To visualize the potential attack method, a reference that shows radar measurements of an 'actual channel' with a few targets using cyclic-prefix OFDM is compared to the attack principle. For the ED/LC, the idea here is that an attacker wants to 'simulate' the same scenario to the radar.

To do this, the cyclic prefix (CP) is recorded from a LoS reception, modified by super-positioning delay- and Doppler-shifted versions, and retransmitting them at the corresponding tail of the OFDM symbols, where the CP was originally taken from. To demonstrate the potential, any additional path loss is neglected, and it is assumed that the radar only receives the signal from the attacker.

The results are shown in Figure 9-8, where it can clearly be seen that the method generates the same radar image by just using the CP part of the signal at the tail of each OFDM symbol. As expected, the signal level is decreased by 12 dB since only one quarter of the energy is received. Furthermore, the noise level is increased. This is caused by the signal only spanning parts of the fast Fourier transform (FFT) time duration, which presents a rectangular function that leads to a sinc-function in frequency domain at each subcarrier, leading to inter-carrier interference. Yet it is important that the radar image is free of any additional artifacts, making such an attack hard to detect.

Finally, it should be mentioned that in reality the attacker is only able to 'add' the desired scene on top of the intended measurement of the radar since it can hardly block the scatterers. Also, the exact position of the simulated targets depends on the relative distance and relative velocity between radar and attacker as well as synchronization offsets in time and frequency.

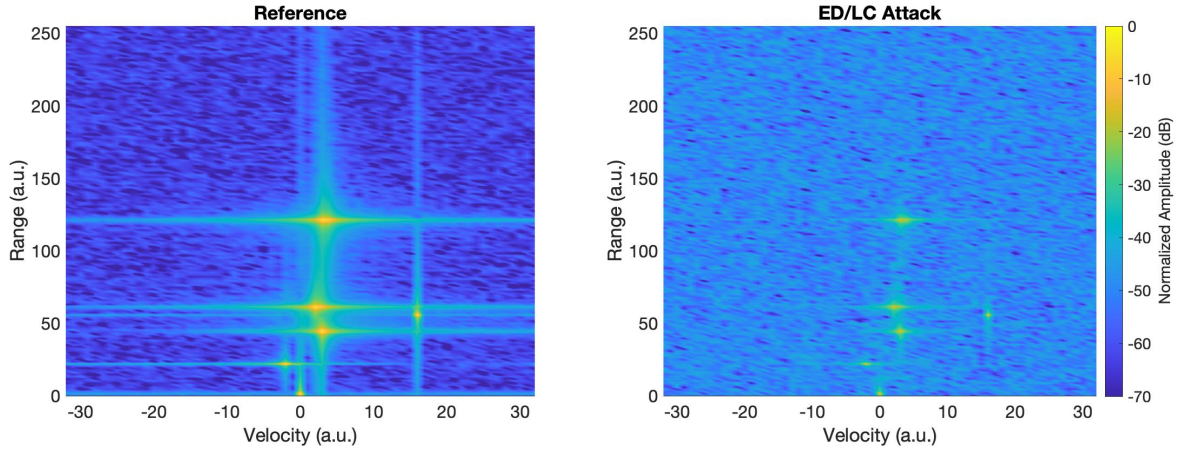

Figure 9-8: Simulation results for ED/LC Attack. Reference vs. ED/LC Attack using cyclic prefix only.

10 Proof-of-concepts and simulators

This chapter highlights various enabler is a proof-of-concept (PoCs) and simulation tools for the evaluation of 6G technologies.

10.1 Link modelling of 6G physical layer

System model: A link-level simulation tool of the downlink 5G PHY has been developed, including models of multi-cluster propagation channels in the sub-THz bands. The simulator provides performance evaluation of D-MIMO and beamforming. The aim is to understand the impact of these enhanced PHY schemes to improve the system performance and to optimize the parameters, especially in mmWave (FR2 frequency bands) and sub-THz.

The simulation chain presented in Figure 10-1 has been implemented, based on the 3GPP specifications [38.104], [38.211], [38.212]. The blocks are developed in Python, using the Sionna open-source libraries as a starting point [Hoy22], offering substantial flexibility in the development, choice of the use cases, etc. It allows the integration of new algorithms/configurations so that the chains can easily evolve.

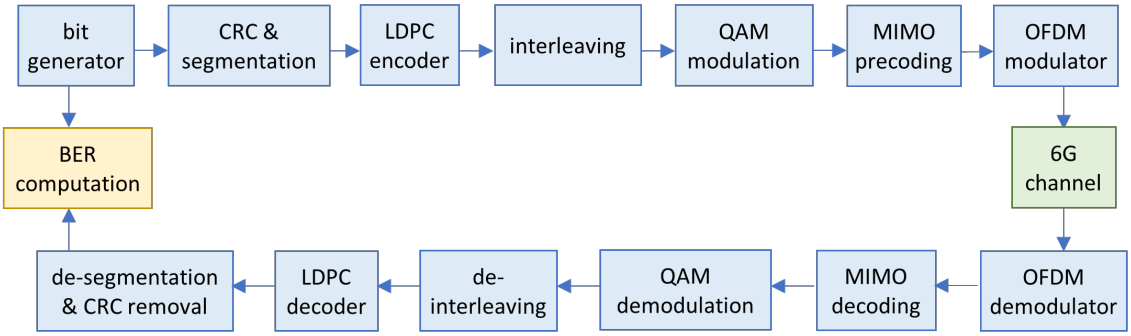

Figure 10-1: Diagram of the 6G PHY layer simulator.

The data flow is randomly generated by a bit generator, and feeds the chain of baseband signal processing blocks: segmentation, cyclic redundancy check (CRC), interleaving, etc. The forward error coding scheme is the LDPC specified in [38.212]. OFDM modulation is implemented, and the signal samples are convolved with a randomly generated channel impulse response. The reception part of the chain includes the demodulators and decoders, leading to an estimation of the transmitted bits. A dedicated block compares the initially generated bits with the estimated bits and computes the bit error rate (BER) and block error rates (BLER).

The first version of the simulator includes an ideal digital MIMO precoding (e.g., based on the singular value decomposition of the channel matrix). In a future deliverable, the obtained BER vs. SNR results are used as reference, and further compared with other MIMO schemes, such as D-MIMO and hybrid beamforming, as discussed in sections 5.1.1 and 5.2.5.

The fast-fading channel model is initially based on the 3GPP specification [38.901], which is valid for carrier frequencies ranging from 0.5 to 100 GHz. This model should evolve towards higher frequencies. The blocking effect that occurs at high frequencies is also considered. At the receiver, the noise is modelled as a Gaussian random variable.

The main input parameter is the received SNR that includes the transmit power, the path loss, and the noise variance. The antenna gains and orientations are included in the fast-fading component of the propagation channel.

The aim of the simulator is to evaluate the performance of the future 6G PHY layer in a large variety of contexts (spectrum, environment, etc.), therefore it can be used to determine whether the conditions of the use cases defined in WP1 are met. The simulations will provide the following metrics: BER, BLER, SNR, spectral efficiency, throughputs.

The proposed link-level simulator is defined at the baseband level, RF aspects are not modelled. The signalling is not modelled so that only data bits are implemented. The transceiver-receiver synchronization is assumed to be perfect.

10.2 Flexible modulation and transceiver design

This section describes initial implementation of a flexible transceiver. This system enables experimental verification of mobile communication system applications and use cases. The idea for this prototyping system is to utilize the flexibility provided by SDR devices to allow testing of dynamic scenarios and challenging use cases for which static configuration of testbed components is not sufficient. Figure 10-2 illustrates an overview of the flexible transceiver system and its components, including

- **SDRs**: 4 USRP X310 are used to provide 4 RF chains for TX and RX (4x4 MIMO), these devices are used for generating and receiving of radio signals
- **Controller**: NI PXIe-1082 Chassis with NI PXIe-8133 embedded controller running LabVIEW software. This component is responsible for forwarding control signals from the host to the SDRs.
- **RF Frontend**: the configuration of our system allows for different frontends, such as dedicated beamforming networks of phased arrays, butler matrices, or antenna arrays, etc. For instance, in the analogue multicarrier demonstrator, a combined with a dipole antenna for joint transmission and reception of the signals for all RF chains. The purpose of the frontend is to radiate/receive radio signals that are generated/processed by USRP's.
- **Host**: any computer which runs an application programming interface (API) to generate control signals/remote procedure calls (RPC) for the controller to orchestrate the flexible transceiver. The Host also provides the in-phase and quadrature (IQ) data samples that are transmitted and receives the IQ samples provided by RX signal chains.

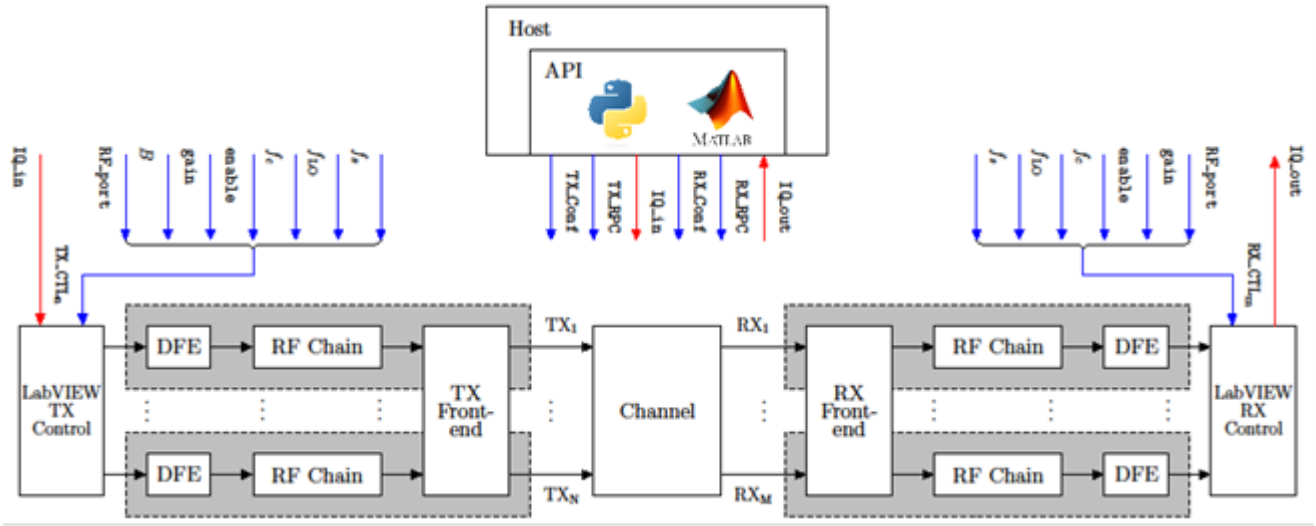

Figure 10-2: Schematic of flexible transceiver.
Signal flows are indicated by arrows. Red arrows are used to highlight IQ data and blue arrows to indicate control signals.

The goal of this transceiver is to provide abstraction to allow researchers to experiment on real hardware with little overhead by merely calling API functions in common programming languages such as Python or MATLAB. The API interacts with the controller, using RPC calls to configure and control the experiments and measurements. A user of the flexible transceiver can provide starting configuration of the experiment for TX and RX chains. A vector of IQ samples is provided to the API by the user. These samples are transferred to the controller, which forwards them for transmission. The signals sent from each TX chain are independently adjustable, allowing for digital beamforming. The receiver records the received signal, and the received IQ samples are forwarded via the controller to the user. Synchronization and timing are managed by the controller to allow for ease of use of the flexible transceiver system. Synchronization is achieved via a 10 MHz reference signal and a 1-pulse-per-second (PPS) for triggering. Furthermore, during experimentation, the RF parameters

for each chain can be dynamically adjusted, including signal bandwidth, gain, enabled RF chains, carrier frequency, local oscillator (LO) frequency, and sample.

An initial laboratory prototype version of the flexible transceiver system is illustrated in Figure 10-3. This version provides basic functionality, including basic API functions to configure TX/RX chains and select custom waveforms represented by the IQ samples sent to the controller. Additional features are under development, and will be incorporated in the future deliverables, such as dynamic adjustment of parameters by RPC, phase coherence of TX/RX which is required in some transmission schemes.

Figure 10-3: Flexible transceiver laboratory setup with combiner.

10.3 AI-native air interface

This subsection describes two demonstrations of crucial enablers of an AI-native air interface. The objective of these demonstrations is to show that ML can provide real-world performance gains in compressing channel state feedback and in enabling pilotless OFDM transmissions.

10.3.1 ML-based channel state feedback compression in a multi-vendor scenario

This PoC aims to demonstrate the feasibility of cross-vendor cooperation, between UE-side ML Model (also referred to as Encoder) and NW-side ML Model (also referred to as Decoder), to enable joint AI solutions for enhanced channel state feedback compression.

In Section: ML-based channel state feedback compression in a multi-vendor scenario, a simulation study is presented that demonstrates that sequential training of multi-vendor ML models achieves similar performance compared to a joint training solution and that a common NW decoder model can be trained through sequential training to deal with multi-UE vendor scenarios. See that specific Section for the results obtained.

Given the simulation results, the next step is the lab testing and Over-The-Air (OTA) evaluation of the proposed scheme. This section describes the planned process for the data collection and tests for this PoC. It is composed of two parts: a lab test and an OTA test. For the lab test, a gNB and a UE device will be connected through an 8x4 channel emulator. Certain fading channel types (to be defined upon OTA evaluation) will be configured for data collection and testing. To emulate a multi-vendor scenario, the lab testing and OTA evaluation will use a Nokia gNB and a Qualcomm UE.

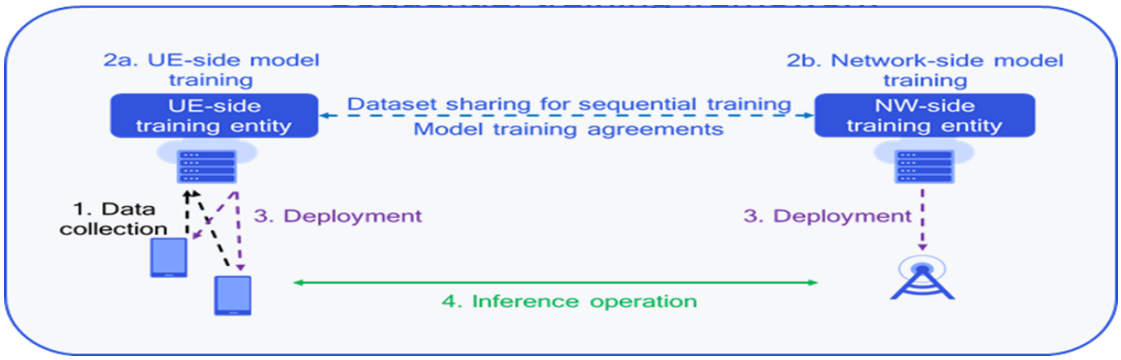

Figure 10-4: Illustration of the sequential training process.

The lab testing process is as follows:

1. Data collection stage: the UE will log estimated CSI RS channels received through the channel emulator for a certain duration (to be defined upon OTA evaluation) to collect sufficient channel data for training. This is the step 1 depicted in Figure 10-4.
2. Offline-training stage: The UE will first train its encoder models with CSI-RS channels collected in the lab (step 2a.), and then shares the dataset with the network, i.e., this is the dataset sharing step. Two encoder ML models, with different type of architecture, will be trained separately to mimic two different UE vendors. Each encoder will share a dataset with the network. The network will then train the decoder models (step 2b NW-side model training). With the individual dataset, the network will train the dedicated decoder model for each encoder. With mixed dataset, the network will train a common decoder that can work with both encoders.
3. Inference test stages: Different UE encoder and network decoder models will then be deployed at the UE and gNB side (step 3. Deployment) in separate tests. The gNB decoder output will be used to calculate the DL precoder for the PDSCH. The DL performance will be measured in a lab environment with ML-based CSF. The squared generalized cosine similarity (SGCS) will be evaluated. The SGCS is calculated based on the UE logging of encoder input and encoder output and the corresponding gNB logging of decoder output. The throughput and SGCS are compared for 4 different encoder/decoder combinations, specifically,
    - Encoder 1 + dedicated decoder 1,
    - encoder 1 + common decoder,
    - encoder 2 + dedicated decoder 2,
    - and encoder 2 + common decoder.

    If each encoder model performs similarly with both its dedicated decoder and the common decoder, it means that a common decoder, trained sequential, is a viable solution to deal with multiple UE vendors in the network. If this is the case, the lab test is successful and the OTA test can begin.

The OTA test will be conducted in an outdoor test area, e.g., a parking lot, with the gNB installed at an elevation of approximately 20 meters to cover the area.

1. Data collection stage: OTA CSI-RS channel will be collected during both mobility and stationary tests. The mobility routes will be chosen to have reasonable coverage in the test area, while the stationary locations will be chosen to sample different UE-gNB distances as well as different angles.
2. Offline-training stage: The mobility data collected from step 1 will be used to train the UE encoder models. Similar to the lab test, two different UE encoder models will be trained. The corresponding data sets will be shared with the network to train its decoder models. Similar to the lab test, the network will train a dedicated decoder for each encoder, and a common decoder model for both encoders. The trained UE encoder and gNB decoder models will then be used to run offline inference tests applied to the stationary data. If the encoder/decoder models give reasonable SGCS when applied to stationary data, the models are ready to be tested in OTA for inference test.
3. Inference test stages: Inference tests at the stationary locations will be performed. Similar to lab test, different encoder/decoder combinations will be deployed, and the SGCS will be evaluated. If for each encoder model, the dedicated decoder and common decoder gives similar performance, this proves that common decoder based on sequential training is a viable solution to deal with multiple UE vendors in the

network. The tests will be repeated in multiple runs. If different runs give comparable results, this will prove that the encoder and decoder models are stable, and the OTA test results are consistent. In that case the OTA test will be considered as passed.

10.3.2 Pilotless operation with a partially learned air interface

System model: The primary target of this PoC is to demonstrate the practical feasibility and performance gains of an ML-based pilotless air interface. The concept is shown in Figure 10-5, which illustrates the considered OFDM link. In particular, the approach involves learning the transmitter constellation (DeepTx) and receiver algorithm (DeepRx) to achieve a system which can communicate without any channel estimation pilots. This will result in throughput gains via the reduced overhead.

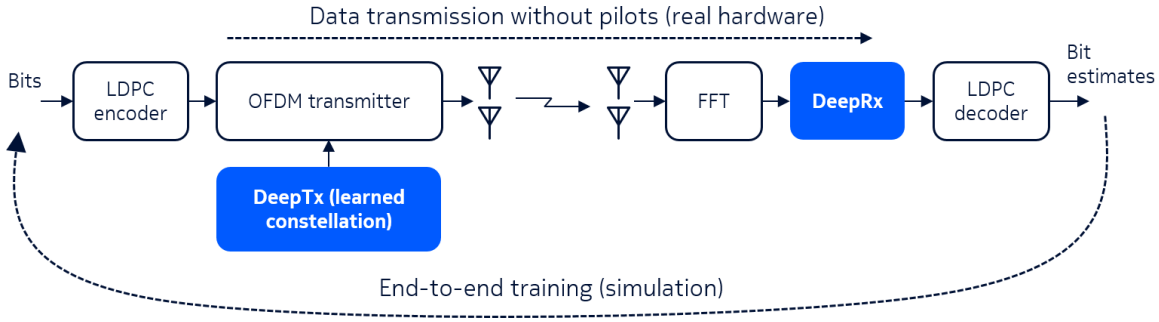

Figure 10-5: AI-based pilotless proof of concept.

The basic approach of the considered PoC is depicted in Figure 10-6, which shows the training and validation methods. In particular, the required ML models are trained in a simulator, after which the models are deployed to the target hardware and the performance is validated with real RF measurements. This ensures that the results show two aspects: (i) a simulator-trained model can generalize to unforeseen real-life channels, and (ii) a ML-based air interface can outperform a pilot-based system. It should also be noted that this PoC is a SISO variant of the approach described in Section 6.1.1.

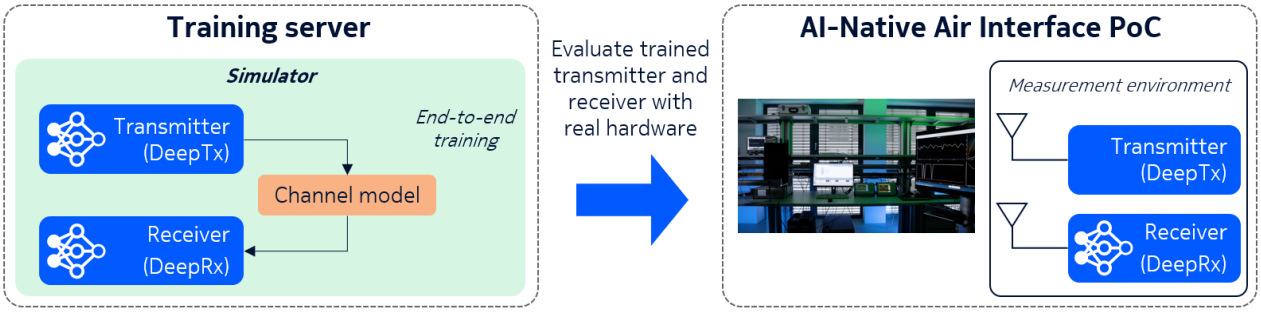

Figure 10-6: Depiction of the training and measurement setup.

The PoC is based on a GPU-based implementation of 5G L1, where some of the functions can be replaced with pre-trained ML models (in this case, the constellation shape and the receiver algorithms are replaced). This makes it also possible to compare the performance of the ML-based air interface to a corresponding 5G air interface, using the very same hardware. The RF signals are processed with USRP X310 software defined radio, which is connected to the GPU with a fibre connection. The channel effects are produced by a channel emulator, which allows for experimenting with different channel environments under laboratory conditions. In practice, the performance of the proposed approach is compared to the baseline by conducting back-to-back measurements with both approaches under the same channel conditions.

Measurement results: The considered air interface options were measured under a vehicular SISO scenario with 60 km/h of mobility, using a 16-point constellation. The resulting throughput gain of the ML-based approach was measured as **21% over a 5G baseline**. The gain can be attributed to two different factors. Firstly,

the higher accuracy of ML-based DeepRx reduces the block error rate, especially under high mobility levels. Secondly, there is a spectral efficiency improvement from pilot overhead removal which also translates to a throughput gain. Altogether, this result shows that the proposed approach achieves tangible gains with real RF signals. The specifications and assumptions are listed in Table 10-1.

Table 10-1: Assumptions for AI/ML-assisted transmissions.

Type of the used AI/ML training method	Supervised
Training	Offline
'Features' and 'labels' for training the models	Autoencoder-type approach for detecting transmitted bits
Type of the AI model	CNN
Model architecture	Convolutional ResNet with a learned multiplicative layer
Loss function for training	Binary cross-entropy
Model deployment	Transmitter and receiver
Training scheme	Centralized

10.4 Bistatic joint communication and sensing

System model: The implemented bistatic sensing system leverages evaluation kits (EVK) from Sivers Semiconductors in 57-71 GHz for the transmitter and receiver radios, coupled with the RFSOC from Xilinx for efficient and high-speed signal processing according to Figure 10-7. This setup is specifically designed to utilize 5G waveforms, enabling us to explore the capabilities of joint bistatic sensing and communication within a communication framework. The objective is to demonstrate a joint communication and sensing proof of concept that showcases the potential of using the same hardware for both communication and sensing.

Demonstration of the POC through measurements: Using the 5G NR standard waveform, different waveforms can be transmitted using QPSK and 16-QAM to 256-QAM signals for the communication demonstration. The SSBs for synchronization is used according to 5G NR standard.

A bistatic sensing scenario is considered, in which the 5G waveform is used for sensing. The sensing is maintained through beam-pair power measurements and time of arrival (TOA) estimation. In both, 50 distinct TX beams and 56 distinct RX beams are used for beam steering in the horizontal dimension and scanning the environment for targets. To measure the moving target and remove the background effect, a background subtraction phase is also applied to the beginning of each measurement. The sensing algorithms are implemented as two parts, where the first part is implemented in the FPGA and the second post-processing part is implemented in the PC. This approach can decrease the processing time and make the update rate of sensing algorithm (for object detection) less than a second. A snapshot of the beam-power map, TOA, and 2-dimensional target location are depicted in Figure 10-8.

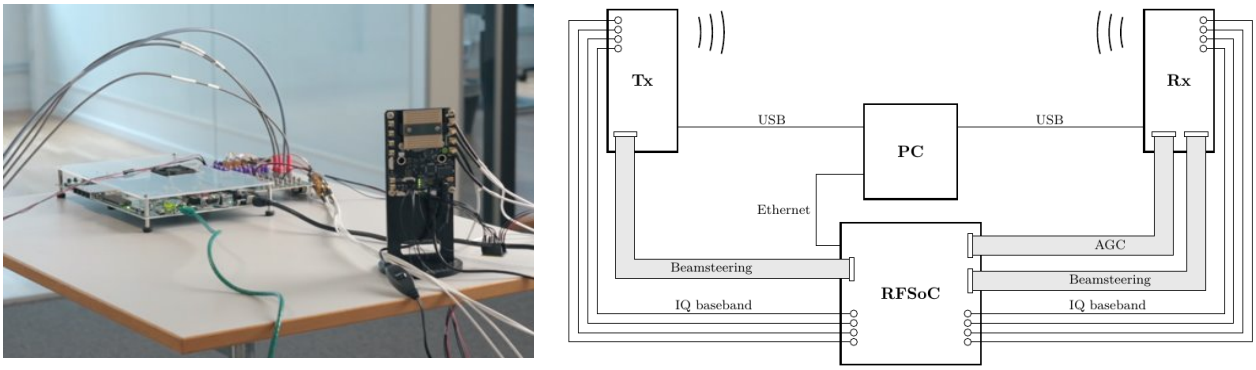

Figure 10-7: Qamcom RF setup (including the Xilinx board and Sivers EVK) for joint communication and sensing.

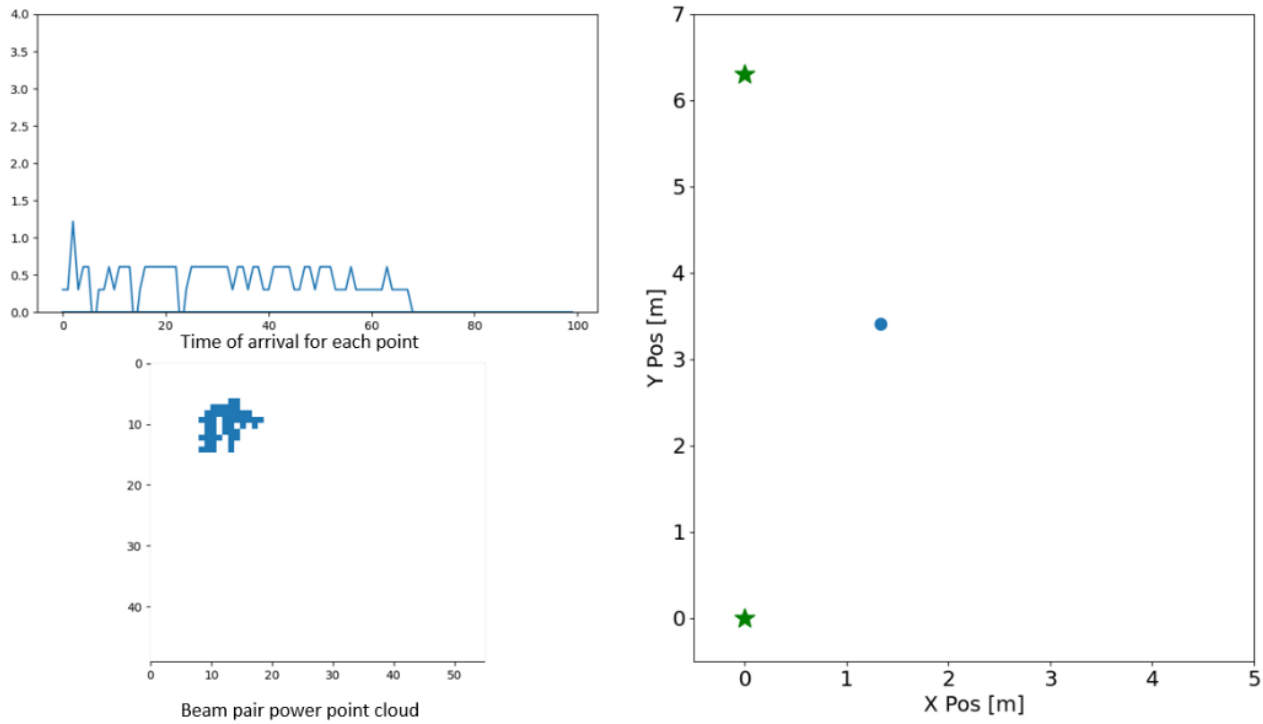

Figure 10-8: Beam-power map on lower left figure (point cloud power of detected targets), TOA on upper left figure, and estimated position using Qamcom JCAS setup on the right figure.

10.5 Power consumption of JCAS

This section focuses on experimental analyses of the power consumption and consumption factor on a mmWave setup. The planned experiments will include according to Qamcom RF setup in Figure 10-7, a transmitter, receiver, and power analyser. The power consumption values will be measured for different situations.

System model: Considering the expected power consumption and consumption factor changes on mmWave systems, it is decided to use the Qamcom Joint Communication and Sensing setup presented in Figure 10-9 to perform the power consumption measurements. The setup contains the RF Module EVKs that are "plug and play" platforms, including patch antennas to evaluate the Sivers Semiconductors beam steering RFICs - TRX BF/01 for unlicensed 5G (IEEE 802.11ad [IE80211]) and TRX BF/02 for licensed 5G. Frequency ranges include 24-29.5 GHz (TRX BF/02) and 57-71 GHz (TRX BF/01). The maximum power lies between 15-40 W. The power consumption measurements and analyses will include different states: (i) power required to turn the device on while the radio interface is down; (ii) power consumption required to generate traffic when the radio interface is up; (iii) power consumption of on and off beacon period; (iv) power consumption during the transmission and reception modes; (v) power consumption when changing propagation conditions (LoS, NLoS). Further, in the measurements, parameters that are important include signal to noise ratio (dB), bandwidth (Hz), frequency (Hz), transmit power (W or dB), receiver power (W or dB), respective gains at the Tx and Rx (dB), distance (m), number of antennas, received signal strength for each beam (dB), data rate (bps), estimation error or accuracy (m) on sensing (required for the selected gesture recognition tests), environment between transmitter and receiver, and sampling rate (Hz).

The power consumption analyses will include the level of the transmit power required to ensure the minimum SNR at the receiver, and the impact that these values have on power consumption and consumption factor. For the measurements, Keysight N6705B Power Analyzer will be used.

Assumptions: All individual device components' efficiency values will be taken from the technical documentation of the device.

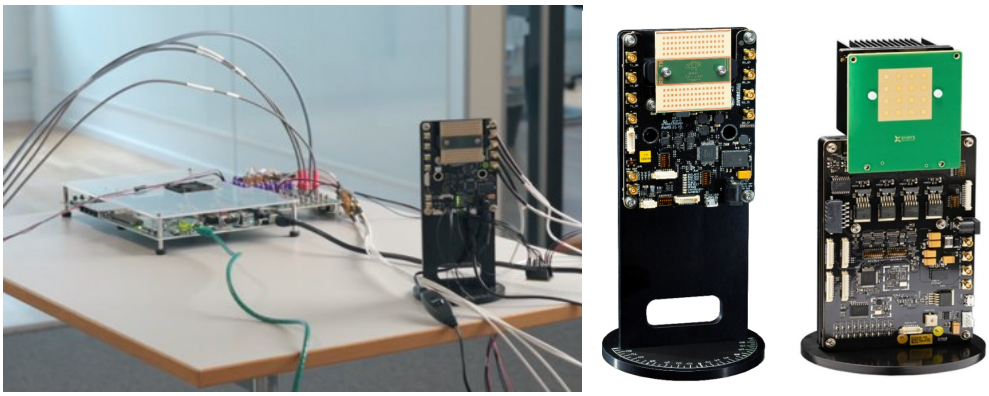

Figure 10-9: Qamcom RF setup together with RF modules for joint communication and sensing.

10.6 EMF Assessment

Background: D-MIMO is considered as a potential candidate technology for beyond 5G and 6G systems as it could offer a solution to break the interference limitation, thus achieving higher network capacity. When a new generation of mobile technology is introduced, questions about electromagnetic field (EMF) exposure may be raised. The EMF exposure limits are given in terms of basic restrictions (physical quantities inside the body) and reference levels (external field quantities derived from the basic restrictions) according to the EU recommended limits and the international EMF exposure guidelines, such as those provided by the International Commission on Non-Ionizing Radiation Protection (ICNIRP) [ICNIRP20].

Aim of the work: To simulate EMF exposure from a D-MIMO system, a full-wave analysis of the antennas and of the surrounding electrically large environment is infeasible due to the extremely large computational demand. A solution is to use hybrid simulation approaches, with which the antennas and the human body model (phantom) are simulated by full-wave methods, while the field propagation is simulated by asymptotic approaches, such as the ray-tracing method. In this study, a hybrid simulation scheme is developed to assess the downlink EMF exposure from 6G D-MIMO deployments. The same scheme is also applied to 5G massive MIMO (mMIMO) deployment for the sake of comparison. Two precoding schemes, including single-user equal-gain transmission (EGT) and multi-user centralized zero-forcing (CZF), are considered. The study is conducted in a realistic industrial indoor environment at 3.5 GHz using representative array antenna designs and a full-body phantom.

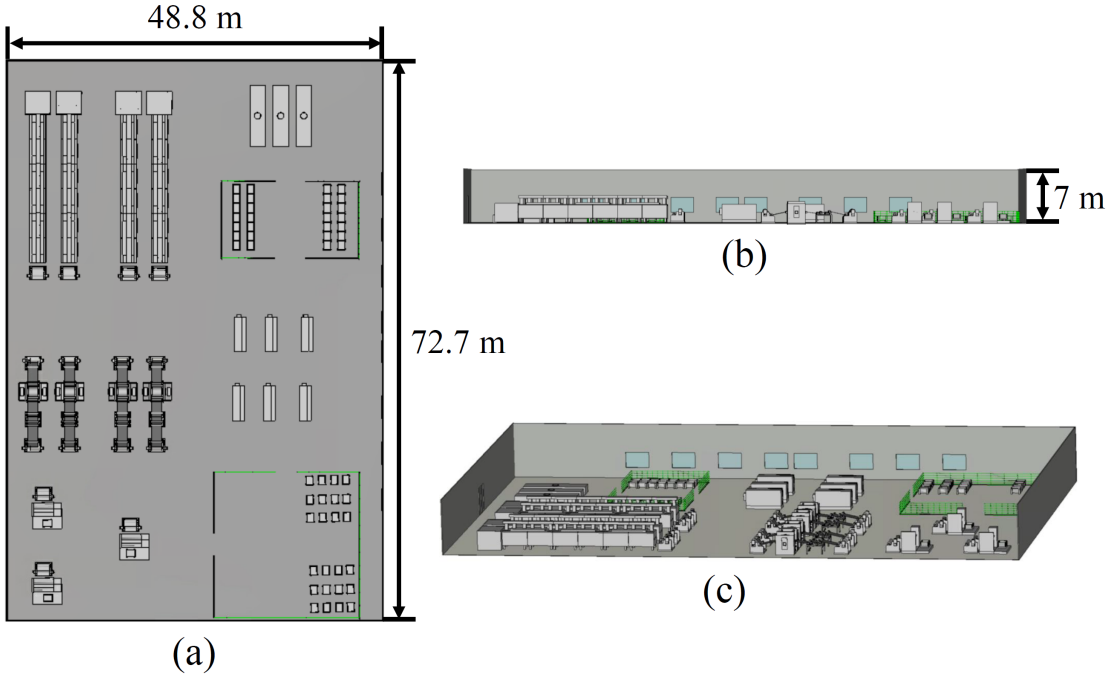

Figure 10-10: Battery factory model used for the study: (a) top view, (b) side view, and (c) perspective view.

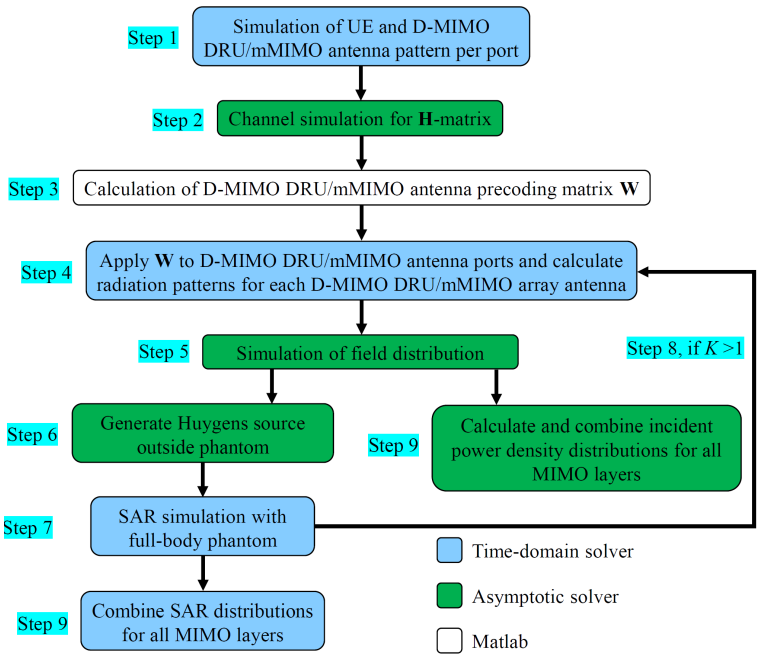

Figure 10-11: Workflow for the EMF exposure assessment for D-MIMO and mMIMO technology by using the hybrid simulation scheme

System model: The employed indoor industrial environment is a battery factory model, as shown in Figure 10-10, provided by CST Studio Suite. The interior size of the factory is 48.8 m × 72.7 m × 7 m. The EMF exposure levels were evaluated at 3.5 GHz for three deployment scenarios, two using D-MIMO (one with 24 distributed radio units (DRUs), and one with 6 DRUs), and one using mMIMO technology (one array antenna). For each D-MIMO DRU, a 2 × 2 array antenna was used, while for mMIMO, a 4 × 8 array antenna was used. The antenna element of these arrays was a dual-polarized circular patch antenna. The UE was represented by a half-wavelength dipole.

In order to compare the EMF exposure for different number of UE antennas and different precoding schemes, the EMF levels were normalized to the total configured power of 1 W of the system. Due to the power tapering used in CZF, the total radiated power was slightly lower than 1 W. Also, the power radiated to serve different UEs was not the same as the power tapering differs for the antenna ports among the layers.

In total, 20 well separated UE positions were selected for statistical analysis of the EMF exposure levels. For the different deployment scenarios, including one D-MIMO scenario with 6 DRUs, one D-MIMO scenario with 20 DRUs, and one mMIMO scenario, 20 different UEs (for EGT) or 20 UE combinations randomly chosen from the defined UE positions (for CZF) were used to evaluate the statistics. In all cases, there was one body phantom per scenario, which was placed around one of the served UEs at distance of 1 m.

Simulation workflow: A flowchart of the developed hybrid simulation workflow is presented in Figure 10-11. CST Studio Suite 2022 was the software used for conducting the study. The time-domain solver based on the finite integration technique (FIT) was used for full-wave simulations, and asymptotic solver based on the shooting and bouncing rays (SBR) method was used for ray-tracing simulations. The quantities obtained from the simulations can be found in Section A.2.4.

Results: Examples for the incident power density (S_{inc}) distributions for CZF with 4 UEs, D-MIMO with 6 DRUs and 24 DRUs, and mMIMO deployment scenarios, are presented in Figure 10-12. These examples correspond to one combination of 4 simultaneously served UEs out of the 20 simulated UE combinations. The S_{inc} distributions in this figure are shown for the horizontal plane z = 1.33 m.

As can be seen from the figure, S_{inc} is overall lower for the 24 DRU scenario compared with S_{inc} for 6 DRU scenario. This can be explained by the fact that power is more spatially distributed with the increasing number of DRUs. The mMIMO scenarios result in a higher peak value of S_{inc} compared to DMIMO due to the higher

EIRP from a single radio unit, while the median levels remain comparable between D-MIMO and mMIMO scenarios. In all studied cases, the EMF exposure, considering both incident power density and SAR, is well below the limit value.

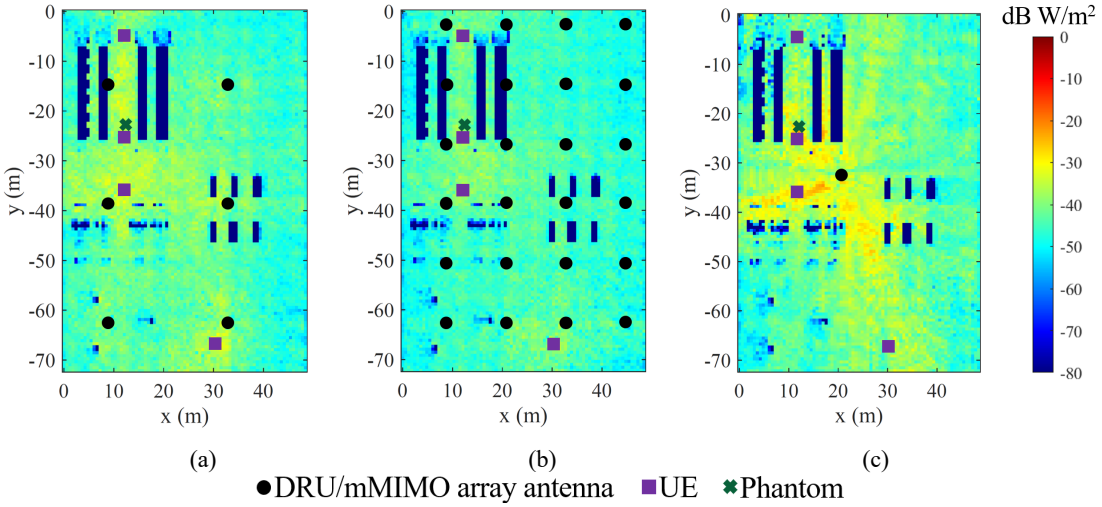

Figure 10-12: Incident power density (S_{inc}) distribution for CZF-precoding with K = 4 UEs for one of the studied scenarios for a total configured power of 1 W for: (a) D-MIMO with 6 DRUs, (b) D-MIMO with 24 DRUs, and (c) mMIMO.

10.7 Channel measurement data and model

Background: Channel measurements play a critical role in channel modelling. The most common methods of channel modelling, such as the stored channel, deterministic, and stochastic channel models, are based on multipath data obtained from measurements. A stored channel model directly replays the measured channel impulse responses which makes the generated channels realistic but can only generate as many channels as there are in the measurements. Measured channels are also indirectly used in deterministic channel modelling, where the channel response is calculated by allowing rays to propagate and interact with different objects in the environment. The amplitude and phase contribution of each interaction depend on the electromagnetic characteristics of each object, which may either be based on a standard or estimated from the measurements. The latter also pertains to the so-called calibration of ray-based propagation tools used for deterministic channel modelling. Finally, stochastic channel models heavily rely on measured multipath data to determine the input channel parameter values. These models can produce large amounts of multipath data with probability density functions consistent with the measured channels for a given scenario. In this section, the measurements performed at sub-THz and Frequency Range 3 (FR3) bands and the channels generated using the developed channel models are presented.

Channel measurements at 142 GHz: Radio channel measurements were performed in an indoor entrance hall and outdoor sites, including suburban, residential, and city centre environments both in line-of-sight (LoS) and non-LoS (NLoS) link conditions. The measurements were taken over a maximum distance of 65 meters for the indoor site and up to 170 meters for outdoor sites. The frequency range scanned was 140 GHz to 144 GHz, using a vector network analyser with frequency converters. The Tx and Rx have omnidirectional and rotator-mounted directional horn antennas, respectively. Both Tx and Rx antennas are vertically polarized. The Rx antenna sweeps the whole horizontal plane with a 5° azimuth step while its elevation is kept at 0°. More information on the channel sounder architecture and measurements can be found in [DHH21, DH23]. The data obtained from these measurements were single-directional, but were extended to double-directional using a ray-launcher [DH23].

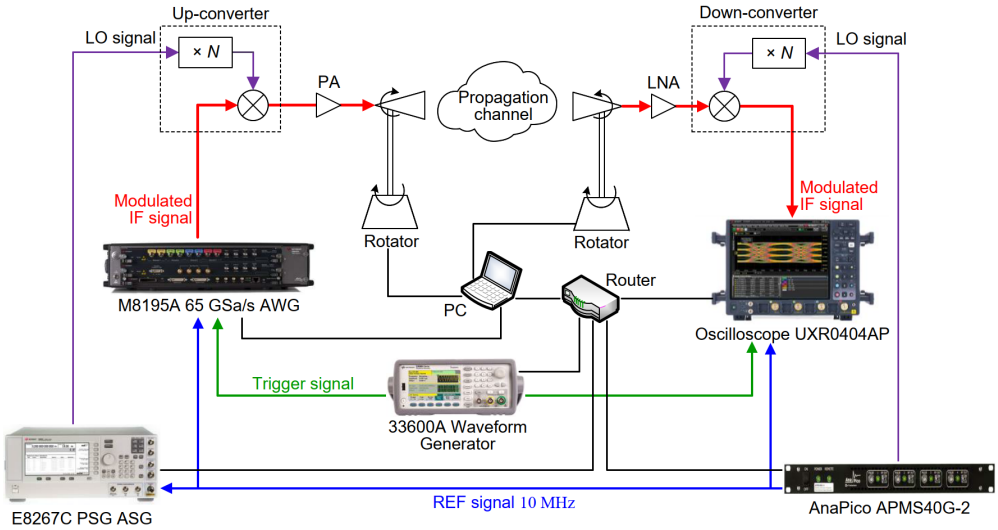

Figure 10-13: COTS instrument-based channel sounder used for measurements at 150 GHz.

Channel measurements at 150 GHz: Another set of channel measurement campaigns at 150 GHz are considered. Preliminary measurements have already been conducted in corridor environments. In the narrow corridor, one LoS and one NLoS location with less than 10 m link distance are measured. Another measurement is conducted in a wider corridor where several LoS locations at link distances around 20 m and 30 m. There are a few more indoor measurements planned for auditorium, smart factory, and workshop environments. All measurements, both performed and planned, are at the centre frequency of 150 GHz frequency and with 2 GHz bandwidth. These measurements use a modular sub-THz channel sounder using commercial off-the-shelf (COTS) instruments as shown in Figure 10-13. The sounding sequence is generated on a personal computer and downloaded to an arbitrary waveform generator (AWG). The modulated IF signal from the AWG is then filtered, up-converted, and amplified before being radiated to the Tx antenna. At the Rx side, a similar process is applied until the received signal is digitized by a real-time oscilloscope. Both Tx and Rx antennas are vertically polarized and mounted on a rotator. Additional information on the design of this channel sounder is presented in [ZFK+24].

Channel measurements at 15 GHz: There is also a measurement planned at 15 GHz, which lies in the FR3 band, in a university campus with LoS and outdoor-to-indoor link conditions. The Tx base station will be installed on a building rooftop, and its antenna half-power beamwidth will cover the area where multiple receiver (Rx) antenna locations will be placed. The channel sounder will use software-defined radios equipped with frequency converters to transmit and receive wideband signals, as shown in Figure 10-14. The sounder will also rely on stable clocks to ensure synchronization between the Tx and Rx.

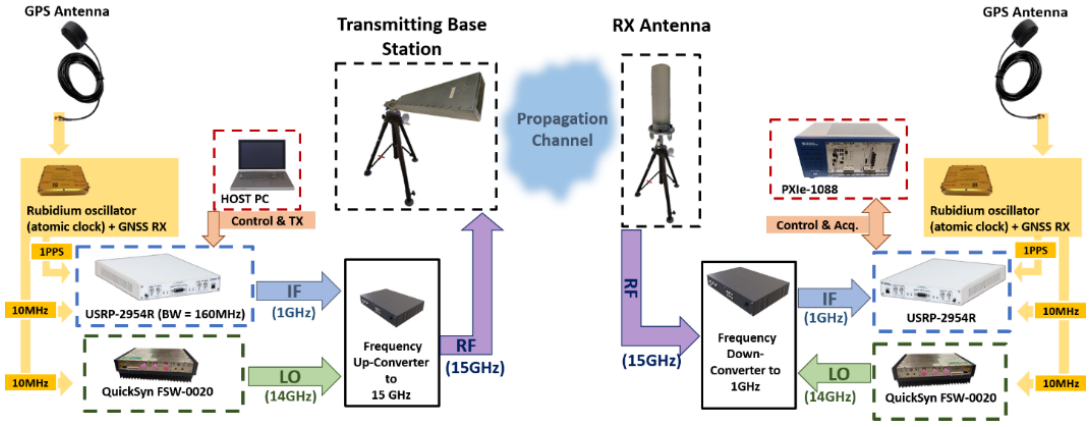

Figure 10-14: Software-defined radio-based channel sounder used for measurements at 15 GHz.

Channel model: The data obtained from the measurements at 140 GHz have already been processed and utilized to develop stored and stochastic channel models. The resulting double-directional multipath data and stored channel model are discussed in Section 3.2 of [HEX23-D23] and can be accessed in [DHK23]. Furthermore, the standardized stochastic channel model, 3GPP TR 38.901, was adopted to generate arbitrary channel responses. The channel model parameters, reported in Section 3.4.1 of this deliverable, are first derived from the measured multipath data and used as an input to the 3GPP TR 38.901 channel modelling framework. Exemplary power angular delay profiles (PADP) of three arbitrary links are shown in Figure 10-15. Future work will consider additional analyses of the channels and channel models based on 150 GHz and 15 GHz measurements.

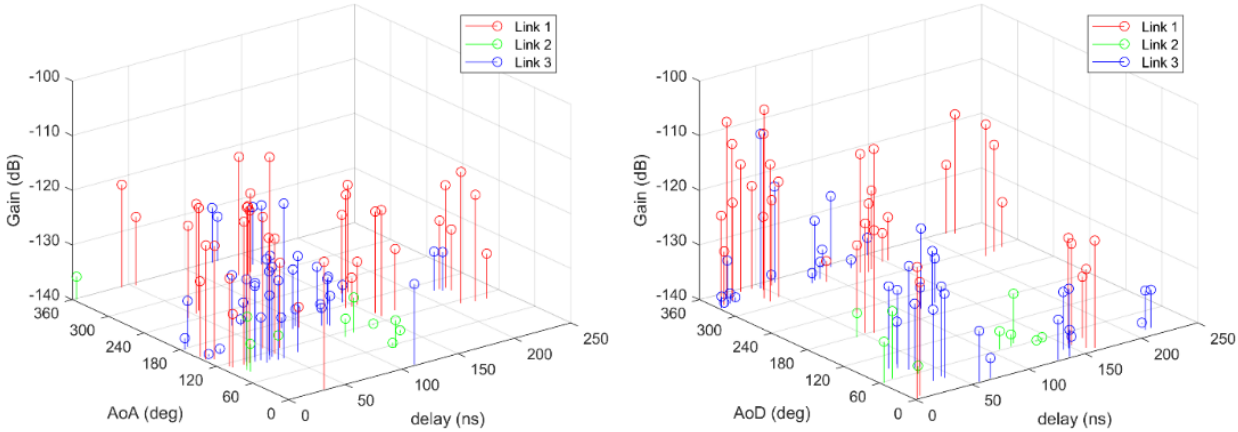

Figure 10-15: Sample PADPs of generated channels using the 3GPP TR 38.901 channel model with the measured 142 GHz channel model parameter values. (left) Azimuth angle of arrival (right) Azimuth angle of departure.

11 Conclusions and next steps

Adopting a holistic flexible design approach to 6G radio presents a promising pathway towards meeting stringent technical requirements for a broad range of emerging use cases, while considering foundational values of sustainability, trustworthiness, and inclusion. This approach is inherently challenging, as it demands interdisciplinary expertise and deep understanding of the interdependencies among various radio components, including hardware, architecture, deployment, signal processing techniques, protocols, and system engineering. Additionally, the presence of numerous technical candidates adds complexity and introduces a vast number of parameters to the radio optimization process. Moreover, design and validation require advanced modelling, computing, simulation, and prototyping tools. As a step towards realizing this vision, this report contributes to establishing a radio design framework and defines the interfaces with other modules in the overall 6G system. This framework aids in mapping various technical innovations and determining their interactions. Additionally, this report details a wide range of technological components and enablers at different levels of the radio system, spanning a broad spectrum from sub-6 GHz to THz, and includes various deployment architectures and options from centralized to distributed, as well as the investigation of new technical components. Various studies are presented and summarized, highlighting the scope, methodology, and results, which facilitate a better understanding of their potential roles and how they interact with different components in the radio system. Such comprehensive groundwork is essential for progressing in the integration phase. Furthermore, the report presents progress in developing design tools for channel modelling, especially for unexplored spectrums, simulation frameworks that consider multiple aspects, and proof-of-concept (PoC) platforms for assessment under realistic conditions.

The following paragraphs summarize the outcomes of the studies in this document:

Channel modelling: The channel parameter values for a stochastic channel model based on sub-THz measurements of indoor and outdoor environments that can be used to generate realistic channels were reported. In addition, a modification to this channel model to account for the near-field effects by determining the propagation distance between each transmit and receive antenna element was proposed. The coverage analysis at THz frequencies shows that such a frequency regime is suitable for providing focused coverage spots in a range up to roughly 100 m, depending on the acceptable system path loss requirements. It was also shown that the reflection loss strongly depends on the reflection point on the location of materials including mortar, carpet tile, and patterned glass at sub-THz frequencies. A simple model of a communication link with reconfigurable intelligent surface (RIS) is derived, revealing the negligible and significant signal-to-noise ratio (SNR) gains of the passive RIS and active RIS, respectively. Lastly, a review of the existing channel models and requirements for joint communication and sensing (JCAS) shows that hybrid models or site-specific models may be preferred over classical statistical geometric models for performance evaluation purposes.

MIMO and RIS techniques: The reports present studies on various multiple-input, multiple-output (MIMO) techniques. The balance between spectral efficiency, sum rate, and energy efficiency has been deeply investigated in several contributions. The clustering approach is applied to enhance the performance of the worst user, while a proposed beamformer design primarily focuses on improving the average sum-rate performance. Furthermore, a collection of one-bit techniques have been proposed for finding a balance that maintains a satisfactory level of spectral efficiency while reducing energy consumption. This chapter analyses and simulates two transmission methods for distributed MIMO (D-MIMO): coherent and non-coherent. The performance of the proposed rotary antenna is comparable to that of a conventional antenna. Massive MIMO (mMIMO) sub-THz is studied, showing that the sub-6GHz assisted and effective antenna dimension reduction can improve the performance of the sub-THz system. RIS-assisted deployment techniques are considered, namely, integrated access and backhaul (IAB) and D-MIMO, as well as dynamic RIS channel estimation. The modulation technique of RIS is also investigated in order to achieve low-rate data transmission.

Waveforms and modulation schemes: The scope is divided into two parts, sub-THz waveforms and constellation candidates, and waveforms and modulation enhancements. In the first segment, CP-OFDM and DFT-s-OFDM eligibility were analysed for sub-THz communications, considering phase noise (PN) impairments on the system numerology. The simulations indicated an improved block error rate (BLER) and

resistance to PN for larger subcarrier spacing. Another contribution explored the energy efficiency of 1-bit quantized zero-crossing modulation (ZXM) over 120 GHz transmissions. The results show a higher energy efficiency compared to QAM schemes at the cost of peak data rate. Furthermore, two new shapes for polar constellations were investigated, and simulations revealed resistance to higher Doppler shifts when compared to QAM schemes. Finally, a sub-THz hardware setup was validated using SC-FDE waveform and M-QAM schemes. In this context, tests indicated communication feasibility at 144 GHz, achieving low BER values. The second part introduces a new waveform entitled adaptive multicarrier modulation (AMCM), a novel low-density parity check (LDPC) code parity matrix design, and an optimisation proposal for bit interleaved coded modulation (DBICM). AMCM is evaluated in terms of power spectral density (PSD) and out-of-band emissions, and the preliminary results indicated a significant gain compared to cyclic prefix (CP)-OFDM. The new LDPC code parity matrix provided a faster and more efficient decoding with half the iterations used in current 3GPP standards. Lastly, the optimised solution for DBICM significantly reduced its complexity and allowed an effective identification of the delayed schemes with reasonable accuracy.

AI applications in radio interface design: Different implications of the artificial intelligence/machine learning (AI/ML) advancements are emphasized, including enhanced network performance, improved energy efficiency, and the facilitation of more intelligent and adaptable telecommunication systems. A key highlight from the modulation and coding segment revealed how AI could optimize MIMO waveforms, enhancing spectral efficiency by 15-20% at signal-to-noise ratios below 15 dB. In the domain of channel state information (CSI) acquisition, the employment of AI-driven techniques demonstrated the potential to reduce overhead significantly while preserving the accuracy of channel information, even in a multivendor scenario, a crucial step towards achieving optimal network performance. Moreover, CSI prediction through ML can be used to improve robustness of CSI compression methods to channel aging in dynamic networks. The discussion on AI-based MIMO transmissions presented innovative approaches to user pairing and beamforming, which are vital for maximizing network capacity and user throughput, and proposed solution to reduce power consumption through antenna muting and optimize pilot assignment in D-MIMO scenario. Notably, the application of AI for hardware impairment compensation illustrated a 35-45% gain in energy efficiency at throughput levels ranging from 1.6 to 2.0 Gbps, showcasing AI's capacity to enhance transmission quality.

JCAS: Deployment scenarios and system optimization scenarios for JCAS are investigated. These scenarios encompassed both localization and sensing applications, including monostatic, bistatic, and multistatic sensing. It is shown that the performance of 6G's non-terrestrial network (NTN) and RIS localization is dependent on the relative orientation between the RIS and the NTN. It is also shown that the integration between monostatic and bistatic sensing through random finite set theory has the potential to enhance the sensing performance compared to the standalone solution of the individual modalities. In the system optimization works, it is shown that increasing the CP duration in OFDM systems increases the maximum sensing distance between the target and the receiver in bistatic sensing scenarios. Furthermore, it was shown that having access to 6 degrees of freedom (6DoF) estimates of the UE position and orientation can enhance the performance of both positioning and communication functionalities through beamforming optimization. Finally, various strategies were investigated to facilitate bistatic sensing between UEs. As a next step, it is planned to conduct a cross-layer study, including both physical layer and higher layers perspective, to explore how optimizing various elements in the communication and sensing pipelines will enhance the JCAS performance. Moreover, it is planned to perform extensive testing of the proposed methods. In these tests, various modifications to the strategies discussed in this report will be explored. For instance, data transmission will be investigated; instead of pilot signals, and fusion between sensing modalities will be conducted using advanced parametric signal processing techniques. Furthermore, the beamforming work is planned to develop 6DoF tracking filters for mobile scenario and learning-based beam design methods to reduce the computational complexity. Finally, the bistatic protocols work might be extended to monostatic and multistatic scenarios between UEs and base station (BS). By investigating these different aspects of JCAS, we come closer to realizing the true potential of JCAS systems.

Spectrum sharing and spectrum access: For spectrum sharing, a deep dive a deep dive into terrestrial (TN) and NTN coexistence is presented. Assumptions and models for spectrum sharing with fixed-satellite service stations are revisited, and it is shown that including more accurate assumptions on radiation patterns, UE deployments and BS activity reduces the separation distance and thus relaxes the spectrum sharing constraints. Thereafter, two sharing case studies are introduced: First, interference caused by 6G networks on fixed satellite

service (FSS) UL in the centimetric range (7-15 GHz) was studied; Second, a stochastic geometry-based framework for modelling S-band sharing was presented. The two studies introduce the modelling approaches for coexistence and provide insights on problematic scenarios with high interference. In addition to TN-NTN coexistence, multi radio access technology (RAT) spectrum sharing between 5G and 6G networks is discussed, and the respective requirements and recommendations are introduced. Furthermore, two approaches for low-latency spectrum access are presented. First, risk-informed random access is introduced. Here, a simulative assessment of interference levels for ALOHA and carrier-sense multiple access (CSMA) is presented. Second, schedule-based access with a two-step connection procedure is introduced. The use of an omni-direction RAT is proposed to facilitate directional access in sub-THz spectrum, allowing to reduce the beam tracking overhead and overall latency. Finally, enhancements for seamless NTN integration towards inclusive radio interface and a proactive resource management approach based on interference prediction are presented.

Trustworthiness: The core value of trustworthiness encompassing key concepts like security, integrity and privacy are investigated. It is shown that exploiting the randomness of the wireless channel and device hardware to generate secret keys in a device-to-device communication systems can ensure security against eavesdropping attacks. Another relevant threat to trustworthiness is jamming attacks. Different jamming models have been designed and their impact have been evaluated as a precursor to designing effective mitigation strategies. Additionally, blind jammer localization without using any prior information about its location or the environment have been investigated. Finally, security and privacy aspects of a general cellular JCAS system, including UE-related security aspects, which is beyond the existing ones connected to communication systems, are analysed.

PoC and simulation tools: Through extensive research and proof-of-concept implementations, significant advancements are outlined in physical layer modelling, AI-native air interfaces, and joint JCAS technologies. The findings and methodologies presented not only demonstrate the feasibility and efficiency of these innovations but also set a foundation for future explorations in 6G technology. Emphasizing the importance of energy efficiency, safety, and cross-vendor cooperation, this report highlights the collaborative efforts necessary to realize the full potential of 6G. Through the exploration of the 6G physical layer link modelling, the report highlights the development of simulation tools that enhance PHY schemes such as D-MIMO and beamforming, crucial for optimizing performance in the challenging mmWave and sub-THz bands. It also explores flexible modulation and transceiver design, showcasing the integration of AI-native air interfaces to improve efficiency and adaptability in communication protocols. The efforts in JCAS and the subsequent analysis of power consumption patterns reflect a commitment to multi-functionality and sustainability within future networks. Moreover, the report addresses electromagnetic filed (EMF) assessment methods, allowing for evaluation of environmental EMF exposure levels from advanced MIMO systems. The detailed channel measurement data and models provide a foundational resource for validating the simulations and theoretical frameworks that underpin 6G development.

Next steps: Building on this report, future efforts will focus on expanding and refining the radio design framework and further development and assessment of the selected enablers. Emphasis will be placed on clustering similar topics to generalize solutions and enhance collaboration across diverse research groups. This initiative will also involve harmonizing terminologies to ensure clear and consistent communication in the project ecosystem. Comprehensive assessments are planned, which will include incorporating multiple performance metrics to thoroughly assess the advantages and limitations of different approaches, as well as evaluating multiple components concurrently, such as integrating more hardware models, and simulating the impact of multiple elements concurrently. Moreover, the focus will shift from independently evaluating individual elements to exploring their interactions and interconnections for better understanding of the system behaviour in a more integrated context. Additionally, efforts will be made to improve interactions with other layers in the 6G blueprint by advancing collaboration with other work packages, which is essential for the integration of innovative radio solution within the broader 6G end-to-end system design. Work on PoCs will continue, aiming at evaluating the developed solutions under more realistic assumptions.

References

[(23)000238] ETSI THz (23)000238 “A channel model modification for large arrays, large bandwidth, and near-field effects”, meeting THz#11, October 2023.

[21.916] 3GPP TR 21.916 V16.2.0 (2022-06), “Release 16 Description; Summary of Rel-16 Work Items”.

[22.837] 3GPP TR 22.837 “Feasibility Study on Integrated Sensing and Communication (Release 19)”, v19.2.0, 2023.

[28.841] 3GPP TR 28.841, “Study on management aspects of Internet of Things (IoT) Non-Terrestrial Networks (NTN) enhancements (Release 18)”, v18.0.0, 2023.

[36.741] 3GPP TR 36.741 “Study on further enhancements to coordinated multi-point (CoMP) operation for LTE,” 2017. V14.0.0.

[36.873] 3GPP TR 36.873, “Study on 3D channel model for LTE”, Rel-12 v12.7.0, January 2005.

[36.897] 3GPP TR 36.897 “Study on elevation beamforming/Full-Dimension (FD) MIMO for LTE,” v13.0.0, 2015.

[38.101] 3GPP TR 38.101 “NR; User Equipment (UE) radio transmission and reception; Part 1: Range 1 Standalone”, v18.4.0, December 2023.

[38.104] 3GPP TS 38.104 “Base Station (BS) radio transmission and reception”, v18.3.0, December 2023.

[38.133] 3GPP TS 38.133 “NR; Requirements for support of radio resource management,” v18.4.0, December 2023.

[38.211] 3GPP TS 38.211 “Physical channels and modulation”, v18.0.0, 2023.

[38.212] 3GPP TS 38.212 “Multiplexing and channel coding (Release 17)”, v17.5.0, 2023.

[38.213] 3GPP TS 38.213 “NR; Physical layer procedures for control”, v18.1.0, 2023.

[38.214] 3GPP TS 38.214 “Physical layer procedures for data (Release 18)”, v18.1.0, 2023.

[38.821] 3GPP TR 38.821, “Solutions for NR to support Non-Terrestrial Networks (NTN)”, v16.2.0, 2023.

[38.843] 3GPP TR 38.843, “Study on Artificial Intelligence (AI)/Machine Learning (ML) for NR air interface”, v18.0.0, 2024.

[38.901] 3GPP TR 38.901 “Study on channel model for frequencies from 0.5 to 100 GHz (Release 17)”, v17.0.0, 2022.

[802.11ay] IEEE 802.11 working group, “IEEE Draft Standard for Information Technology-Telecommunications and Information Exchange Between Systems Local and Metropolitan Area Networks-Specific Requirements Part 11: Wireless LAN Medium Access Control (MAC) and Physical Layer (PHY) Specifications-Amendment: Enhanced Throughput for Operation in License-Exempt Bands Above 45 GHz,” IEEE 802.11ay, 2021.

[ACN+21] I. B. F. de Almeida, M. Chafii, A. Nimr, G. and Fettweis, “Blind Transmitter Localization in Wireless Sensor Networks: A Deep Learning Approach,” IEEE 32nd Annual International Symposium on Personal, Indoor and Mobile Radio Communications (PIMRC), 2021.

[AGT21] I. Atzeni, B. Gouda, and A. Tölli, “Distributed precoding design via over-the-air signaling for cell-free massive MIMO,” IEEE Transactions on Wireless Communications, vol. 20, no. 2, pp. 1201–1216, 2021.

[AMG+14] A. Alkhateeb, J. Mo, N. Gonzalez-Prelcic and R. W. Heath, "MIMO precoding and combining solutions for millimeter-wave systems", IEEE Commun. Mag., vol. 52, no. 12, pp. 122-131, Dec. 2014.

[AT22] I. Atzeni and A. Tölli, “Channel estimation and data detection analysis of massive MIMO with 1-bit ADCs,” IEEE Transactions on Wireless Communications, vol. 21, no. 6, pp. 3850–3867, 2022.

[ATD21] I. Atzeni, A. Tölli, and G. Durisi, “Low-resolution massive MIMO under hardware power consumption constraints,” in Proc. Asilomar Conference on Signals, Systems, and Computers (ASILOMAR), 2021.

[ATM19] R. Ahmed, F. Tosato and M. Maso, "Overhead Reduction of NR type II CSI for NR Release 16", 23rd International ITG Workshop on Smart Antennas, Vienna, Austria, 2019.

[BHH+18] T. W. C. Brown, D. A. Humphreys, M. Hudlicka, and T. H. Loh, ‘‘Prediction of SINR using BER and EVM for massive MIMO applications,’’ in Proc. 12th Eur. Conf. Antennas Propag., 2018, p. 5.

[BJ19] G. Bu and J. Jiang, “Reinforcement learning-based user scheduling and resource allocation for massive MU-MIMO system,” IEEE/CIC International Conference on Communications in China (ICCC), pp. 641–646, 2019.

[BM82] J. A. Bondy, U. S. R. Murty, and Others, Graph theory with applications, vol. 290. Macmillan London, 1976.

[CH08] N. Costa and S. Haykin "A Correlation-Based Wideband MIMO Channel Model." International Union of Radio Science XXIX General Assembly 2008.

[CLM+23] Y. Cui, F. Liu, C. Masouros, J. Xu, T. X. Han, and Y. C. Eldar, “Integrated sensing and communications: Background and applications,” in Integrated Sensing and Communications. Springer, 2023, pp. 3-21.

[CTB98] G. Caire, G. Taricco, and E. Biglieri, “Bit-interleaved coded modulation,” IEEE transactions on information theory, vol. 44, no. 3, pp. 927–946, 1998.

[CTT+16] X. Chen, L. Tian, P. Tang and J. Zhang, “Modelling of human body shadowing based on 28 GHz indoor measurement results,” IEEE 84th Vehicular Technology Conference (VTC2016-Fall), pp. 1-5, 2016.

[CVR19] A. Chiskis, G. Reina, R. Verbin, " US10594520B2 System and method unifying linear and nonlinear precoding for transceiving data", 2019.

[DH23] M. F. De Guzman and K. Haneda, “Analysis of wave-interacting objects in Indoor and outdoor environments at 142 GHz,” in IEEE Transactions on Antennas and Propagation, vol. 71, no. 12, pp. 9838-9848, Dec. 2023.

[DHK23] M. F. de Guzman, K. Haneda and P. Kyösti, “Measurement-based MIMO channel model at 140 GHz,” https://doi.org/10.5281/zenodo.7640352, 2023, version 1.

[DLR23] German Aerospace Center, “Deutschen Zentrums für Luft- und Raumfahrt: Antenne (30 Meter),” 2023, https://www.dlr.de/en/research-and-transfer/research-infrastructure/the-30-metre-antenna.

[DPS18] E. Dahlman, S. Parkvall, and J. Sköld, “5G NR: The Next Generation Wireless Access Technology,” Academic Press, 2018.

[DWS+11] M. Deng, K. Wuyts, R. Scandariato, B. Preneel, W. Joosen, “A privacy threat analysis framework: supporting the elicitation and fulfillment of privacy requirements, Requirements”, Engineering Journal, volume 16, issue 1, pages 3-32, Springer-Verlag, 2011

[ECM+22] A. M. Elbir, S. Chatzinotas, K. V. Mishra, M. Bennis, “TeraHertz band integrated sensing and communication: Challenges and opportunities,” arXiv preprint arXiv:2208.01235 (2022), https://arxiv.org/abs/2208.01235, Aug. 2022.

[EE14] A. A. Emran and M. Elsabrouty “Simplified variable-scaled min sum LDPC decoder for irregular LDPC codes,” IEEE 11th Consumer Communications and Networking Conference (CCNC), 2014

[Ell21] S.W. Ellingson, “Path loss in Reconfigurable Intelligent Surface-Enabled Channels’’. IEEE 32nd Annual International Symposium on Personal, Indoor and Mobile Radio Communications (PIMRC), Sept. 2021

[FDB+19] G. Fettweis, M. Dörpinghaus, S. Bender, L. Landau, P. Neuhaus, and M. Schlüter, “Zero crossing modulation for communication with temporally oversampled 1-bit quantization,” in Proc. 53rd Asilomar Conference on Signals, Systems, and Computers, Pacific Grove, CA, USA, Nov. 2019, pp. 207–214

[FHS23] H. Farhadi, J. Haraldson, M. Sundberg, “A deep learning receiver for non-linear transmitter”, IEEE ACCESS, vol. 11, 2023.

[FLV+23] X. Fu, D. Le Ruyet, R. Visoz, V. Ramireddy, M. Grossmann, M. Landmann, W. Quiroga “A Tutorial on Downlink Precoder Selection Strategies for 3GPP MIMO Codebooks.” IEEE Access. PP. 1-26. 10.1109/ACCESS.2023.3338866, 2023

[GAT23] B. Gouda, I. Atzeni and A. Tölli, "Uplink Power Control for Distributed Massive MIMO with 1-Bit ADCs," GLOBECOM 2023 - 2023 IEEE Global Communications Conference, Kuala Lumpur, Malaysia, 2023, pp. 7188-7193.

[GDS+24] F. Gast, M. Dörpinghaus, P. Sen, A. Nimr, G. Fettweis, “Hardware-Aware Energy Efficiency Optimization in Wireless Communications using a Gearbox-PHY,“ IEEE Communication Letters, in revision.

[GLQ14] K. Grover, A. Lim, and Q. Yang, “Jamming and anti-jamming techniques in wireless networks: a survey,” in Int. J. Ad Hoc Ubiquitous Comput., vol. 17, no. 4, pp 197–215, December 2014, DOI: 10.1504/IJAHUC.2014.066419.

[GSM+23] S. Gunarathne, T. Sivalingam, N. H. Mahmood, N. Rajatheva, and M. Latva-Aho, “Decomposition Based Interference Management Framework for Local 6G Networks,” in Globecom Workshops, 2023, KL, Malaysia.

[HCA+22] J. Hoydis, S. Cammerer, F. Ait Aoudia, A. Vem, N. Binder, G. Marcus, and A. Keller, “Sionna: An open-source library for next-generation physical layer research,” arXiv preprint, Mar. 2022.

[HDS+16] X. He, H. Dai, W. Shen, P. Ning and R. Dutta, "Toward Proper Guard Zones for Link Signature," in IEEE Transactions on Wireless Communications, vol. 15, no. 3, pp. 2104-2117, March 2016, doi: 10.1109/TWC.2015.2498621.

[HEX21-D22] Hexa-X, “Deliverable D2.2: Initial radio models and analysis towards ultra-high data rate links in 6G.” Dec. 2021.

[HEX223-D12] Hexa-X-II, “Deliverable D1.2: 6G Use Cases and Requirements”, Dec. 2023.

[HEX223-D32] Hexa-X-II, “Deliverable D3.2: Initial Architectural enablers”, Oct. 2023

[HEX223-D42] Hexa-X-II, “Deliverable D4.2: Radio Design and Spectrum Access requirements and key enablers for 6G Evolution”, Oct. 2023

[HEX224-D53] Hexa-X-II “Deliverable D5.3: Initial design and validation of technologies and architecture of 6G devices and infrastructure,” 2024.

[HEX23-D23] Hexa-X, “Deliverable D2.3: Radio models and enbling techniques towards ultra-high data rate links and capacity in 6G.” Mar. 2023.

[HH17] R. Hayakawa, and K. Hayashi, “Convex Optimization-Based Signal Detection for Massive Overloaded MIMO Systems.” IEEE Trans. on Wireless Communications, vol. 16, no. 11, pp. 7080–7091, 2017.

[HJ19] Z. Hossain, J. M. Jornet, “Hierarchical bandwidth modulation for ultra-broadband Terahertz communications”, IEEE International Communications Conference (ICC), May 2019.

[HKH21] M. Honkala, D. Korpi, and J. M. J. Huttunen, “DeepRx: Fully convolutional deep learning receiver,” IEEE Transactions on Wireless Communications, vol. 20, no. 6, pp. 3925–3940, Jun. 2021.

[Hos21] G. Hosoya, “Analysis of delayed bit-interleaved coded modulation for APSK,” in 2021 20th International Symposium on Communications and Information Technologies (ISCIT), 2021, pp. 193–198.

[Hoy22] J. Hoydis, “Sionna: An open-source library for next-generation physical layer research,” 2022 available on: https://arxiv.org/abs/2203.11854

[HW21] H. Halbauer, T. Wild, “Towards Power Efficient 6G Sub-THz Transmission,” Joint EuCNC & 6G Summit, June 8-11, 2021, Porto, Portugal

[HWW+18] H. Halbauer, A. Weber, D. Wiegner and T. Wild, "Energy Efficient Massive MIMO Array Configurations," 2018 IEEE Globecom Workshops (GC Wkshps), Abu Dhabi, UAE, Dec. 2018.

[HYL17] W. Hamilton, Z. Ying, and J. Leskovec, “Inductive representation learning on large graphs,” Advances in Neural Information Processing Systems, vol. 30, 2017.

[HZA+19] C. Huang, A. Zappone, G. C. Alexandropoulos, M. Debbah and C. Yuen, "Reconfigurable Intelligent Surfaces for Energy Efficiency in Wireless Communication," in IEEE Transactions on Wireless Communications, vol. 18, no. 8, pp. 4157-4170, Aug. 2019.

[IBN+19] G. Interdonato, E. Björnson, H. Q. Ngo, P. Frenger, and E. G. Larsson, “Ubiquitous cell-free massive MIMO communications,” EURASIP J. Wireless Commun. Netw., vol. 2019, no. 1, pp. 1–13, Dec. 2019.

[ICNIRP20] International Commission on Non-Ionizing Radiation Protection. “Guidelines for limiting exposure to electromagnetic fields (100 kHz to 300 GHz),” Health physics, vol. 118, no.5, pp. 483-524, 2020.

[IDLAB-01] Imec iLab.t testbeds’ documentation, https://doc.ilabt.imec.be/ilabt/wilab/index.html

[Int23] Intelsat, “Supporting End-to-End Service Through Eight Teleport Gateways,” 2023, https://www.intelsat.com/global-network/terrestrial-network/teleport-chart.

[ITU-5D716] ITU-R, Report on the 38th meeting of Working Party 5D (5D/716) Ch 4 Annex 4.4, “Characteristics of terrestrial component of IMT for sharing and compatibility studies in preparation for WRC-23”, https://www.itu.int/dms_ties/itu-r/md/19/wp5d/c/R19-WP5D-C-0716!H4-N4.04!MSW-E.docx

[ITU-CPM23] ITU-R, “Report of the CPM on technical, operational and regulatory/procedural matters to be considered by the World Radiocommunication Conference 2023,” 2023

[ITU-M.2101] ITU-R, “Modelling and simulation of IMT networks and systems for use in sharing and compatibility studies,” 2017.

[ITU-M.2160] ITU-R, Recommendation ITU-R M.2160-0: Framework and overall objectives of the future development of IMT for 2030 and beyond, November 2023.

[ITU-P.2108] ITU-R, “Prediction of clutter loss,” 2021.

[ITU-P.452] ITU-R, “Prediction procedure for the evaluation of interference between stations on the surface of the Earth at frequencies above about 0.1 GHz,” 2021.

[ITU-P.833-4] ITU-R, “Attenuation in Vegetation”, 2004.

[ITU-RA4.17] ITU-R Annex 4.17 to Document 5D/1776-E, “Supporting material for WRC-23 agenda item 1.2 - Sharing and compatibility studies of IMT systems in the frequency band 6 425-7 025 and 7 025-7 125 MHz”, section 1.12, https://www.itu.int/md/R19-WP5D-C-1776/en

[ITU-RTG5] ITU-R TG5/1 Document 5-1/36-E, “Liaison statement to Task Group 5/1 - Spectrum needs and characteristics for the terrestrial component of IMT in the frequency range between 24.25 GHz and 86 GHz”, attachment 2 section 5.4, https://www.itu.int/md/R15-TG5.1-C-0036/en

[ITU-S.2368] ITU-R, “Report ITU-R S.2368: Sharing studies between International Mobile Telecommunication-Advanced systems and geostationary satellite networks in the fixed-satellite service in the 3 400-4 200 MHz and 4 500-4 800 MHz frequency bands in the WRC study cycle leading to WRC-15,” 2015

[ITU-S.465] ITU-R,” Recommendation ITU-R S.465: Reference radiation pattern for earth station antennas in the fixed-satellite service for use in coordination and interference assessment in the frequency range from 2 to 31 GHz,” January 2010.

[JA11] J. M. Jornet, I. F. Akyildiz, “Channel modelling and capacity analysis for electromagnetic wireless nanonetworks in the Terahertz band”, IEEE Transactions on Wireless Communications, vol. 10, no. 10, pp. 3211-3221, Oct. 2011

[JC94] W. C. Jakes and D. C. Cox, “Microwave Mobile Communications,” Wiley-IEEE Press,1994.

[JKH+19] B. Jang, M. Kim, G. Harerimana, and J. W. Kim, “Q-learning algorithms: A comprehensive classification and applications.” IEEE access, vol. 7, pp. 133653-133667, 2019.

[JSM+23] C. Jayawardhana, T. Sivalingam, N. H. Mahmood, N. Rajatheva, and M. Latva-Aho, “Predictive resource allocation for URLLC using empirical mode decomposition,” in 2023 EuCNC | 6G Summit, 2023, Gothenburg, Sweden, pp. 174–179.

[KHH21] D. Korpi, J. Huttunen, and M. Honkala, “DeepRx MIMO: Convolutional MIMO detection with learned multiplicative transformations,” in Proc. IEEE International Conference on Communications (ICC), Jun. 2021.

[KHH23] D. Korpi, M. Honkala, and J. Huttunen, “Deep learning-based pilotless spatial multiplexing,” in Proc. 47th Asilomar Conference on Signals, Systems and Computers, Oct. 2023.

[KLM+17] P. Kyösti, J. Lehtomäki, J. Medbo and M. Latva-aho, "Map-Based Channel Model for Evaluation of 5G Wireless Communication Systems," in IEEE Transactions on Antennas and Propagation, vol. 65, no. 12, pp. 6491-6504, Dec. 2017.

[KW17] T. N. Kipf and M. Welling, “Semi-supervised classification with graph convolutional networks,” in International Conference on Learning Representations, 2017.

[LCW+22] S. Lin, F. Chen, M. Wen, Y. Feng, and M. Di Renzo, “Reconfigurable intelligent surface-aided quadrature reflection modulation for simultaneous passive beamforming and information transfer,” IEEE Transactions on Wireless Communications, vol. 21, no. 3, pp. 1469–1481, 2022.

[LDG18] L.T.N. Landau, M. Dörpinghaus, and G. Fettweis. "1-bit quantization and oversampling at the receiver: Sequence-based communication." *EURASIP Journal on Wireless Communications and Networking* 2018.1 (2018): 1-24.

[LDL+21] Guillaume Larue, Louis-Adrien Dufrene, Quentin Lampin, Paul Chollet, Hadi Ghauch, et al., "Blind Neural Belief Propagation Decoder for Linear Block Codes," EnCNC 2021, Jun 2021, Porto, Portugal. ffhal-03275838.

[LKR+21] P. Leu, M. Kotuliak, M. Roeschlin, and S. Capkun. "Security of Multicarrier Time-of-Flight Ranging," In Annual Computer Security Applications Conference, Dez. 2021, pp. 887-899

[LKR21] Patrick Leu, Martin Kotuliak, Marc Roeschlin, and Srdjan Capkun, "Security of Multicarrier Time-of-Flight Ranging ", ACSAS'21, 2021, USA.

[LMS+21] A. Li, C. Masouros, A. L. Swindlehurst, and W. Yu, "1-bit massive MIMO transmission: Embracing interference with symbol-level precoding," *IEEE Commun. Mag.*, vol. 59, no. 5, pp. 121–127, 2021.

[LQY21] Y. Liao, M. Qiu, and J. Yuan, "Design and analysis of delayed bit-interleaved coded modulation with LDPC codes," IEEE Transactions on Communications, vol. 69, no. 6, pp. 3556–3571, 2021.

[LYL+22] C. Liu, W. Yuan, S. Li, X. Liu, H. Li, D. W. K. Ng, and Y. Li, "Learning-based predictive beamforming for integrated sensing and communication in vehicular networks". IEEE Journal of Selected Areas in Communication, vol. 40, no. 8, pp. 2317-2334, Jun. 2022.

[M.2135] ITU-R Report M.2135, "Guidelines for evaluation of radio interface technologies for IMT-Advanced", M.2135, 2009.

[M.2412-0] ITU-R M.2412-0 "Guidelines for evaluation of radio interface technologies for IMT-2020", 2017.

[MKS+13] V. Mnih, K. Kavukcuoglu, D. Silver, A. Graves, I. Antonoglou, D. Wierstra, and M. Riedmiller, "Playing Atari with deep reinforcement learning," NIPS Deep Learning Workshop, 2013.

[MLA+21] N. H. Mahmood, O. A. López, H. Alves and M. Latva-Aho, "A predictive interference management algorithm for URLLC in beyond 5G networks," in IEEE Communications Letters, vol. 25, no. 3, pp. 995-999, March 2021, doi: 10.1109/LCOMM.2020.3035111.

[MLY+16] H. Ma, W. Leung, X. Yan, K. Law, and M. Fossorier, "Delayed bit interleaved coded modulation," in 2016 9th International Symposium on Turbo Codes and Iterative Information Processing (ISTC). IEEE, 2016, pp. 86–90.

[MMC+23] A. Mayya, M. Mitev, A. Chorti, G. Fettweis, "A SKG Security Challenge: Indoor SKG Under an On-The-Shoulder Eavesdropping Attack," Global Communications Conference (2023).

[MN14] M. A. Maddah-Ali and U. Niesen, "Fundamental limits of caching," IEEE Transactions on information theory vol. 60, no. 5, pp. 2856-2867, 2014.

[MNM+24] Marasinghe, D., Nguyen, L. H., Mohammadi, J., Chen, Y., Wild, T., & Rajatheva, N. (2023). Constellation Shaping under Phase Noise Impairment for Sub-THz Communications. arXiv preprint arXiv:2311.12433. To be published in in Proc. IEEE International Conference on Communications (ICC), 2024.

[Mol11] A. F. Molisch, "Wireless Communications," 2nd ed. Hoboken, NJ, USA, Wiley, 2011.

[MRH+10] R. Mesleh, M. Di Renzo, H. Haas, and P. M. Grant, "Trellis coded spatial modulation," IEEE Transactions on wireless communications, vol. 9, no. 7, 2010.

[MSFT-01] Microsoft, 'The STRIDE Threat Model', Available: https://learn.microsoft.com/en-us/azure/security/develop/threat-modeling-tool-threats

[MSW+22] J. M. Mateos-Ramos, J. Song, Y. Wu, C. Häger, M. F. Keskin, V. Yajnanarayana, and H. Wymeersch, "End-to-end learning for integrated sensing and communication," in

Proceedings IEEE International Conference on Communications (ICC), Seoul, Korea, Republic of, 2022, pp. 1942–1947.

[Mur23] B. Murmann, “ADC Performance Survey 1997-2023,” [Online]. Available: https://github.com/bmurmann/ADC-survey.

[NHP16] S. L. H. Nguyen, K. Haneda and J. Putkonen, “Dual-Band Multipath Cluster Analysis of Small-Cell Backhaul Channels in an Urban Street Environment,” 2016 IEEE Globecom Workshops (GC Wkshps), Washington, DC, USA, 2016.

[NKA19] Q. Nadeem, A. Kammoun and M. -S. Alouini, "Elevation Beamforming with Full Dimension MIMO Architectures in 5G Systems: A Tutorial," in IEEE Communications Surveys & Tutorials, vol. 21, no. 4, 2019.

[NSN21] L. V. Nguyen, A. L. Swindlehurst, and D. H. N. Nguyen, “Linear and deep neural network-based receivers for massive MIMO systems with one-bit ADCs”, IEEE. Transactions on Wireless Communications, vol. 20, no. 11, pp. 7333–7345, 2021.

[OBL+19] Ö. Özdogan, E. Björnson, E. G. Larsson, “Intelligent reflecting surfaces: Physics, propagation, and pathloss modelling,” IEEE Wireless Commun. Lett., vol. 9, no. 5, pp. 581–585, May 2020.

[ÖBL19] Ö. Özdogan, E. Björnson and E. G. Larsson, "Massive MIMO With Spatially Correlated Rician Fading Channels," in *IEEE Transactions on Communications*, vol. 67, no. 5, pp. 3234-3250, May 2019, doi: 10.1109/TCOMM.2019.2893221.

[ORAN23] O-RAN Use Cases Detailed Specification v12.0, Oct 2023.

[Orf16] S. J. Orfanidis, “Electromagnetic Waves and Antennas,” Sophocles J. Orfanidis, 2016.

[PHM+21] C. Padilla, R. Hashemi, N. H. Mahmood, and M. Latva-Aho, “A Nonlinear Autoregressive Neural Network for Interference Prediction and Resource Allocation in URLLC Scenarios,” in 2021 International Conference on ICT Convergence, 2021, Jeju Island, Korea, pp. 184–189.

[PS08] John G. Proakis, Masoud Salehi, “Digital Communications” (see Chapter 16.4 Multiuser MIMO systems for broadcast channels), 5th edition, McGraw-Hill Higher Education, 2008

[PZ22] H. Pirayesh and H. Zeng, "Jamming Attacks and Anti-Jamming Strategies in Wireless Networks: A Comprehensive Survey," in IEEE Communications Surveys & Tutorials, vol. 24, no. 2, pp. 767-809, March 2022, DOI: 10.1109/COMST.2022.3159185.

[QDR] QUAsi Deterministic RadIo channel generator, QuaDRiGa [Accessed by: December 2023].

[R1-1813177] Nokia and Nokia Shangai Bell, “Scenarios, frequencies and new field measurements results from two operational factory halls at 3.5 GHz for various antenna configurations.” Document R1-1813177, 3GPP, Sophia Antipolis, France, Nov. 2018. [Online]. Available: https://www.3gpp.org/ftp/tsg ran/WG1 RL1/TSGR1 95/Docs/

[R1-2203550] R1-2203550, “Evaluation on AIML for CSI feedback enhancement”, 3GPP TSG RAN WG1 #109-e, e-Meeting, May 2022.

[R2-2301269] CMCC, CATT, Huawei, Lenovo, vivo, “Service Link Switching with PCI unchanged”, 3GPP TSG RAN WG 2 # 121, Athens, 2023.

[R2-2311212] Sequans, “Common signalling of HO common information”, 3GPP TSG RAN WG 2 # 123bis, Xiamen, 2023.

[R2-2311223] Sequans, “Unchanged PCI solution vs PCI change only”, 3GPP TSG RAN WG 2 # 123bis, Xiamen, 2023.

[RMR+21] N. Rajapaksha, K. B. S. Manosha, N. Rajatheva and M. Latva-Aho, “Deep learning-based power control for cell-free massive MIMO networks,” ICC 2021 - IEEE International Conference on Communications, 2021, pp. 1-7, doi: 10.1109/ICC42927.2021.9500734.

[RMR+23] N. Rajapaksha, K. B. S. Manosha, N. Rajatheva, and M. Latva-aho, “Unsupervised learning-based joint power control and fronthaul capacity allocation in cell-free massive MIMO with hardware impairments,” in IEEE Wireless Communications Letters, doi: 10.1109/LWC.2023.3265348.

[RMW+23] Rajapaksha, N., Mohammadi, J., Wesemann, S., Wild, T., and Rajatheva, N., “Minimizing Energy Consumption in MU-MIMO via Antenna Muting by Neural Networks with Asymmetric Loss”, arXiv e-prints, 2023. doi:10.48550/arXiv.2306.05162.

[RP-234078] Huawei, “New WID: Non-Terrestrial Networks (NTN) for NR Phase 3”, 3GPP TSG RAN # 102, Edinburgh, 2023

[RXM+17] T. S. Rappaport, Y. Xing, G. R. MacCartney, A. F. Molisch, E. Mellios and J. Zhang, "Overview of Millimeter Wave Communications for Fifth-Generation (5G) Wireless Networks—With a Focus on Propagation Models," in *IEEE Transactions on Antennas and Propagation*, vol. 65, no. 12, pp. 6213-6230, Dec. 2017, doi: 10.1109/TAP.2017.2734243

[SAN21] H. Sarieddeen, M.-S. Alouini, T. Y. A.-Naffouri, “An overview of signal processing techniques for TeraHertz communications,” https://arxiv.org/abs/2005.13176v3, Aug. 2021.

[SFG+03] Schreckenbach, Frank, N. Gortz, Joachim Hagenauer, and Gerhard Bauch. "Optimization of symbol mappings for bit-interleaved coded modulation with iterative decoding." IEEE Communications Letters 7, no. 12, pp. 593-595, 2003.

[SJM+21] Pirmin Schoeder, Vinzenz Janoudi, Benedikt Meinecke, David Werbunat, and Christian Waldschmidt, "Flexible direction-of-arrival simulation for automotive radar target simulators,” IEEE Journal of Microwaves 1.4, 2021, pp 930-940.

[SLI+19] V. Syrjälä, T. Levanen, T. Ihalainen, and M. Valkama, “Pilot Allocation and Computationally Efficient Non-Iterative Estimation of Phase Noise in OFDM,” IEEE Wireless Commun. Lett., vol. 8, no. 2, pp. 640–643, Apr. 2019.

[SPS+04] Spencer, Q. H., Peel, C. B., Swindlehurst, A. L., and M. Haardt, “An introduction to the multi-user MIMO downlink”. IEEE communications Magazine, 61, 2004.

[SRZ+21] Mridula Singh, Marc Roeschlin, Ezzat Zalzala, Patrick Leu, and Srdjan Čapkun, “Security analysis of IEEE 802.15.4z/HRP UWB time-of-flight distance measurement”, In Proceedings of the 14th ACM Conference on Security and Privacy in Wireless and Mobile Networks (WiSec '21), 2021, pp 227–237.

[SSH04] Q. H. Spencer, A. L. Swindlehurst, and M. Haardt, “Zero-forcing methods for downlink spatial multiplexing in multiuser MIMO channels,” IEEE Transactions on Signal Processing, vol. 52, no. 2, pp 461-471, 2004.

[STK+23] E. Semaan, E. Tejedor, R. Kumar Kochhar, S. Magnusson, S. Parkwall,” 6G spectrum - enabling the future mobile life beyond 2030”, GFTL-23:000243 Uen, Ericsson White Paper, March 2023

[STS07] M. Sadek, A. Tarighat and A. H. Sayed, “A leakage-based precoding scheme for downlink multi-user MIMO channels,” in IEEE Transactions on Wireless Communications, vol. 6, no. 5, pp. 1711-1721, May 2007, doi: 10.1109/TWC.2007.360373.

[SYH+23] Z. Shan, X. Yi, H. Yu, C. S. Liao, and S. Jin, “Learning to code on graphs for topological interference management,” arXiv: 235.07186 (2023).

[T99] I. E. Telatar, “Capacity of multi-antenna Gaussian channels”, European Transactions on Telecommunications, vol. 10, no. 6, pp. 585-595, November 1999.

[TLP+20] O. Tervo, T. Levanen, K. Pajukoski, J. Hulkkonen, P. Wainio and M. Valkama, "5G New Radio Evolution Towards Sub-THz Communications," *2020 2nd 6G Wireless Summit (6G SUMMIT)*, Levi, Finland, 2020, pp. 1-6, doi: 10.1109/6GSUMMIT49458.2020.9083807.

[TSS05] A. Tarighat, M. Sadek, and A. H. Sayed, “A multi-user beamforming scheme for downlink MIMO channels based on maximizing signal-to-leakage ratios.” In Proc. IEEE International Conference on Acoustics, Speech, and Signal Processing, (Vol. 3, pp. iii-1129). March 2005.

[TV05] D. Tse and P. Viswanath, “Fundamentals of wireless communication,” Cambridge University Press, 2005.

[VA17] Vaswani, Ashish, et al. “Attention is all you need,” Advances in neural information processing systems, 2017.

[WPM07] Wong, K., Paulraj, A., & Murch, R. (2007), “Efficient High-Performance Decoding for Overloaded MIMO Antenna Systems”. IEEE Trans. on Wireless Communications, 6(5), 1833–1843.

[WS22a] H. Wymeersch, and G. Seco-Granados, "Radio localization and sensing—Part I: Fundamentals," IEEE Communications Letters 26, no. 12 (2022): 2816-2820.

[WS22b] H. Wymeersch, and G. Seco-Granados, "Radio Localization and Sensing—Part II: State-of-the-Art and Challenges,” IEEE Communications Letters 26, no. 12 (2022): 2821-2825.

[WTL+22] J. Wang, W. Tang, J. C. Liang, L. Zhang, J. Y. Dai, X. Li, S. Jin, Q. Cheng, T. J. Cui, “Reconfigurable Intelligent Surface: Power Consumption Modeling and Practical Measurement Validation”, 10.48550/arXiv.2211.00323., 2022

[XHL+19] K. Xu, W. Hu, J. Leskovec, and S. Jegelka, “How powerful are graph neural networks?” in International Conference on Learning Representations, 2019.

[XR21] Y. Xing and T. S. Rappaport, “Terahertz wireless communications: Cosharing for terrestrial and satellite systems above 100 GHz,” IEEE Communications Letters, vol. 25, no. 10, pp. 3156–3160, 2021.

[YGY+23] H. Yu, H. Guo, X. Yi and T. Svensson, "A Robust Approach to Dynamic Pilot Assignment in Distributed Massive MIMO Networks," 2023 IEEE 24th International Workshop on Signal Processing Advances in Wireless Communications (SPAWC), Shanghai, China, 2023, pp. 606-610, doi: 10.1109/SPAWC53906.2023.10304481.

[YH15] S. Yang and L. Hanzo, "Fifty Years of MIMO Detection: The Road to Large-Scale MIMOs," in IEEE Communications Surveys & Tutorials, vol. 17, no. 4, pp. 1941-1988, Fourth quarter 2015

[ZCB+23] P. Zheng, H. Chen, T. Ballal, M. Valkama, H. Wymeersch, and T. Y. Al-Naffouri, "JrCUP: Joint RIS Calibration and User Positioning for 6G Wireless Systems," IEEE Transactions on Wireless Communications (2023).

[ZDC+23] Z. Zhang, L. Dai, X. Chen, C. Liu, F. Yang, R. Schober, and H. V. Poor, “Active RIS vs. passive RIS: Which will prevail in 6G?”, IEEE Transactions on Communications, vol. 71, no. 3, March 2023.

[ZFK+24] P. Zhang, C. B. Fındık, P. Kyösti, V. Hovinen, K. Nevala, N. Tervo, M. E. Leinonen, and A. Pärssinen, “A Modular COTS-based High-Efficient Sub-THz Channel Sounder and Experimental Validations,” in Proc. 17th Eur. Conf. Antennas Propag. (EuCAP), Mar. 2024, pp. 1–5.

[ZLM+20] J. Zhang, G. Li, A. Marshall, A. Hu and L. Hanzo, "A New Frontier for IoT Security Emerging From Three Decades of Key Generation Relying on Wireless Channels," in IEEE Access, vol. 8, pp. 138406-138446, 2020, doi: 10.1109/ACCESS.2020.3012006.

[ZMZ23] Zhu, Lipeng, Wenyan Ma, and Rui Zhang. "Movable Antennas for Wireless Communication: Opportunities and Challenges." arXiv preprint arXiv:2306.02331, 2023.

[ZRS+21] A. Zappone, M. Di Renzo, F. Shams, X. Qian and M. Debbah, "Overhead-Aware Design of Reconfigurable Intelligent Surfaces in Smart Radio Environments," in IEEE Transactions on Wireless Communications, vol. 20, no. 1, pp. 126-141, Jan. 2021

Appendix

A.1 Channel modelling

A.1.1 3GPP channel model

Table A.1-1: Large-scale parameters.

Parameter		Entrance hall		Indoor – Office [38.901		Residential		UMi-street canyon [38.901]	
		LoS	NLoS	LoS	NLoS	LoS	NLoS	LoS	NLoS
DS $\mathrm{lgDS} = \log_{10}(\mathrm{DS}/1\mathrm{s})$	μ_{lgDS}	-7.84	-7.62	-7.71	-7.78	-7.74	-7.67	-7.66	-7.35
	σ_{lgDS}	0.12	0.19	0.18	0.27	0.42	0.45	0.38	0.62
ASD $\mathrm{lgASD} = \log_{10}(\mathrm{ASD}/1°)$	μ_{lgASD}	1.09	1.32	1.6	1.62	0.89	0.76	1.1	1.03
	σ_{lgASD}	0.27	0.21	0.18	0.25	0.37	0.4	0.41	0.57
ASA $\mathrm{lgAS}A = \log_{10}(\mathrm{ASA}/1°)$	μ_{lgASA}	1.39	1.54	1.37	1.63	0.99	1.32	1.56	1.64
	σ_{lgASA}	0.17	0.19	0.38	0.32	0.42	0.33	0.31	0.41
ZSD $\mathrm{lgZOD} = \log_{10}(\mathrm{ZOD}/1°)$	μ_{lgZSD}	0.36	0.53	-0.85	1.08	0.04	0.14	[38.901]	[38.901]
	σ_{lgZSD}	0.27	0.25	0.58	0.36	0.3	0.36	[38.901]	[38.901]
ZSA $\mathrm{lgZSA} = \log_{10}(\mathrm{ZSA}/1°)$	μ_{lgZSA}	0.72	0.83	0.88	1.06	0.3	0.48	0.51	0.83
	σ_{lgZSA}	0.33	0.33	0.18	0.55	0.32	0.41	0.25	0.26
SF (dB)	σ_{lgSF}	0.9	7.3	3	8	1.1	8.2	4	7.8
K-factor (dB)	μ_{K}	6.2	NA	7	NA	7.8	NA	9	NA
	σ_{K}	5.4	NA	4	NA	7.9	NA	5	NA
Path loss	α (dB)	73.6	74.4	75.4	70.9	79.2	52.5	75.4	68.2
	β	2.1	2.8	1.7	3.8	1.7	3.9	2.1	3.5

Table A.1-2: Small-scale parameters.

Parameter		Entrance hall		Indoor – Office [38.901]		Residential		UMi-street canyon [38.901]	
		LoS	NLoS	LoS	NLoS	LoS	NLoS	LoS	NLoS
Delay scaling parameter	r_τ	4.1	2.2	3.6	3	5.3	3.3	3	2.1
Number of Clusters N_c	$\mu_{\mathrm{N_c}}$	24	18	15	19	6	3	12	19
Number of rays per cluster M	μ_{M}	2.3	2.3	20	20	1.8	2.1	20	20

Cluster DS (ns) CDS	μ_{CDS}	4	3.7	3.91	3.91	2.1	1.7	5	11
Cluster ASD (°) CASD	μ_{CASD}	2.3	2.1	5	5	1.4	1.2	3	10
Cluster ASA (°) CASA	μ_{CASA}	3.2	3	8	11	2.8	1.4	17	22
Cluster ZSD (°) CZSD	μ_{CZSD}	1.4	1.1	0.1	4.5	0.6	0.5	[38.901]	[38.901]
Cluster ZSA (°) CZSA	μ_{CZSA}	2.5	2	9	9	1.2	1.1	7	7
Per cluster shadowing (dB) ζ	μ_{ζ}	10.2	6.1	6	3	8	6.4	3	3

Table A.1-3: Cross-correlation parameters.

Parameter 1	Parameter 2	Entrance hall		Indoor – office [38.901]		Residential		UMi-street canyon [38.901]	
		LoS	NLoS	LoS	NLoS	LoS	NLoS	LoS	NLoS
ASD	DS	0.2	0.3	0.6	0.4	0.4	0.3	0.5	0
ASA	DS	0.5	0.4	0.8	0	0.3	0.6	0.8	0.4
ASA	SF	-0.2	0.4	-0.5	-0.4	-0.3	0.4	-0.4	-0.4
ASD	SF	-0.7	0.3	-0.4	0	-0.2	0	-0.5	0
DS	SF	-0.2	0.4	-0.8	-0.5	0.3	0.2	-0.4	-0.7
ASD	ASA	0.3	0.1	0.4	0	0.2	0.1	0.4	0
ASD	K	-0.5	NA	0	NA	-0.2	NA	-0.2	NA
ASA	K	-0.6	NA	0	NA	-0.2	NA	-0.3	NA
DS	K	-0.2	NA	-0.5	NA	0.1	NA	-0.7	NA
SF	K	0.6	NA	0.5	NA	0.7	NA	0.5	NA
ZSD	SF	-0.5	0.2	0.2	0	-0.5	0.4	0	0
ZSA	SF	-0.4	0.2	0.3	0	-0.2	-0.1	0	0
ZSD	K	-0.7	NA	0	NA	-0.7	NA	0	NA
ZSA	K	-0.9	NA	0.1	NA	-0.5	NA	0	NA
ZSD	DS	-0.1	0.3	0.1	-0.3	0.2	0.2	0	-0.5
ZSA	DS	0.2	0.2	0.2	-0.1	0	0	0.2	0
ZSD	ASD	0.5	0.5	0.5	0.4	0.6	0.2	0.5	0.5
ZSA	ASD	0.3	0.3	0	0.2	0.2	-0.1	0.3	0.5
ZSD	ASA	0.5	0.2	0	-0.1	0.3	0.5	0	0
ZSA	ASA	0.6	0.5	0.5	0.4	0.3	0.4	0	0.2
ZSD	ZSA	0.7	0.6	0	0.4	0.4	0.4	0	0

A.1.2 Coverage analysis at THz frequencies

System model for coverage analysis at THz frequencies: While both Line-of-Sight (LoS) and non-LoS (NLoS) multipath components are significant in mmWave, at THz frequencies the NLoS paths can be considered insignificant [ECM+22].

At THz frequencies, the path loss is characterized by the spreading loss and the molecular absorption loss.

The spreading loss accounts for the attenuation due to the expansion of a wave as it propagates through the medium, i.e., the free-space path loss [JA11].

The molecular absorption loss also determines the available transmission bandwidth, which drastically shrinks with distance. For communication distances below one metre, where the number of molecules found along the path is small, the THz band behaves as a single transmission window THz wide. As the transmission distance increases, molecular absorption defines multiple transmission windows, each of them tens or hundreds of GHz wide. The bandwidth of each individual transmission window shrinks with the transmission distance. Therefore, as the distance increases (i.e., the number of absorbing molecules augments), not only the absorption loss increases, but also the transmission windows shrink [ECM+22], [HJ19], [SAN21].

Since water vapor (H_2O) dominates the absorption losses at high frequencies [SAN21], [JA11], the frequency-dependent molecular absorption coefficient $k(f_c)$ is considered for H_2O, leading to the value of 0,045 m^{-1} at 600 GHz, retrieved from [JA11]. The frequency of 600 GHz has been selected considering the availability of the above-mentioned transmission windows, the values of $k(f_c)$ as a function of frequency and the selection of a frequency value still in the lower range of the THz frequencies, looking at feasibility aspects in terms of future early stages of technology availability.

The coverage evaluation has been performed for the same path loss values for both mmWave and THz frequencies, in a range of 110 – 130 dB, which are achievable for mmWave at the upper limits of distance and frequency in the range of validity of **(3-1)** and **(3-2)**.

Mathematical model for coverage analysis at THz frequencies:

The involved parameters with their definitions and relevant references are listed hereafter:

PL Path loss [38.901], [M.2412-0], [ECM+22], [SAN21], [HJ19], [JA11]

d_{2D} 2D distance between BS and UE [38.901], [M.2412-0]

d_{3D} 3D distance between BS and UE [38.901], [M.2412-0]

f_c centre frequency [38.901], [M.2412-0]

$k(f_c)$ frequency-dependent molecular absorption coefficient for H_2O (0,045 m^{-1} at 600 GHz) [JA11]

e Euler's number (2,718281828459)

c light speed in free space ($3x10^8$ m/s)

h_{BS} BS antenna height (3 m) [M.2412-0]

h_{UE} UE antenna height (1.5 m) [M.2412-0]

Assumptions for coverage analysis at THz frequencies:

- It is considered a LoS scenario without multipath effects, with ideal isotropic antennas at both transmitting and receiving side.
- Path loss evaluation at 100 GHz is evaluated from 3GPP [38.901] and ITU-R [M.2412-0] channel modelling via (3-1) and (3-2).
- Path loss evaluation at THz frequencies is evaluated starting from [ECM+22], [SAN21], [HJ19], [JA11] via (3-3).

Results evaluation for coverage analysis at THz frequencies: For mmWave InH – Office – LoS scenario, from (3-1) at the upper limits of d_{3D} = 150 m and f_c = 100 GHz, the resulting path loss is equal to 110,05 dB.

For THz – LoS scenario, from (3-3) at f_c = 600 GHz, the same path loss (109,96 dB) is achieved at d_{3D} = 10 m. In this case:

- Molecular absorption loss (600 GHz, 10 m) = 1,954 dB with $k(f_c)$ = 0,045 m^{-1} (molecular absorption coefficient for H_2O)
- Spreading loss (600 GHz, 10 m) = 108,005 dB

Therefore, almost all the path loss is governed by the spreading loss, with a negligible contribution coming from the molecular absorption loss.

It is worthwhile noting that:

- applying (3-1) instead of (3-3) at f_c = 600 GHz (and consequently out of the range of validity of (3-1)) and at d_{3D} = 10 m would have led to a path loss of 105,26 dB instead of 109,96 dB, with a reduction of 4.7 dB, i.e. a 4.3% reduction error in path loss evaluation;
- applying (3-2) instead of (3-3) at f_c = 600 GHz (and consequently out of the range of validity of (3-2)) and at d_{3D} = 10 m would have led to a path loss of 106,12 dB instead of 109,96 dB, with a reduction of 3.84 dB, i.e. a 3.5% reduction error in path loss evaluation.

For mmWave InF – LoS scenario, from (3-2) at the upper limits of d_{3D} = 600 m and f_c = 100 GHz, the resulting path loss is equal to 129,57 dB.

For THz – LoS scenario, from (3-3) at f_c = 600 GHz, the same path loss (129,86 dB) is achieved at d_{3D} = 45 m. In this case:

- Molecular absorption loss (600 GHz, 45 m) = 8,794 dB with $k(f_c)$ = 0,045 m^{-1} (molecular absorption coefficient for H_2O)
- Spreading loss (600 GHz, 45 m) = 121,069 dB

Therefore, the contribution coming from the molecular absorption loss accounts for nearly 7% of the overall path loss.

It is worthwhile noting that:

- applying (3-1) instead of (3-3) at f_c = 600 GHz (and consequently out of the range of validity of **(3-1)**) and at d_{3D} = 45 m would have led to a path loss of 116,56 dB instead of 129,86 dB, with a reduction of 13.3 dB, i.e. a 10.2% reduction error in path loss evaluation;
- applying **(3-2)** instead of **(3-3)** at f_c = 600 GHz (and consequently out of the range of validity of **(3-2)**) and at d_{3D} = 45 m would have led to a path loss of 120,17 dB instead of 129,86 dB, with a reduction of 9.69 dB, i.e. a 7.5% reduction error in path loss evaluation.

For THz – LoS scenario, from **(3-3)** at f_c = 600 GHz and d_{3D} = 100 m, the resulting path loss is equal to 147,55 dB. In this case:

- Molecular absorption loss (600 GHz, 100 m) = 19,543 dB with $k(f_c)$ = 0,045 m^{-1} (molecular absorption coefficient for H_2O)
- Spreading loss (600 GHz, 100 m) = 128,005 dB

Therefore, the contribution coming from the molecular absorption loss accounts for about 13% of the overall path loss.

It is worthwhile noting that:

- applying **(3-1)** instead of **(3-3)** at f_c = 600 GHz (and consequently out of the range of validity of **(3-1)**) and at d_{3D} = 100 m would have led to a path loss of 122,56 dB instead of 147,55 dB, with a reduction of 25 dB, i.e. a 16.9% reduction error in path loss evaluation;
- applying **(3-2)** instead of **(3-3)** at f_c = 600 GHz (and consequently out of the range of validity of **(3-2)**) and at d_{3D} = 100 m would have led to a path loss of 127,62 dB instead of 147,55 dB, with a reduction of 19.93 dB, i.e. a 13.5% reduction error in path loss evaluation.

The path loss of 147,55 dB is not achievable even at the upper limits of d_{3D} = 600 m and f_c = 100 GHz for mmWave InF – LoS scenario, from **(3-2)**, where the path loss only achieves 129,57 dB and consequently it is not possible to perform a coverage reduction evaluation in such a case.

As expected, the higher d_{3D} the higher the error in path loss evaluation when applying **(3-1)** and **(3-2)** out of the range of their validity in terms of f_c, instead of applying **(3-3)**.

A.2 MIMO transmission

A.2.1 D-MIMO with Rotary ULAs

The simulation parameters are listed in Table A.2-4. A spatially correlated Rician fading channel model [ÖBL19] is considered, where the path-loss coefficients are modelled according to a channel model validated by 3GPP for indoor industrial scenarios [R1-1813177]. Perfect hardware and perfect synchronization are assumed. Still, some practical limitations would be the finite angular resolution, angular speed and power consumption of the servo motor, and imperfect synchronization among APs.

Table A.2-4: Simulation Parameters.

Parameter	Notation	Value
Total Number of Antenna Elements	M	16
Number of APs	Q	[1,2,4,8]
Number of active devices in each timeslot	K	16
Length of the side of square coverage area	l	100 m
Uplink Transmit power	p	100 mW
Noise power	σ^2	-92 dBm
Noise figure	N_F	9 dB
Height of the APs	h_{AP}	12 m
Height of the devices	h_{AP}	1.5 m
Carrier frequency	f_c	3.5 GHz
Signal bandwidth	B	20 MHz

A.2.2 Distributed-MIMO with analogue fronthaul

Experimental setup: Figure A.2-1 displays the block diagram of the experimental setup. Within this configuration, TRxP 1 uses an analogue radio over fibre (ARoF) fronthaul link, whereas TRxP 2 fronthaul utilizes a 1.2-meter coaxial cable. These tests use a 10 MHz orthogonal frequency-division multiplexing (OFDM) signal with a subcarrier spacing (SCS) of 30 kHz, consisting of 24 resource blocks (RBs), and operating at a carrier frequency of 622 MHz, i.e., New Radio (NR) band n71.

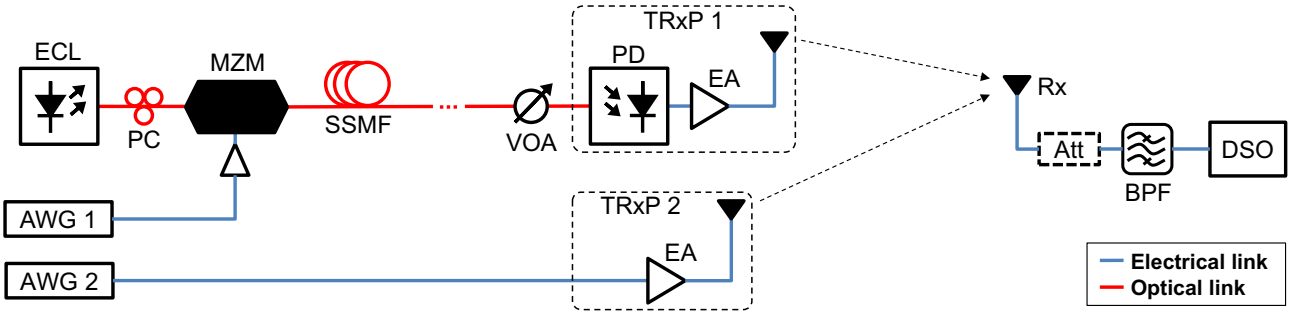

Figure A.2-1: Experimental setup block diagram.

To send the ARoF signal to TRxP 1, an external cavity laser (ECL) operating at a wavelength of 1550.9 nm, with a linewidth below 100 kHz, and providing an output power of 12 dBm, is employed as the light source. The generation of OFDM analogue signals at the RF carrier is accomplished using an arbitrary waveform generator (AWG) with a sampling frequency of 50 GSa/s. These analogue signals modulate the output of the ECL through a single-drive Mach-Zehnder modulator (MZM), producing ARoF signals by operating the MZM close to the quadrature point. A polarization controller (PC) is utilized to adjust the light polarization at the MZM input. The output from the MZM is transmitted through standard single-mode fibre (SSMF), and the

received optical power is adjusted using a variable optical attenuator (VOA) before optical heterodyne detection in a photodetector (PD) with an analogue bandwidth of 9 GHz. After photodetection, the signal is amplified by an electrical amplifier (EA) with a gain of 22 dB and a noise figure (NF) of 5.5 dB. Similarly, the electrical signal transmitted to TRxP 2 is amplified by an EA featuring a gain of 30 dB and a NF of 6 dB. For wireless transmission, multiband antennas with a peak gain of about 3 dBi were utilized. The chosen EAs offer comparable performance for both TRxPs, despite their different fronthaul implementations.

Following wireless transmission, the received signal is filtered with a narrow bandpass filter (BPF) with a central frequency of 622 MHz. For coherent joint transmission (CJT) tests, there's an optional utilization of an electrical attenuator (Att) preceding the BPF. This is done to regulate the received signal power, ensuring validation of the CJT power and diversity gains. Additionally, it's important to note that the setup's geometry is adjusted to approximate flat fading conditions for the received signals from both TRxPs. However, maintaining the same distance between the TRxPs and the receiver antenna was difficult. As a result, the distance between the receiver antenna and TRxP 1 is 1 meter, while it's 1.3 meters for TRxP 2. Moreover, the spacing between the antennas of the TRxPs is around 3 wavelengths, approximately 1.5 meters at a carrier frequency of 622 MHz. Subsequently, the received signals are stored in a digital storage oscilloscope (DSO) for further offline signal processing. Figure A.2-2 shows a photo of the experimental setup.

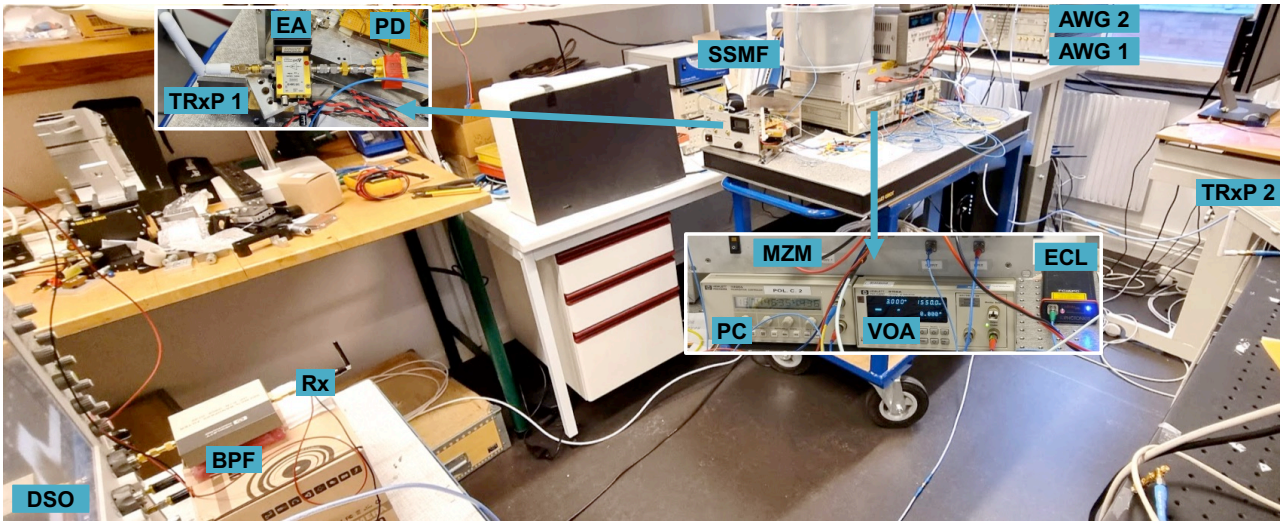

Figure A.2-2: Experimental setup photo.

Following analogue-to-digital conversion, initially a digital Costas loop is used for carrier recovery, followed by digital down conversion (DDC) to bring the signal to baseband. Then, after the removal of cyclic prefix (CP) and conversion from time domain to frequency domain using the fast Fourier transform (FFT), a zero-forcing (ZF) equalizer is calculated. The coefficients of the equalizer are computed, averaged, and interpolated, following the methodology outlined by standardization bodies [38.104].

In channel estimation, the receiver performs the channel estimation and provides explicit channel estimation information to the transmitter. The least squares estimator (LSE) is employed to derive the channel estimate. To compute the estimates of both TRxPs, the same signal is separately transmitted using each TRxP. The instantaneous channel estimate in the frequency domain per subcarrier is determined as follows:

$$\widehat{\mathbf{H}} = \mathbf{Y}\mathbf{X}^{\mathrm{H}}\left(\mathbf{X}\mathbf{X}^{\mathrm{H}}\right)^{-1}, \qquad \textbf{(A.2-1)}$$

where $\mathbf{X}$ stands for a diagonal matrix containing known symbol sequences, $\mathbf{Y}$ represents the sequences aligned in time subsequent to wireless transmission, and $\widehat{\mathbf{H}}$ denotes the channel estimate. It's important to note that $\widehat{\mathbf{H}}$ comprises the amplitude and phase alterations arising from the wireless channel, analogue front-ends, and fronthaul links. Subsequently, to implement CJT, only the signal from TRxP 2 is aligned in time and precoded. The precoder is computed using the complex ratio $\hat{\mathbf{h}}_1/\hat{\mathbf{h}}_2$, where $\hat{\mathbf{h}}_1$ and $\hat{\mathbf{h}}_2$ represent the vector channel estimates of subcarriers for TRxP 1 and TRxP 2, respectively. This ensures that the OFDM signal transmitted by TRxP 2 is both time and phase aligned with the signal transmitted by TRxP 1.

A.2.3 MU-MIMO optimization in diverse device scenarios

In diverse devices scenarios (see Figure A.2-3) the full optimization of all DL MU-MIMO scheme parameters (e.g., precoding, channel estimation, feedback, etc.) may be prohibitively difficult and computationally intensive. This work targets to investigate intelligent optimization methods and trade-offs to deliver required performance but also reduce the computational cost (and related energy consumption) on the Base Station and UE sides. A possible UL connection with the DL optimization is also discussed. The focus is on TDD mode of operation.

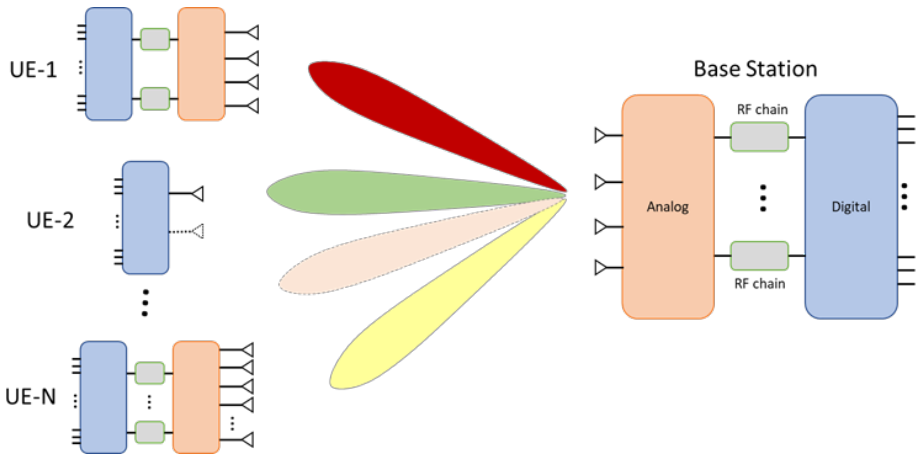

Figure A.2-3: MU-MIMO optimization of the DL in diverse devices scenario.

Main part of the development in this work so far, has been the conceptional construction of the flexible "effective antennas" concept, a tool of dimensionality reduction at arrays, and a preliminary simulation of the interference rejection scenario. The term **Effective Antenna (EA), for RX or TX antenna array,** defines a set of linear combinations over RX or TX array. The purpose of such definition is to have EAs "clean" from interference, that can be then the aim for the DL precoder, instead of the physical antennas.

In the following, "Effective" objects are denoted by a bar over the respective parameter. For example, for the RX array of size $N_{R_{(u)}}$, a weighted combination of the received signals $\boldsymbol{r}_{(u)}$ is denoted as (see Figure A.2-4):

$$\bar{r}_{(u)}(\mathrm{n}) = \boldsymbol{w}_{(u)n}^{H}\boldsymbol{r}_{(u)}, \qquad \dim \boldsymbol{w}_{(u)n} = \dim \boldsymbol{r}_{(u)} = N_{R_{(u)}} \times 1. \tag{A.2-2}$$

Every EA combines the components of the received signals vector from the full set of RX antennas into a complex-valued scalar. This combination acts as if a single effective RX antenna (it will be observed that it has however more properties than 1 physical antenna). Here n is the index of a specific weight row vector (specific "equalizer"). Each combination defines an Effective Antenna (EA). Only effective antennas (and not all physical antennas) will be then clean from the interference and be the aim for the DL precoder.

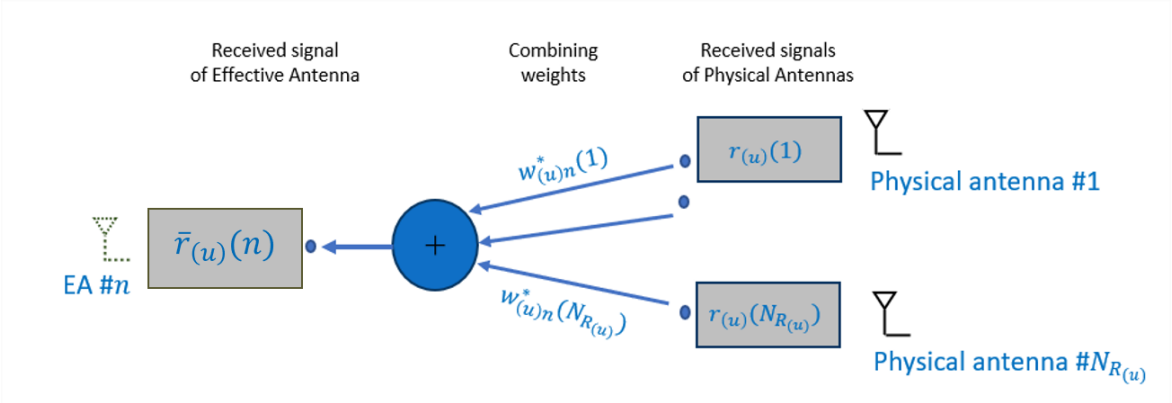

Figure A.2-4: Illustration of the UE RX Effective Antenna concept.

The above framework should help the 6G MU-MIMO systems to overcome some *basic* challenges:

- Incorporation of devices with large number of antenna elements
  - especially for total number of all UE devices RX antennas $N_R \equiv \sum_{u=1}^{N_U} N_{R_{(u)}}$ being larger than BS TX antennas: $N_R > N_T$, or $N_R \gg N_T$
  - and escape their pollution by multi-user interference.
- Extension of the range of the communication
- Reduction of the response and adaptation times (especially for large UE arrays)
- Interference rejection (e.g., from other cells and in the small cells)
- Channel Ageing problems for DL precoder construction

Array dimensionality reduction via Effective Antennas: In a MU-MIMO system with large total number of UEs RX antennas, they cannot be all discriminated by BS DL ZF precoder if $N_R > N_T$. This may lead to interference noise over UEs arrays. However, using EAs concept, the discrimination becomes possible. The dimensionality reduction has been introduced in 2004 [SSH04] as "Coordinated Transmit-Receive Processing". In that work, it was assumed that the number of EAs is equal to the number of the information layers per UE. However, in the presented EA concept, the number of EAs can be also smaller or larger (e.g., due to incorporation of the interference reduction). A smaller number of EAs can be used in the overloaded mode (see e.g. [WPM07], [HH17]): the mode yet to be researched.

The EAs idea is illustrated below via the projection method, considering a single layer transmission to all users. The RX equation in that case is:

$$\boldsymbol{r}_{(u)} = \boldsymbol{H}_{(u)}\boldsymbol{P}\boldsymbol{s} + \boldsymbol{n}_{(u)}, \quad \textbf{(A.2-3)}$$

where $\boldsymbol{r}_{(u)}$ is the received vector over the full RX array, $\boldsymbol{H}_{(u)}$ is the physical channel matrix for user # u, $\boldsymbol{P}$ is the precoder matrix for all N_U users, $\boldsymbol{s}$ denote the symbols for all users, and $\boldsymbol{n}_{(u)}$ is the noise vector for user # u at its RX physical array. Every user $u\epsilon\{1{:}\,N_u\}$ is equipped with $N_{R(u)}$ RX antennas and treats its received signal vector $\boldsymbol{r}_{(u)}$, $\dim \boldsymbol{r}_{(u)} = N_{R_{(u)}} \times 1$, with an "equalizer" row vector $\boldsymbol{w}_{(u)}^H$, $\dim \boldsymbol{w}_{(u)}^H = 1 \times N_{R_{(u)}}$ as $\boldsymbol{w}_{(u)}^H \boldsymbol{H}_{(u)}$. The output of this projection is a 1-layer scalar reduced dimension signal:

$$\bar{r}_{(u)} = \boldsymbol{w}_{(u)}^H \boldsymbol{r}_{(u)} = \boldsymbol{w}_{(u)}^H \boldsymbol{H}_{(u)} \boldsymbol{P}\boldsymbol{s} + n_{(u)}. \quad \textbf{(A.2-4)}$$

Then, the Base Station may construct the zero-forcing solution from the modified channel:

$$\overline{\boldsymbol{H}} = \begin{bmatrix} \boldsymbol{w}_{(1)}^H \boldsymbol{H}_{(1)} \\ \vdots \\ \boldsymbol{w}_{(N_U)}^H \boldsymbol{H}_{(N_U)} \end{bmatrix}, \quad \dim \overline{\boldsymbol{H}} = N_U \times N_T \,, \quad \dim \boldsymbol{w}_{(u)}^H \boldsymbol{H}_{(u)} = 1 \times N_T \quad \textbf{(A.2-5)}$$

This allows to construct a DL precoder (construction of such precoder is discussed, e.g., in [PS08] and [SPS+04]).

$$\boldsymbol{P} = \mathrm{pinv}(\overline{\boldsymbol{H}}) * \boldsymbol{D} \quad \textbf{(A.2-6)}$$

Note that a precoder can be linear (as currently specified for use in the 4G and 5G systems) or nonlinear as it is discussed in the presented references. Here, the nonlinear precoders will not be discussed but an interesting possibility of mixing linear and nonlinear precoding can be noted (see e.g. [CVR19]). A possible better channel estimation accuracy due to the usage of EAs (or due to the "decoding from data" discussed further) may facilitate construction of nonlinear precoders which are known to be sensible to the channel errors.

$$\boldsymbol{P} = \mathrm{pinv}(\overline{\boldsymbol{H}}) * \boldsymbol{D} \quad \textbf{(A.2-7)}$$

In general, the total $\bar{N}_{R_{(u)}}$ rows of the equalizer vectors can be stacked into an equalizer matrix $\boldsymbol{G}_{(u)}$:

$$\boldsymbol{G}_{(u)} = \begin{bmatrix} \boldsymbol{w}_{(u)1}^H \\ \cdots \\ \boldsymbol{w}_{(u)\bar{N}_{R(u)}}^H \end{bmatrix} \quad \textbf{(A.2-8)}$$

Then, this leads to:

$$\bar{\boldsymbol{r}}_{(u)} = \boldsymbol{G}_{(u)} * \boldsymbol{r}_{(u)}\,, \quad \dim \boldsymbol{G}_{(u)} = \bar{N}_{R_{(u)}} \times N_{R_{(u)}}\,, \quad \dim \bar{\boldsymbol{r}}_{(u)} = \bar{N}_{R_{(u)}} \times 1 \qquad \textbf{(A.2-9)}$$

The EAs shrink the full channel represented by the channel matrix $\boldsymbol{H}_{(u)}$ with $N_{R(u)}$ rows (each having length of N_T of the BS array) and of dimension $\dim \boldsymbol{H}_{(u)} = N_{R_{(u)}} \times N_T$, into the transformed channel with reduced number of rows:

$$\bar{\boldsymbol{H}}_{(u)} = \boldsymbol{G}_{(u)} * \boldsymbol{H}_{(u)}, \quad \dim \bar{\boldsymbol{H}}_{(u)} = \bar{N}_{R_{(u)}} \times N_T\,, \qquad \textbf{(A.2-10)}$$

Each row in $\bar{\boldsymbol{H}}_{(u)}$ represents channel from BS antennas to each UE RX EA:

$$\boldsymbol{h}^H_{(u)n} \equiv \bar{\boldsymbol{H}}_{(u)}(n, 1{:}\,N_T) = \boldsymbol{w}^H_{(u)n}\boldsymbol{H}_{(u)}\,, \quad n = 1{:}\,\bar{N}_{R_{(u)}}\,, \quad \dim \boldsymbol{h}^H_{(u)n} = 1 \times N_T \qquad \textbf{(A.2-11)}$$

In Figure A.2-5, it is shown show that estimation of channel realised at any set of UE RX EAs can be delivered to the BS in the TDD reciprocity mode via uplink reference signal such as, e.g., the sounding reference signal (SRS) transmission used in 4G and 5G.

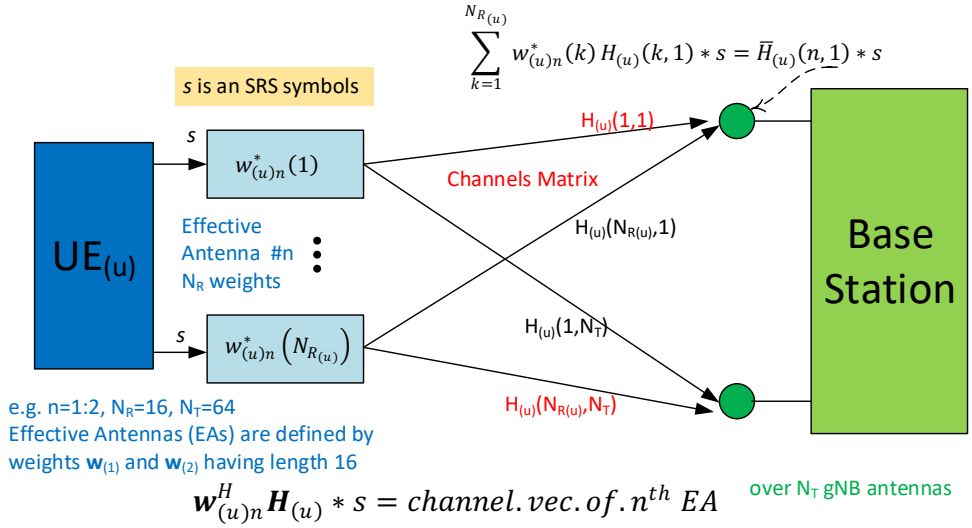

Figure A.2-5: SRS transmission to deliver channel $\boldsymbol{h}^H_{(u)n} \equiv \boldsymbol{w}^H_{(u)n}\boldsymbol{H}_{(u)}$ corresponding EAs with index "n".

As a further ramification of the EAs approach, every UE can suggest to BS an enlarged set of "candidate" EAs, and BS may choose and indicate which EAs to use. Note that UE does not know the EAs of the other users (e.g., various EAs between different UEs can be highly correlated), hence, choice from the BS with wider system view can be beneficial.

Now, matrix $\boldsymbol{G}_{(u)}$ can be different for each user and its dimensionality reduction can be done in several, $N_{G_{(u)}}$, steps:

$$\boldsymbol{G}_{(u)} = \prod_{n=1}^{N_{G_{(u)}}} \boldsymbol{G}^{(n)}_{(u)}, \qquad \textbf{(A.2-12)}$$

where every matrix $\boldsymbol{G}^{(n)}_{(u)}$ can belong to possibly different "alphabet" sets (general or defined by parameters from a predefined set, e.g., rows of a pre-defined transform) which also can realize different architectures (e.g., fully digital, mix of digital and analogue, fully analogue such as phase shifters having quantized values).

For example, in case of two-step dimensionality reduction:

$$\boldsymbol{G}_{(u)} = \boldsymbol{G}^{(1)}_{(u)}\boldsymbol{G}^{(2)}_{(u)},$$
$$\dim \boldsymbol{G}^{(1)}_{(u)} = \bar{N}_{R_{(u)}} \times N^{(\text{dim}-\text{reduction 2})}_{(u)}, \qquad \dim \boldsymbol{G}^{(2)}_{(u)} = N^{(\text{dim}-\text{reduction 2})}_{(u)} \times N_{R_{(u)}} \qquad \textbf{(A.2-13)}$$

In that case, the "outer" element, $\boldsymbol{G}^{(2)}_{(u)}$, performs the larger dimensionality reduction and can be updated (using the SRS) less frequently. Even if the channel slightly changes, $\boldsymbol{G}^{(2)}_{(u)}$ will still focus the power onto the EAs,

thus performing more precise channel estimation. On the other hand, having the "inner" element, $\boldsymbol{G}_{(u)}^{(1)}$, adjusting more frequently, according to the changing channel $\boldsymbol{H}_{(u)}$, allows exact ZF to be performed. Better effective channel estimation accuracy allows faster channel acquisition (with no or few repetitions).

The "fine" structured matrix $\boldsymbol{G}_{(u)}^{(1)}$ can be fixed per smaller sets of resources (e.g., per RE) and the "rough" matrix $\boldsymbol{G}_{(u)}^{(2)}$, can be defined per larger sets of resources, e.g., per sub-band, per whole frequency band, or per frequency regions with quasi-static channel (see Figure A.2-6).

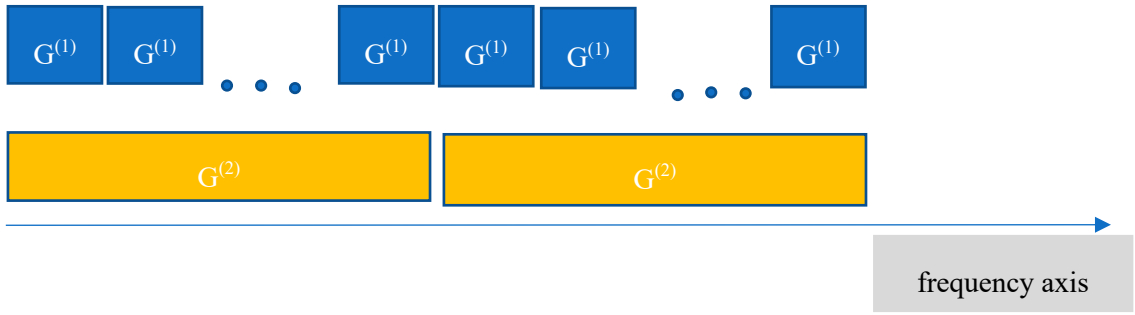

Figure A.2-6: Possible allocations of the "fine" $\boldsymbol{G}_{(u)}^{(1)}$ and the "rough" $\boldsymbol{G}_{(u)}^{(2)}$ matrices along the frequency axis.

Considering for example, the following sizes:

$$\bar{N}_{R_{(u)}} = 2,\ N_{(u)}^{(\text{dim-reduction 2})} = 4,\ N_{R_{(u)}} = 64 \qquad \textbf{(A.2-14)}$$

the decomposition process reduces 64 physical antennas to 2 EAs in two steps. These two EAs can serve 1 or 2 information layers. For reduction performed in two steps, the relation $\bar{\boldsymbol{r}}_{(u)} = \boldsymbol{G}_{(u)} * \boldsymbol{r}_{(u)}$ can be represented as in Figure A.2-7, also considering a design option of mixed digital and analogue steps. Note that such architecture can make the array be cost effective and simpler, and the analogue part can belong to a predefined alphabet efficient for the implementation. Of course, other design options are possible, including twos steps that are only digital or only analogue.

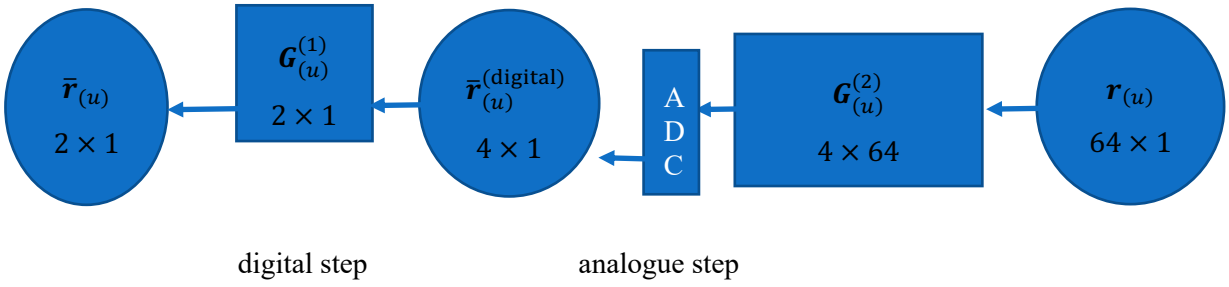

Figure A.2-7: Example of two-step processing for the mixed architecture arrays having analogue and digital hardware elements.

A very important aspect of the proposed methodology is that the UE array may incorporate the interference rejection mechanisms into the UE RX EAs construction to treat the noise vector term by a linear transform matrix $\boldsymbol{T}_{(u)}$ as:

$$\boldsymbol{r}_{(u)}^{(\text{modified})} \equiv \boldsymbol{T}_{(u)}\boldsymbol{r}_{(u)} = \boldsymbol{T}_{(u)}\boldsymbol{H}_{(u)}\boldsymbol{P}\boldsymbol{s} + \boldsymbol{T}_{(u)}\boldsymbol{n}_{(u)} = \boldsymbol{H}_{(u)}^{(\text{modified})}\boldsymbol{P}\boldsymbol{s} + \boldsymbol{n}_{(u)}^{(\text{modified})} \qquad \textbf{(A.2-15)}$$

Thus, the interference rejection can be inserted into the EAs by adjusting EAs toward the modified channel. For example, the EAs can be constructed as:

$$\boldsymbol{G}_{(u)} = \begin{bmatrix} \boldsymbol{u}_{(u)1}^{(\text{modified})H} \\ \dots \\ \boldsymbol{u}_{(u)\bar{N}_{R(u)}}^{(\text{modified})H} \end{bmatrix} \quad \textbf{(A.2-16)}$$

from the best (corresponding to the largest values of the $\sigma_{(u)k}^{(\text{modified})}$) hermitically conjugated left eigenvectors $\boldsymbol{u}_{k(u)}^{(\text{modified})H}$ of the SVD decomposition of the modified physical channel $\boldsymbol{H}_{(u)}^{(\text{modified})} = \sum_{k=1}^{\min(N_{R(u)},N_T)} \sigma_{(u)k}^{(\text{modified})} \boldsymbol{u}_{(u)k}^{(\text{modified})} \boldsymbol{v}_{(u)k}^{(\text{modified})H}$. One may note that the celebrated [T99] solution is for the white noise; with interference present, it is not optimal. After pre-whitening the coloured noise becomes white again, but the [T99] SVD decomposition is to be applied above the modified channel.

The multi-step approach for dimensionality reduction allows more flexible construction with optional interference rejections at every step (i.e., for no rejection, a $\boldsymbol{T}_{(u)}^{(n)}$ will be a unit matrix):

$$\boldsymbol{G}_{(u)} = \prod_{n=1}^{N_{G(u)}} \boldsymbol{G}_{(u)}^{(n)} \boldsymbol{T}_{(u)}^{(n)}, \quad \textbf{(A.2-17)}$$

e.g., $\boldsymbol{G}_{(u)} = \boldsymbol{G}_{(u)}^{(1)} \boldsymbol{T}_{(u)}^{(1)} \boldsymbol{G}_{(u)}^{(2)}$, (2-step reduction with no rejection at outer step)

As visualised in Figure A.2-8, the outer dimensionality reduction can act similarly to the physical channel matched filter (e.g., based on the best SVD $N_{(u)}^{(\text{dim}-\text{reduction }2)}$ components) while the interference rejection then applied at the inner step can be simpler learned (e.g., due to smaller size of whitening matrixes).

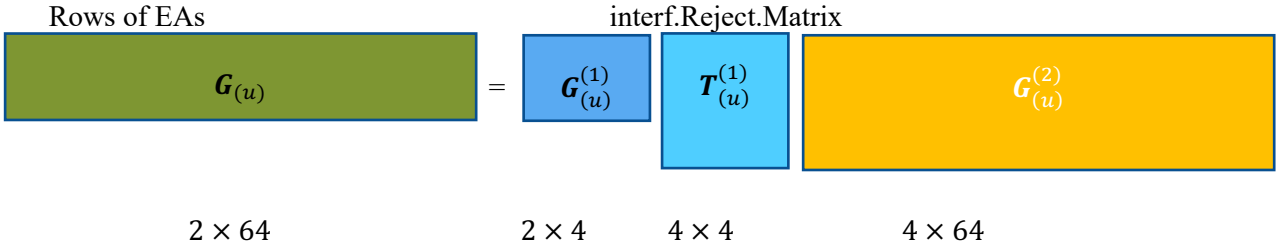

Figure A.2-8: Example of interference rejection at the intermediate dimensionality reduction stage.

An important observation is that since the multi-user interference is absent on the EAs, then one can alternatively use $\boldsymbol{G}_{(u)}^{(2)}$ to be the actual EAs. Thus, considering the example above (no rejection at outer step), such approach allows to treat interference rejection and EAs independently (Figure A.2-9). Then, the number of EAs is usually larger than the number of the information layers and is determined by the needed size of the array to reject the present interference.

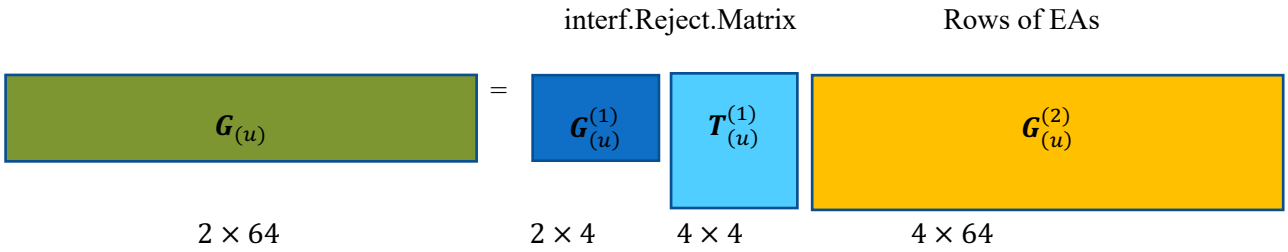

Figure A.2-9: Example of independent interference rejection and EAs construction.

In that case, the number of EAs is usually larger than the number of the info layers and is determined by the needed size of the array to reject the present interference. The above example and observation show an essential "breezing" construction. After the interference is learned, the number of EAs can be reduced (from 4 to 2 in the example), to, e.g., allow more users to enter MU-MIMO. When the interference (or the channel) changes significantly, the EAs are to be re-learned and the structure returns to a larger size (to 4 in the example). If 4x4

interference rejector is not enough, then the sizes of $\boldsymbol{T}_{(u)}^{(1)}$ and $\boldsymbol{G}_{(u)}^{(2)}$ are to be further increased (e.g., to 6 or 8 EAs).

It is crucial again here to stress the deep difference between 1 physical antenna and 1 EAs: even a single EA can reject the interference, while single physical antenna cannot. Treatment of the interference can be of high importance in 6G due to large density of the UE devices and small size of the cells.

Optimized dimensionality reduction - Learning channel from decoded data: The concept of EAs can of course be applied towards the transmit direction, i.e., to construct UE TX EAs. However, the UE RX EAs (performing the DL reception) and UE TX EAs (for UL transmission) can be different, e.g., because the RX EAs may need to reject the interference. When the TX/RX EA sets are constrained to be the same, EAs construction is a joint optimization. That case allows to apply the interesting and powerful concepts of "learning channel from the decoded data" where BS (see Figure A.2-10).

- decodes the UL transmissions (by means of FEC) from the UE TX EAs
- uses the abundant decoded data (from data signals or pilots if present, with or without errors, checked by CRC after the FEC) to combine back symbols from the decoded bits (via Rate Matching machinery) and decode the channel matrices by using frequency/time averaging and *pinv* (or its regularisations and generalizations with forgetting weights).
- then, using this most recent estimated channel (deduced from the UL decoded transmissions), constructs the MU-MIMO DL precoder.

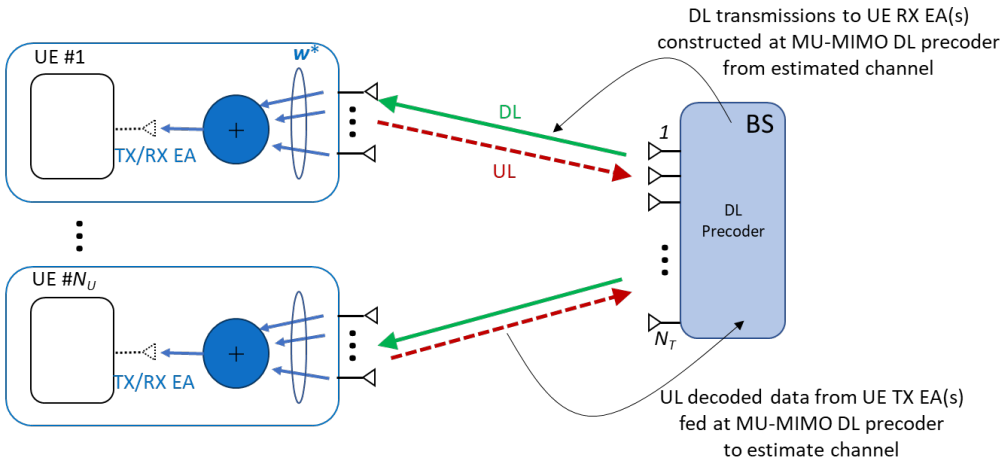

Figure A.2-10: Optimized dimensionality approach including UL decoding usage (from all UEs) to construct the BS DL precoder and perform DL transmission. Example for single TX/RX EA UEs.

The DL precoder at the BS is constructed from the estimated channel:

$$\boldsymbol{P}_{N_T \times N_{\text{total}}} = \text{pinv}\left(\left(\widehat{\boldsymbol{H}}_{N_T \times N_{\text{total}}}\right)^T\right) \boldsymbol{D}_{N_{\text{total}} \times N_{\text{total}}} \qquad \textbf{(A.2-18)}$$

where estimation of the channel matrix from already decoded by FEC data (for MU-MIMO) can be done as:

$$\begin{gathered} \boldsymbol{r} = \sum_{n=1}^{N_{\text{total}}} \boldsymbol{h}_n * s_n + \boldsymbol{n} = \boldsymbol{H}\boldsymbol{s} + \boldsymbol{n}\,, \\ \dim \boldsymbol{r} = N_T \times 1,\ \dim \boldsymbol{n} = N_T \times 1,\ \dim \boldsymbol{h}_n = N_T \times 1, \dim \boldsymbol{H} = N_T \times N_{\text{total}}\,, \\ \dim \boldsymbol{s} = N_{\text{total}} \times 1 \end{gathered} \qquad \textbf{(A.2-19)}$$

Above, $\boldsymbol{N}_{\text{total}}$ is the total number of the spatial streams from all users (e.g., for 3 users with 4 spatial streams each, $N_{\text{total}} = 3 * 4 = 12$).

Considering that N_E total REs surrounding the RE at the estimation (with channel assumed approximately constant) are used for channel estimation, the above equation can be written as:

$$\left[\boldsymbol{r}_{(i=1)}, \ldots, \boldsymbol{r}_{(i=N_E)}\right] = \boldsymbol{H} * \left[\boldsymbol{s}_{(i=1)}, \ldots, \boldsymbol{s}_{(i=N_E)}\right] + \left[\boldsymbol{n}_{(i=1)}, \ldots, \boldsymbol{n}_{(i=N_E)}\right] \qquad \textbf{(A.2-20)}$$

introducing matrices

$$\boldsymbol{R}_{N_T \times N_E} = \left[\boldsymbol{r}_{(i=1)}, \ldots, \boldsymbol{r}_{(i=N_E)}\right], \quad \boldsymbol{S}_{N_{\text{total}} \times N_E} = \left[\boldsymbol{s}_{(i=1)}, \ldots, \boldsymbol{s}_{(i=N_E)}\right] \tag{A.2-21}$$

and rewrite the above equation now in the matrix form:

$$\boldsymbol{R}_{N_T \times N_E} = \boldsymbol{H}_{N_T \times N_{\text{total}}} * \boldsymbol{S}_{N_{\text{total}} \times N_E} + \boldsymbol{N}_{N_T \times N_E} \tag{A.2-22}$$

and applying the pseudoinverse of the $\boldsymbol{S}$ matrix (and using that $N_{\text{total}} \leq N_E$), $\text{pinv}(\boldsymbol{S}) = \boldsymbol{S}^H * (\boldsymbol{S}\boldsymbol{S}^H)^{-1}$, leads to the closed analytical relation for the channel estimator:

$$\widehat{\boldsymbol{H}}_{N_T \times N_{\text{total}}} = \boldsymbol{R}_{N_T \times N_E} * \text{pinv}\left(\boldsymbol{S}_{N_{\text{total}} \times N_E}\right) \tag{A.2-23}$$

The elements of $\boldsymbol{S}\boldsymbol{S}^H$ are correlations of the uncorrelated data streams. Assuming symbols have average unit power, an approximated simplistic computationally effective relation is (yet to be investigated further, including post-processing smoothing)

$$\widehat{\boldsymbol{H}}_{N_T \times N_{\text{total}}} \approx \frac{1}{N_E} \boldsymbol{R}_{N_T \times N_E} * \boldsymbol{S}^H \tag{A.2-24}$$

Advantages of EA methodology: The EAs advantages over single antenna elements include the following:

- *More Users*: EAs allows more users to participate in the MU-MIMO, assuming UEs have more than 1 physical antenna (BS cleans the transmission only over EAs, not over the large UE array). It solves $N_R > N_T$, or $N_R \gg N_T$ problem (where: $N_R \equiv \sum_{u=1}^{N_U} N_{R_{(u)}}$).
- *Better Gain*: EAs have (much) larger gain than the gain for individual UE antennas; this can be of especial importance for the small wavelength arrays.
- *Better Range and CE at BS*: EAs channels can be better estimated by the BS. This extends the range in TDD regime (channel estimation via uplink from UE is usually a weak point)
- *Speed Up the Communication*: Since only EAs channels are needed to be delivered to the BS, this speeds up the SRS transmission. Especially in the update regime, where the EAs equalizers are fixed and only their channel needs to be delivered.
- *Flexibility*: EAs are flexible in their construction and update (see below the multi-step dimensionality reduction); they can blend different array architectures: e.g., fully digital steps with analogue steps.
- *Interference Rejection*: EAs can include the outer cell interference rejection inside of the EAs construction equalizer. This may improve for example:
    - performance of the users closer to the cell border (for general case of the cells)
    - allow usage of smaller size 6G cells which suffer from interference. This can be an essential part of the 6G technology (small cells may be a "friendly" way to reduce the BS TX power, use smaller voltage electronics, hence reduce non-linearities, make BS electronics be economically cheaper).
- *Dynamic Number of EAs*: The number of EAs can be dynamic and include "breezing" structures (as it will be explained below) and which can be essential for the MU-MIMO ensembles.
- *Channel from Data*: UE RX EAs and UE RX EAs are considered in generally different, but if they are constrained to be identical, then the possibility of decoding from data is opened.
- *BS TX EAs*: For BS consisting of small antenna elements, they can also be amalgamed into larger parts for more powerful transmission.

Assumptions:

- Simultaneous communication of massive number of antennas from UE devices with, e.g., a lower number of BS antennas.
- Availability of control signalling provided by the UEs to BS.
- UEs with various antenna arrays architectures (e.g., fully digital, or hybrid analogue-digital).

Note that the construction and in particular the "ignition" (i.e., the primary construction) of the EAs can be done in multiple ways. For example, it can be done based on the channel estimation of the reference signals sent by BS toward all UEs. However, it can also be done randomly (several EAs will then be delivered to BS), based on prior history, etc. This is an area for further investigation.

Simulation and results: Performances of the following schemes are compared below:

- 8x UE RX array
- 4x UE RX array
- Dimensionality reduction scheme 8x → 4x
- Optimized dimensionality reduction scheme 8x → 4x

The 1-info layer case and different number of strong interferers are investigated. These are represented as interference channels from another cell(s). The knowledge of the interference channel is not assumed, but of the noise total correlation matrix and perform whitening (which corresponds to the Gauss-Markov estimator).

For simplicity and generality, the interferer channel "signatures" over the 8x array are assumed to be independent complex gaussian vectors. This can be due to a multi-path environment, or assuming that 8x is not the original array size but a dimensionality reduction of a large RX array (then multiple sources are added thus becoming approximately Gaussian after that).

Whitening for strong interferers (if their number is smaller than the number of the Rx antennas) acts similarly to nulling approximately performing ZF of the interferers. For example, when interference signature on the $N_{R(u)}$ -size array is given by a strong interference channel vector $\boldsymbol{h}_{\text{inrterf}}$, then the whitener becomes $\boldsymbol{T} = \mathbf{1} - \frac{\boldsymbol{h}_{\text{inrterf}}\boldsymbol{h}_{\text{inrterf}}^{H}}{\|\boldsymbol{h}_{\text{inrterf}}\|^2}$, where $\mathbf{1}$ has dimension of NR(u)×NR(u). This is clearly observable in Figure A.2-11 below, with 4 Rx antennas performing ZF of 3 interferers. One may create dimensionality reduction couples (in simulation or in HW) in the natural order and to use input permutations to arrange different pairs. Interestingly, the permutations before the dimensionality reduction can rise the SNR. This is due to the decorrelation of the whitening from the projection by the approximate null space of the interferer. Whitening and BP (best permutation) approach performs very close to the 8x case, despite the whitening is performed over 4x dimensions. The number of different input antenna array index permutation (used in the simulation) to construct n different pairs from total (2n) indices of the full array is $\frac{(2n)!}{n!2^n}$, hence for n=4 pairs out of 8 antennas there are 105 possibilities to perform pair-based dimensionality reductions (and the exhaustive search is performed). (Proof is "easy": (2n)! is the total number of array antennas arrangement, n! is the total number of the dimensionality reduction arrangement, and $2^n$is the total number of changes inside pairs) This stresses the importance of the Dimensionality reductions optimizations, and its possible effectiveness.

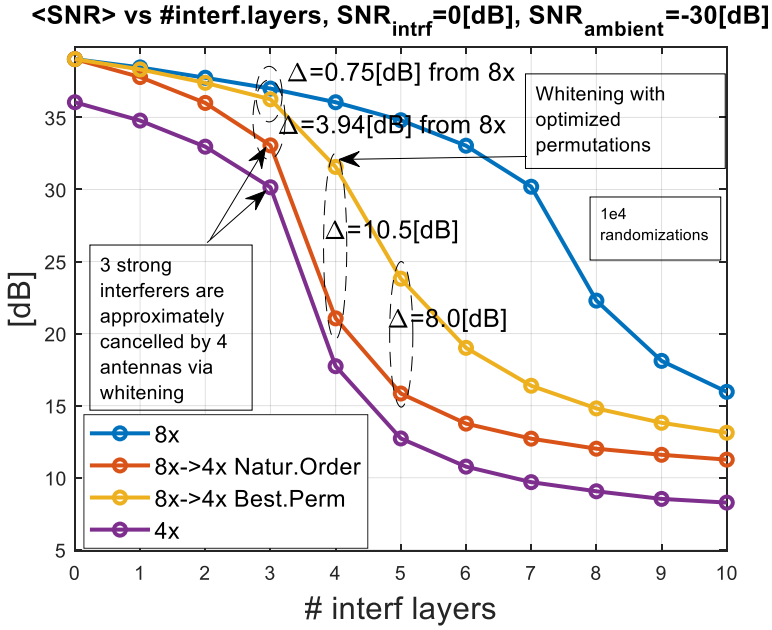

Figure A.2-11: Perfect CSI. The BP (best permutation) approach works well and is much better than the NO (natural ordering) up to 10.5 dB gap (BP is almost identical with 8x up to 3 interferers).

Additional information on mathematical formulations: Here, 1-info layer case is investigated under strong interference noise the assuming it be Complex Gaussian realizations of N_{interf} components; the total noise power is identical to the info-power.

$$\boldsymbol{n} = \boldsymbol{CN}_{8\times1}\left(0, \sigma^2_{ambient}\right) + \frac{1}{\sqrt{N_{\text{interf}}}}\sum_{n=1}^{N_{\text{interf}}} \boldsymbol{CN}_{8\times1}\,(0{,}1). \quad \textbf{(A.2-25)}$$

Let us write the original equation:

$$\boldsymbol{r} = \boldsymbol{h}s + \boldsymbol{n} \quad \textbf{(A.2-26)}$$

and perform dimensionality reduction from N to $N/2$ equations by weighted average of every two components as (this corresponds to matched filtering approach for the outer stage)

$$\begin{bmatrix} \boldsymbol{w}_1^H \boldsymbol{r}(1{:}\,2) \\ \boldsymbol{w}_2^H \boldsymbol{r}(3{:}\,4) \\ \boldsymbol{w}_3^H \boldsymbol{r}(5{:}\,6) \\ \boldsymbol{w}_4^H \boldsymbol{r}(7{:}\,8) \end{bmatrix} = \begin{bmatrix} \boldsymbol{w}_1^H \boldsymbol{h}(1{:}\,2) \\ \boldsymbol{w}_2^H \boldsymbol{h}(3{:}\,4) \\ \boldsymbol{w}_3^H \boldsymbol{h}(5{:}\,6) \\ \boldsymbol{w}_4^H \boldsymbol{h}(7{:}\,8) \end{bmatrix} s + \begin{bmatrix} \boldsymbol{w}_1^H \boldsymbol{n}(1{:}\,2) \\ \boldsymbol{w}_2^H \boldsymbol{n}(3{:}\,4) \\ \boldsymbol{w}_3^H \boldsymbol{n}(5{:}\,6) \\ \boldsymbol{w}_4^H \boldsymbol{n}(7{:}\,8) \end{bmatrix} \quad \textbf{(A.2-27)}$$

The projection weights $\boldsymbol{w}_k$ ($\dim \boldsymbol{w}_k = 2 \times 1$, $k = 1{:}\,4$) be the MF (matched filters) for the corresponding indices of the channel chunks are:

$$\boldsymbol{w}_1 = \boldsymbol{h}([1{:}\,2])\,,\ \boldsymbol{w}_2 = \boldsymbol{h}([3{:}\,4]),\ \boldsymbol{w}_3 = \boldsymbol{h}([5{:}\,6]),\ \boldsymbol{w}_4 = \boldsymbol{h}([7{:}\,8]) \quad \textbf{(A.2-28)}$$

Alternatively, every weight can also be scaled such that $\|\boldsymbol{w}_k\|^2 = 1$. For example, $\boldsymbol{w}_1([1{:}\,2]) = \frac{\boldsymbol{h}([1:2])}{\|\boldsymbol{h}([1:2])\|}$, etc.

This leads to the equations:

$$\boldsymbol{G}^{(2)}_{4\times8}\boldsymbol{r} = \boldsymbol{G}^{(2)}_{4\times8}\boldsymbol{h}s + \boldsymbol{G}^{(2)}_{4\times8}\boldsymbol{n} \quad \textbf{(A.2-29)}$$

where the matrix $\boldsymbol{G}^{(2)}_{4\times8}$ is:

$$\boldsymbol{G}^{(2)}_{4\times8} = \boldsymbol{f}(\boldsymbol{h}_{8\times1}) = \begin{bmatrix} \boldsymbol{w}_1^H & \boldsymbol{0}_{1\times2} & \boldsymbol{0}_{1\times2} & \boldsymbol{0}_{1\times2} \\ \boldsymbol{0}_{1\times2} & \boldsymbol{w}_2^H & \boldsymbol{0}_{1\times2} & \boldsymbol{0}_{1\times2} \\ \boldsymbol{0}_{1\times2} & \boldsymbol{0}_{1\times2} & \boldsymbol{w}_3^H & \boldsymbol{0}_{1\times2} \\ \boldsymbol{0}_{1\times2} & \boldsymbol{0}_{1\times2} & \boldsymbol{0}_{1\times2} & \boldsymbol{w}_4^H \end{bmatrix} \quad \textbf{(A.2-30)}$$

The reduced dimension received vector relation is:

$$\tilde{\boldsymbol{r}}_{4\times1} = \widetilde{\boldsymbol{h}}_{4\times1} * s + \widetilde{\boldsymbol{n}}_{4\times1}, \quad \textbf{(A.2-31)}$$

where

$$\tilde{\boldsymbol{r}}_{4\times1} = \boldsymbol{G}^{(2)}_{4\times8}\boldsymbol{r}\ ,\ \ \widetilde{\boldsymbol{h}}_{4\times1} = \boldsymbol{G}^{(2)}_{4\times8}\boldsymbol{h}\ ,\ \ \widetilde{\boldsymbol{n}}_{4\times1} = \boldsymbol{G}^{(2)}_{4\times8}\boldsymbol{n}. \quad \textbf{(A.2-32)}$$

The optimal dimensionality reduction of from 4 to 1 (estimating the single layer) is given by the Gauss-Markov estimator (and it can be derived in multiple ways) $\widetilde{\boldsymbol{w}}^H\tilde{\boldsymbol{r}}_{4\times1}$, where

$$\widetilde{\boldsymbol{w}}^H = \alpha * \widetilde{\boldsymbol{h}}^H_{4\times1}\boldsymbol{C}^{-1}_{\widetilde{\boldsymbol{n}}_{4\times1}}\ ,\ \ \alpha = \frac{1}{\widetilde{\boldsymbol{h}}^H_{4\times1}\boldsymbol{C}^{-1}_{\widetilde{\boldsymbol{n}}_{4\times1}}\widetilde{\boldsymbol{h}}_{4\times1}} \quad \textbf{(A.2-33)}$$

with SNR

$$SNR = \left(\widetilde{\boldsymbol{h}}_{4\times1}\right)^H \boldsymbol{C}^{-1}_{\widetilde{\boldsymbol{n}}_{4\times1}}\widetilde{\boldsymbol{h}}_{4\times1} \quad \textbf{(A.2-34)}$$

Here,

$$C_{\tilde{\boldsymbol{n}}_{4\times1}} = \langle \tilde{\boldsymbol{n}}_{4\times1}\tilde{\boldsymbol{n}}_{4\times1}^{H}\rangle = \boldsymbol{G}_{4\times8}^{(2)}\langle \boldsymbol{n}\boldsymbol{n}^{H}\rangle \boldsymbol{G}_{4\times8}^{(2)H} = \boldsymbol{G}_{4\times8}^{(2)}\boldsymbol{C}_{n}\boldsymbol{G}_{4\times8}^{(2)H} \quad \textbf{(A.2-35)}$$

This leads to

$$SNR_{\text{dim.red }8\to4} = \left(\boldsymbol{G}_{4\times8}^{(2)}\boldsymbol{h}_{8\times1}\right)^{H}\left(\boldsymbol{G}_{4\times8}^{(2)}\boldsymbol{C}_{n\ 8\times8}\left(\boldsymbol{G}_{4\times8}^{(2)}\right)^{H}\right)^{-1}\left(\boldsymbol{G}_{4\times8}^{(2)}\boldsymbol{h}_{8\times1}\right) \quad \textbf{(A.2-36)}$$

Note that the $G_{(1\times4)}^{(1)}T_{(4\times4)}^{(1)}$ part is represented by the above row-vector $\tilde{w}^{H} = G_{(1\times4)}^{(1)}T_{(4\times4)}^{(1)}$ (having dimension of 1×4). The Gauss-Markov estimator computes two these matrices in one-step.

The equalizer for υ layers is visualised in Figure A.2-12.

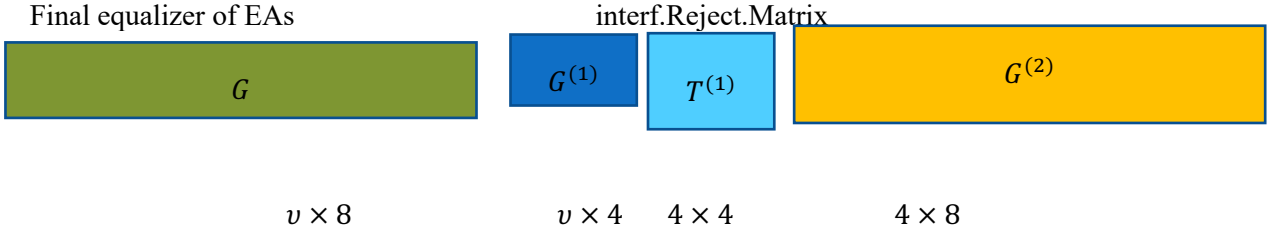

Figure A.2-12: Example of equalizer for υ layers

Equalizer with permutational degrees of freedom Π matrix (which permutes the Rx inputs, here 8 inputs) is visualised in Figure A.2-13.

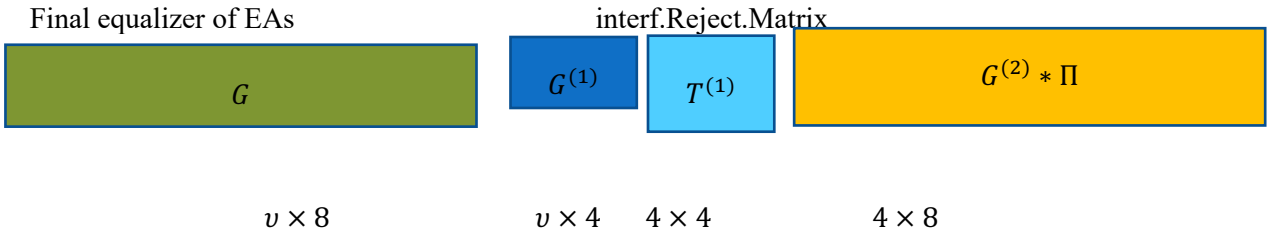

Figure A.2-13: Example of equalizer with permutational degrees of freedom Π matrix.

For the single layer $\upsilon = 1$, the equalizer is (this may define the single EA which rejects the interference):

$$\boldsymbol{G} = \boldsymbol{w}_{8\times1}^{H} = \boldsymbol{G}_{(1\times4)}^{(1)}\boldsymbol{T}_{(4\times4)}^{(1)}\boldsymbol{G}_{4\times8}^{(2)} \quad \textbf{(A.2-37)}$$

where $\boldsymbol{T}_{4\times4}$ is the whitening matrix.

The RX equations can also be permuted as:

$$\boldsymbol{P}\boldsymbol{r} = \boldsymbol{P}\boldsymbol{h}\boldsymbol{s} + \boldsymbol{P}\boldsymbol{n} \quad \textbf{(A.2-38)}$$

where $\boldsymbol{P}$ is a permutation matrix. Then, the development can be repeated.

The permutation which brings the largest SNR is to be selected.

$$SNR_{\text{dim.red }8\to4}^{(P)} = \left(\boldsymbol{G}_{4\times8}^{(2)(P)}\boldsymbol{h}_{8\times1}^{(P)}\right)^{H}\left(\boldsymbol{G}_{4\times8}^{(2)(P)}\boldsymbol{C}_{n\ 8\times8}^{(P)(P)}\left(\boldsymbol{G}_{4\times8}^{(2)(P)}\right)^{H}\right)^{-1}\left(\boldsymbol{G}_{4\times8}^{(2)(P)}\boldsymbol{h}_{8\times1}^{(P)}\right) \quad \textbf{(A.2-39)}$$

Here (P) indicates that the channel is permuted and the matrix $\boldsymbol{G}_{4\times8}^{(2)(P)}$ is calculated after this permuted channel. Namely, for

$$\boldsymbol{w}_1 = \boldsymbol{h}_{8\times1}^{(P)}([1{:}\,2])\ ,\ \boldsymbol{w}_2 = \boldsymbol{h}_{8\times1}^{(P)}([3{:}\,4]),\ \boldsymbol{w}_3 = \boldsymbol{h}_{8\times1}^{(P)}([5{:}\,6]),\ \boldsymbol{w}_4 = \boldsymbol{h}_{8\times1}^{(P)}([7{:}\,8]) \quad \textbf{(A.2-40)}$$

This gives:

$$\boldsymbol{G}_{4\times 8}^{(2)(P)} = \boldsymbol{f}\left(\boldsymbol{h}_{8\times 1}^{(P)}\right) = \begin{bmatrix} \boldsymbol{w}_1^H & \mathbf{0}_{1\times 2} & \mathbf{0}_{1\times 2} & \mathbf{0}_{1\times 2} \\ \mathbf{0}_{1\times 2} & \boldsymbol{w}_2^H & \mathbf{0}_{1\times 2} & \mathbf{0}_{1\times 2} \\ \mathbf{0}_{1\times 2} & \mathbf{0}_{1\times 2} & \boldsymbol{w}_3^H & \mathbf{0}_{1\times 2} \\ \mathbf{0}_{1\times 2} & \mathbf{0}_{1\times 2} & \mathbf{0}_{1\times 2} & \boldsymbol{w}_4^H \end{bmatrix} \quad \textbf{(A.2-41)}$$

Note that this can be rewritten as:

$$\boldsymbol{C}_{n\,8\times 8}^{(P)(P)} = \boldsymbol{C}_{n\,8\times 8}(\boldsymbol{p}, \boldsymbol{p}) \quad \textbf{(A.2-42)}$$

Where $\boldsymbol{p}$ is the permutation vector, which can also be formally represented via the permutation matrix $\boldsymbol{P}$:

$$\boldsymbol{p} = \boldsymbol{P} * [1{:}\,8]^T \quad \textbf{(A.2-43)}$$

In practice, it is simpler to construct possible permutation vectors. One can show that for 8→4 reduction, there are 105 permutations.

A.2.4 EMF exposure metrics

The EMF exposure was evaluated by using incident power density and SAR in Section 10.6 according to the ICNIRP guidelines [ICNIRP20]. The equivalent plane-wave incident power density is defined as:

$$S_{\text{inc}} = \frac{1}{2\eta_0}|E_{\text{fs}}|^2, \quad \textbf{(A.2-44)}$$

where η_0 is the free-space wave impedance (Ω); $|E_{\text{fs}}|$ is the magnitude of the electric field in free-space (V/m). For the general public, a limit value of 10 W/m^2 for the incident power density was considered. While such value is intended to be spatially averaged over the whole-body surface, in this study, spatial peak power density was conservatively used in the analysis.

SAR is evaluated in the body phantom. The SAR is defined as:

$$SAR = \frac{\sigma|E_{\text{hb}}|^2}{2\rho} \quad \textbf{(A.2-45)}$$

where σ and ρ are the electrical conductivity (S/m) and mass density (kg/m^3) of human tissue; $|E_{\text{hb}}|$ is the magnitude of the electric field in the tissue. The local SAR was averaged over a volume of tissue in the shape of a cube with a mass of 10-g. The corresponding local SAR limit for the general public is 2.0 W/kg for 10-g averaging scheme.

The whole-body average SAR was also calculated:

$$WBSAR = \frac{P_{\text{abs}}}{m_{\text{WB}}} \quad \textbf{(A.2-46)}$$

where P_{abs} is the power absorbed by the phantom (W), and m_{WB} is the mass of the body (kg).

When considering the EMF exposure from different MIMO layers, signals are uncorrelated. Therefore, incident power density and SAR are combined in uncorrelated way.

A.3 Waveform, modulation, and coding

A.3.1 Evolution New Radio – Available frequency blocks and occupied channel bandwidth

The available frequency blocks in W- and D-bands, following the ECC recommendation are presented in Table A.3-5. Channel bandwidth (CBW) and occupied channel bandwidth (OCB) for 264 physical resource blocks (PRB) with 4096 IFFT size and with different subcarrier spacings (Δf, μ being the scaling factor exponent) are presented in Table A.3-6.

Table A.3-5: Available frequency blocks in W and D bands.

	W Band	D Band
Carrier frequency (CEPT)	92 – 114.25 GHz	130 – 174.8 GHz
Available frequency blocks (ECC recommendation)	2 GHz (92 - 94) 5.9 GHz (94.1 - 100) 7.5 GHz (102 - 109.5) 2.5 GHz (111.8 - 114.25)	4 GHz (130 - 134) 7.5 GHz (141 - 148.5) 12.9 GHz (151.1 - 164) 7.8 GHz (167 - 174.8)

Table A.3-6: Cyclic prefix lengths, channel bandwidths and occupied channel bandwidths for different subcarrier spacings with 4k FFT.

		BW, 4k FFT	CP length, 4k FFT		
μ	Δf (kHz)	CBW (GHz)	OCB, 264 PRBs (GHz)	Regular CP (μs)	Extended CP (μs)
0	15	0.05	0.05	4.6875	16.667
1	30	0.1	0.10	2.3428	8.333
2	60	0.2	0.19	1.1719	4.167
3	120	0.4	0.38	0.5857	2.083
4	240	0.8	0.76	0.2930	1.042
5	480	1.6	1.52	0.1465	0.521
6	960	3.2	3.04	0.0732	0.260
7	1920	6.4	6.08	0.0366	0.130
8	3840	12.8	12.17	0.0183	0.065
9	7680	25.6	24.33	0.0092	0.033

A.3.2 Evolution New Radio – SCS and PN tolerance

Simulations were carried out in 140 GHz carrier frequency to study the performance of the CP-OFDM and DFT-s-OFDM waveforms under common phase error CPE and ICI PN with different SCS. The PN model used was from Hexa-X deliverable D2.3 Section 4.2.1 [HEX23-D2.3], and either CPE or inter-carrier interference (ICI) compensation was used to fight the PN. From the results in Figure A.3-14, it can be seen that the largest currently supported SCS for FR2-2 of 120 kHz is not sufficient for mitigating the PN effects in this frequency band. Extending the SCS to 960 kHz or 1920 kHz is needed to fight the PN for both CP-OFDM and DFT-s-OFDM waveforms.

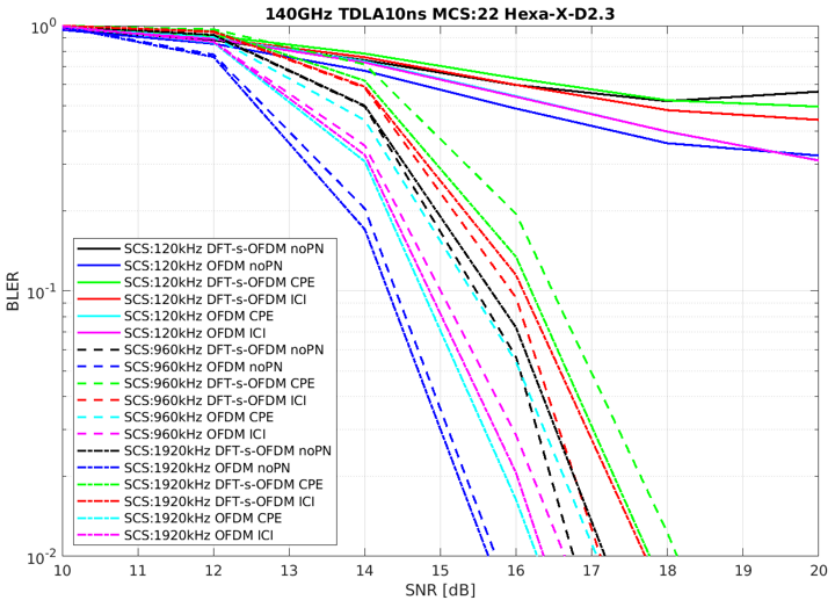

Figure A.3-14: Comparison of CP-OFDM and DFT-s-OFDM with different SCS under Hexa-X PN in 140 GHz.

A.3.3 Evolution New Radio – Required output backoff

In Figure A.3-15 [TLP+20], the required output back-off is shown for CP-OFDM and SC-FDMA waveforms, when assuming 20 dB adjacent channel leakage ratio (ACLR) requirement and modulation specific error vector magnitude (EVM) requirement. It can be observed that depending on the modulation order, CP-OFDM requires approximately from 3 dB to 5 dB more output power back-off, indicating that SC-FDMA is able to provide significantly better coverage.

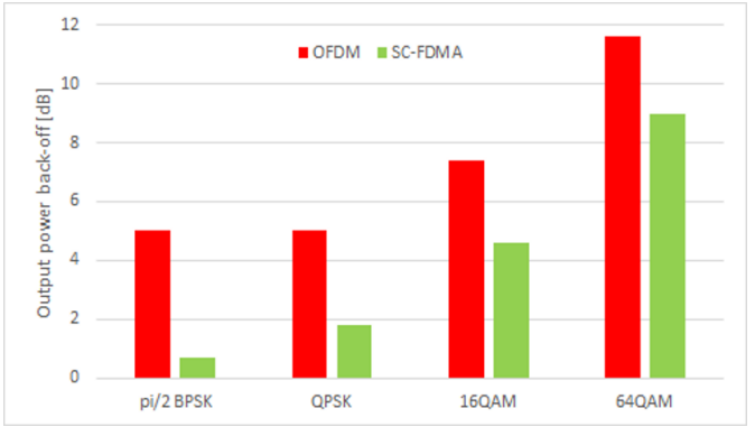

Figure A.3-15: Comparison of PA output power back-off with 20 dB ACLR requirement and modulation specific EVM requirement [TLP+20].

A.4 Intelligent radio air interface design

A.4.1 Learned MIMO Waveforms

The high-level description of the objective and scenario for the enabler “learned MIMO waveforms” is presented in Section 6.1.1. The detailed system parameters used for training and validating the models are presented in Table A.4-7, Table A.4-8 and Table A.4-9 list the different assumptions behind the simulation results.

Table A.4-7: Detailed system parameters.

Parameter	Notation	Value
Number of BS	N/A	1
Number of UEs	N/A	1
BS number of RX antennas	N_R	4
UE speed	N/A	0-5 m/s
UE number of TX antennas	N_T	2
Frequency band	N/A	3.5 GHz
Subcarrier spacing	N/A	30 kHz
Slot length	N_S	14 OFDM symbols
Number of subcarriers	N_F	72
Channel model	N/A	CDL-A, CDL-B, CDL-C
RMS delay spread	N/A	10-300 ns

Table A.4-8: Key assumptions.

Hardware impairment	None
Synchronization	Assumed perfect
CSI availability at transmitter, receiver, RIS (if applicable)	Not available
Waveform	CP-OFDM

Table A.4-9: Assumptions for AI/ML-assisted transmissions

Type of the used AI/ML training method	Supervised learning
Training	Offline
'Features' and 'labels' for training the models	Autoencoder-type approach for detecting transmitted bits
Type of the AI model	CNN
Model architecture	Convolutional ResNet with a learned multiplicative layer
Loss function for training	Binary cross-entropy with SNR-based weighting and an additional term based on the quality of the learned constellation
Model deployment	Transmitter and receiver
Training scheme	Centralized

To gain further insight into the considered ML-based scheme, observe the learned constellations in Figure A.4-16. It is evident that the learned constellations are asymmetric, which is an obvious requirement for blind and pilotless detection. Moreover, when considering the differences in the constellations of the overlapping spatial streams, it can be observed that at least one of the overlapping constellations has some outliers. This is

likely a useful feature for the considered DeepRx receiver when it learns to do pilotless separation of the spatial streams, as such differing outliers are more easily detectable.

Next, the proposed learned pilotless scheme is compared to a conventional QAM-OFDM waveform and a nonlinear K-Best detector using either perfect channel state information or a demodulation reference signal-based channel estimate. The former represents essentially the highest achievable performance under the considered simulation scenario, while the latter utilizes a DMRS pattern consisting of two pilot-carrying OFDM symbols within the slot, with the pilots located on the 3rd and 12th OFDM symbols.

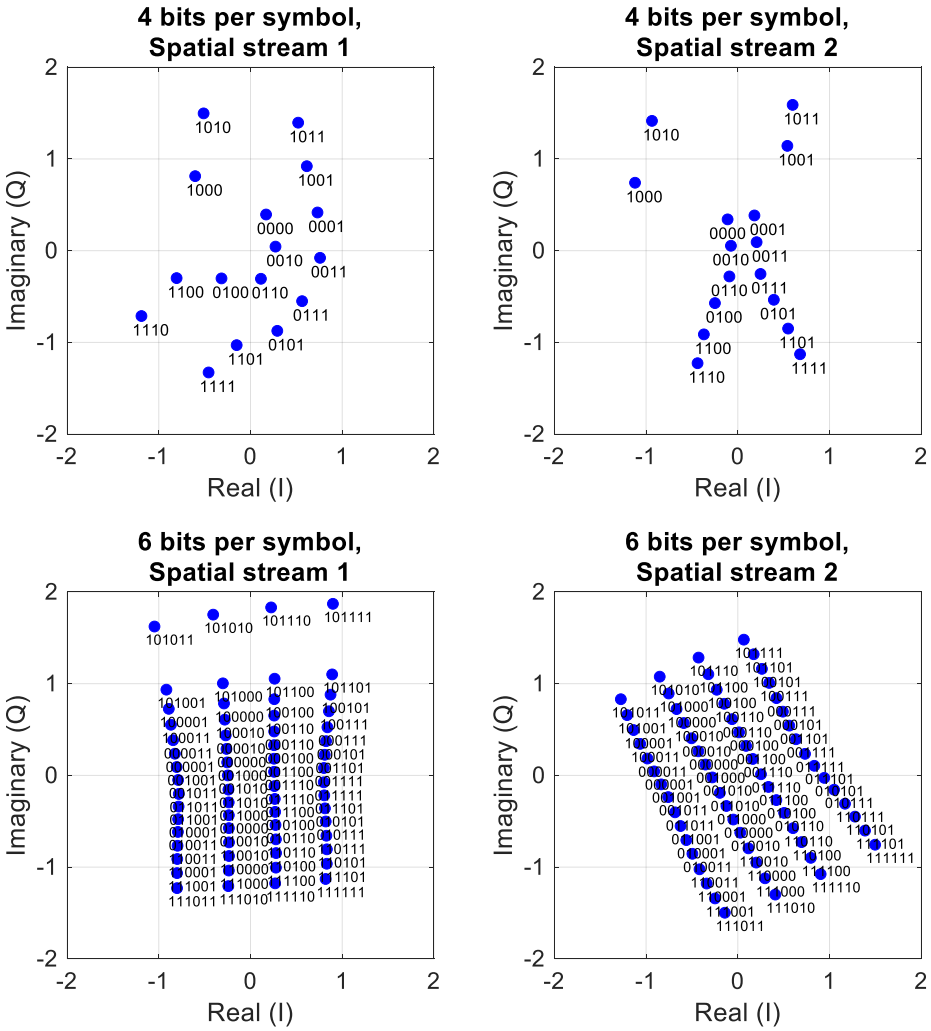

Figure A.4-16: Learned constellation for both spatial streams and both modulation orders

In order to compare the different schemes in terms of the achieved throughput, the spectral efficiency has been defined as follows:

$$SE = (1 - BLER)(1 - CP)\frac{N_D}{N_{tot}}N_T CM \qquad \textbf{(A.4-47)}$$

Where $BLER$ is the target block error rate (here it is assumed 10%), CP is the relative overhead due to cyclic prefix, N_D is the total number of data symbols per slot, N_{total} is the total number of resource elements, including those reserved for DMRS, C is the code rate, and M is the modulation order.

Figure A.4-17. shows the spectral efficiencies of the different schemes with respect to the SNR, calculated using the above definition. The modulation order and code rate are selected to be the highest possible under which the BLER target of 10% is achieved. In addition, also the MCS index utilized by each scheme is indicated on the plot, the MCSs being similar to 5G NR MCS index table 2 for the considered modulation

orders [38.214]. It can be observed that at the lower SNRs the ML-based pilotless scheme achieves the BLER target with the same MCS as the pilot-based scheme, which translates to a higher spectral efficiency. However, when the 64-point constellation is used (from MCS index 7 upwards), the spectral efficiency of the ML-based scheme starts to deteriorate compared to the conventional DMRS-based system. Indeed, when the SNR goes above 16 dB, the spectral efficiency of the ML-based scheme is slightly lower than that of the DMRS-based scheme.

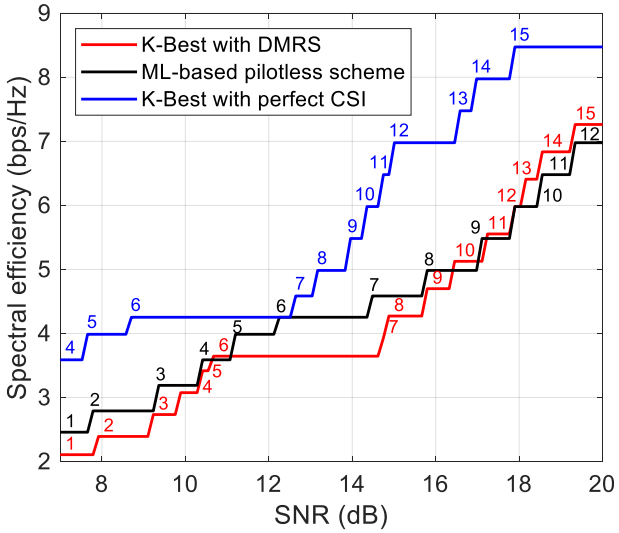

Figure A.4-17: The spectral efficiency of the considered schemes with BLER of 10%. The used MCS indices are also shown.

A.4.2 ML-based channel state feedback compression in a multi-vendor scenario

This section details the scenario and system, hardware parameters as well as the AI/ML assumption considered for the enabler ML-based channel state feedback compression in a multi-vendor scenario (see Section 6.2.1).

For this simulation-study the scenario assumes 19 gNBs, with 3 cells per gNB, each with 32 antennas, and with inter-cell distance of 200 meters. Each cell is serving 5 UEs, each with 4 antennas. The UEs are randomly deployed around the gNB following a Uniform distribution. The pathloss of each UE depends on the location of the UE with respect to the gNB. The UEs have a pedestrian-like mobility of 3km/h.

A Dense Urban deployment scenario with Urban Micro channel model is considered, with a system operating in the FR1 band, at 4GHz, with an 20MHz bandwidth and subcarrier spacing of 30kHz. Four resource blocks per sub-band are assumed; with 13 sub-bands in the 20MHz bandwidth. A TDD frame configuration and OFDM waveform are considered.

There is no hardware impairment included and the channel state information at the transmitter and receiver is assumed realistic. The simulations are with full buffer traffic and FTP traffic with varying resource utilization.

The scenario and parameters are summarized in the tables below.

The evaluation metric is the SGCS between the eigenvectors of the ground truth CSI Q and the reconstructed CSI $\hat{Q}$. The cosine similarity (cs) measures the angles between two vectors, it is defined as:

$$\mathrm{cs}(\mathbf{q},\mathbf{d}) = \frac{\boldsymbol{q}^T\boldsymbol{d}}{\|\boldsymbol{q}\|\|\boldsymbol{d}\|} \quad \textbf{(A.4-48)}$$

where, $\|\boldsymbol{q}\| = \sqrt{\Sigma_i q_i^2}$ is the l2-norm of $\mathbf{q}$. The SGCS is given as,

$$\rho^2 = \frac{1}{N_{sb}}\sum_{k=0}^{N_{sb}-1}\left(\frac{\|\boldsymbol{w}_k^{\mathrm{H}}\boldsymbol{w}'_k\|}{\|\boldsymbol{w}_k\|\|\boldsymbol{w}'_k\|}\right)^2 \quad \textbf{(A.4-49)}$$

where $\boldsymbol{w}_{\mathrm{k}}$ is the true CSI eigenvector for the k-th sub-band and $\boldsymbol{w}'_{\mathrm{k}}$ is the reconstructed CSI eigenvector for the k-th sub-band. N_{sb} is the number of sub-bands, i.e., 14.

Table A.4-10: Detailed system parameters.

Parameter	Notation	Value	Notes
Number of BS	N/A	19	Each gNB has 3 cells
Number of UEs	N/A	5 UE per cell	
BSx location	N/A		The inter-cell distance is 200 meters.
BSx speed	N/A	Fixed	
BSx number of TX / RX antennas	N/A	32	
UEx location	N/A	Random	Uniformly distributed
UEx orientation	N/A	Random	Uniformly distributed
UEx speed	N/A	3km/h	
UEx number of TX/RX antennas	N/A	4	
Frequency band	N/A	4GHz	
Subcarrier spacing	N/A	30 kHz	

Table A.4-11: Details on Hardware parameters.

Hardware impairment	No HW impairment is considered.
Synchronization	Realistic
Channel model	Realistic channel model
CSI availability at transmitter, receiver	Imperfect.
Waveform	OFDM

Table A.4-12: Assumptions for AI/ML-assisted transmissions.

Type of the used AI/ML training method	Supervised learning
Training	Offline
'Features' and 'labels' for training the models	Features: CSI Labels: CSI
Type of the AI model	Proprietary at UE and gNB
Model architecture	Proprietary
Loss function for training	
Model deployment	At both transmitter and receiver
Training scheme	Distributed and sequential

A.4.3 Intelligent CSI compression

This section provides further details on the Intelligent CSI compression enabler, introduced in Section 6.2.2. while this section discusses the defined system and mathematical models, the underlying assumptions, and the main results achieved so far.

System model: This research work concentrates currently on the SU-MIMO side of the CSI-compression, where a precoder at BS treats a single UE (see example in Figure A.4-18). Generally, a larger MU-MIMO precoder, treating multiple UEs, can be also constructed from the UE CSI report (e.g., a ZF precoder).

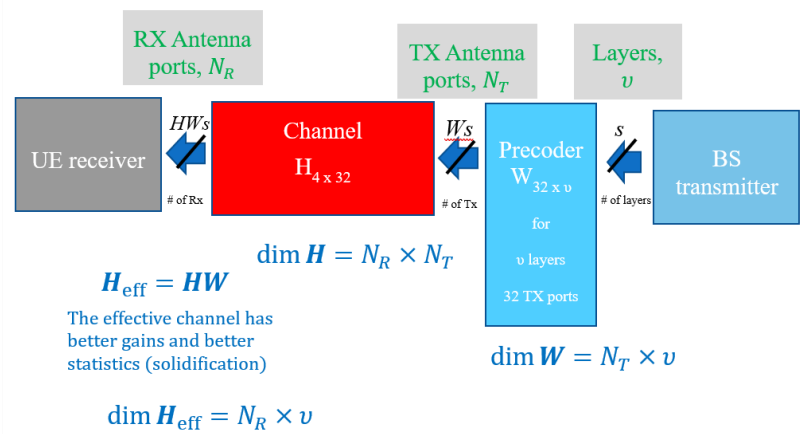

Figure A.4-18: DL transmission for the SU-MIMO, including DL Precoder at BS with N_T antennas for a single UE with N_R antennas.

Mathematical model: The received signal at a UE RE (resource element) is:

$$\boldsymbol{r} = \boldsymbol{HWs} + \boldsymbol{n} \qquad \textbf{(A.4-50)}$$

where $\boldsymbol{r}$ is the receiving vector, $\boldsymbol{H}$ the channel matrix, $\boldsymbol{W}$ the precoding matrix, $\boldsymbol{s}$ the transmitted symbol and $\boldsymbol{n}$ the noise, with following dimensions: $\dim \boldsymbol{r} = \dim \boldsymbol{n} = N_R \times 1$, $\dim \boldsymbol{H} = N_R \times N_T$, $\dim \boldsymbol{W} = N_T \times \upsilon$.

It is well known, since [T99], that the capacity is maximized when precoder $\boldsymbol{W}$ utilizes (per RE) the "best" (corresponding to the largest eigenvalues) eigen-vectors of the channel corelation matrix $\boldsymbol{C} = \boldsymbol{H}^H\boldsymbol{H}$, i.e., precoder is constructed as:

$$\boldsymbol{W} = [\boldsymbol{e}_1, \dots, \boldsymbol{e}_\upsilon]\boldsymbol{D}_{\upsilon\times\upsilon} \quad , \quad \|\boldsymbol{e}_k\|^2 = 1 \qquad \textbf{(A.4-51)}$$

Here $\boldsymbol{e}_k$ are: $\boldsymbol{C}\boldsymbol{e}_k = \lambda_k \boldsymbol{e}_k$ for $k = 1{:}\upsilon$, and $\boldsymbol{D}_{\upsilon\times\upsilon}$ is a diagonal matrix with redistributed power between layers. Note that for N_R=1 case, the (single) channel matrix row is automatically the eigenvector of $\boldsymbol{C}$ (it can be scaled further for 1-norm). The Telatar's solution becomes the Tx MRC, which performs optimal combining of the TX streams: "synchronizing" channel phases for the coherent addition with weights matched to the channel amplitudes.

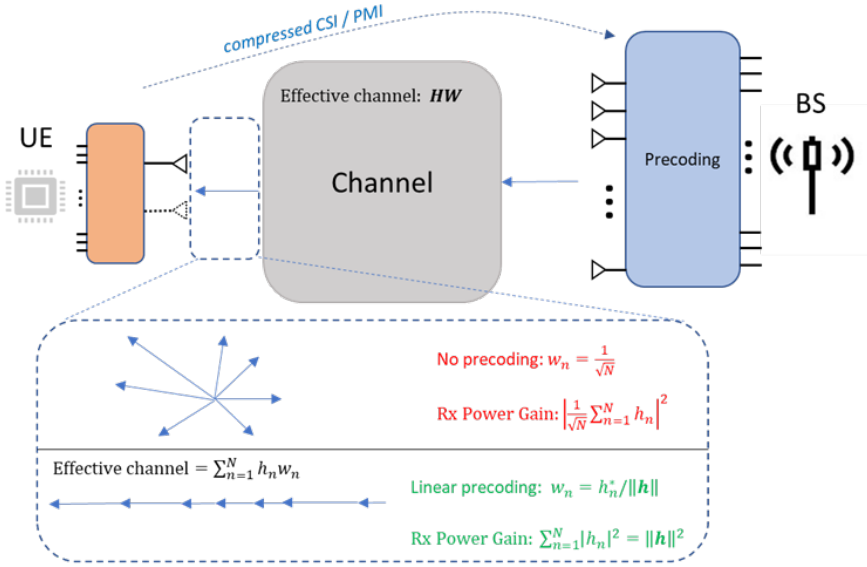

Figure A.4-19: Example of SU-MIMO channel improvement via linear precoding under unit TX power constraint.

In Figure A.4-19, an example of SU-MIMO channel improvement via linear precoding under unit TX power constraint is presented. The full channel matrix cannot be delivered back digitally in full per every RE (and it is costly even per sub-band, as 5G Type2, even with its large coefficients quantization) due to its large size, hence the need for the Advanced CSI-compression. In 5G NR standard, this is done with further frequency compression of the sub-band precoder via eType2, or via AI-based schemes (discussed in Rel.18 and further).

Sometimes, as is the case in 5G, the power is identically distributed between layers (despite some non-optimality of this solution):

$$\boldsymbol{W} = \frac{1}{\sqrt{v}}[\boldsymbol{e}_1, \dots, \boldsymbol{e}_v] \quad \textbf{(A.4-52)}$$

How to "synchronize" different channels inside of a sub-band for the optimal result is an open question. Telatar's approach can be heuristically generalized for sub-band precoder construction by performing correlation matrix averaging in every sub-band (sometimes a simplistic channel averaging is used, and the correlation matrix is then constructed from the averaged channel; the averaging of the channel and the correlation matrix over sub-band may also be mixed). This constructs the sub-band (SB) target precoder, which is then further compressed. Note that precoding may aim either towards (effective) channel bettering or towards MU-MIMO improvement. To achieve any of these aims, the BS needs the channel knowledge which is done with a typically lossy compression in the FDD regime (sometimes, the TDD regime may utilise this scheme to extend the range). It is noted that the MU-MIMO aim may demand a better channel similarity (after reconstruction at the BS). MU-MIMO part is often ignored at the UE and self-performance optimization is done to construct the template sub-band precoder which is further compressed and then delivered digitally to the BS.

In many AI schemes for the CSI-compression (typically NN-based), the power per-layer optimization ($\boldsymbol{D}_{v\times v}$) is not considered, and the "bare" 1-norm scaled eigenvectors represent the input $\boldsymbol{x}$ to the CSI-compression scheme (and such schemes are often trained on the averaged cosine similarity criterion). The AI-based CSI-compression and feedback approach, despite multiple possible NN topologies, can be described as [R1-2203550]:

$$\hat{\boldsymbol{x}} = g_{\text{decoder}}(f_{encoder}\,(\boldsymbol{x}, \boldsymbol{\theta}_{\text{encoder}}), \boldsymbol{\theta}_{\text{decoder}}) \quad \textbf{(A.4-53)}$$

where $\boldsymbol{\theta}_{\text{decoder}}$ and $\boldsymbol{\theta}_{\text{encoder}}$ are parameters of the decoder and encoder functions and typically represent weights of their related NNs (see Figure A.4-20). Note that the encoder can be also alphabet based. This simplifies the decoder and eliminates the need in $\boldsymbol{\theta}_{\text{decoder}}$.

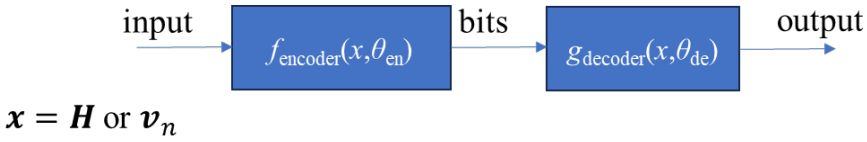

Figure A.4-20: AI-based CSI feedback neural network performing lossy compression (e.g., of the input eigenvectors at every sub-band "*n*").

Assumptions: In current analysis, perfect channel knowledge is assumed. In future steps, it is planned to introduce impairments and investigate their influence on performance.

Simulation and results: In Figure A.4-21, the capacity performance of the eType2 precoder is compared in terms of number of bits per RE averaged by the number of layers. The precoder uses parameters $p_v = 1/4$ (leading to 5 Fourier beams ($\lceil 19/4 \rceil = 5$) and $\beta = 3/4$ (governing non-zero coefficients). The spectral efficiency in the figure is normalised by the number of layers. It can be observed a good closeness of the eType2 precoder to both the target sub-band precoder as well as to the SVD bound in the L=6 beam space. On the other hand, a large gap with Type1 precoder is observed: $3 * \Delta bits = 3 * (6.33 - 4.78) = 4.65[dB]$. This confirms the **advantage** and **importance** of the eType2 precoder.

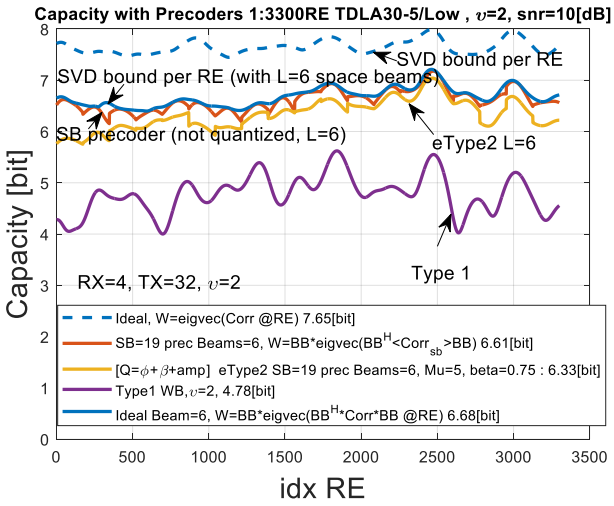

Figure A.4-21: Performance of the eType2 precoder for TDLA-30-5/LOW channel, υ =2 information layers, and use of *L*=6 spatial beams.

Note the gap between the SVD bound with the *full* channel basis for $\dim \boldsymbol{H} = 4 \times 32$ (which may be also interpreted as L=16 beams, corresponding to 2*16=32 TX antennas of the BS) and the SVD in the L=6 basis (total columns' length is 2*6=12) calculated for the channel $\boldsymbol{H}_{N_R \times 2L} = \boldsymbol{H}_{N_R \times N_T} \boldsymbol{B}\boldsymbol{B}_{N_T \times 2L}$. The gap is about 1[bit] (7.65[bit] vs 6.68[bit]) which corresponds to 3[dB] gap.

In Figure A.4-22, the performance for the 3-layer case and L=4 spatial beams is examined (p_υ and β are kept as same before). A gap with Type1 precoder is observed again: $3 * \Delta bits = 3 * (4.5 - 4.04) = 1.38[dB]$. This gap is still important but is much smaller than for the 2-layer case. It is observed that the precoder is less aligned with the SB precoder, and in future work a possibility of improvement will be investigated. The current construction incorporates the suggestion from [ATM19]. It is interesting to see that the SB precoder performs very close to the bound. Note also that 4-beams based precoder (even if a more refined design will be somehow possible and bring eType2 closer to the SB precoder) still will perform far from the SVD bound of the full basis. The gaps between the two SVD bounds (full basis and 4-beam basis based) are 3*(6.87 – 5.23) =4.92[dB]. Hence, trade-offs delivering better compression and preserving a larger basis size (in 5G number of beams) may be essential.

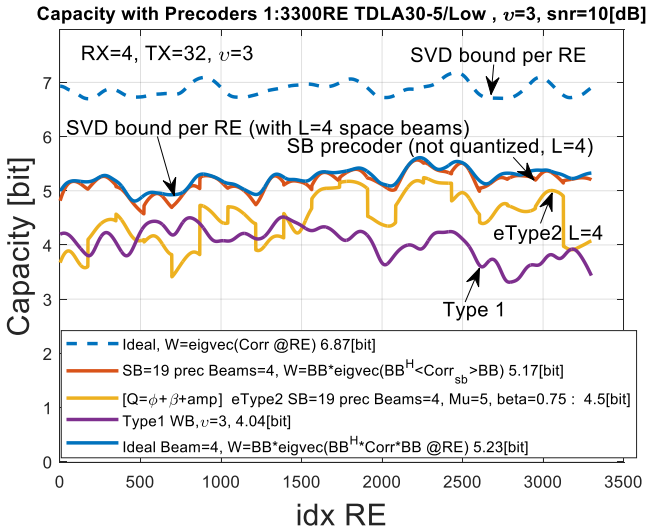

Figure A.4-22: Performance of the eType2 precoder for TDLA-30-5/LOW channel, *υ=3* information layers and use of *L=4* spatial beams.

Table A.4-13: Detailed system parameters and assumptions.

Parameter	Notation	Value	Notes
General deployment and environment			
Number of BS		1	
Number of UEs		1	Per UE, hence 1 (while in MU-MIMO there are more)
Detailed deployment and architecture			
BS number of TX antennas	N_T	32	For N_{TX} = 32. It can be 4-32 or in general more.
BS number of RX antennas	N/A		Typically, the same as TX
UE number of TX antennas	N/A		Not important for DL CSI-compression
UE number of RX antennas	N_R	1-4	1-4 is primarily considered for DL CSI-compression. But it can generally be more
Frequency range and bandwidth			
Frequency band	FR1		
Bandwidth		10-100 MHz	More if multiband system
Details on Hardware parameters			
Ideal hardware	Yes		
Assumptions			
Channel model			5G channels, e.g., TDLA-30-5/LOW, maybe also stochastic
CSI availability at transmitter			Compressed CSI at transmitter

A.4.4 CSI prediction

This section provides further details on the enabler "CSI prediction" presented in Section 6.2.3.

The channel prediction problem is formulated as image prediction problem in the temporal-frequency domain. Specifically, given a channel image of state a sequence of images is predicted which represents the sequence of future channel states as outlined in the following.

A. Autoencoder (AuE) for CSI compression

First of all, a brief description of the CSI compression based on autoencoder is here provided. The aim of AE-based CSI compression is to minimize signal overhead or reconstruction error through dimensionality reduction.

Figure A.4-23 (a) illustrates the AE-based CSI feedback enhancement based on autoencoder with encoder ϕ and decoder ϕ^{-1}. The encoder part of autoencoder is located on the UE side to compress channel data into a reduced dimensional space while its decoder part is applied on the BS side to reconstruct the original channel data from the compressed feedback.

Dimension reduction occurs when high-dimensional states H_k are encoded to a low dimensional approximation, latent code $z_k = \phi(H_k)$, which enables to minimize the feedback overhead imposed by z_k. Unfortunately, the CSI available at the BS becomes outdated due to the channel variation over time and the performance of precoding design based on the outdated CSI is limited by channel aging. Moreover, it is not

possible to predict the temporal evolution of radio channel under the AE-based CSI feedback schemes currently being considered within Release-18.

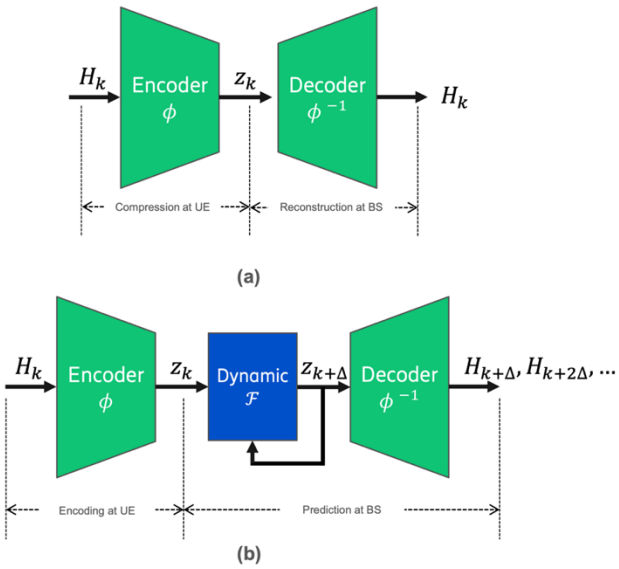

Figure A.4-23 Schematic diagrams of two deep learning models: (a) CSI compression by Autoencoder (b) CSI prediction by proposed evolutional CSI neural network (evoCSINet)

B. evolutional CSI Neural Network (evoCSINet) for CSI prediction

Aiming to achieving multi-step-ahead predictions based on the single feedback information, a dynamicNet F is introduced that learns the temporal evolution of radio channel in a latent space. In particular, the latent dynamic model identifies a low-dimensional representation of channel dynamics from channel data to predict a latent code one step forward in time as follows:

$z_{k+\Delta} = F(z_k)$, where Δ denotes a configurable stride in slot time and F represents the same dynamical system as F but in a different space.

A diagram of the proposed evoCSINet is shown in Figure A.4-23 (b). The evoCSINet applies the combination of autoencoder with dynamicNet. In the proposed evoCSINet model, an autoencoder, composed of ϕ and ϕ^{-1}, achieves an end-to- end CSI compression and reconstruction by learning the state representation in the original channel state space. The two ingredients of autoencoder and dynamicNet enable a dynamics representation of radio channel as

$$H_{k+\Delta} = \phi^{-1}(F(\phi(H_k))) \quad \textbf{(A.4-54)}$$

where dynamicNet F uses the encoder output $\phi(H_k)$ as an input to produce its output $\phi(H_k + \Delta)$ and it is processed by the decoder to produce $H_{k+\Delta}$.

The factorized decomposition of channel dynamics above is especially advantageous for the problem setting since the decomposition of φ and φ−1 along with F in a latent space allows evoCSINet to fit into the CSI feedback procedure.

More importantly, as shown in Figure A.4-23(b), a multi-step channel prediction can be achieved in latent space by applying the dynamicNet F in a recursive manner. A recursive multi-step-ahead prediction in the

latent space can be generated with F by predicting a channel state at a time step and feeding in the new prediction as an input for the next prediction.

A.4.5 Beamforming with imperfect CSI

This section details the "Beamforming with imperfect CSI" enabler, presented in Section 6.3.1.

It should be noted that in this work the amount of information that is fed to the ML beamformer is intentionally limited. For example, it does not receive historical channel estimates, which precludes that the ML beamformer can learn to predict future channels, but instead it is forced to form beams that are robust to potential imperfections in the channel estimates. A natural progression of this is to apply some form of channel prediction to the estimated channels and use a channel predictor that can also estimate prediction uncertainties, like a Kalman filter or one of its ML counterparts.

ML Beamformer

The ML model is based on multi-head attention from the transformer architecture [VA17] (Figure A.4-24). Parameters related to the architecture and training procedure are defined in Table A.4-14. The estimated channels ($\widehat{H}_k$) for the multiplexed users are normalized jointly, converted to real values by stacking the real and imaginary parts along the last axis, reshaped to remove the receive antenna dimension (which is assumed to be one), and then fed through a dense layer with N_{emb} activations applied in the last dimension.

The core part of the architecture is the Encoder, which heavily inspired by the transformer [VA17]. It consists of N_{enc} stacked Encoder blocks (depicted in Figure A.4-25). The encoder blocks use multi-head attention to account for all interactions between users. This makes the architecture user permutation equivariant which in turn makes training efficient and supports generalization over number of users. Since the users does not have a natural order, the positional encodings are omitted, which are present in the original transformer architecture. Each user embedding is then processed individually by a feed forward block consisting of two dense layers with N_{emb}*4 and N_{emb} activations respectively, and ReLU activation function after the first layer.

The output from the encoder is then fed to a dense layer (operating in the embedding dimension), reshaped to restore the receive antenna dimension, converting the stacked real and imaginary parts to complex numbers and then each precoder is normalized to unit power before transposing it to suitable output dimensions. This model is applied to the channel estimates of each Resource Block Group independently.

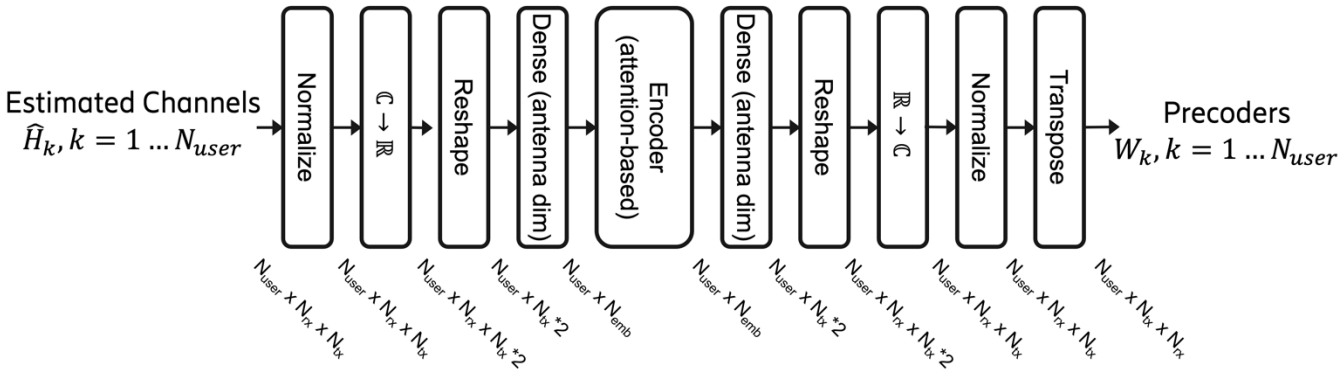

Figure A.4-24: The ML model architecture is based on the encoder of the Transformer [VA17]. One of its core components is the attention that models interactions between users. This makes the architecture equivariant to user permutations which makes it computationally

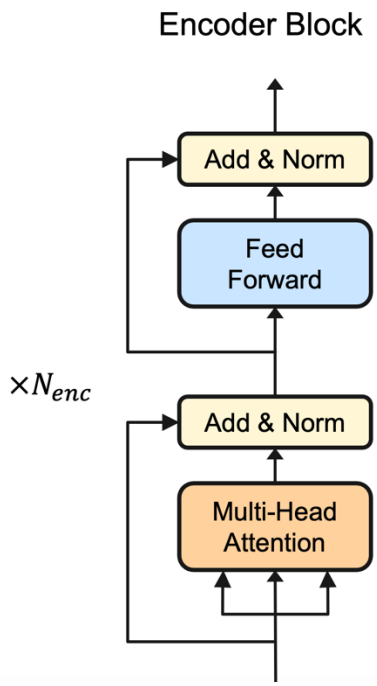

Figure A.4-25: Encoder block from the transformer [VA17]. It consists of a Multi-Head Attention block where all interactions between users are modelled, as well as a feed forward block that performs processing individually for each user.

Table A.4-14: Summary of ML parameters.

Parameter	Value	Symbol
Embedding dimension	64	N_{emb}
Number of encoder blocks	2	N_{enc}
Number of attention heads	4	
Number of training epochs	200	
Learning rate	1e-4	
Optimizer	Adam	

Evaluation: During the training time, it is assumed to have access to a differentiable evaluation function $v = f(W, H)$) that takes the selected precoders as well as the true channels and outputs a scalar that will be maximized. In this study, the spectral efficiency has been used, which can be expressed as

$$v = \sum_{k} log_2(1 + \gamma_k) \quad \textbf{(A.4-55)}$$

where γ_k is the Signal to Interference and Noise Ratio for the received signal of user k and can be expressed as

$$\gamma_k = \frac{\|H_k W_k\|^2}{\sigma_k^2 + \sum_{i=1, i \neq k}^{N_{user}} \|H_k W_i\|^2} \quad \textbf{(A.4-56)}$$

where $W_k \in \mathbb{C}^{N_{tx} \times N_{rx}}$ is the precoding matrix for user k, $H_k \in \mathbb{C}^{N_{rx} \times N_{tx}}$ is the *true* downlink channel matrix for user k, and σ_k^2 is the noise variance for user k. Since this function depends on the type of receive processing that is applied in the UE, which is typically not specified by the standard in 3GPP systems, it can be seen as a proxy for the true instantaneous performance.

Assumptions and limitations: In the following, some of the assumptions and limitations in this work are discussed.

- *Offline training*: The training procedure assumes availability of the perfect channel state information which is typically not available in an online setting.
- *Equal power for all UEs*: The expression for spectral efficiency assumes that the same power is used for all UEs. Precoders are normalized per user both for the ML beamformer and SLNR.
- *The same evaluation function for training and testing*: It is assumed that the evaluation function ($v = f(W, H)$) is known and used both for training and evaluation. Since this depends on the type of receiver, which is typically not specified by the standard in 3GPP systems, it is assumed that it is possible to come up with a reasonably accurate proxy for the receiver.
- *Single antenna UEs*: The expression for spectral efficiency above assumes single antenna at the receiver.

SLNR Baseline method: As a baseline method, the Signal to Leakage and Noise precoder [STS07] is used. The precoder $W_k \in \mathbb{C}^{N_{tx} \times N_{rx}}$ for user k can be expressed as

$$W_k = \beta \left(\boldsymbol{I} + \sum_{i=1, i \neq k}^{N_{user}} \frac{1}{\sigma_i^2} \widehat{H}_i \widehat{H}_i^H \right)^{-1} \widehat{H}_k \qquad \textbf{(A.4-57)}$$

where $\widehat{H}_k \in \mathbb{C}^{N_{rx} \times N_{tx}}$ is the *estimated* downlink channel matrix for user k, σ_k^2 is the noise variance for user k, and β is a scaling factor that normalizes precoders to unit power per user, i.e., $W_k W_k^H$=1.

A.4.6 User pairing for MU-MIMO

This section discusses in further details the "User pairing for MU-MIMO" enabler presented in Section 6.3.3. The objective of this study is to define a ML algorithm that can select the UEs that can be co-scheduled in MU-MIMO, using only partial channel information.

System model: multi user MIMO (MU-MIMO) is a wireless communication technology that allows multiple users to transmit and receive data simultaneously on the same radio channel. It is a variation of MIMO technology that was originally developed for use in wireless networks. With MU-MIMO, a base station or access point can communicate with multiple devices (users) at the same time and using the same carriers, by using multiple antennas to separate the signals transmitted to each user. This increases the network's capacity and efficiency, as more data can be transmitted at once, and the time required for each user to complete their communication is reduced.

MU-MIMO optimization is one of the potential use cases (Use Case 22) described in O-RAN specification [ORAN23], and in particular the problem of grouping is under study as a specific use case (UC 14) for massive SU/MU-MIMO. In O-RAN UC 22 for MU-MIMO optimization, full channel matrices describing the channel state for each user are not available: only a limited amount of information is available, including e.g., CQI, PMI, RI, buffer status, etc. In O-RAN architecture this information is exchanged between O-CU/O-DU nodes and a near-real time RIC through the E2 interface: since the overhead of exchanging full channel state information (CSI) through the E2 interface could be too big, only partial CSI is currently assumed in this architecture. While different solutions exist for MU-MIMO user pairing and precoder computation when the full channel matrix of users are available (e.g., Zero Forcing [SSH04] or SLNR [TSS05] based approaches), a potential usage of machine learning can be envisaged for scenarios like the one of O-RAN UC 22, where only limited channel state information is available. As stated in O-RAN work, addressing this use case can also

open the door for future expansion of MU-MIMO to support cooperative multi-point transmission (CoMP), covering both inter-cell interference cancellation (ICIC) and joint multi sites MU-MIMO.

The objective of this study is to define a ML algorithm that can select the UEs that can be co-scheduled in MU-MIMO, using only partial channel information. There are currently different studies that introduce the use of reinforcement learning (RL) to physical layer communication, and in particular to address MU-MIMO [BJ19]. The basic framework for RL studies is Markov decision processes (MDP). The main variables in a MDP are:

- The **state** (**s**) – what an **agent** observes in the **environment** in a certain moment,
- The **action** (**a**) – something the agent can do in the environment,
- The **reward** (**r**) – a value the agent receives as feedback from the environment after performing action **a** which pushes the environment in a new state **s'**;

These variables can be packed in a so-called «**transition**» (s,a,r,s'). As shown in Figure A.4-26, a transition is described probabilistically as a distribution $p(s', r|s, a)$. Which action is taken is, in the more general scenario, described probabilistically by a «**policy**» $\pi(a|s)$. The policy can also be deterministic, in which case the selected action is a direct function of the state, $a = u(s)$.

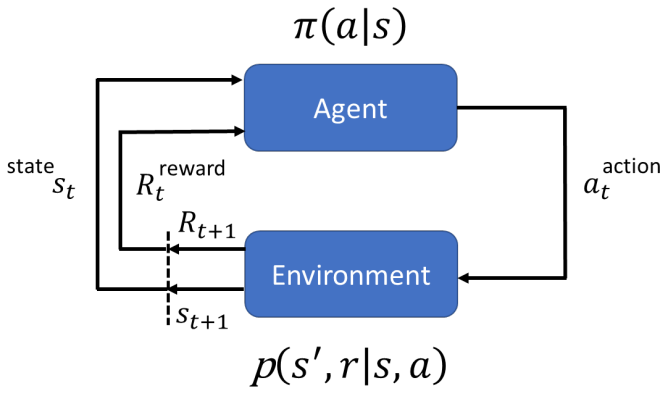

Figure A.4-26: A transition in a Markov Decision Process

At a given instant t, the environment will be in the **state** $\mathrm{s}(t)$, the agent will perform the **action** $\mathrm{a}(t)$, and consequently the agent will receive a **reward** $r = R(t+1)$ and the environment will move to the new state $\mathrm{s}' = \mathrm{s}(t+1)$. An **episode** is defined as an iteration where the environment starts from a certain state, and the agent plays a certain number of actions until a certain condition is met to end the episode (e.g., the environment reaches a certain wanted state, the agent plays a given number of actions, etc..).

The objective of the agent is to maximize the **return**, i.e., the sum of the future rewards:

$$G = \sum_{\tau} R(t+\tau) \qquad \textbf{(A.4-58)}$$

or some other objective that is a function of the reward.

In this context, one of the most known algorithms for RL is the so-called Q-Learning, and its neural network-based variant, the deep Q-network (DQN) algorithm [MKS+13]. DQN solves the problem iteratively, playing several episodes and learning the **action-state value function Q**, using the Bellman equation [JKH+19]. The action-state value function estimates the average return that the agent will get at the end of the episode, by following the policy $\pi(a|s)$ and performing action $\mathrm{a}(t)$ when the environment is on state $\mathrm{s}(t)$.

$$Q_\pi(s,a) = E\{G(t)|S(t) = s, A(t) = a\} \quad \textbf{(A.4-59)}$$

Once the action-state value function Q is known, the agent can directly derive its policy by simply taking in each state $s(t)$ the action $a(t)$ that maximizes $Q_\pi(s,a)$.

To apply the DQN solution to the MU-MIMO pairing problem, the proposed algorithm considers N users with a certain amount of data B to transmit in their buffer. The **state** of the system is described by the CQI, PMI and buffer status B of each user. The **action** performed by the agent is the selection of which users should be served in the next scheduling interval. Once a user is selected, the transmission to that user will be performed using the precoder indicated by the user PMI. To support MU-MIMO, the set of possible actions that the agent can take includes all possible users pairing. The maximum number of users that can be paired together by the agent can be limited to a value $M \leq N$, which defines the maximum cluster size that can be scheduled together in a given scheduling interval. The **reward** is then computed based on the amount of data that is served, which depends on the CQI, PMI, and amount of data in the buffer of the selected user(s). Note that when multiple users are selected, the amount of data served to a selected user can be reduced compared to the amount that would have been granted if the user was served alone. This is due to power sharing between co-scheduled users, and possible mutual interference if the users' transmission channels are not orthogonal. Nonetheless, the overall amount of data achieved by summing together all co-scheduled users could be higher than that granted by single user transmission, if the users are paired smartly. Since the achieved data rate is a measure of the quality of the pairing, this value has been linked to the reward. Moreover, in the proposed model, the reward initially computed based on the data rate was then reduced of a certain amount, to "pay" for the action taken, applying the concept of "living penalty". In this way the agent will try to minimize the number of actions to reach its final goal. Selecting a user that has no data in the buffer is also considered a penalty, and it is therefore mapped to a negative reward. The final goal for the agent is to empty all users buffers as fast as possible. Reaching the goal is paid with a large reward, and ends one episode of "the game". Once the action is taken, the state changes as the amount of data in the users buffers changes. CQI and PMI are assumed constant in an episode.

Using the DQN approach, the algorithm learns the Q-function through a Deep Neural Network, associating to each state the Q-value of each possible action that can be taken.

Simulation and results: the DQN model has been trained in a simple simulated scenario. In the simulator, N users are dropped randomly in the coverage area of a single Base Station, and pathloss is computed according to 3GPP specification TR38.901 [3GPP38901]. To simulate the effect of a random fast fading channels, for each user an ideal random channel matrix is generated with Rayleigh distributed channel coefficients. The channel matrix is then spatially correlated to simulate a La Plician distributed power angular spread around a randomly generated angle of arrival, as discussed in [CH08][YVT+14]. The detailed simulation parameters and assumptions are provided in Table A.4-15, Table A.4-16 and Table A.4-17. The proposed solution has been compared with results obtained assuming:

- a round robin (RR) scheduling approach (without MU-MIMO support),
- a greedy «genie» (GG) algorithm that at each scheduling step maximizes the served data-rate, computing the achievable data rate for all possible pairing of users, based on their full channel matrix and current buffer status, and selecting the pairing that maximizes the computed data rate at each scheduling step.

The DQN based algorithm has been trained over 25.000 episodes assuming 5 users per cell and a maximum cluster size M=3 (i.e., pairing maximum 3 users). The algorithm has then been tested over 200 episodes, comparing its behaviour with the traditional round robin approach and the greedy genie solution.

Figure A.4-27 shows the number of scheduling steps required to empty all users buffers with the different solutions under study. As it can be seen, DQN always outperforms the Round Robin solution, and its performance are close to the greedy genie algorithm, which however benefits from a complete channel knowledge, and can therefore be considered as an upper bound. More in detail, Figure A.4-28 provide the box plots (a) and cumulative distribution (b) of the obtained number of steps, showing that not only DRL is close in performance to the greedy genie algorithm, but these two approaches reduce the variability on the number

of required steps, determining a lower variance on the expected number of steps necessary to empty all users' buffers.

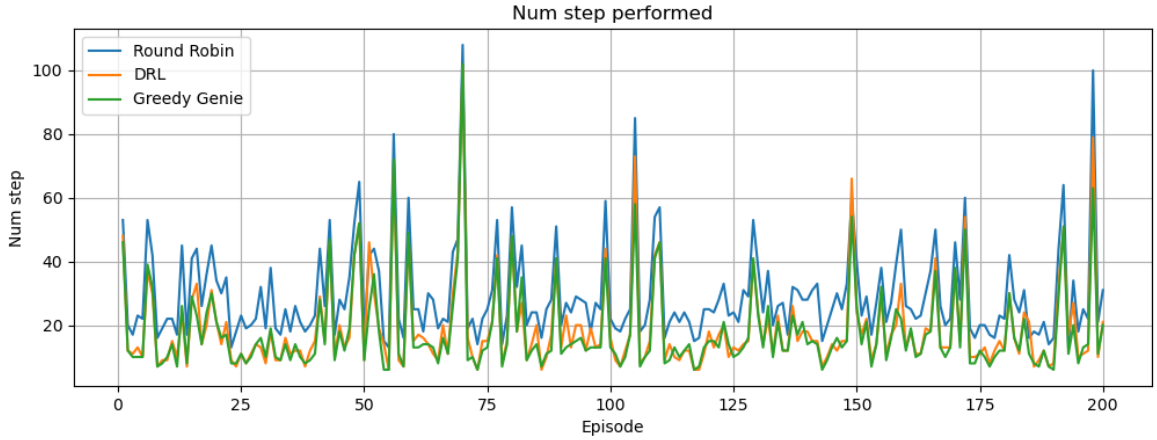

Figure A.4-27: Number of scheduling steps required to empty all users buffers with different algorithms

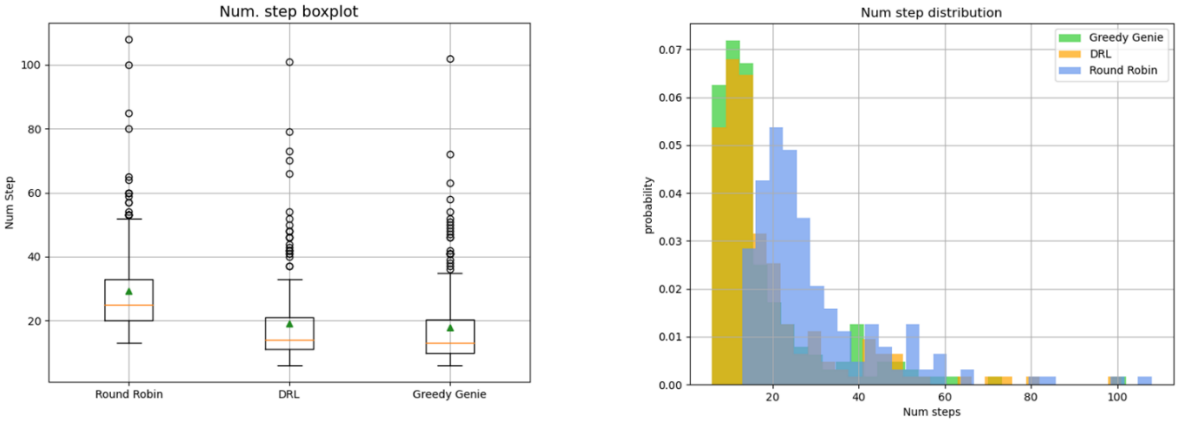

(a) (b)

Figure A.4-28: Box plot (a) and distribution (b) of the scheduling steps required to empty all users buffers with the different algorithms.

Overall, as shown in Table 6-2, DQN solution is ~38% faster in emptying user buffers compared to Round Robin, and it is only slightly slower than the Greedy Genie solution.

Taking into account the size of users' buffers and the amount of time required to empty them, it is possible to evaluate the achieved user rate and overall cell data rate. This information is reported in Figure A.4-29 and Figure A.4-30 respectively, where probability density function (pdf) and cumulative distribution function (CDF) for the user rate and cell data rate are plotted. Note that since DRL is faster than round robin in emptying user buffers, the obtained data rate per user and on the overall cell rate are significantly higher, and close to those achievable with the Greedy Genie solution.

By dividing the achieved cell data rate for the simulated bandwidth, it is possible to obtain the spectral efficiency achieved by the different algorithms, as summarized in Table 6-2.

While the results here obtained are promising, it should be noted that the considered scenario is ideal, with no inter cell interference, and a fading channel with strong spatial directivity, which can be easily exploited by the precoding matrices available in the codebook. Further analyses are needed in a more realistic channel scenario to fully assess the quality of the proposed solution. Moreover, the proposed greedy genie algorithm, used as an upper bound for DQN, can still find a suboptimal solution, as at each step it selects the pairing that

maximize the rate for that step, without considering the optimization problem as a whole. Better results might be achieved with a solution that exhaustively searches the whole space of the existing pairing solutions throughout the whole episode. A recursive solution can be designed to achieve this task, but it is expected that an exhaustive search could be very demanding in terms of computational time. Being able to exploit the full channel knowledge, the Greedy Genie algorithm here proposed has been considered as a valid upper-bound for DQN, that allowed to obtain good results within reasonable simulation time. The implementation of an exhaustive search algorithm will be part of future activities. Finally, more advanced deep reinforcement learning techniques could be considered to solve this problem, in particular if the complexity is increased by considering more users or more complex simulation scenarios. Advantage actor critic (A2C) is for example a promising solution that could be explored in further evolutions of this study.

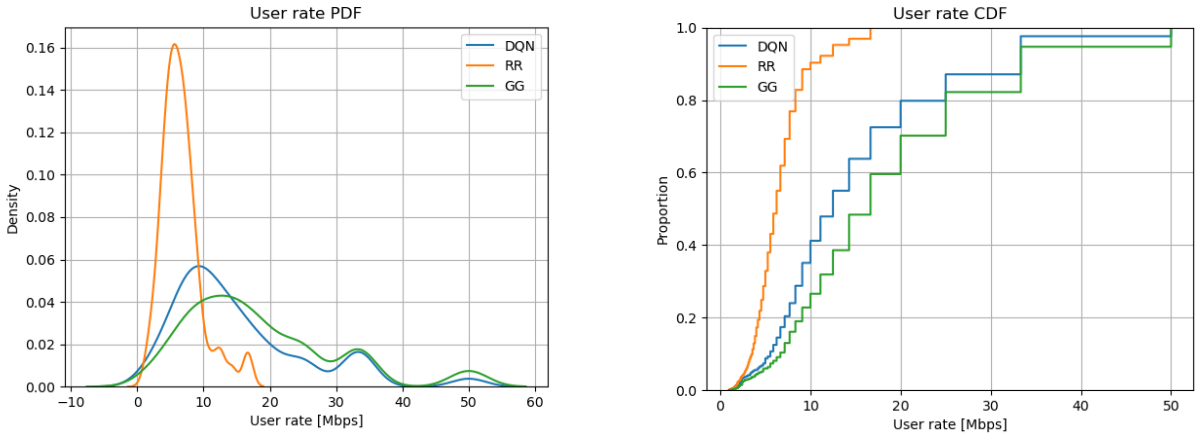

(a) (b)

Figure A.4-29: PDF (a) and CDF (b) of user data rate with the different algorithms (Round Robin – RR, Greedy Genie -GG and Deep Reinforcement Learning DRL).

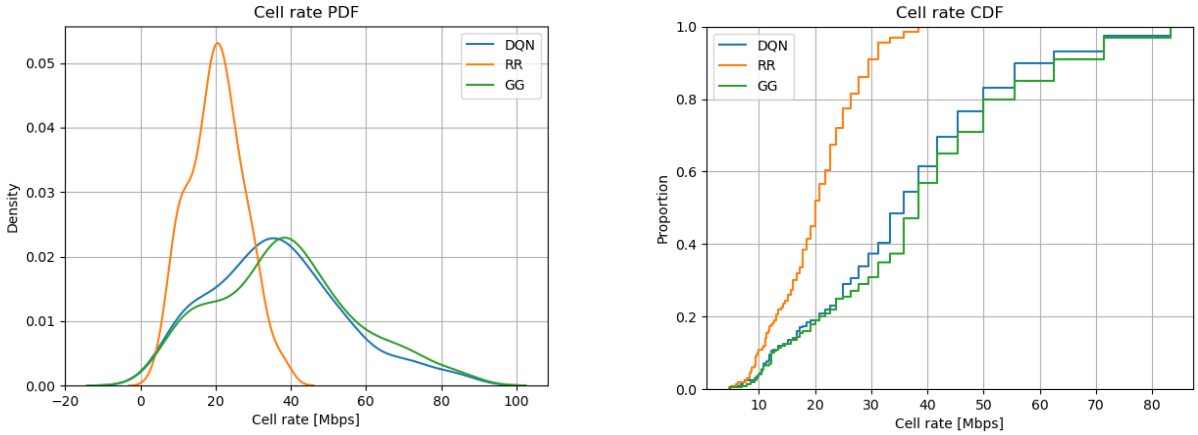

(a) (b)

Figure A.4-30: PDF (a) and CDF (b) of cell data rate with the different algorithms.

Table A.4-15: Detailed system parameters.

Parameter	Notation	Value	Notes
General deployment and environment			
Number of BS		1	
Number of UEs		5	
Cell range	Meters	1250	A large cell has been considered to have a reasonable CQI distribution

			even in the absence of other cells interference
Detailed deployment and architecture			
BSx number of TX antennas		32	Planar array: with N1=8 elements per row and N2=2 elements per column, Polarization = 2 (cross-polarized antenna elements)
Scheduling period	ms	1	
UEx speed	kmh	0	Static UEs
UEx number of RX antennas		2	1 cross-polarized antenna element
UE receiver architecture		MMSE	
UE Buffer Size	Kbit	100	
Frequency range and bandwidth			
Frequency band		FR1 and FR2	The actual carrier frequency does not impact on the proposed algorithm. In the current model it only impacts on the computation of propagation losses.
Bandwidth	MHz	10	
Details on Hardware parameters			
Ideal hardware		yes	

Table A.4-16: General Assumptions.

Hardware impairment	None
Synchronization	Ideal
Channel model	Channel is modelled with a Rayleigh distributed channel coefficients, with spatial correlation between the different channel coefficients introduced through a spatial correlation matrix, as discussed in [CH08] and [YVT+14].
Capacity Computation Formula	SNR values obtained at the receiver are converted in data rates using Shannon law. Single layer transmission is assumed.
CSI availability at transmitter	Only partial CSI available, in the form of channel quality indicator and precoding matrix indicator.
Precoding Codebook	Precoding used for PMI computation based on 3GPP TS 38.214 v15.16.0 [3GPP38214] Table 5.2.2.2.1-5, with N1=8, O1=1, N2=2, O2=1, one layer

Table A.4-17:Assumptions for AI/ML-assisted transmissions.

Type of the used AI/ML training method	Reinforcement Learning
Training	Offline
'Features' and 'labels' for training the models	Features: PMI, CQI, and Buffer status (in Kbit) per UE Labels: N/A
Type of the AI model	DQN (deep Q-learning network)
Model architecture	Neural network with one input layer of size 15, two hidden layers of size 23 and 38, one output layer of size 25
Loss function for training	N/A
Model deployment	Transmitter

Training scheme	Centralized

A.4.7 Pilot assignment for D-MIMO

This section provides further insights on the enabler "Pilot assignment for D-MIMO", presented in Section 6.3.4.

The proposed method consists of two components: RL and GNN. GNN is utilized to approximate the group to which a given node belongs, while RL applies specific principles to the output of GNN in order to accomplish the objective. The RL can be represented by the following Markov decision processes (MDP) elements as:

A) State: The RL state for each node is specified as a vector $\boldsymbol{s} = [s_i, i \in \mathcal{V}] \in \{1,2,\dots,K,0\}^{\mathcal{V}}$, where $s_i = k$ represents that the node i is assigned the k-th colour, $s_i = 0$ denotes the state is initialized to all "deferred", once all nodes have been assigned colours or reached the time limitation.

B) Action: Given a state vector $\boldsymbol{s}$, the action $\boldsymbol{a} = [a_i : i \in \mathcal{V}] \in \{1,2,\dots,K,0\}$ denotes the vertex I is assigned the colour k if $a_i = k$ or deferred if $a_i = 0$. Note that, the vertex that has been colored in previous stages will not be given any new action.

C) Transition: The LCG colouring method can typically address both (K, r)-local colouring problems and K-colouring problems. As a consequence of focusing exclusively on the colouring issue in this work, the transition of local colouring is disregarded. Additionally, the availability of local colouring ensures that the LCG method can be tailored to various objective functions and is extensible to other communication performance metrics. For colouring problem, the RL transition from state $\boldsymbol{s}^t$ to $\boldsymbol{s}^{t+1}$ through two steps: update and clean-up-I. In the update step, the vertex is marked as deferred in the previous state is defined as the action, i.e., $s_i^{t+1} = a_i^t$, where t determines the previous state. The cleaning-up-I phase involves verifying the colouring rules. If a vertex fails to respect to the colouring rules, specifically by assigning the same colour to two adjacent vertices, the corresponding nodes are mapped to the "deferred" state.

D) Reward: The reward in the approach consists of two parts: the cardinality reward R_c, and the early-terminated reward R_t as $R = R_c + \beta R_t$. The cardinality reward from state s^t to state s^{t+1} can be defined as

$$R_c(\boldsymbol{s}^t, \boldsymbol{s}^{t+1}) = \sum_{i \in \mathcal{V}_{t+1} \setminus \mathcal{V}_t'} 1 - \sum_{i \in \mathcal{V}_{t+1} \setminus \mathcal{V}_t} 1, \tag{A.4-60}$$

The agent will be rewarded if more nodes are assigned in the new state, and it encourages the RL to extend the cardinality of the successfully assigned node set. To encourage the agent making the decision as soon as possible, the reward R_t will be given when the process terminates at the time t in the given limitation B, thus the early-terminated reward can be written as

$$R_t = \frac{B - t}{B}. \tag{A.4-61}$$

To sum up, rewarding the agent for assigning additional nodes to the new state rewards the RL for increasing the cardinality of the node set that was effectively assigned. In order to encourage the agent to make the decision promptly, the early-terminated reward R_t is provided upon the process terminating at time t within the specified limitation B.

E) The model applies the Actor-Critic reinforcement learning based on graph convolutional neural networks. Both policy network $\pi(\boldsymbol{a}|\boldsymbol{s})$ and value network $q(\boldsymbol{s}, \boldsymbol{a})$ consist of 4-layers GraphSAGE networks [HYL17] with GCN aggregator [KW17]. The n-th layer performs the following transformation on input $\boldsymbol{H}$:

$$h^n(\boldsymbol{H}) = \mathrm{ReLU}\left(\boldsymbol{H}\boldsymbol{W}_1^{(n)} + \boldsymbol{D}^{-\frac{1}{2}}\boldsymbol{B}\boldsymbol{D}^{-\frac{1}{2}}\boldsymbol{H}\boldsymbol{W}_2^{(n)}\right), \quad \textbf{(A.4-62)}$$

where $\boldsymbol{B}$ and $\boldsymbol{D}$ represent the adjacency matrix and degree matrix, respectively, and $\boldsymbol{W}_1^{(n)}$ and $\boldsymbol{W}_2^{(n)}$ are the weights updated during the training process. The policy and evaluation of networks utilize softmax and graph read-out functions with sum pooling [XHL+19] instead of ReLU. The current iteration index of MDP and the sum of one-hot encoding of the neighbour's state are applied as the neural network's input.

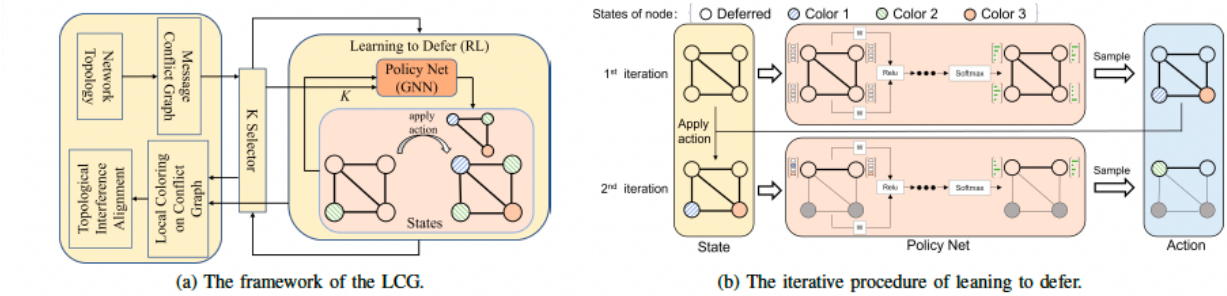

(a) The framework of the LCG. (b) The iterative procedure of leaning to defer.

Figure A.4-31: Learning to code on graph structure figure. Figure (a) illustrates the structure neural network, and Figure (b) presents the concept clean up.

A.4.8 AI-based PA-nonlinearity compensation

The architecture of the neural network is described in Table A.4-18.

Table A.4-18: The neural network specification.

parameters	setting
Number of input neurons	3
Number of output neurons	log2(M)
Number of hidden layers	3
Number of neurons in each layer	64
The activation function of each hidden layer	ReLu
The activation function of the output layer	linear

The assumptions regarding training of ANN de-mapper are summarized in Table A.4-19.

Table A.4-19: The neural network training parameters.

Parameters	setting
Number of Res	1.152e6
Optimizer	Adam
Mini batch size	1024
Learning rate	0.0001
Epochs	100

UE and network capabilities: In this case, the network needs to be capable of PA post distortion and the UE also need to comply with a new specification allowing for increased in-band distortions. This would have impact on UE hardware implementations, 3GPP RAN4 in-band requirements and likely a new performance specification.

Training data generation: it is essential that the base station can collect training data from different UEs and that it knows that the collected data represents the UE operating modes expected in the field. To acquire the labels based on UE hardware operating conditions (not known to the base station) the UE could for example transmit a pseudo-random bitstream known to the base station (Figure A.4-32). The operating points of the UE Tx should still be diverse enough to cover the expected operation in the field.

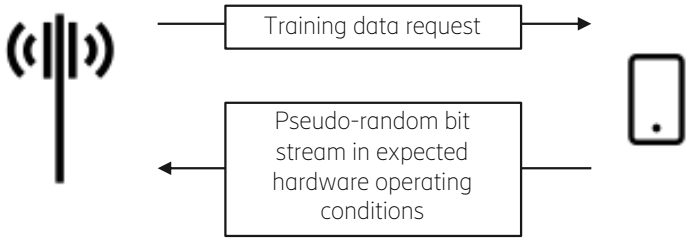

Figure A.4-32: Training data generation scheme.

Simulation and results: The performance of the AI-empowered receiver against a legacy receiver with conventional de-mapper in presence of PA non-linearity and linear PA is compared in this section. Table A.4-20 summarizes simulation assumptions.

Table A.4-20: Simulation assumption for training and validation.

Parameters	Values
Waveform	DFT-s-OFDM
FFT size	4096
PA back off	4, 5, 6, 7, 8, 9 dB
PA type	CMOS (memoryless) [FHS23] GaN (memory) [FHS23]
PRB	250
Carrier bandwidth (MHz)	400
Subcarrier spacing (Hz)	120e3
Carrier frequency	30e9
MCS table	MCS Table II
BS antenna rows	4
BS antenna columns	8
Polarization	2
MCS	Link adaptation (10% target BLER)

Operation point: Simulations are performed to measure the in-band distortions in term of EVM and out of band (OOB) distortions for different PA back-off values. Figure A.4-33 shows the power spectral density (PSD) of the transmitted signal and measured ACLR for different PA back-off values. The measured ACLR fulfils the ACLR requirements in FR2 which is 17 dB, hence, for the considered operating points, out of band emission requirements comply with the 3GPP RAN4 requirements in the existing standard. The simulated EVM values for different PA back-off values are shown in Figure A.4-34. Reasonable operating points for 256QAM while still fulfilling EVM requirements in the current standard is around 8-9 dB backoff.

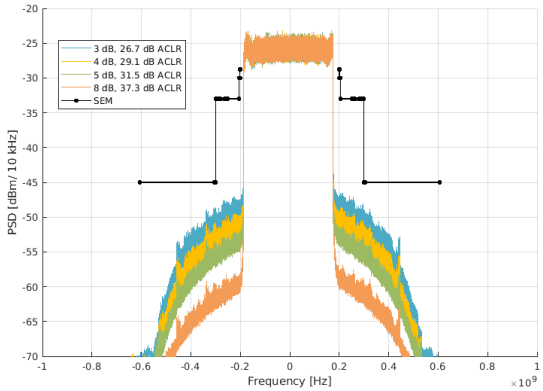

Figure A.4-33: Power spectral density for different power amplifier back-off

Simulated EVM [%]

	Backoff [dB]			
	10	8	6	4
16QAM	2.2	2.6	3.5	7.4
64QAM	2.2	2.7	3.6	7.7
256QAM	2.2	2.7	3.7	7.8

Figure A.4-34: Simulated EVM for different PA back-off

Simulation scenarios: The advantage of the proposed method is investigated under four scenarios namely fixed transmitter, fixed throughput, fixed pathloss, and improved pathloss which are outlined in the following.

Fixed transmit scenario: In this scenario, the UE transmit conditions (e.g., PA back-off) are fixed and performance is compared at a certain SNR in terms of throughput. The intention is to investigate what happens when turning on an AI/ML based receiver in the current operation of the transmitter. The findings are as follows.

Reasonable operating modes for the PA while still fulfilling the current EVM requirements for 256QAM are estimated to be 8-9 dB backoff. Both operating points are shown in Figure A.4-35 to understand the benefits of simply turning on AI/ML in current receivers. The throughput gains at SNR=13 dB and 17 dB are shown in Table A.4-21.

Table A.4-21: Throughput gain of the AI/ML receiver in fixed transmit scenario.

Backoff [dB]	SNR [dB]	Gain [%]
8	13	3 %
	17	14%
9	13	6%
	17	2%

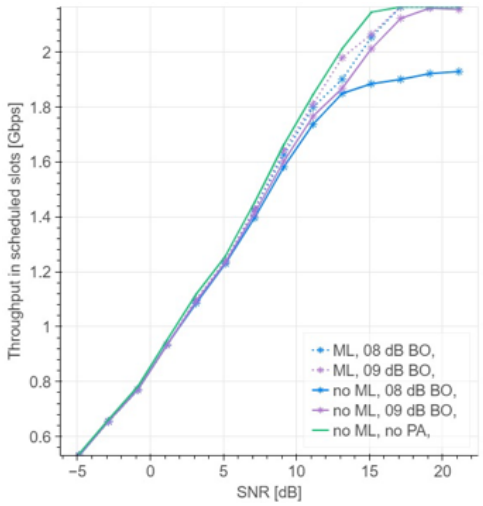

Figure A.4-35: Throughput of the AI/ML receiver, and the legacy receiver for operating point comply with the standard requirements.

Fixed pathloss scenario: In this case, power-limited scenario with fixed pathloss and fixed packet to be delivered are considered. The intention is to investigate, at a power-limited operation in an existing system, how can throughput performance be improved while energy efficiency increases.

In a power-limited scenario, where the UE can increase the transmit output power with PA post distortion, given that the receiver can handle the increased distortion using the new feature, the throughput can increase. An example in Figure 4-36 shows 10% increase in throughput (taking the most promising backoff value for ML, out of some backoff candidates, see green circles). The impact on energy consumption for the class A power efficiency model is 13% reduction. As highlighted earlier, the assumption on the PA efficiency profile impacts gain/loss figures considerably.

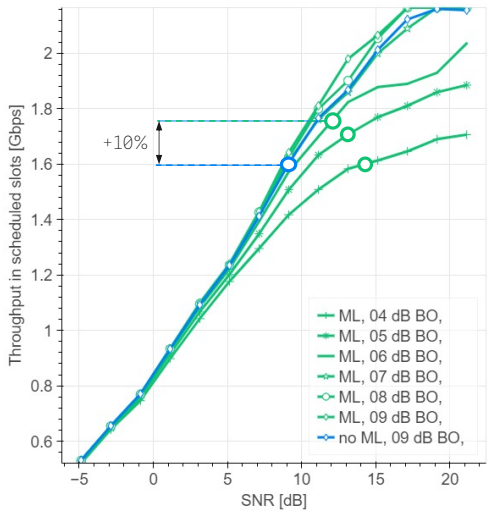

Figure A.4-36: Throughput versus SNR performance.

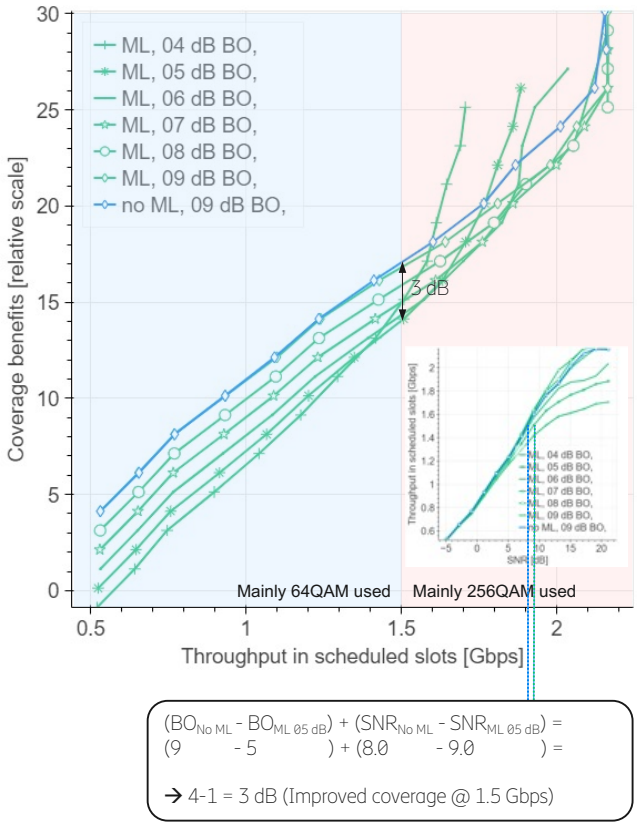

Figure A.4-37: Coverage benefit versus throughput.

Improved pathloss scenario: In this case considering a power-limited scenario, at a given fixed throughput, this study investigates how much coverage and energy efficiency can be improved. The intention is to investigate, at a power-limited operation in today's system, how much can coverage and energy efficiency be improved while reaching the desired throughput.

In addition to the <Fixed THP> evaluations on energy efficiency, in a power limited case, the PA post distortion can be used to increase "coverage" (the cell area where a certain throughput can be reached). Around 2-3 dB in coverage gain can be seen in throughput ranges used by 256QAM, as shown in Figure 4-37.

A.5 Flexible spectrum sharing and coexistence

A.5.1 Assumptions and models to determine sharing possibilities

Parameters and deployment considerations

The following tables present the relevant system and deployment parameters for comparison, mainly derived from agreed technical and operational characteristics in the International Telecommunications Union (ITU) expert Working Party 5D (WP 5D) [ITU-CPM23].

Table A.5-22: Mobile network system and deployment-related parameters.

Parameter	Value
BS Carrier frequency	3.85 GHz
BS Channel bandwidth	100 MHz
BS Antenna height	10 m
BS Cell radius	400 m
Sectorization	1 sector
Frequency reuse	1
BS TDD activity factor	75%
Network loading factor	100% and 50%
UE height	1.5 m
Simultaneous UE in cell	3 per sector
UE deployment	Uniform and Rayleigh distributions

Table A.5-23: Antenna and power characteristics for a base station (AAS).

Parameter	Value
Antenna pattern	Refer to [ITU-M.2101]
Element gain (incl. Ohmic loss) (dBi)	6.4
Horizontal/vertical 3 dB beamwidth of single element (deg)	90º for H, 65º for V
Horizontal/vertical front to back ratio (dB)	30 for both H/V
Antenna polarization	Linear ±45º
Antenna array configuration (row × column) *	8×8 and 4×4
Horizontal/vertical radiating element spacing (wavelength)	0.5 for H, 0.7 for V
Array Ohmic loss (dB)	2
Conducted power (before Ohmic loss) per antenna element for 8×8 and 4×4 AAS** (dBm)	5.5 (8×8) 17.5 (4×4)
BS max. coverage angle in the horizontal plane (deg)	±60
BS vertical coverage range (deg)	90-120
BS mechanical down-tilt (deg)	10
Max. BS equivalent isotropic radiated power (EIRP) for 8×8 and 4×4 AAS (dBm/100 MHz)	51

* For the small/micro cell case, for example, 8×8 means there are 8 vertical and 8 horizontal radiating elements.

** For example, for an 8×8 AAS, the conducted power per element assumes 8×8×2 elements (i.e., power per H/V polarized element).

The FSS ES parameters in this analysis adhere to ITU expert group WP 4A's agreed technical and operational characteristics [ITU-S.2368]. Additional parameters are based on deployments in Germany, such as Fuchsstadt [Int23] and DLR [DLR23]. The following tables present the FSS ES parameters and the FSS protection criteria. The latter pertain to the time-associated availability of FSS links. Monte Carlo sharing studies may involve additional considerations, like geographical locations or deployment domains, which don't vary over time. Thus, percentages should be understood in contexts beyond time, such as location and probability.

Table A.5-24: FSS system and deployment-related parameters.

Parameter	Value
Antenna diameter (m)	4.8 (DLR) and 32 (Fuchsstadt)
Peak antenna gain (dBi)	44 (DLR) and 61 (Fuchsstadt)

Antenna pattern	Based on Rec. ITU-R S.465 [ITU-S.465] and on a more realistic pattern based on Bessel functions [Orf16]
Receiving system noise temperature	120 K for small antennas (1.2-3 m) 70 K for large antennas (4.5 metres and above)
Min. antenna elevation angle (degrees)	16.1 (DLR) and 8.4 (Fuchsstadt)
Antenna height (m)	14 (DLR) and 20 (Fuchsstadt)

Table A.5-25: FSS ES Protection Criteria.

Frequency Ranges	I/N Criteria (dB)	Percentage of time for which the I/N value could be exceeded (%)
3 600-3 800 MHz (space-to-Earth)	−10.5	20%

For this analysis, the interference from a single BS is assessed. Particularly, the single BS is always facing the FSS ES to account for the worst-case. Figure A.5-38 shows an example of the BS and a FSS ES when they are positioned facing each other with a separation distance of 3 km. In each snapshot of the Monte Carlo simulation, 3 UEs are deployed within each BS sector following a uniform or Rayleigh distribution as shown in Figure A.5-39. It is noted that a Rayleigh distribution is deemed more appropriate for some networks, e.g., local networks, provided that these networks are deployed where users are expected to remain in the local network cell, rather than moving between different cells as in public mobile networks. Furthermore, the BS transmit power is assumed to be split equally among its UEs, meaning that the transmit power for each UE is 10log10(1/3) = -4.77 dB lower than the total transmit power of the BS. Additionally, the FSS ESs in Table A.5-24 are located in 48.086° N, 11.281° E (DLR site), and 50.119° N, 9.924° E (Fuchsstadt site). For simplicity, a common latitude of 49° is used for both sites.

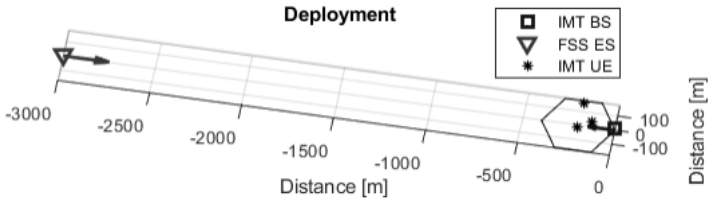

Figure A.5-38: Deployment comprising a single FSS ES and a single BS.

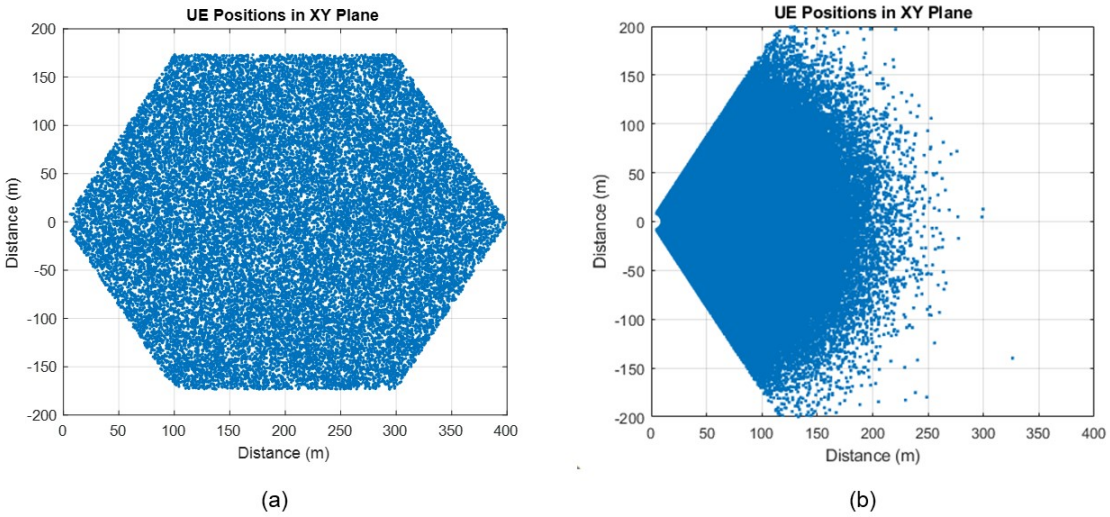

Figure A.5-39: UE deployment: (a) uniform distribution and (b) Rayleigh distribution.

Propagation: The Recommendation [ITU-P.452] is used in this analysis to model the basic propagation loss between stations on the surface of the Earth as specified by the ITU-R WP 3K and 3M. A smooth earth surface

is assumed. Furthermore, to extend ITU-R P.452 model time percentage (Tpc) range to 0-100%, the ITU-R study group 3 (SG 3) guidance suggests that when Tpc > 50%, the basic transmission losses remain the same as when Tpc = 50. Hence, a random variable with a uniform distribution between 0-100% is applied for Tpc.

Additionally, due to the lack of exact information regarding vegetation/forest areas and other obstacles along the propagation path, the use of the clutter loss model in Recommendation [ITU-P.2108] is a good compromise to account for the additional attenuation due to vegetation and/or other objects. Thus, the clutter losses for terrestrial paths are calculated in accordance with Rec. ITU-R P.2108-1 using a fixed percentage of locations equal to 50% on at least one of the ends of the propagation path. It is noted that this Recommendation indicates that statistical models are to be used when precise knowledge of the radio path is not known such as the width of streets, heights of buildings, and depth of vegetation.

Parabolic reflector radiation pattern: In addition to the model in [ITU-S.465], the following normalized antenna gain pattern is used to model the FSS ES antenna pattern. This pattern is associated with a standard reflector antenna featuring a circular aperture [Orf16]:

$$\begin{cases} 1 & \text{for } \theta = 1 \\ 4\left|\dfrac{J_1(k \cdot a \sin\theta)}{k \cdot a \ \sin\theta}\right|^2 & \text{for } 0 < |\theta| \leq 90° \\ 4\left|\dfrac{J_1(k \cdot a \sin 90°)}{k \cdot a \ \sin 90°}\right|^2 & \text{for } 90° < |\theta| \end{cases} \quad \textbf{(A.5-63)}$$

where $J_1(x)$ represents the Bessel function of the first kind and first order, θ is the angle measured from the antenna's main beam, a denotes the radius of the antenna, and $k = 2\pi f/c$ is the wave number where f is the frequency and c is the speed of light in vacuum. It is noted that $k \cdot a$ represents the number of wavelengths on the circumference of the aperture and remains constant regardless of the operating frequency.

As example, Figure A.5-40 shows the gain pattern cuts of the DLR and Fuchsstadt antennas along with fitting masks:

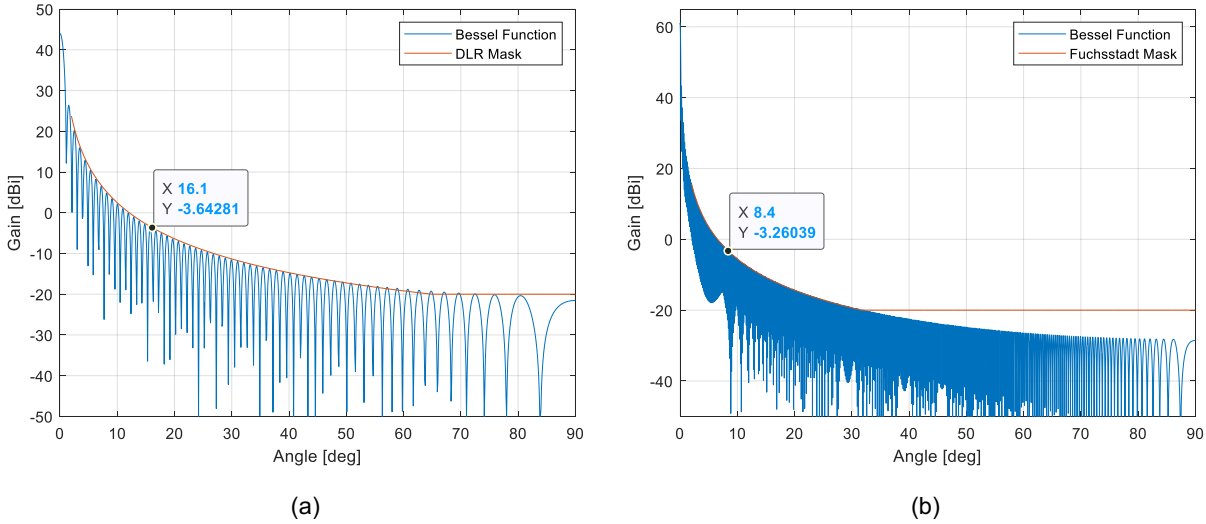

Figure A.5-40: Gain pattern cut of (a) DLR and (b) Fuchsstadt antennas at 3.8 GHz.

The fitting masks depicted in Figure A.5-40 are used in the Monte Carlo simulations. The gain of the DLR and Fuchsstadt antennas towards horizon are around -3.64 dB and -3.26 dB respectively at their corresponding minimum elevation angles. Lastly, the validity of the radiation patterns is assessed by computing the total integrated gain (TIG) as it should be equal to the efficiency of the antennas:

$$TIG = \frac{1}{4\pi} \int_{-\pi}^{\pi} \int_{0}^{\pi} G(\theta, \varphi) \sin(\theta)\, d\theta d\varphi = \eta \quad \textbf{(A.5-64)}$$

The obtained TIG values are -1.716 dB and -1.212 dB for the DLR and Fuchsstadt antennas respectively. These values correspond to efficiencies of 67.3% and 75.6%, which are considered reasonable provided their sizes.

A.5.2 Spectrum sharing between 6G and FSS UL in the centimetric range

Table A.5-26: Selection of antenna and deployment-related parameters for IMT.

	6425-10500 MHz	**24.25-33.4 GHz**
Deployment type	Macro urban	Urban hotspot
Antenna pattern	Refer to Recommendation ITU-R M.2101 Annex 1, section 5	Refer to Recommendation ITU-R M.2101 Annex 1, section 5
Element gain (dBi)	5.5	5
Antenna array configuration (row x column)	16 x 8 elements	8 x 8 elements
Horizontal/Vertical radiating element spacing	0.5 of wavelength for H, 0.5 of wavelength for V	0.5 of wavelength for both H/V
Array Ohmic loss (dB)	2	3
Conducted power (before Ohmic loss) per antenna element (dBm/200 MHz)	22	10
Mechanical downtilt (degrees)	10	10
Antenna height above ground level (m)	18	6

Table A.5-27: Satellite parameters

	Starlink	**One Web**
Average orbit height (km)	550	1200
Antenna gain (dBi)	32	32
Bandwidth (MHz)	200	200
Nadir footprint diameter (km)	43	94
Active BS in the Nadir footprint	430	850

A.5.3 TN-NTN spectrum sharing in S-Band: parameters for co-existence studies

The serving TN BS is assumed to be the nearest BS to the TN user and serves the TN UE in the DL direction. It is assumed that the same frequency band is shared among all TN BS and with the NTN that provides coverage over the TN cluster. This causes co-channel interference at the TN UE's reception.

The satellite transmit power, cell radius, and maximum antenna gain are $p_T = 46$ dBm, 25 km, and 30 dBi, respectively. The main lobe gain of the BS antennas is assumed to be 17 dBi. The BS transmit power is assumed to be $p_T = 46$ dBm. The altitude is set to {200, 600, 1200} km, unless stated otherwise. Inter-site distances for TN network are assumed to be 0.75 km and 7.5 km for urban and rural areas, respectively. The number of BS on each TN cluster is assumed to be 19. The operating frequency and bandwidth are set to be 2 GHz and 20 MHz, respectively.

A.5.4 Sub-THz access: simulation assumptions

The following list gives an overview on the general simulation setup with a few used assumptions:

- Focus is on the simulation of the sub-THz access scheme, i.e., beam pairing as well as resource assignment and interference in dynamic scenarios. The omni-directional part is not modelled. Shared data is directly

transferred between the entities. Goal is to check under which circumstances the access scheme works properly and what key performance indicators can be achieved.
- One of the simulated use cases is a train station scenario. A lot of people leave a train, connect to the sub-THz network and transfer data while moving through a corridor. Only a limited amount of time is available to transfer the data and the beam pairing is demanding.
- Directed beams as well as beam steering (antenna array) is simulated; antenna array dimensions and output power can be varied.
- Line-of-sight paths are handled. Reflections are ignored. Multiple-input multiple-output transmission and polarization effects are not included.
- Communication bandwidth, carrier frequency, modulation scheme can be varied.
- Data rate is defined by bandwidth, modulation, and duration; no dynamic selection of transmission parameters beside TDD patterns are included.
- Physical layer and layer 2, e.g., coding, HARQ, medium access control, RLC, are not simulated; only time and resources for a transmission/reception are defined and checked against the required and achieved SINR.

A.5.5 Risk-informed random access: simulation assumptions

Table A.5-28 shows the assumed parameters taken for the UEs in the simulation. The properties of antennas, UEs, and the base station can be set using the built-in settings of the Wireless InSite. A pre-defined directive antenna model is assumed for the base station and omnidirectional antennas are used for UEs.

Table A.5-28: Satellite parameters.

Parameter	Value, values or range
UE transmission power	23 dBm
UE height	2 m
UE SINR limit	18 dB
Probability of packet generation	0.01 ... 0.99, step = 0.01
Post-collision send probability (CSMA only)	0.1
Number of mini-slots in one slot (CSMA only)	100
Detection threshold	-90 dBm

A.5.6 Inclusive radio interface via TN/NTN enhancements

Reduction of NTN HO signalling overhead

To examine if there is really benefit for overhead reduction in signalling of HO commands by using CS, this work considers a simplified model of the two possible ways of delivering the common information and it can be seen that there exists a trade-off when using dedicated versus CS [R2-2311212]:

- Dedicated: It can be assumed an amount of X resources, or physical resource blocks (PRB) are used in average per HO command and n HO commands are required per second for each UE in cell. In that case, the average resource usage can be calculated as: $n*X$ PRB/s.
- Common: Here, this can consider Y PRB per CS occurrence and m CS occurrences per second for the group of UE. In general, Y is to be expected larger than X, as it will need to correspond at least to the maximum of PRB per HO needed for a UE in the group; link adaptation cannot be optimized for all UE in the group. For example, in case CS is ensured by broadcast signalling (i.e., CS to all UEs in cell), Y would correspond to cell edge conditions so that all UE in the cell would be able to decode the common information.
  Regarding m, a) in case CS is ensured by broadcast, it would need to be large enough to ensure connected UEs always have an opportunity to acquire it before HO, but small enough to not compromise the expected signalling gain; b) in case CS is ensured by group signalling (i.e., CS to defined subset group of UE within the cell), it can be assumed to be n/S, where S define the average group size. In that latter case, one should also take into account additional signalling (G) required for groups configuration.

In general, the average resource usage with CS can be calculated as: *m*Y (+G)* PRB/s.

It can be seen that it is questionable whether CS is always a good solution for HO signalling overhead reduction, also considering the possibility of extra feedback required in UL for network to ensure that such transmission was effectively received by the UE.

QoS aware omission of HO common information: It is also possible to omit HO common information in HO command message and UE acquires some of the required parameters while in source cell, during source/target overlap time. This is beneficial to reduce interruption time in case some parameters can be available (and also within valid duration) from source cell through other means during overlap time. For example, in 3GPP Rel.17/Rel.18, an important signalling is "*target cell NTN-config*" information element (IE) which bears the whole ephemeris and common TA information. This IE can be carried in HO/CHO message, where it is possible that its validity expires way before HO is executed. But this IE can be also carried from a more frequent common signalling message, SIB19. To reduce signalling overhead in HO/CHO, network should be allowed to omit NTN-config in HO/CHO message while ensuring that the UE would benefit from a more recent NTN-config received "for free" from a source cell SIB19 update (see Figure A.5-41). To ensure that the relevant HO information is up to date for the UE (e.g., aligned epoch/validity duration of serving and target cell and valid NTN-config at the time of HO/CHO execution) the UE may have to read/receive the regular CS (e.g., SIB19) more often. This could be requested by the network through an indication during UE configuration.

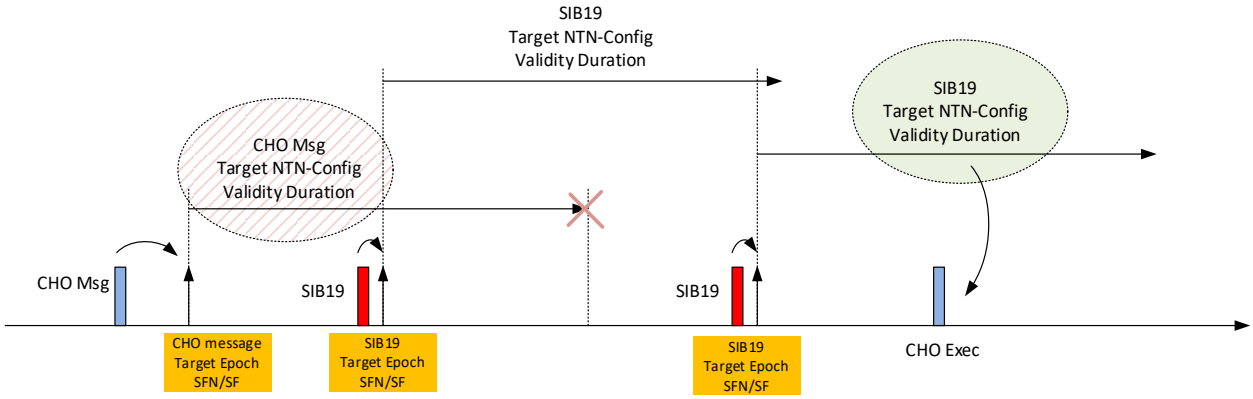

Figure A.5-41: Example (5G standard) of acquiring HO parameters in source cell and omitting common information in HO command message. UE uses a more recent NTN-config from a source cell SIB19 update instead of a CHO message with expired validity before CHO execution.

Cell change without HO

For the PCI unchanged solution, the following drawbacks can be observed [R2-2311223]:

- Questionable interruption time reduction, as target cell needs to be synchronized after leaving source cell. In 5G, interruption time at HO, defined as the time between HO command and start of random-access transmission to new cell (not including the RRC procedure delay), can be modelled as [38.133]:

  $$T_{interrupt} = T_{search} + T_{IU} + T_{processing} + T_{\Delta} + T_{margin} \text{ ms}$$

  where T_{search} is the time required to search the target cell when the HO command is received by the UE, T_{Δ} is time for fine time tracking and acquiring full timing information of the target cell, $T_{processing}$ is the time for UE processing (e.g., RF/baseband re-tuning), T_{margin} is the time for post-processing of the SSB, T_{IU} relates to the interruption uncertainty in acquiring the first available physical random access channel (PRACH) occasion in the target cell, and T_{rs} is the periodicity of the SSB-based measurement timing configuration periodicity of the target cell, a time window introduced to notify the UE about the periodicity and the timing of the SSB that the UE must use for cell quality measurements.
  The general assumption in [38.133] test parameters is $T_{IU} = T_{processing} = T_{\Delta} = T_{search} = T_{rs} = 20$ ms, and $T_{margin} = 2$ms. Without the need for $T_{processing}$ in case HO procedure for UE is avoided, and considering that the cell is known (i.e., $T_{search} = 0$), the resulted interruption time should be $T_{interrupt} = 62$ms. PCI unchanged solution although removes $T_{processing}$, it adds back $T_{search} = 20$ms, resulting into similar overall interruption time, in case of hard satellite switch, which is a common practical case.

- Impact on other UEs: There can be UEs in the system whose mechanism for mobility mostly relies on soft switch, with a temporary overlap between source and target cells (e.g., legacy Rel-17 NTN UEs). UEs deployed on such "unchanged PCI" network, requiring hard switch, would suffer impact on HO interruption, as they will have an additional penalty of T_{search} = 20ms, within the benefit of removing $T_{processing}$, leading to $T_{interrupt}$ = 82ms compared to existing example above.
  Another possible concern is the behaviour of legacy UEs in case of same cell HO, traditionally used for, e.g., key refresh, not for resynchronizing the cell. Normally, for the hard service link switch scenario, legacy UE shall use a HO (reconfiguration with sync) with different PCI. The target cell is unknown and would be synchronized from scratch by the UE. However, if deployed in "unchanged PCI" network, the hard switch scenario would need a same cell HO: reconfiguration with sync, with same PCI. In such case, the target cell is very well known. A sensible UE implementation would use this information (just as for a HO to another known cell). Hence, the scenario is different, and it is unclear to which extent this would work without issues for legacy UEs.
  Finally, if other UEs do not support time-based CHO, a HO message would have to be sent. Compared to the hard service link switch scenario with different PCI, there is an additional constraint when PCI is unchanged: as long as the service link switch has not occurred, source cell synchronization messages (i.e., SSB in NR) are sent. Thus, the HO message would need to be sent at the very last time as there should be no source cell SSB after the HO message and before the switch. Otherwise, there is a risk that the UE just sync again to the source cell (see Figure A.5-42).

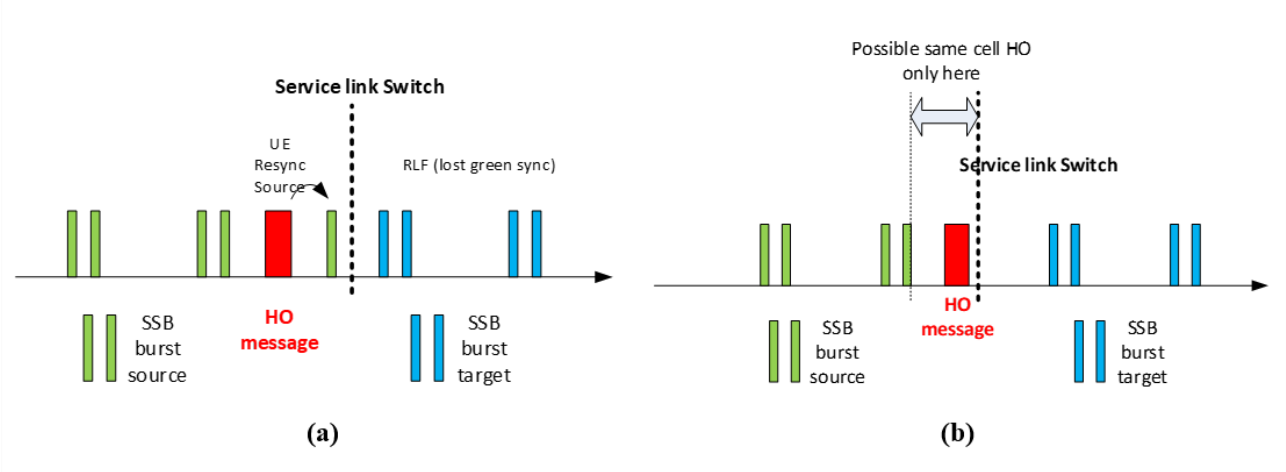

Figure A.5-42: (a) Issue of source cell resync; (b) Implementation constraint.

- Additional ephemeris / common TA provisioning.
  Although the unchanged PCI solution involves no HO command, there are main configuration parameters that are changed at the time of the switch (e.g., ephemeris and common TA parameter, included in NTN-config signalling for 5G). The UE needs those parameters to (again) access the cell. These could be read from existing common signalling (e.g., SIB19) in target cell, after the service link switch (thus, with increased interruption time) or from source cell new common signalling/mechanism (thus, could not be used by legacy UEs).